RESPONSE OF ULTRA HIGH PERFORMANCE FIBER REINFORCED CONCRETE BEAMS UNDER FLEXURE AND SHEAR

By

Roya Solhmirzaei

A DISSERTATION

Submitted to
Michigan State University
in partial fulfillment of the requirements
for the degree of

Civil Engineering - Doctor of Philosophy

2021

ABSTRACT

RESPONSE OF ULTRA HIGH PERFORMANCE FIBER REINFORCED CONCRETE BEAMS UNDER FLEXURE AND SHEAR

By

Roya Solhmirzaei

Ultra high performance concrete (UHPC) is an advanced cementitious material made with low water to binder ratio and high fineness admixtures, and possesses a unique combination of superior strength, durability, corrosion resistance, and impact resistance. However, increased strength of UHPC results in a brittle behavior. To overcome this brittle behavior of UHPC and improve post cracking response of UHPC, steel fibers are often added to UHPC and this concrete type is designated as Ultra High Performance Fiber Reinforced Concrete (UHPFRC). Being a relatively new construction material, there are limited guidelines and specifications in standards and codes for the design of structural members fabricated using UHPFRC. To develop a deeper understanding on the behavior of UHPFRC flexural members, seven beams made of UHPFRC are tested under different loading conditions. The test variables include level of longitudinal reinforcement, type of loading (shear and flexure), and presence of shear reinforcement. Further, a finite element based numerical model for tracing structural behavior of UHPFRC beams is developed in ABAQUS. The developed model can account for the nonlinear material response of UHPFRC and steel reinforcement in both tension and compression, as well as bond between concrete and reinforcing steel, and can trace the detailed response of the beams in the entire range of loading. This model is validated by comparing predicted response parameters including load-deflection, load-strain, and crack propagation against experimental data obtained from tests on UHPFRC beams with different material characteristics and under different loading configurations. The validated model is applied to conduct a set of parametric studies to quantify the effect of

different parameters on structural response of UHPFRC beams, including the contribution of stirrups and concrete to shear capacity of beams, to explore feasibility of removing the need for shear reinforcement in UHPFRC beams.

Results from experiments and numerical model reveal that UHPFRC beams exhibit distinct cracking pattern characterized by the propagation of multiple micro cracks followed by widening of a single crack leading to failure. Also, UHPFRC beams exhibit high flexural and shear capacity, as well as ductility due to high compressive and tensile strength of UHPFRC and fiber bridging developing at the crack surfaces that leads to strain hardening in UHPFRC after cracking. Thus, absence of shear reinforcement in UHPFRC beams does not result in brittle failure, even under dominant shear loading. Data from the conducted experiments as well as those reported in literature is utilized to develop a machine learning (ML) framework for predicting structural response of UHPFRC beams. On this basis, a comprehensive database on reported tests on UHPFRC beams with different geometric, fiber properties, loading and material characteristics is collected. This database is then analyzed utilizing different ML algorithms, including support vector machine, artificial neural networks, *k*-nearest neighbor, support vector machine regression, and genetic programing, to develop a data-driven computational framework for predicting failure mode and flexural and shear capacity of UHPFRC beams. Predictions obtained from the proposed framework are compared against the values obtained from design equations in codes, and also results from full-scale tests to demonstrate the reliability of the proposed approach. The results clearly indicate that the proposed ML framework can effectively predict failure mode and flexural and shear capacity of UHPFRC beams with varying reinforcement detailing and configurations. The research presented in this dissertation contributes to the development of preliminary guidance on evaluating capacity of UHPFRC beams under different configurations.

In dedication to my beloved husband and parents.

ACKNOWLEDGMENTS

I would like to express my deep gratitude to my advisor, Dr. Venkatesh Kodur, for his support, invaluable guidance, and encouragement during the course of my studies. I am very grateful for his motivation and perseverance, and for providing an opportunity for a valuable learning experience. I would like to thank the members of my committee Dr. Neeraj Buch, Dr. Weiyi Lu, and Dr. Thomas Pence for their valuable guidance, helpful comments, time, and support. Also, I would like to thank Dr. Parviz Soroushian for his guidance on experimental program.

I would like to thank my peers and friends; Srishti Banerji, Ankit Agrawal, Anuj Shakya, Amir Arablouei, Mohannad Naser, Esam Aziz, Saleh Mohammad Alogla, Pratik Bhatt, Svetha Venkatachari, Puneet Kumar, Augusto Masiero Gil, and Derek Hibner. I would like to express my appreciation to the manager of civil infrastructure laboratory Mr. Siavosh Ravanbakhsh and Mr. Charles Meddaugh for their support and help during the experimental program in this research. Additionally, I would like to thank Laura Taylor, Laura Post, Margaret Conner, and Bailey Weber for all the administrative assistance they provided. I am thankful for the support from the Department of Civil and Environmental Engineering and College of Engineering for several resources during my graduate studies through fellowships, travel grants, and workshops. In addition, I acknowledge the funding from U.S. Airforce Research Laboratory (AFRL) and Metna Company.

Last but not least, I am grateful to my dear husband, Hadi, for his unconditional love, understanding, and support. I would not have been able to make it without his never-ending encouragement and support. I would like to express my deepest gratitude to my dear parents and sisters, Neda and Raheleh, for their endless love and many years of support.

TABLE OF CONTENTS

LIST OF TABLES

LIST OF FIGURES

CHAPTER 1

1 INTRODUCTION

1.1 Background

Concrete is the most widely used construction material due to locally available ingredients, economical efficiency, ease of fabrication, low maintenance cost, sustainability, and durability. In the last four decades, a number of studies have been carried out to improve the concrete technology. The research and development efforts have led to the emergence of Ultra High Performance Concrete (UHPC). UHPC is a new class of cementitious material possessing excellent strength properties, improved durability, and impact resistance [1,2]. However, increased strength of UHPC also results in a relatively more brittle behavior than conventional concrete. To surmount this brittle behavior of UHPC, addition of steel fibers is often recommended and this concrete type is designated as Ultra High Performance Fiber Reinforced Concrete (UHPFRC). UHPFRC exhibit superior strength, improved ductility, fracture toughness, energy absorption capacity, and enhanced post cracking (tensile) response [2–4].

In recent years, UHPFRC is finding increasing applications in infrastructure projects owing to its superior strength [2–9]. Currently, there are limited design provisions in the national codes (France, Japan and Korea) as well as best practice documents for structural applications of UHPFRC [10–12]. Also, there are no design specifications for UHPFRC structural members in US codes and standards for widespread application in civil infrastructure. This clearly highlights the current limitations in design provisions for UHPFRC beams. In order to develop better understanding on structural response of UHPFRC members and also design methodology to promote the applicability of UHPC in concrete structures, further experiments and numerical studies on structural behavior of UHPFRC beams are needed.

1.2 Development of UHPFRC

Since early years of 20th century, there have been efforts to advance concrete technology to improve the properties of concrete including strength and ductility [10]. Although the concept of using fibers to improve the behavior of construction materials is old and intuitive, the development of fiber reinforced concrete (FRC) started in 1960s [11]. Romualdi [12] and Baston, Romualdi and Mandel [13] brought FRC to the attention of researchers. Lankard [14] developed high toughness concrete by including fibers to use seismic resistance precast frames, and this concrete was called Slurry Infiltrated Fiber Concrete (SIFCON). Then, in 1990s, an improved version of SIFCON called Slurry Infiltrated Mat Concrete (SIMCON) by utilizing a non-woven steel fiber mat was developed by Hackman et al. [15]. Also, Engineered Cementitious Composite (ECC) characterized by pseudo strain hardening and improved tensile cracking was developed by Li and Wu [16] with including discontinuous polyethylene fibers in concrete. The low tensile strength and brittle characteristics of concrete have been overcome by using fibers. Fibers with different geometrical characteristics and made from different materials such as steel, glass, carbon, etc. have been using for development of FRC. Among all different types of fibers, steel are the most widely used fiber in concrete [17].

High strength concrete (HSC) with compressive strength over 60 MPa was developed in early 1970s. In 1980s, HSC with compressive strength of more than 110 MP have been developed for application in buildings and prestressed members. Compressive strength and durability continued to be the focus of concrete technology that led to development of high performance concrete. Ultra high strength cement paste with low porosity was introduced by Yudenfreund et al. [18] and Roy et al. [19] in the 1970s. Yudenfreund et al. [18] developed a cement paste with a compressive strength of about 240 MPa by using low water to cement ratio of 0.2 and a special treatment to ground clinker. Roy et al. [19] developed a cement paste with a compressive strength of 510 MPa with approximately zero porosity by applying heat curing at 250°C and pressure of 50 MPa.

In early 1980s, with developing of pozzolanic admixtures, and high range superplasticizers (water reducing agents), Bache [20] and Birchall et al [21] developed two different types of ultra high strength and highly packed concretes, namely densified with small particles (DSP) concrete and macro-defect free (MDF) pastes. DSP concrete developed by Bache [20] had compressive strength of 120 MPa to 270 MPa, which was achieved by densely packing and using extremely low water content and high range superplasticizers, as well as ultra high strength aggregates. MDF pastes were developed by Birchall et al [21] and had compressive strength over 200 MPa and flexural strengths of 60–70 MPa without using fiber reinforcement or high-pressure compaction, by removing macroscopic flaws during material preparation. The idea in both DSP and MDF was to minimize the micro pores in the paste by compacting the materials and improve homogenization in microstructure of concrete.

In mid-1990s, reactive powder concrete (RPC), which is the forerunner of UHPFRC, was developed by Richard and Cheyrezy [22]. To obtain ultra high strength matrix, the granular mixture was optimized with low water to cement ratio (0.15-0.19) resulting in homogenization of microstructure. Also, heat (90°C and 400°C) and pressure treatments were applied. In addition, to improve tensile strength and ductility and toughness, straight steel fibers with volume fraction of 1.5-3% with length of 13 mm and diameter of 0.15 mm were added. The developed RPC exhibited compressive strength of 200-800 MPa and fracture energy of upto 40 kJ/m^2.

To date, besides RPC, different type of UHPFRC with different designations have been developed. UHPFRC called Ductal® developed by three companies of Lafarge, Bouygues and Rhodia was industrialized and commercialized. Ductal® offers high compressive strength of 160 to 240 MPa and tensile strength more than 10 MPa. This UHPFRC was developed by optimization of the granular mix and elimination of coarse aggregates to enhance homogeneity and density and also heat treatment. The water to cement ratio of 0.2 and 2% volume fraction of steel fibers with dimeter and length of 0.2mm and 13-15mm was utilized. Ductal® has been optimized to satisfy rheological criteria (workability and self-placing capability), mechanical criteria and durability criteria [23,24]. Korea Institute of Construction Technology (KICT) in Korea developed K-UHPC having compressive strength over 150MPa and tensile strength over 8MPa. The developed K-UHPC include 2% volume fraction of steel fibers with a length of 13 mm and diameter of 0.2 mm [10]. Table 1-1 summarizes some of the milestones in high performance concrete development.

Many researchers around the world have developed concretes that could be classified as UHPC. Although there are differences among types of UHPC, there are also many overall similarities. French recommendation [25] defines UHPFRC as a cement matrix material with a high binder content with special aggregates having compressive strength of more than 150 MPa, and high ductility facilitated by steel fibers. The Japanese recommendation [26] defines UHPFRC as a material exhibiting strain hardening under uniaxial tensile stress, with cracking stress of over 4 MPa and tensile strength of over 5 MPa at crack width of 0.5mm, respectively, together with high compressive strength in excess of 150 MPa.

Table 1-1. Studies on the development of high performance concrete [27]

Reference	Year	f_c' (MPa)	Name	Special conditions
Yudenfreund, Skalny et al.	1972	230		Paste, vacuum mixing, low porosity, small specimens
Roy et al. (US)	1972	510		Paste, high pressure and high heat curing, small specimens
Birchall et al. (UK)	1981	200	MDF	Paste, addition of polymer, bending strength upto 150 MPa
Bache, Hjorth (Denmark)	1981-1983	120-250	DENSIT, COMPRESSIT	Mortar and concrete, normal curing, use of microsilica
Bache, Young, Jennings, Aitcin (Demark, US, Canada)	1980's	120-250	DSP	Improved particle packing, use of microsilica, use of superplasticizer
Many reserachers worldwide	1980's	Up to 120	HSC, HPC	Concrete with special additives & aggregates for structural applications, superplasticizers, normal curing, better durability
Lankard, Naaman (US)	1980's	Up to 210	SIFCON	Fine sand mortar with high volume fractions of steel fibers (V_f=8-15%)
Bache (Denmark)	1987	Up to 140	CRC	Concrete with high volume of steel fibers used with reinforcing bars
Naaman	1987	Open range	HPFRCC	Mortar and concrete with fibers leading to strain-hardening response in tension
Reinhardt and Naaman (Germany, US)	1991	Open range	HPFRCC	Toward reducing the fiber content
Li and Wu (US)	1992	Open range	ECC	Mostly mortar with synthetic fibers, strain-hardening behavior in tension
De Larrard (France)	1994	> 150	UHPC	Optimized material with dense particle packing and ultra fine particles
Richard and Cheyrezy	1995	Up to 800	RPC	Paste and concrete, heat and pressure curing, particle packing
Larfage (Chanvillard, Rigaud, Behloul), (France)	1998	Up to 200	DUCTAL	90°C heat curing for 3 days, steel fibers up to 6% (commercially available)
Rossi et al.	2000	Up to 200	CEMTEC	Up to 9% fibers, hybrid combinations
Many researchers worldwide (Graybeal, Ulm, Rossi)	2000	Up to 200	UHPC and UHP-FRC	Many formulations based on DUCTAL
KICT	2003	Up to 300	K-UHPC	Use of fillers and nano size binders, 2% steel fibers, heat curing
Karihallo (UK)	2005	Up to 140	CARDIFRC	Optimized particle packing and mixing procedure
Jungwirth (Switzerland)	2005	Up to 200	CERACEM	Formulation similar to DUCTAL, larger fibers and aggregates
Fehling and Schmidt (Germany)	2005, 2008	> 150	UHPC	Many formulations similar to DUCTAL, with and without heat curing, with and without fibers
Wille and Naaman (US, Germany)	2011	Up to 290	UHP-FRC	No heat curing, optimized packing
Ranade et al.	2013	160	HSHDC	Very high fiber strength and aspect ratio, 2% fibers, no heat curing
Sbia et al. (US)	2014	150	UHPC	An optimized dosages of carbon nanofiber and polyvinyl alcohol fibers as nano and microscale reinforcement, steam curing

1.3 UHPC Compositions

The strength, ductility and stiffness properties of concrete are the most important properties that are needed in construction applications. The basic principles utilized in UHPC are enhancement of homogeneity and packing density of concrete by eliminating coarse aggregates in mix, optimizing size distribution of granular constituents, and heat-treating [22]. These principles result in matrix with very high compressive strength as a result of homogeneity, maximum particle packing density, minimum size of flaws and pores [28–30]. Further, ductility and toughness in UHPC is improved by incorporating steel fibers [22].

UHPC is composed of cement, silica fume, filling powder, aggregates, and superplasticizer. In conventional UHPC mixes typically coarse aggregate are eliminated and only fine aggregates (sand) are utilized. A relatively high proportion of cement is used in UHPC as compared to NSC and HSC. Because of very low water to binder ratio in UHPC, only part of cement hydrates during curing. Therefore, up to 30%, 36%, and 40% of volume of cement in UHPC can be replaced by crushed quartz, blast furnace slag, or fly ash, respectively without reducing compressive strength [31–33].

In order to obtain high packing density, supplementary cementitious materials finer than cement (e.g. silica fume, and fly ash) can be added to fill the voids between cement particles. Including silica fume as a binder improves the mix by filling voids between larger particles (cement), enhances rheological properties and workability due to lubricant effect resulting from sphericity of the particles. Further, silica fume enhances strength properties of UHPC by its pozzolanic reactions with lime resulting from primary hydration [22,31,34]. Results from different studies recommend silica fume dosage of 20-30% of the total binder to obtain high packing density [35–37,37].

In UHPC very low water to binder ratio is used. An optimum w/b ratio of 0.13-0.20 was recommended in different studies to ensure maximum relative density and spread flow [22,38–41]. To overcome reduced workability of UHPC due to very low w/b ratio, superplasticizer is added to the UHPC mix. The required dosage of superplasticizer depends on the mix gradient and type of superplasticizer. For example, an UHPC mixture incorporating a limestone micro-filler is more workable as compared to a mix including higher surface area metakaolin with the same superplasticizer dosage [42]. Superplasticizer dosages ranging from 1 to 8% weight of cement were used in different studies to ensure workability [29,43,44]. Wille et al. [45] recommended superplasticizer dosages of 1.4 to 2.4 % by cement weight. Steel fibers are added to UHPC mix to improve ductility as UHPC is brittle due to very high strength and homogeneity. The most commonly used steel fiber is of 13mm in length and 0.2mm in diameter [29,41,43,44,46,47]. The typical mean particle size of components in UHPFRC is shown in Figure 1-1. Further, microstructure of NSC, HSC, and UHPFRC is compared in Figure 1-2.

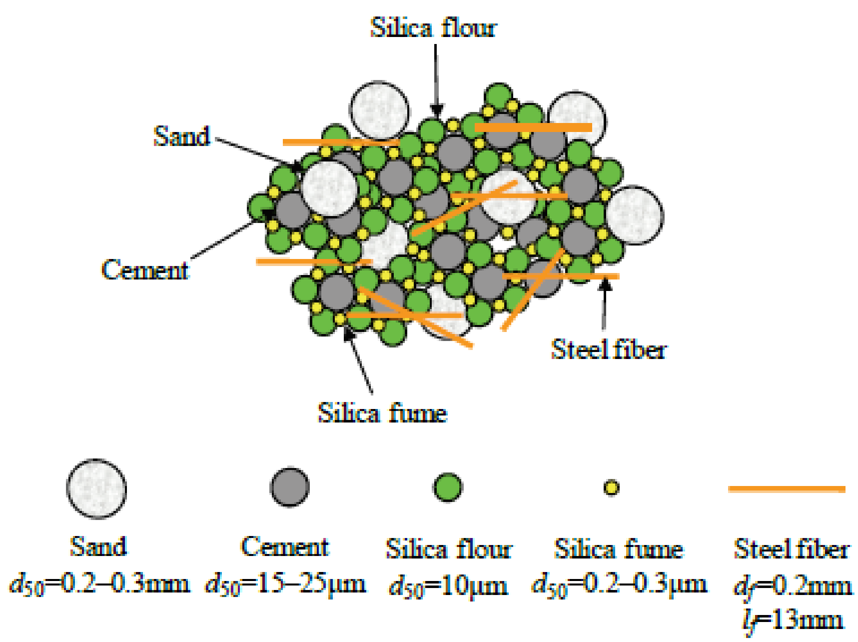

Figure 1-1. Comparison of particle sizes of ingredients in a typical UHPFRC mix structure [10]

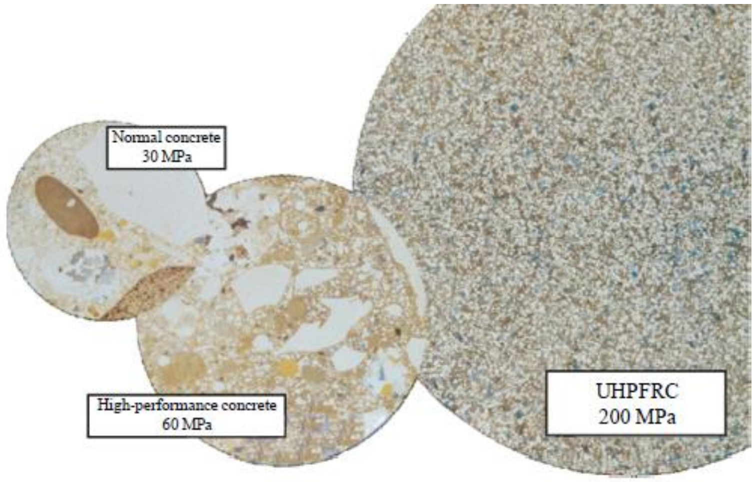

Figure 1-2. Microstructure of different concrete; NSC, HSC, and UHPFRC [10]

1.4 Mechanical Properties of UHPC

The strength and ductility and stiffness properties of concrete are the most important properties that are needed for construction applications. Typical range of mechanical properties of normal strength concrete (NSC), conventional steel fiber reinforced concrete (FRC), high strength concrete (HSC), UHPC, and UHPFRC is presented in Table 1-2. The comparison of compressive and tensile stress strain response of different types of concrete (NSC, FRC, HSC, UHPC, and UHPFRC) are also shown in Figure 1-3 and Figure 1-4 .

As can be seen, UHPFRC exhibits substantially higher compressive, and flexural strength, as well as ductility as compared to NSC, FRC, and HSC. Tensile strength and elastic modulus of UHPFRC is about 5 and 2 times higher than NSC. Further, UHPFRC exhibits ductile behavior even under tension as opposed to conventional concretes (see Figure 1-4). This ductile behavior is due to fiber bridging facilitated by presence of fibers, which results in strain hardening behavior in tension as well as flexure [10]. It should be noted that presence of steel fibers increase compressive strength of UHPFRC by about 15% as compared to UHPC. Tensile strength of

UHPFRC can be increased significantly as compared to UHPC depending on the volume fraction, type, and orientation of fibers.

Bridging effects facilitated by the presence of fibers in UHPFRC results in redistribution of stresses, strain hardening under tension, and improved post cracking stiffness. High tensile strength and ductile characteristics (strain hardening and high ultimate tensile strain) of UHPFRC can be utilized to realize high shear resistance in UHPFRC beams. The high shear resistance of UHPFRC can help reduction of shear reinforcement in beams.

Table 1-2. Mechanical properties different types of concrete [10,34,48]

Type of concrete	Compressive strength (MPa)	Flexural strength (MPa)	Tensile strength (MPa)	Elastic Modulus (GPa)
NSC	21-40	1-3	2-3	21-35
FRC	30-50	4-12	4-8	30-40
HSC	80-100	5-10	3-5	30-47
UHPC	130-180	12-22	4-10	45-55
UHPFRC	150-220	20-45	8-16	45-55

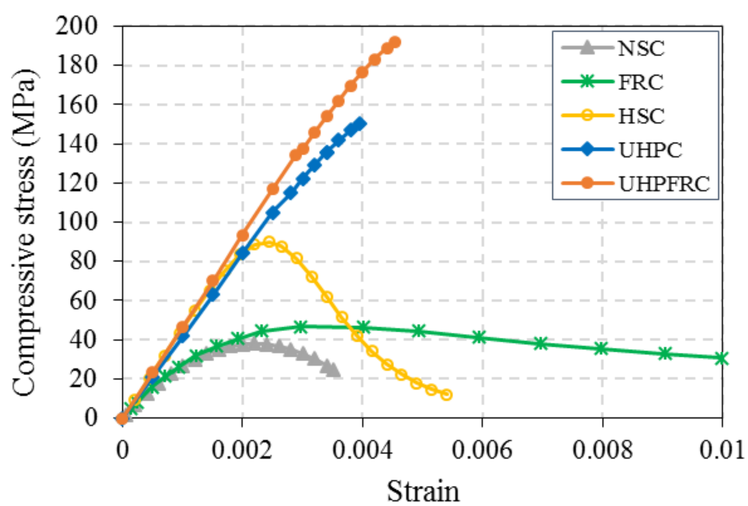

Figure 1-3. Comparison of compressive stress strain response of different types of concrete

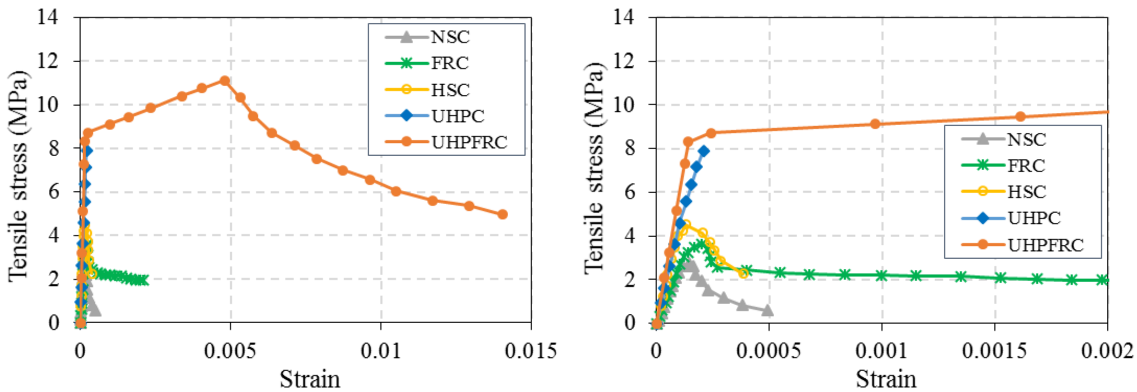

(a) Tensile stress strain response (b) Zoomed view

Figure 1-4. Comparison of tensile stress strain response of different types of concrete

1.5 Knowledge Gaps

Despite recent efforts to study material behavior of UHPFRC, limited guidelines and recommendations exist for design of structural members fabricated by UHPFRC. This clearly highlights the current limitations in design provisions for UHPC beams that is mainly due to limited studies on structural behavior of UHPFRC. In order to promote the applicability of UHPFRC in concrete structures and develop design methodologies that can optimize the superior range of properties offered by this new class of material, better understanding of structural response of UHPFRC members is necessary. The following are some of the aspects which further research is needed:

- Conventional UHPFRC mixes do not contain coarse aggregates and have a relatively high packing density and therefore require use of specialized raw materials and mixing equipment with no coarse aggregates. Field production of UHPFRC using locally available raw materials that can be prepared in conventional ready-mix truck has not been established.
- There are limited studies on structural response of UHPFRC beams. The conducted experimental studies mostly focused on flexural response with only limited studies giving consideration to shear behavior of UHPFRC beams.

- There is lack of data on structural response of UHPFRC beams without stirrups. Also, comparative response of UHPFRC beams subjected to flexural and dominant shear loading has not been established.
- Numerical studies relied upon small-scale experiments for validation and focused on predicting load deflection response with no attention to local response such as crack propagation direction, and contribution of compression block, interfacial resistance, and stirrups to shear capacity.
- There is limited design methodology for UHFRC structural members in current codes and standards. Due to significant differences in properties of UHPFRC, available design expressions for structural members made of conventional concrete cannot be applied to UHPFRC structural members.

1.6 Research Approach

1.6.1 Hypothesis

To overcome some of the current knowledge gaps on structural behavior of UHPFRC beams and develop a better understanding on UHPFRC beams structural behavior, this research is developed with the following hypotheses.

- UHPFRC due to its improved tensile strength and ductility properties can yield high shear capacity in flexural members and thus the need for addition of shear reinforcement in the form of stirrups can be eliminated.

1.6.2 Objectives

The key objectives to address some of the above stated knowledge gaps are as follows:

- Carry out a detailed state-of-the-art review on the structural performance of UHPFRC beams.

- Conduct experiments on UHPFRC beams under flexural and dominant shear loading to develop a better understanding of performance of UHPFRC beams.
- Develop a finite element based numerical model to trace structural response of UHPFRC beams, in the entire range of loading, from preloading to collapse stage.
- Validate the developed numerical model against data generated from experiments on different configurations of UHPFRC beams.
- Conduct a parametric study to evaluate the effect of loading, depth, reinforcement ratio, shear reinforcement ratio, and fiber volume fraction on structural response of UHPFRC beams. Also to specifically study the feasibility of removing shear reinforcement in UHPFRC beams.
- Develop simplified design expressions for shear capacity of UHPFRC beams based on data generated from tests conducted in this study and also literature.

1.6.3 Tasks

The above mentioned objectives are achieved through the following tasks:

Task 1. Design and fabricate UHPFRC beams to conduct experiments.

Task 2. Study comparative behavior of UHPFRC beams subjected to flexural and shear loading.

Task 3. Undertake finite element analysis for predicting structural response of UHPFRC beams. In addition, validate the numerical model using measured data from experiments.

Task 4. Apply the validated finite element model to conduct parametric studies.

Task 5. Use results of available experiments to develop a method to predict capacity of UHPFRC beams.

1.6.4 Methodology

The above mentioned objectives will be realized through experimental and numerical studies on UHPFRC beams. Two sets of experiments are conducted. For the first stage of experiments, four UHPFRC beams with different reinforcement ratios are designed and fabricated to be tested under flexural and shear loading to evaluate comparative behavior of beams under flexural and shear loading. For the second stage of experiments, three beams with different configurations are designed to study effect of removing shear reinforcement in UHPFRC beams subjected to dominant shear loading.

For predicting flexural behavior of UHPFRC beams, a simplified calculation method based on cross-sectional analysis and strain compatibility is developed in MATLAB. For finite element analysis, ABAQUS 6.17 with available plasticity model is used to capture behavior of UHPFRC beams. Data from tests is utilized to validate the numerical model.

The validated numerical model is applied to study the effect of different parameters including loading configuration, reinforcement ratio, stirrups ratio, depth, etc. Results from experiments and parametric studies are utilized to evaluate structural response of UHPFRC beams.

Finally, a data-driven machine learning (ML) framework for predicting failure mode and capacity of UHPFRC beams is developed. To this end, a comprehensive database on reported tests on UHPFRC beams with different geometric, fiber properties, loading and material characteristics is collected. This database is then analyzed utilizing different ML algorithms. The outcome of this analysis is a computational ML framework that is capable of predicting failure mode, flexural and shear capacity of UHPC beams.

1.7 Organization of the Dissertation

This dissertation has been organized into seven chapters. In the first chapter of the thesis, background information on the development of UHPC is presented. Also, knowledge gaps and the research methodology of this thesis is presented. In chapter 2, a detailed state-of-the-art review regarding mechanical properties as well as structural response of UHPC beams is presented. Chapter 3 outlines the experimental program designed to evaluate flexural and shear response of UHPC beams. Detailed results measured in experiments are utilized to validate the numerical model. In Chapter 4, development of analytical approach for evaluating sectional moment-curvature response of UHPC beams is laid out. Further, a finite element based numerical model for tracing structural response of UHPC beams is developed. The validity of the developed model is also established in this chapter. In Chapter 5, a set of parametric studies are performed using the developed model to study effect of different parameters such as reinforcement ratio, stirrups ratio, volume fiber fraction, and loading condition. Also, shear mechanism of beam action and arch action in the analyzed beam is evaluated. Chapter 6 presents a machine learning-based data interpretation framework for predicting mode of failure (i.e. flexure, flexure-shear, and shear) as well as flexural and shear capacity of UHPC beams. Finally, Chapter 7 summarizes the work performed under this project, provides key conclusions and discusses future research directions.

CHAPTER 2

2 STATE-OF-THE-ART-REVIEW

2.1 General

Ultra-high performance fiber reinforced concrete (UHPFRC), is an emerging class of cementitious material offering a unique combination of very high compressive strength (>150 MPa); high tensile strength (> 8 MPa), high ductility, and good impact resistance [1,49,50]. These superior properties are an outcome of an optimized microstructure resulting from pre-tailored granular mixture design along with low water-to binder ratio, superplasticizers and fibers in the UHPFRC batch mix [49,51,52]. The improved properties of UHPFRC have made this material attractive for a number of structural applications [5,6,53].

A number of studies have been carried out at material level by various researchers to evaluate the influence of mix design, curing condition, fiber type, fiber dosage, fiber geometry, and fiber orientation on mechanical properties of UHPFRC [4,32,51,54–60]. At structural level, experimental and numerical studies focused on evaluating behavior of UHPFRC beams have been conducted in the past two decades [5,46,49,61–63]. The conducted studies at material and structural level are presented in detail in following subsections.

2.2 Studies at Material Level

The properties of concrete are dependent on number of factors such as type of cementitious materials, size of aggregates, size and shape of specimen, etc. In particular UHPFRC, is made with low water to binder ratio, high fineness admixtures, and heat treatment, thus is more affected by type of cementitious material, curing condition, aggregate size as compared to conventional concrete. Also, properties of UHPFRC is highly influenced by fiber dosage and distribution characteristics which are affected by casting process [10]. In following sections number of studies on material level characteristics of UHPFRC is reviewed.

2.2.1 Mix proportions

Conventional UHPC mix designs do not contain coarse aggregates which causes high cost of UHPC production due to high volume of binders and fillers. Several studies have been recently conducted to develop modified UHPC batch mixes incorporating certain amount of coarse aggregates to reduce production cost. In addition, including coarse aggregates results in reduction of cementitious material and in turn can reduce autogenous shrinkage [64]. Ma et al. [65] developed a flowable UHPC mix with including coarse aggregates that obtained compressive strength of 150-165MPa. The authors showed that compressive strength of UHPC was not noticeably affected by presence of coarse aggregate. This is consistent with findings of Collepardi et al. [64] that showed compressive strength was not affected by replacing fine sand with coarse aggregate of a maximum size of 8 mm. Will et al. [45], according to experimental data collected from international symposium on UHPC in 2004 and 2008, reported that UHPFRC mixes including coarse aggregates with maximum grain size of 7-16mm exhibited average compressive strength of 178 MPa, which was slightly higher than average compressive strength of UHPFRC mixes without coarse aggregates being 162 MPa. Collepardi et al. [64] also showed that including coarse aggregate resulted in higher elastic modulus and therefore lower strain capacity. The authors also illustrated that including coarse aggregates led to reduction in flexural strength and this can be attributed to lower bond strength of fibers.

Chan and Chu [36] showed that with increasing silica fume content upto 30% in UHPFRC mix, bond strength and fiber pullout resistance increased significantly. Rougeau and Borys [42] showed that although including silica fume results in best mechanical performance of UHPFRC, other fine admixures such as limestone microfiller, metakaolin, siliceous microfiller, pulverized fly ash, and micronized phonolith can be utilized to obtain compressive strengths above 150 MPa. Results from studies by Yazici et al. [66,67] also exhibited that including ground granulated blast furnace slag and fly ash increased the flexural strength and toughness of UHPFRC, regardless of the curing process. Also, replacing silica fume with ground granulated blast furnace slag and fly ash up to 40% caused no reduction in compressive strength of mix. Van Tuan et al. [68] illustrated that including rice husk ash being an agricultural waste product, did not significantly decrease compressive strength as compared to UHPFRC with fly ash. The authors also showed that the combined use of 10% rice husk ash and 10% silica fume due to their synergic effect resulted in highest compressive strength (as compared to other combinations).

Ambily et al [69] showed feasibility of using copper slag which is a waste materials as fine aggregate replacement in UHPC. Results demonstrated that it is possible to produce UHPC with compressive strength above 150 MPa by including of copper slag. Also, complete replacement of sand by copper slag resulted in compressive strength reduction of about 15–25% without any reduction in flexural strength and fracture energy.

In addition, a number of studies have been carried out at material level, to evaluate the influence of fiber type, fiber dosage, fiber geometry, and fiber orientation on mechanical properties of UHPFRC [1,4,32,51,54–59,70]. El-Dieb [71] showed that including steel fiber changes mode of failure under compression from sudden explosion to ductile failure without chipping concrete. This can be attributed to restraining and confining effect of steel fibers for concrete under compression.

It is generally assumed that fiber addition mostly affects tensile behavior without much influence on compressive strength. Thus, not many researchers have explicitly studied the impact of fiber addition on compressive strength. Recent studies [1,3,4,34,49] have shown that presence of steel fibers having relatively high specific surface area (small aspect ratio) can lead to 20-40% increase in compressive strength of UHPFRC. However, steel fibers with higher aspect ratio does not seem to improve compressive strength and also introduce problems of fiber balling and uneven distribution of fibers in UHPFRC [1,3,4,34,49].

Using data from literature [4,55,72–78], normalized compressive strength ($f'_{c,UHPFRC}/f'_{c,UHPC}$) is plotted as a function of fiber content in Figure 2-1. Details of compressive strength of UHPC and fiber size taken from these tests [4,55,72–78] are also summarized in Table 2-1. Data plotted in Figure 2-1 indicates that there is variation in effect of fiber addition on compressive strength of UHPFRC from different studies. Graybeal [72,75] reported 30% increase in compressive strength of UHPC by adding 2% steel fiber with aspect ratio of 65. An increase in compressive strength (about 20%) for fiber content of 2.5% by volume and fiber aspect ratio of 30 was noted in study conducted by Voit et al. [79]. This increase can also be attributed to a confining effect provided by the presence of steel fibers, similar to what is observed in reinforced concrete beams due to presence of stirrups [80]. It is important to note that this confining effect may reduce for fibers with a larger aspect ratio as observed in Yoo et al [81] study, since including fiber content and increasing the fiber volume fraction did not improve compressive strength (Table 2-1). Also, addition of steel fibers results in less entrapped air, therefore improves density and as a result compressive strength in UHPFRC.

The results from different studies showed that a higher amount of steel fibers upto an optimum fiber content can improve compressive strength. The optimum fiber content that results in maximum compressive strength was different in different research studies due to the fact that compressive strength is significantly influenced by homogeneity of fiber distribution [4,82,83].

However, Yunsheng et al. [48] and Wu et al. [77] reported continuous increase of compressive strength with increasing fiber volume fraction up to 4%.

It should be noted that decreasing trend or no improvement in compressive strength with including higher volume fractions of fibers in some studies can be attributed to poor distribution of fibers within the concrete matrix. Also, increased concentration of steel fibers can create fiber balling and in turn lead to weak regions, which can reduce the efficiency of fibers, hence decreasing compressive strength.

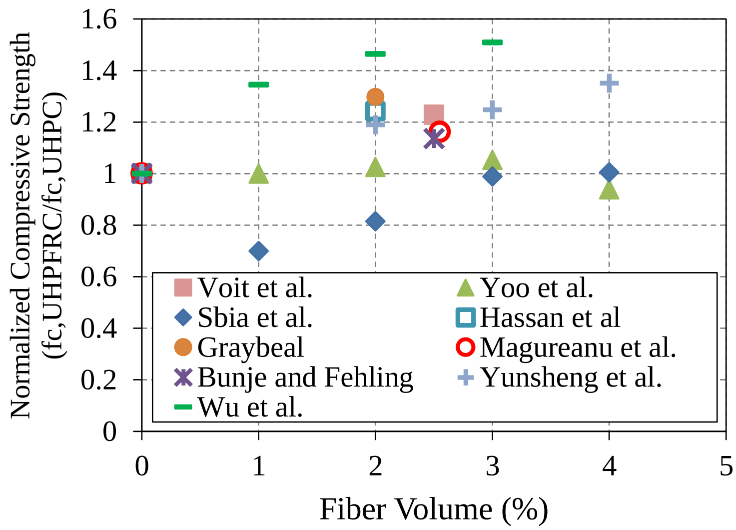

Figure 2-1. Normalized compressive strength of UHPFRC with varying fiber content

Table 2-1. Test parameters for evaluating compressive strength of UHPFRC

Study	$f'_{c,UHPC}$ (MPa)	Fiber length (mm)	Fiber diameter (mm)	Aspect ratio
Voit et al. [73]	158.85	6	0.2	30
Yoo et al. [4]	196.8	13	0.2	65
Libya et al. [55]	152.68	13	0.175	74
Magureanu et al [74]	136	25, 6	0.4, 0.175	62.5, 34.2
Graybeal [72,75]	157	13	0.2	65
Hassan et al [76]	121.3	13	0.2	65
Wu et al. [77]	110	13	0.2	65
Bunje and Fehling [78]	179.6	9	0.2	45
Yunsheng et al. [48]	155	13	0.175	74

The results from different studies showed that including steel fibers significantly improves flexural strength of UHPC [1,4,48,74]. Kang et el. [1] studied effect of steel fiber on flexural tensile strength of UHPFRC by conducting 3-point bending tension tests on notched prisms with varying steel fiber volume fraction from 0% to 5%. The authors reported that flexural tensile strength linearly increases with increasing fiber volume fraction. For example, the flexural strength of UHPFRC with short straight steel fiber at volume fraction of 5% was found to be about 64 MPa, which is seven times larger than that of UHPC without fibers [1].

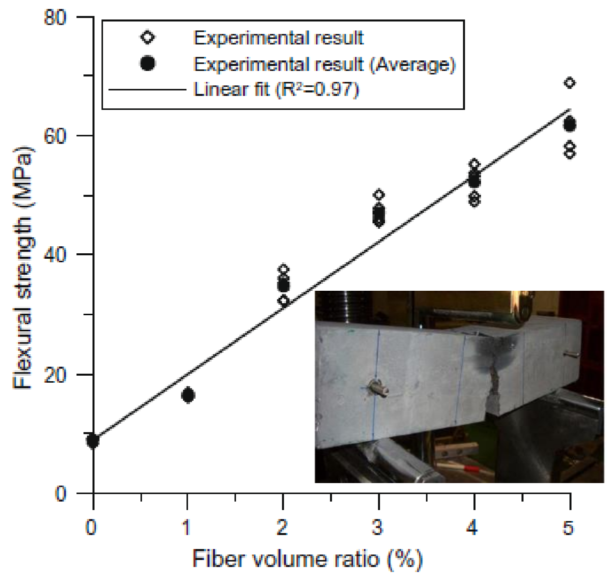

Figure 2-2. Flexural tensile strength of UHPFRC with different fiber volume fraction [1]

Yoo and Yoon [49] also reported that twisted steel fibers resulted in about 1.7 times higher flexural strength as compared to beams with short straight steel fibers. Also, Wille and Naaman [84], and Kim et al. [58] showed that use of twisted and hooked end steel fibers resulted in significant improvement of tensile strength and post-cracking strain capacity of UHPFRC, due to improved fiber pullout capacity as compared to short straight steel fibers [84,85]. The specimens with 2% volume fraction of twisted steel fibers exhibited a tensile strength of 14.9 MPa and a strain capacity of 0.61% which these values are about 32% and 205% higher than those with 2% volume fraction of short straight steel fibers [85] (see Figure 2-3).

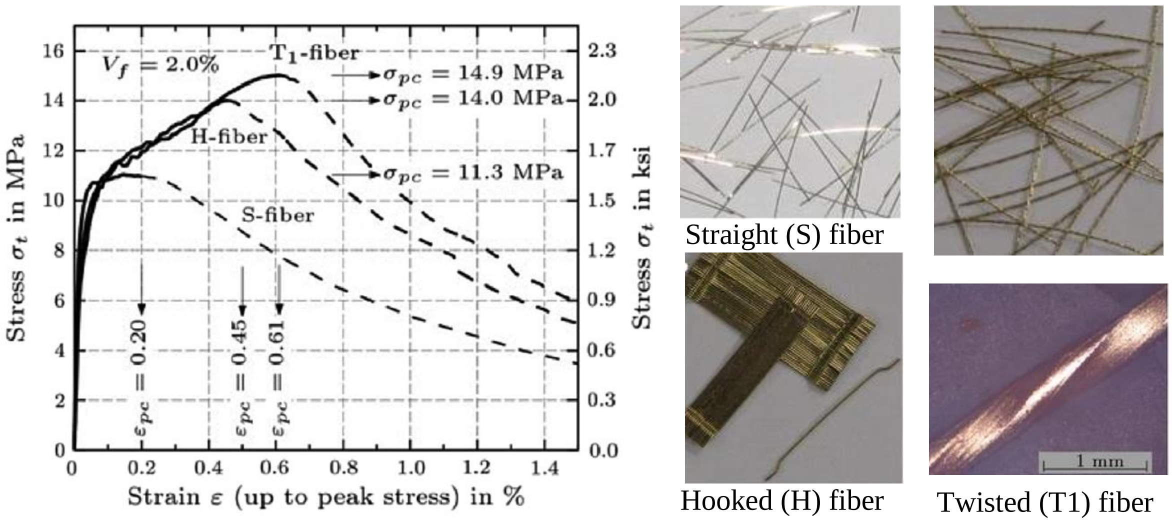

Figure 2-3. Direct tensile response of UHPFRC with different fibers geometry [85]

Further, results from Yoo et al [51,86] and Aydin and Baradan [59] showed that increasing fiber length (up to 19.5mm) resulted in improving fracture energy capacity, tensile and flexural performance due to increase in bonding area between the fiber and the matrix leading to higher fiber pullout capacity (see Figure 2-4). However, fibers with longer length (30 mm) may cause fiber balling, poor fiber dispersion, and less number of fibers across crack surfaces and in turn deterioration of flexural strength and tensile performance [51]. As can be seen in Figure 2-4, UHPFRC with straight steel fibers with length of 19.5mm exhibited about 26% and 13% higher flexural strength and 153% and 67% higher deflection capacity than UHPFRC with medium steel fiber with length of 16.3mm and short steel fibers with length of 13mm, respectively. Results from Ye et al. [87] study showed that including fibers with smaller diameter (higher aspect ratio) in UHPC mix resulted in improved flexural capacity as compared to mixes with fibers having larger diameter. The reason behind this is that in the mix with fibers having smaller diameter, number of fibers increased at the cracks surfaces. This leads to enhanced bridging effects of fibers and therefore improved flexural strength [28,87].

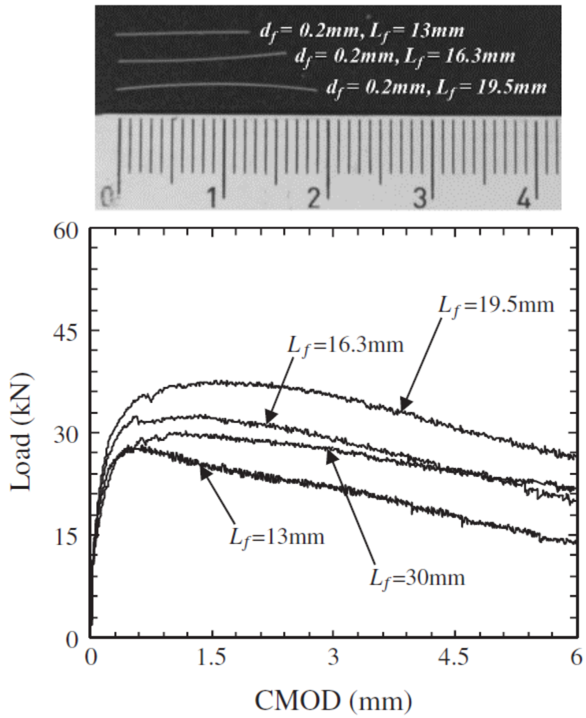

Figure 2-4. Flexural response of UHPFRC with fibers with varying length [51]

In order to illustrate effect of fiber fraction on tensile strength of UHPFRC, using data from literature [34,55,85,88,89] normalized tensile strength ($f_{t,UHPFRC}/f_{t,UHPC}$) is plotted as a function of fiber content in Figure 2-5. Significant parameters regarding UHPC tensile strength and fiber size are summarized in Table 2-3. It should be noted that the fibers were straight steel fibers. It can be seen in Figure 2-5 that the tensile strength of UHPFRC increases significantly with increase in fiber content (by volume). The maximum increase in tensile strength of UHPFRC (about 230%) was reported for fiber content of 3% (by volume) in experimental investigations by Wille et al [88].

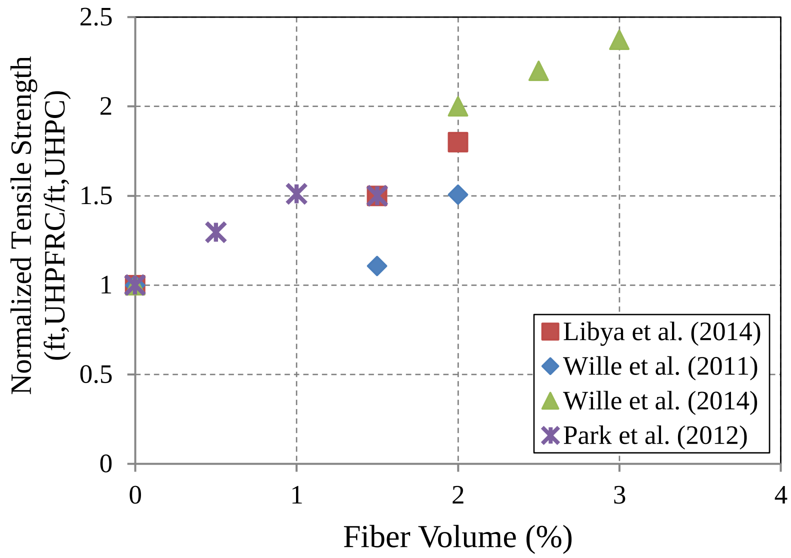

Figure 2-5. Normalized compressive strength of UHPFRC with varying fiber content

Table 2-2. Test parameters for evaluating tensile response of UHPFRC

Study	$f_{t,UHPC}$ (MPa)	Fiber length (mm)	Fiber diameter (mm)	Aspect ratio
Libya et al. [34,55]	5	13	0.175	30
Wille et al. [90]	7.5	13	0.2	65
Wille et al. [88]	7.5	13	0.2	65
Park et al. [89]	8.8	30	0.3	100

Sbia et al. [54] developed a new class of UHPC with including carbon nanofiber (CNF) ad poly vinyl alcohol (PVA) fiber as nano and microscale reinforcement in UHPC. An optimized dosages of CNF and PVA (with 0.047% and 0.37% volume fraction) was experimentally identified to improve flexural strength, ductility, energy absorption capacity, impact resistance, abrasion weight loss, and compressive strength of plain UHPC by 9.2, 1000, 700, 158, 34, and 7.5%,, without compromising the fresh mix workability [54]. Polymer fibers offer improved stability in corrosive environments as compared to steel fiber. Also, having lower diameters, and higher aspect ratios benefits their reinforcement efficiency in concrete. However, polymer fibers provide lower elastic modulus than steel that results in lower reinforcement efficiency. Results from Sbia et al.

[54] study showed that CNF are effective to control microcracks inception and growth as compared with microscale (PVA) fibers.

Further, Sbia et al. [55] recommended optimum volume fraction of steel fiber and carbon nanofiber with 1.1% and 0.04%, respectively, for improvement of flexural strength, ductility, energy absorption capacity, impact, and abrasion resistance of UHPFRC. The optimum combination of steel fiber with carbon nanofiber led to 50%, 240%, 2700%, 236%, 1200%, and 5% improvement in the flexural strength, ductility, energy absorption capacity, impact resistance, abrasion resistance, and compressive strength of UHPC, respectively. Micro- and nanoscale reinforcement offer the potential for complementary actions in cementitious matrices since they function of different scales, and nanofibers can improve the bonding and pullout behavior of microscale fibers.

2.2.2 Curing

Heat treatments have generally been applied to accelerate the hydration reactions and increase the density in UHPC production [91]. Thermal curing improves pozzolanic reactions leading to formation of additional hydration products (i.e. calcium silicate hydrate) [92]. These hydration products fill small pores and results in dense microstructure and in turn improve mechanical properties of UHPC [50,64,92–94]. The heat treatment from 90ºC to 400ºC for 2 to 6 days for UHPC have been reported in the literature [22,50,95,96].

Number of studies reported up to 40% average increase in compressive strength in UHPC with 90ºC heat treatment as compared to untreated specimens [97–99]. Graybeal [47,72] investigated the curing conditions effects and concluded that steam treatment increases UHPC compressive strength by 53% (to 193 MPa), and elastic modulus by 23% (to 52.4 GPa). Also, steam curing decreases UHPC creep coefficient from 0.78 to 0.29, and eliminates long-term shrinkage [50].

Field applications of UHPC have emphasized production of precast elements [100–103], and repair/rehabilitation of concrete structures [11] due to issues regarding field application of UHPC especially curing. In order to address these issues, Sbia et al. [41] developed mix design procedures and production methods for field application of UHPC using locally available materials and concrete production facilities. The developed mix was batched in a ready-mixed concrete plant and mixed/transported using a conventional concrete truck. The authors showed that readily available insulating blanket was effective to facilitate field thermal curing of UHPC using heat generated from hydration of the cementitious binder in UHPC.

However, the use of heat treatment at construction site may be difficult due to difficulties in controlling moisture and temperature. For this reason, number of studies have been conducted to evaluate effects of curing at room temperature on mechanical properties of UHPC. Park et al [104] showed that at a curing temperature of 60ºC, 48 to 72 hours of curing is required to achieve compressive strength of 180 MPa. They showed that a longer period of curing (about 96 hours) is required at curing temperature of 40ºC. Koh et al [105] showed that wet curing at 20ºC for 91 days resulted in the same compressive strength of about 200 MPa as UHPFRC with steam curing at 90ºC as shown in Figure 2-6.

Yunsheng et al. [48] showed that although high temperature curing can increase the hydration rate and accelerate formation of hydration products leading to high early strength, compressive strength of 200 MPa or greater can be obtained at 20ºC and relative humidity of 100% if the curing ages is prolonged (e.g. 90 days). This curing has advantages for field applications of UHPC, due to easy operation, and lower energy consumption. Wille et al. [45] developed an UHPC mix that obtained compressive strength exceeding 200 MPa without the use of any heat and treatment or special mixer using commercially available materials in the US market. The authors proposed an optimum sand to cement ratio, silica fume, high range water reducer, and water to cement ratio.

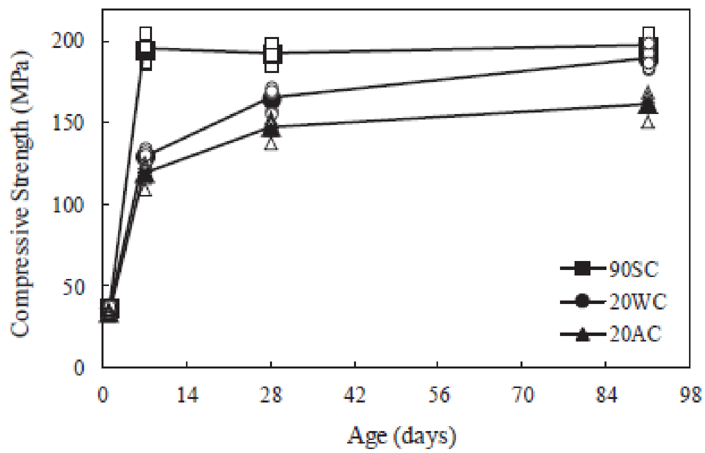

Figure 2-6. Compressive strength of UHPFRC with different curing at different ages; 90SC: steam curing at 90ºC, 20WC: wet curing at 20ºC, and 20AC: air curing at 20ºC [105]

2.2.3 Compressive Response of UHPC

In order to undertake detailed structural analysis and design, material models relating stress to strain under compression and tension are needed. While such models are well established for both NSC and HSC, there is limited relations for tracing uniaxial compressive and tensile stress-strain behavior of UHPFRC. Some of the available material models under compression and tension are reviewed in sections 2.2.3 and 2.2.4.

Empelmann et al. [106] have proposed a generalized model for predicting compressive behavior of UHPFRC with explicit consideration to fiber content (by volume). This approach approximates the uniaxial compressive stress-strain behavior of UHPFRC with a quad-linear model with an accurate description of the softening branch as well. The relationship accounts for the filling degree, compressive strength, elastic modulus, strain at ultimate stress, fiber content (by volume) and fiber aspect ratio. A schematic representation of quad-linear approximation of the stress-strain response of UHPFRC assumed in this approach is shown in Figure 2-7.

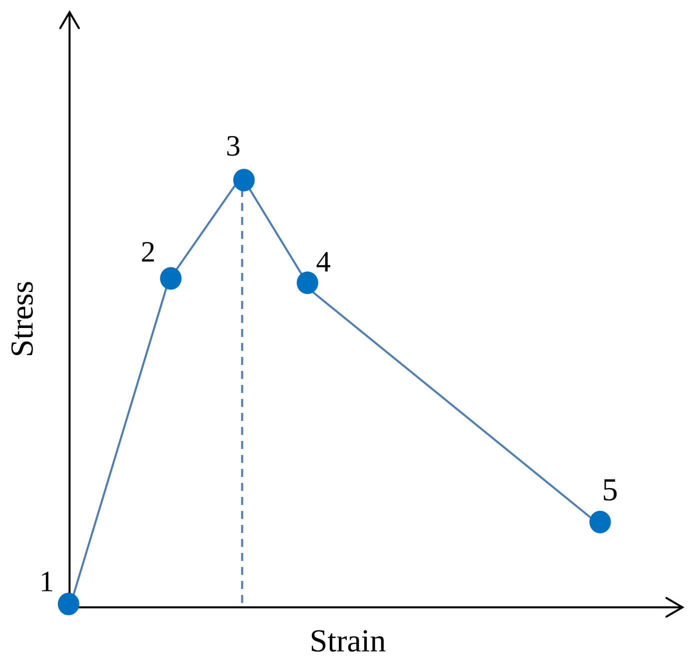

Figure 2-7. Quad-linear approximation for compressive stress-strain behavior of UHPFRC

The ascending branch in the proposed model (points 1, 2 and 3 in Figure 2-7), are calculated using relations suggested by Schumacher [107]. On the other hand, the descending branch (points 4 and 5 in Figure 2-7), is obtained based on empirically derived values from experiments conducted by Empelmann [106]. The relations to calculate these five key points based on concrete properties, fiber content (by volume) and fiber size (aspect ratio) are presented in Table 2-3.

Furthermore, Empelmann et al. [106] validated predictions from the above analytical model with data generated on UHPFRC cylinder specimens with a fiber content of 2.47% by volume (designated B4Q-0), fiber length of 9 mm and fiber diameter of 0.15 mm (aspect ratio = 60). A reasonable correlation was obtained between predicted compressive stress-strain response and the data generated from tests results as shown in Figure 2-8.

Table 2-3. Relations for calculating quad linear stress-strain approximation of UHPFRC under compression

Point i	$\varepsilon_{ci}/\varepsilon_{cu}$	f_{ci}/f_{cu}
1	0	0
2	$(2\alpha_{in}-1)/E_{cm}$	$(2\alpha_{in}-1)$
3	1	1
4	1.25	$0.35\sum v_f l_f/d_f$
5	5	$0.1\sum v_f l_f/d_f$

ε_{ci}, f_{ci} are strain and stress at point i; α_{in} is the filling degree; v_f is the fiber volume in percent; l_f is the length of fiber and d_f is the diameter of fiber.

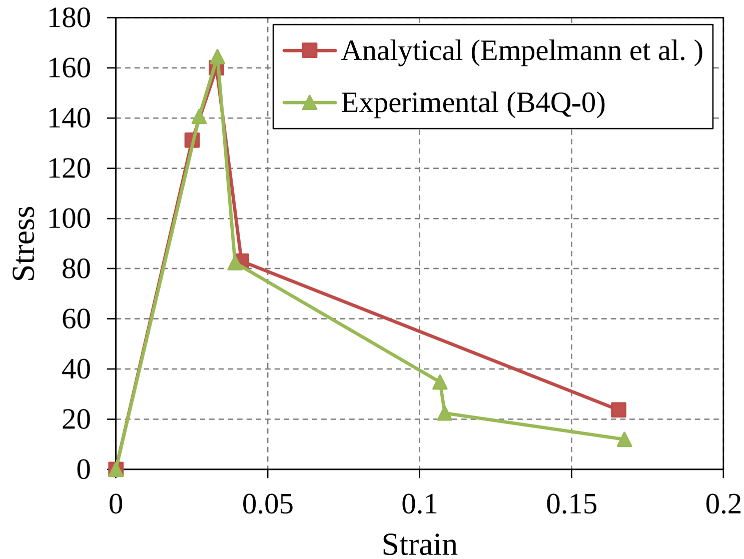

Figure 2-8. Comparison of predicted stress-strain relation of UHPC with test data

Utilizing the above approach the effect of varying fiber content (by volume) on the compressive stress-strain behavior of UHPFRC can be evaluated. The stress-strain response of UHPFRC in compression is plotted in Figure 2-9 for three different volume fractions (V_f) of steel fibers, namely, 1%, 2% and 5%. Results plotted in Figure 2-9 indicate that increasing fiber content does not have much effect on compressive strength. However, fiber content has a significant influence on post-peak behavior and ductility improves significantly with increasing fiber content.

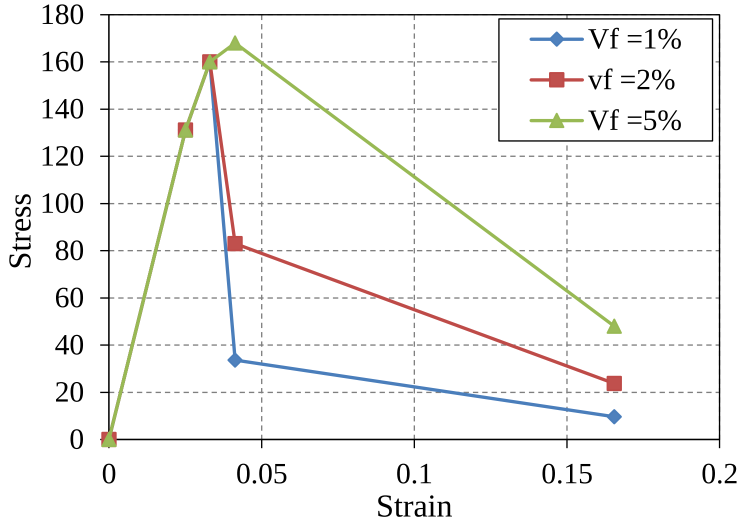

Figure 2-9. Effect of fiber content on compressive stress-strain behavior of UHPFRC

Fiber size (aspect ratio) is another key parameter that influences compressive stress-strain response of UHPFRC. The predicted response for short fibers (with aspect ratio = 65) and long fibers (with aspect ratio = 100) is compared in Figure 2-10. It can be seen in Fig. 4, that the aspect ratio (AR) of fibers does not influence compressive strength of UHPFRC. However, aspect ratio has slight influence on post-peak response and UHPFRC with fibers of larger aspect ratio produce a more ductile response. Empelmann et al. [106] also made similar observations based on data from experiments. They suggested that a smaller volume of longer steel fibers (> 17 mm) is required to achieve the same level of ductility in UHPFRC as that with shorter fibers (= 9 mm), thus implying fibers with larger aspect ratio lead to higher improvement in ductility.

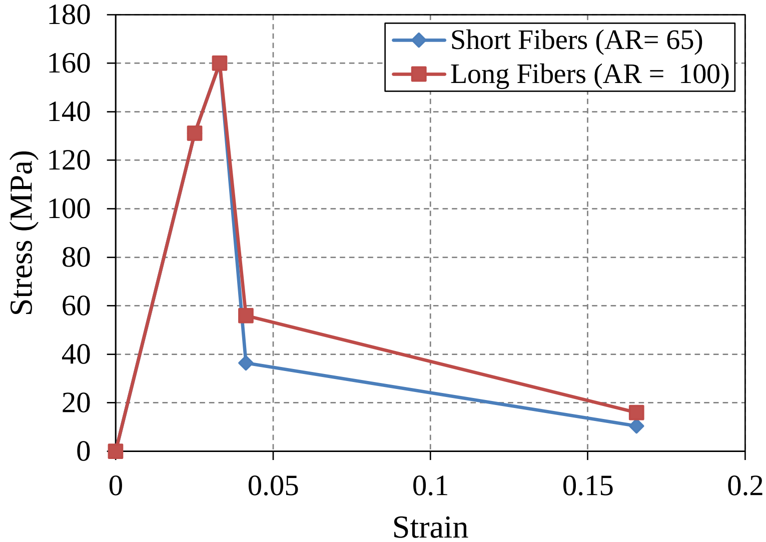

Figure 2-10. Effect of fiber aspect ratio on compressive stress-strain behavior of UHPFRC

Experiments conducted by Graybeal [72] showed that stress-strain response of steam treated and untreated UHPFRC was linear elastic upto 80% and 70% of their compressive strength (see Figure 2-11). Graybeal implemented an analytical technique to define stress strain response of UHPFRC. The stress strain response was defined by Eq. (2-1), wherein stress and strain were related by elastic modulus and a reduction factor.

$$f_c = E\varepsilon(1 - \alpha) \tag{2-1}$$

$$\alpha = a\, e^{\frac{E\varepsilon}{b\, f_c'}} - a \tag{2-2}$$

$$E = 3840\sqrt{f_c'} \tag{2-3}$$

where ε, E, f_c', and α are compressive strain, elastic modulus, compressive strength, and reduction factor, respectively. The fitting parameters a and b, were defined as 0.001 and 0.24, respectively.

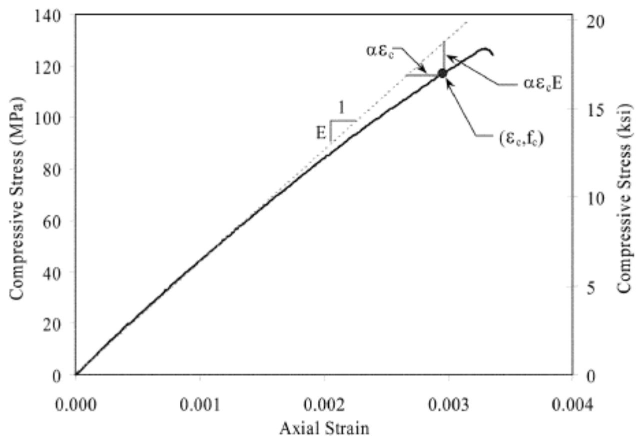

Figure 2-11. Compressive stress strain of UHPFRC compared to linear elastic behavior [72]

However, number of studies [5,49,61,108] have reported that UHPFRC exhibits a linear stress strain response until attaining peak compressive strength, and then fails in a brittle manner i.e. the load suddenly drops to zero after reaching peak compressive strength as shown in Figure 2-12. However, significant fragmentation was not observed for UHPFRC under compression due to confinement effects of steel fibers. Therefore, stress strain response of UHPFRC can be obtained with knowing compressive strength and elastic modulus (see Figure 2-12(c)).

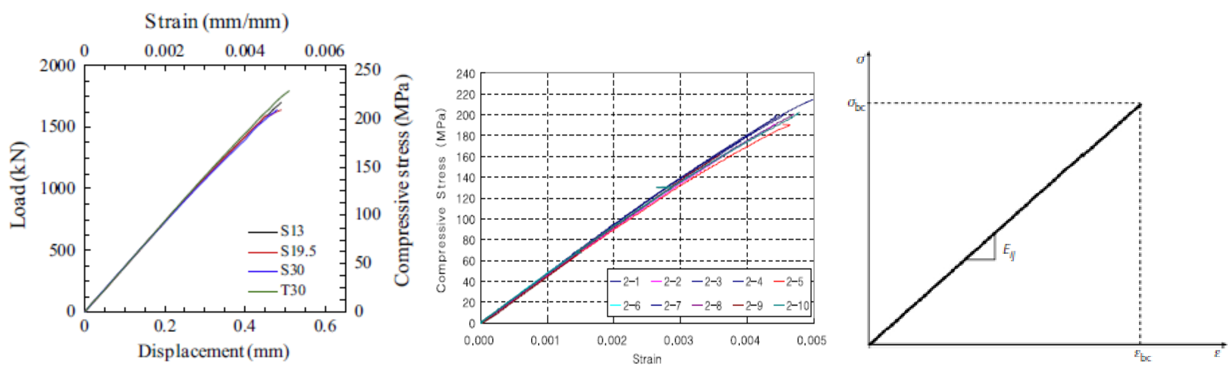

(a) Yoo and Yoon [49] (b) Yang et al. [61] (c) Yang et al. [5]

Figure 2-12. Compressive stress strain response of UHPFRC

2.2.4 Tensile Response of UHPC

The tensile behavior of UHPFRC primarily depends on various factors such as characteristic strength of the concrete matrix, fiber type, orientation and distribution of fibers, fiber aspect-ratio and fiber content (by volume). The load bearing behavior of UHPFRC under tension can be effectively studied through flexural tests. The flexural strength measured in these tests can be used to calculate uniaxial tensile strength as well. Thus, flexural strength is critical in determining fracture capacity of UHPFRC. However, flexural capacity alone cannot be utilized to describe the complete fracture mechanism. A comprehensive model involving crack initiation, followed by tensile softening behavior due to the presence of fibers, is needed to describe complete tensile response of UHPFRC. The fibers present in UHPFRC induce significant bridging stress between open crack faces. This bridging stress between opened cracks faces leads to a relatively higher fracture toughness and ductility in UHPFRC. Therefore, it is essential that this fiber bridging mechanism is effectively incorporated in modeling tensile fracture of UHPFRC.

Kang et al. [1] applied the inverse analysis method, as suggested by Uchida and Kurihara [109], to develop a tensile fracture model for UHPFRC. In this methodology, load-displacement curves obtained from flexural tensile tests were utilized to perform an inverse analysis through finite element analysis and poly-linear approximation method proposed by Kitsutaka [110]. The optimum solution of the inverse analysis can be used to develop a simplified stress-crack opening relation. The developed relations can be then employed for structural design or nonlinear analysis of structures involving crack propagation and fracture [81].

In the relation proposed by Kang et al. [1], the tensile fracture behavior is approximated by a trilinear softening response which has an initial softening branch due to matrix cracking, and a bridging plateau region followed by a final softening branch, as depicted in Figure 2-13.

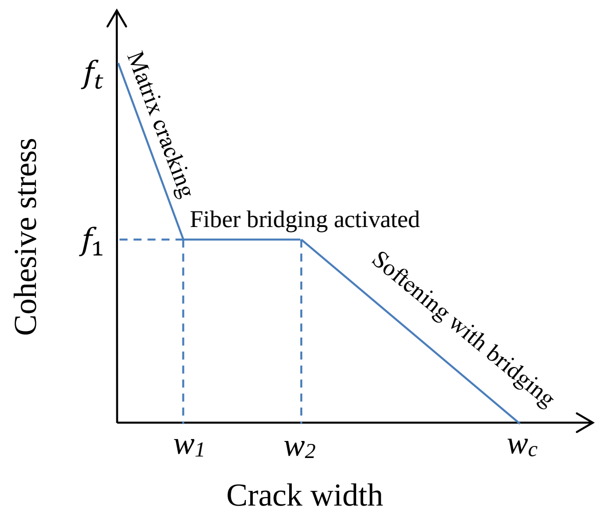

Figure 2-13. Tri-linear approximation for tensile softening behavior of UHPFRC [1]

The five parameters (f_t, f_1, w_1, w_2 and w_c) depicted in Figure 2-13 can be approximated using the relationships below (Eqs. (2-4) to (2-9)) which take into account the fiber content (by volume) and length (aspect ratio) as well:

$$f_t = a_{f_t} V_f + b_{f_t} \tag{2-4}$$

$$f_1 = a_{f_1} V_f + b_{f_1} \tag{2-5}$$

$$w_1 = b_{w_1} \tag{2-6}$$

$$w_2 - w_1 = a_{w_2}(1 - e^{-b_{w_2} V_f}) \tag{2-7}$$

$$w_c = l_f/2 \text{ for } V_f < b_{w_c} \tag{2-8}$$

$$w_c = \frac{l_f}{2} e^{-(V_f - b_{w_c})} + a_{w_c}(1 - e^{-(V_f - b_{w_c})}) \text{ for } V_f \geq b_{w_c} \tag{2-9}$$

In the above Eqs. (2-4) to (2-9), f_t and f_1 are strength parameters indicating initiation of cracking and activation of bridging; V_f is the fiber content (by volume) ratio; l_f is the fiber length. The various coefficients obtained through regression analysis on experimental are: $a_{f_t} = 7.09$, $b_{f_t} = 16.2$, $a_{f_1} = 3.79$, $b_{f_1} = 3.69$, $b_{w_1} = 0.0242$, $a_{w_2} = 0.5$, $b_{w_2} = 0.54$, $a_{w_c} = 4.64$ and $b_{w_c} = 1.29$.

Kang et al. [1] validated the above relations for tensile response of UHPFRC by comparing the predicted load deflection response by a finite element model (developed using the proposed tensile fracture model) with measured data from flexural tests. The comparison for a particular case with a fiber content (by volume) of 4% is plotted in Figure 2-14. It can be seen in Figure 2-14 that there is reasonable agreement even at higher fiber content by volume (4% in the presented case) using the above approach.

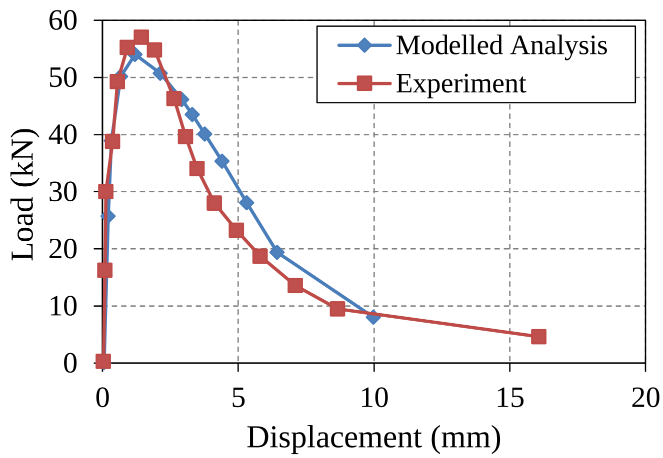

Figure 2-14. Comparison of predicted and measured load deflection response of UHPFRC with 4% fiber content

The above approach was also utilized to study the effect of changing fiber content on the tensile behavior of UHPFRC. The cohesive stress-crack width relationship of UHPFRC for a fiber length of 13 mm is plotted in Figure 2-15 for three different volume fractions (V_f) of steel fibers, namely, 1%, 2% and 5%. Results plotted in Figure 2-15 indicate that tensile fracture stress is greatly enhanced by increasing fiber content. Also, the stress-constant bridging zone increases while the stress-resisting zone decreases with increasing fiber content. In general, higher fiber content (by volume) greatly enhances the tensile performance of UHPFRC.

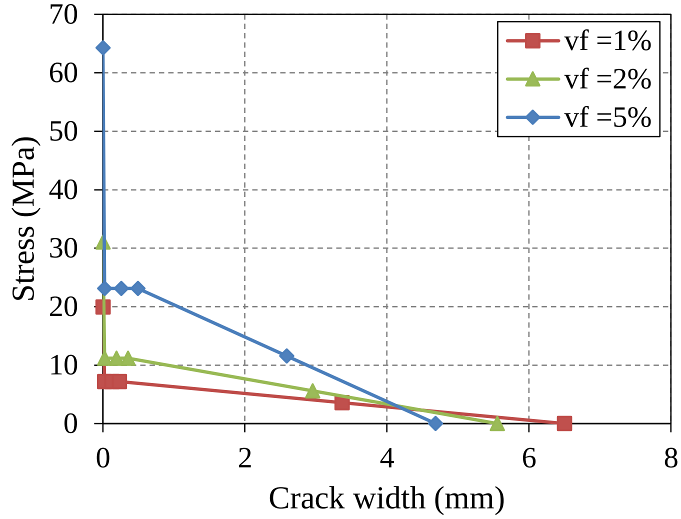

Figure 2-15. Tensile softening response in UHPFRC varying fiber content

Fiber size (aspect ratio) can have significant influence on both cracking stress and ductility of UHPFRC. Tensile fracture response of UHPFRC with long fibers (30 mm) and short fibers (13 mm) is plotted in Figure 2-16. UHPFRC with longer fibers yields better response than shorter fibers when it comes to tensile behavior of UHPFRC. A significant improvement is seen in fracture toughness and ductility when longer fibers are used in UHPFRC.

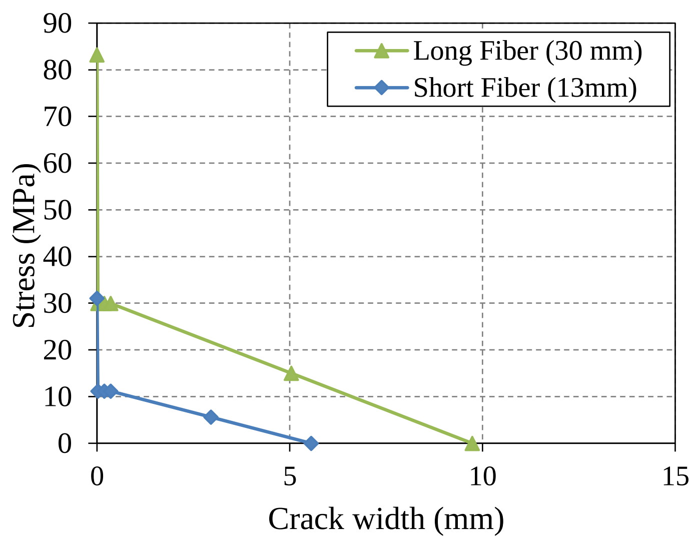

Figure 2-16. Tensile softening response of UHPFRC with varying fiber length

In addition, Yoo et al. [4] also studied tensile fracture properties of UHPFRC considering effects of fiber content and proposed tensile softening model. The authors proposed a bi-linear tension softening model for UHPFRC with different fiber volume fractions using three-point bending tests and inverse analyses. In this study, micro steel fiber with length of 13 mm and diameter of 0.2 mm were utilized. The proposed bi-linear tension softening model is presented in Figure 2-17 and Eq. 2-10 to 2-12. As can be seen, the stress f_1 and crack opening at the end of bridging plateau (w_1) increased with increasing fiber volume fraction. However, maximum crack width was not affected by fiber content. Further, Yoo et al. [51] proposed a trilinear tension softening curves utilizing three-point bending tests and inverse analyses for UHPFRC for different fiber length (13mm, 16.3mm, 19.5mm, and 30mm).

$$\sigma = f_1 \ \text{for} \ w < w_1 \tag{2-10}$$

$$\sigma = \frac{f_1}{w_c - w_1}(w_c - w_1) \ \text{for} \ \ w_1 < w < w_c \tag{2-11}$$

$$\sigma = 0 \text{ for } w_c < w \tag{2-12}$$

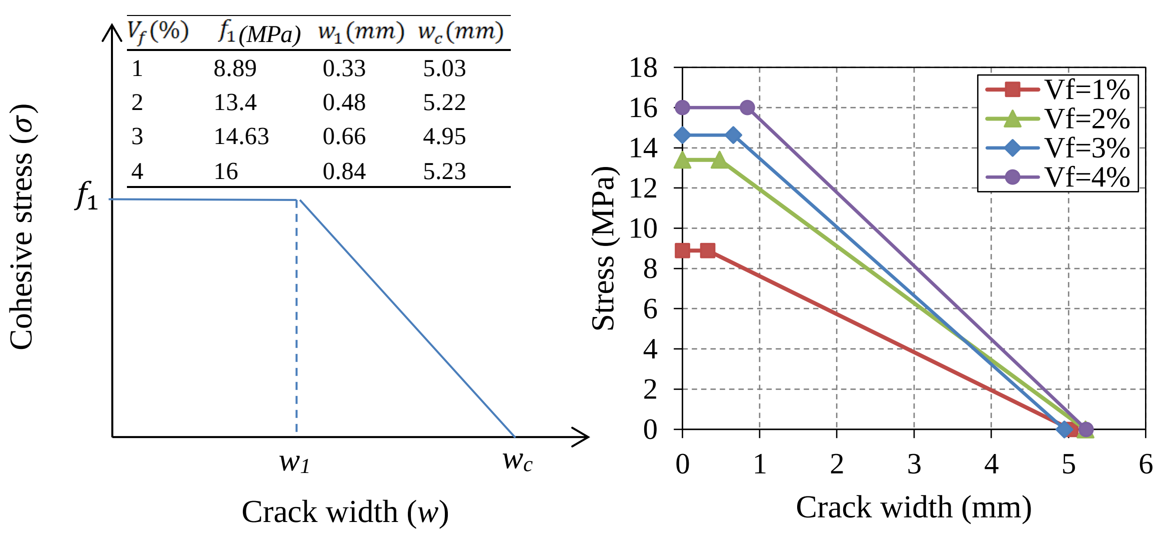

Figure 2-17. Bi-linear approximation for tensile softening behavior of UHPFRC [4,26]

Wille et al [88] conducted direct tensile tests on UHPFRC specimens with three types of steel fibers (straight, hooked, and twisted), each in three different fiber volume fractions. Wille and Naaman [111] showed that tensile stress strain response of UHPFRC can be idealized into three parts of elastic, strain hardening which is associated with multiple cracks and fiber bridging, and crack opening softening parts. The experiments showed that tensile response of UHPFRC strongly depended on fiber volume fraction. However, in their study tensile strength, stains, and energy absorption capacity was not influenced significantly by type of fibers. This was attributed to high bond strength observed between straight fibers and UHPC which allowed development of high tensile strength and ductility. The authors developed expression either empirically or from mechanics to define tensile stress strain response of UHPFRC [88,112].

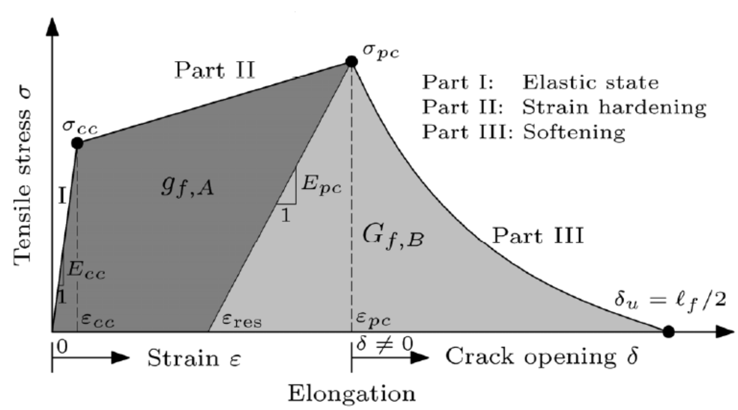

Figure 2-18. Idealized stress-strain response of UHPFRC under tension [111]

The first part can be calculated using elastic modulus and cracking stress using Eq. 2-13 to 2-14. In these expressions E_c, E_s, V_f, and f_c are elastic modulus of matrix, elastic modulus of fibers, fiber volume fraction, and compressive strength, respectively. σ_{cc} is the transition point from linear elastic to strain hardening response. The second part (strain hardening) can be obtained using strain hardening modulus and stress at peak as shown in Figure 2-19.

$$E_{cc} = (1 - V_f)E_c + V_f E_s;\ E_c = 9150\, f_c^{\frac{1}{3}} \tag{2-13}$$

$$\sigma_{cc} = -(V_f - 4)^2 + 14 \tag{2-14}$$

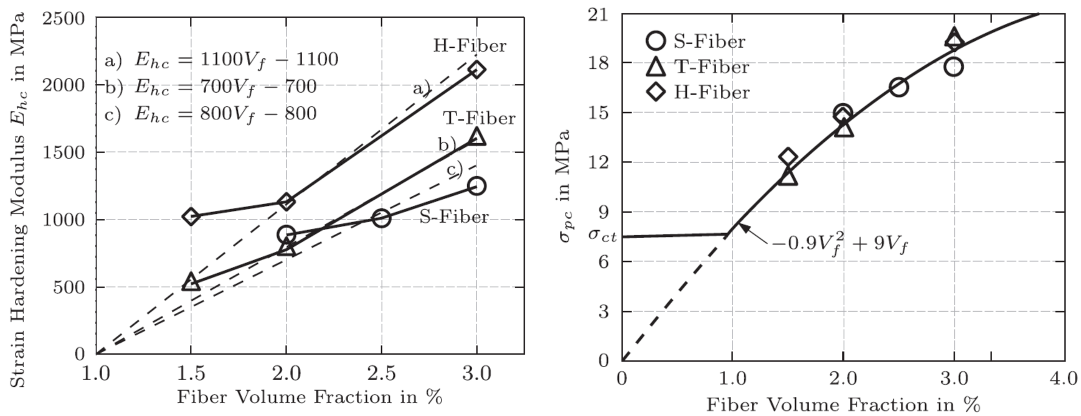

Figure 2-19. Tensile stress-strain parameters for UHPFRC with different fibers [88,112]

2.3 Studies on Structural Response of UHPC beams

2.3.1 Experimental Studies

The previous studies discussed above mainly focused on properties of UHPFRC at material level. A number of experimental studies have also been reported to evaluate structural behavior of beams fabricated with UHPFRC. Some of the major studies are presented in this section and summarized in Table 2-4.

Yoo and Yoon [49] studied flexural response of UHPFRC beams by testing a number of reinforced UHPFRC beams of rectangular cross section with stirrups. The UHPFRC was made with different types of steel fibers (straight and twisted) and with different lengths (13mm, 19.5mm, and 30 mm). The beams were designed with two different reinforcement ratios of 0.94% and 1.50%. Based on these tests, Yoo and Yoon [49] showed that including steel fiber at 2%

volume fraction significantly enhanced post cracking stiffness, flexural capacity of the beams as compared to beams without steel fibers as shown in Figure 2-20. In addition, the results showed that using longer straight steel fibers and twisted fibers (instead of straight fibers) can improve post cracking stiffness and ductility of the beams. It should be noted that beams with fibers exhibited lower ductility indices as compared to beams without fibers.

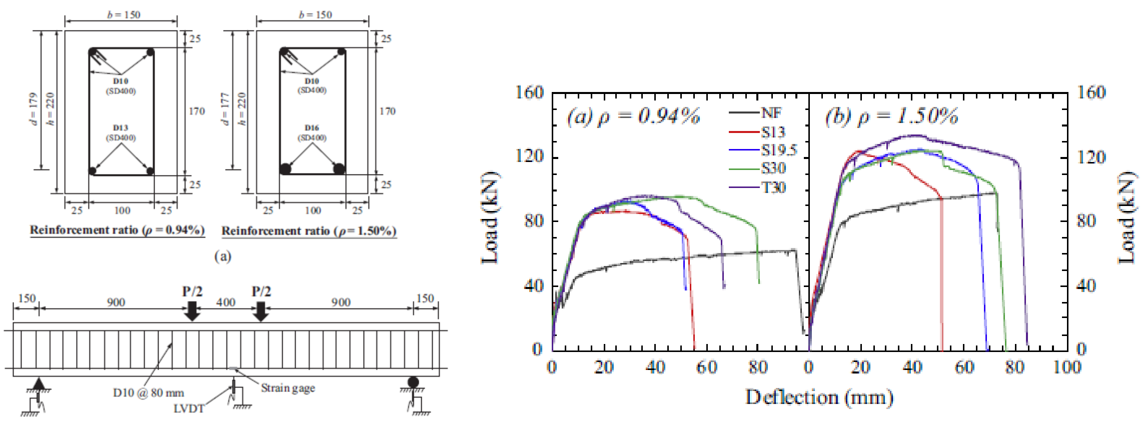

Figure 2-20. Beam details, load configuration, and load-deflection response of UHPFRC beams subjected to flexural loading

Yang et al. [61] conducted flexural tests on beams with rectangular cross section fabricated with UHPFRC with an average compressive and tensile strength of 194 MPa and 11 MPa, respectively. The tests variable included reinforcement ratio and palcement method of concrete. Results from these studies inferred that placing method (casting process) influences distribution and alignment of fibers in UHPFRC structural members. The orientation and dispersion of steel fibers in turn can have significant influence on flexural strength and stiffness which govern deflection of UHPFRC members. Yang et al. [61] illustrated that placing concrete at one end of the beams resulted in better performance due to orientation of fibers to the direction of beam length at critical section of the beams. The results also showed that UHPFRC beams exhibited ductile behavior with ductility indices ranging from 1.60 to 3.75 and addition of steel fibers to UHPC was effective in controlling cracking in UHPFRC beams.

Singh et al [113] studied flexural response of UHPFRC beams with stirrups. The beams had cross section of 250mm×250mm and 150mm×150mm, and span of 3250, 2700mm, and 1350 mm and were tested under different loading configurations. All the beams exhibited ductile flexural failure, and experienced steel reinforcement rupture.

Yoo et al. [63] evaluated flexural response of UHPFRC beams reinforced with glass fiber reinforced polymer (GFRP) bars and hybrid reinforcements (steel+GFRP bars). The results from this study showed that UHPFRC beams with hybrid reinforcement exhibited slightly lower stiffness (after rebar yielding) and ultimate moment capacity as compared to UHPFRC beams with only GFRP. Therefore, Yoo et al. recommended using GFRP bars with UHPFRC rather than using hybrid reinforcement. The authors also concluded that UHPFRC is a solution to overcome drawbacks limiting the application of FRP since GFRP reinforced UHPFRC beams exhibited significantly increased stiffness and very fine microcarcks that are major drawbacks of FRP reinforced conventional concrete and FRC beams.

Graybeal [46] evaluated flexural response of full-scale prestressed UHPFRC I-girder (AASHTO Type II girder) containing 26 prestressing strands for application in bridges [46,62]. The results showed that a UHPFRC I-girder possesses larger flexural capacity as compared to conventional concrete girders with similar cross sectional geometry. Data from the experiment showed inversely proportional crack spacing to the maximum tensile strain. Based on the results of this experiment, Graybeal [46] proposed flexural design philosophy for prestressed UHPFRC girders.

Significant effort has been spent on study of steel fiber reinforced concrete subjected to shear [17,114–122]. The authors reported that addition of steel fibers to a reinforced concrete beam can significantly enhance shear strength and suppress brittle shear failure. However, these studies focused on normal-strength and moderately high strength concrete. There are limited studies on shear behavior of UHPFRC beams and most of the available studies are on I-section and T-section beams. Voo et al [123] evaluated shear capacity of UHPFRC beams through tests on I-section prestressed UHPFRC beams. The beams were 8.6 m long with variable span length, and 650 mm deep. The width of the flanges and web were designed to be 500 mm and 50mm, respectively. The test variables included length of fibers, percentage of fibers, shear span to effective depth ratio, and lack of stirrups in beams. The tests showed a significant distribution of shear cracking occurred in the web of the beams before widening of the major crack leading to failure (see Figure 2-21). The results showed that higher shear capacity was achieved by using a higher fiber volume content in UHPFRC and a lower shear span to depth ratio.

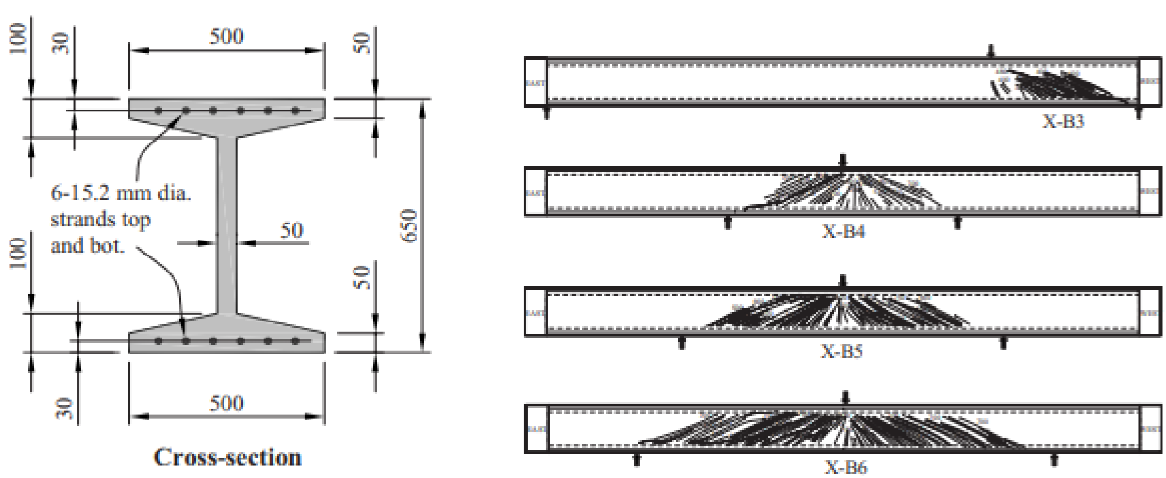

Figure 2-21. Cross section of the tested beams and the observed cracking pattern in the experiments [123]

Yang et al. [124], conducted tests on UHPC I-section beams without stirrups subjected to dominant shear loading. They investigated the effects of ratio of shear span to effective depth, steel fiber content, and presence of prestress. This study also showed that shear strength improved with increasing steel fiber content and decreasing shear span to depth ratio. For instance, including steel fibers of 2.5% volume fraction resulted in improving shear capacity by 177% as compared to beams without fibers. Decreasing shear span to depth ratio from 3.4 to 2.5, resulted in enhancing shear capacity of I-beams by 30-99% and 50-63% for non-prestressed and prestressed beams, respectively [124].

Xia et al. [125] investigated mechanism of shear failure in UHPFRC beams with high strength steel rebars. The results from this study showed that shear failure of the UHPFRC beams was ductile with high post-crack shear resistance due to presence of fibers bridging as opposed to conventional concrete beams that exhibited brittle response and abrupt load reduction.

Baby et al. [126] conducted shear tests on I-shaped girders. The test variables included the presence of steel fibers and shear reinforcement, and use of prestressing or steel bars. The results showed that including steel fibers with volume fraction of 2.5% resulted in 250% increase in shear capacity of the girder. In order to examine the fiber orientation effect on shear performance of I-girders, prisms were drilled out of the ends of the girders at different inclination angles, and were tested under three-point flexural loading. Results from this study inferred that fiber orientation significantly influenced flexural behavior of UHPFRC, therefore, it was recommended that this factor is to be taken into account in shear design of girders. The authors also reported that design recommendations in AFGC-SETRA were conservative.

Bunje and Fehling [78] carried out four-point tests on UHPC beams with rectangular sections without stirrups to determine shear capacity. The beams were provided with different reinforcement ratios (2.5 to 7.2%), with and without steel fibers. The results showed that beams with fiber reinforced UHPC turned out to have much higher shear capacity as compared to beams with UHPC without fibers. The results showed that full bending capacity was reached in all UHPFRC beams and failure was ductile flexural. Only UHPFRC beam with high longitudinal reinforcement ratio of 7.2 exhibited combined flexural shear failure. However, UHPC beams (without fibers) exhibited shear failure. Figure 2-22 illustrated the change in mode of failure from brittle shear to ductile flexure in UHPC beam with including steel fibers.

(a) UHPC beam without steel fibers

(b) UHPFRC beam with steel fibers

Figure 2-22. Change of mode of failure from brittle shear to ductile shear in UHPC beams with including steel fibers

Pourbaba et al. [127] conducted parametric studies on 38 beam specimens made with NSC and UHPFRC. Studied parameters included type of concrete (NSC and UHPFRC), shear span to depth ratio (0.8, 1.2, and 2.8), reinforcement ratio (2.2% to 7.8%), type of reinforcement (mild steel and high strength steel), and reinforcement anchorage. The beams were 559 mm in length, 102 and 152 in width, and 76, 152, and 203mm in depth. Results from this experimental study showed that beams with shorter shear span and higher reinforcement ratio exhibited higher shear strength. Also, anchorage did not influence the response of UHPFRC beams however, it improved ductility of NC beams. Normalized shear strength ($\frac{V}{\sqrt{f_c'}b_w d}$) of the beams with different type of longitudinal reinforcement showed that high strength steel contributed about 14% to shear strength in both NSC and UHPFRC beams. This was attributed to improved dowel action in high strength steel reinforcement. Results also showed that regardless of type of reinforcement, UHPFRC beams showed 77% higher normalized shear strength as compared to similar NSC beams as shown in Figure 2-23. On average, shear capacity of UHPFRC beams was 3.5 times larger than similar NSC beams. However, the results may be different if larger specimens were used as the tested beams had length of 559 mm.

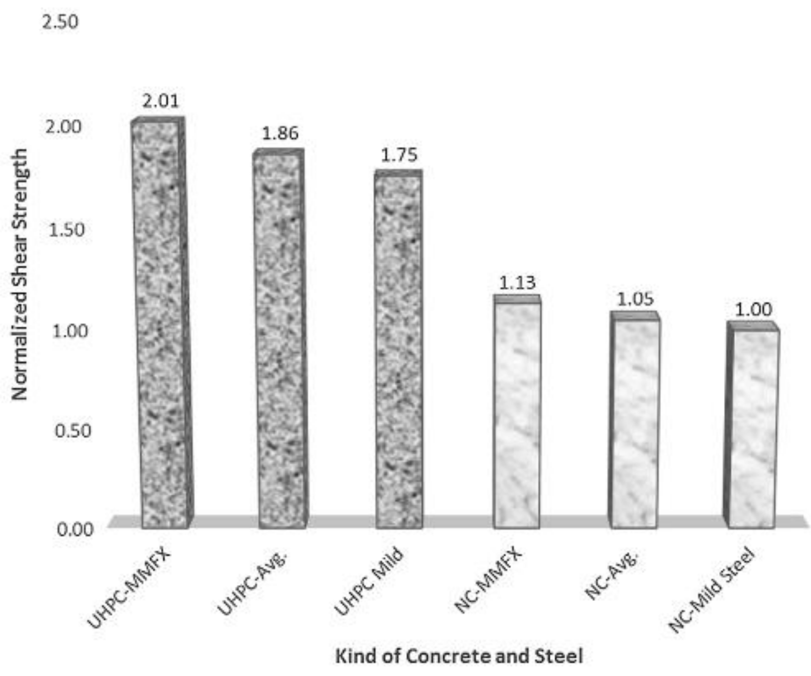

Figure 2-23. Normalized shear strength of UHPFRC and NSC beams [127]

Table 2-4. Reported experimental studies on flexural and shear behavior of UHPFRC beams and girders

Reference	Beam cross section	f_c' (Mpa)	Fiber type and size	Fiber Fraction (%)	Loading Pattern	Studied Parameters
Yoo and Yoon (2015)	Rectangle	200-232	Straight steel fiber (Lf =13, 19.5, 30 mm, df=0.2, 0.3 mm); Twisted steel fiber (Lf =30 mm, df=0.2mm)	0, 2	4-point loading (Flexure)	Type of steel fibers; Length of fibers
Yang et al (2010)	Rectangle	190-197	Straigth steel fiber (Lf =13 mm, df=0.2 mm)	2	4-point loading (Flexure)	Reinforcement ratio; Concrete palcing method
Singh et al. (2017)	Rectangle	143	End-hooked steel fiber (Lf =35 mm, df=0.5 mm)	2.25	4-point and 3-point loading (Flexure)	Size of the beams; loading configuration
Graybeal (2006 & 2008)	I-girder (prestressed)	200	Straigth steel fiber (Lf =13 mm, df=0.2 mm)	2	4-point loading (Flexure and shear)	Flexural and shear behavior of AASHTo type II girder
Yoo et al (2016)	Rectangle	197	Straigth steel fiber (Lf =13 mm, df=0.2 mm)	2	4-point loading (Flexure)	Reinforcement ratio; Type of reinforcement (GFRP and steel bars)
Baby et al (2013)	I-girder (prestressed)	157-205	Straight steel fiber (Lf =13, df=0.2 mm, and Lf = 20 mm, df= 0.3 mm); Organic fibers	0, 2.5, and 4.7	4-point loading (Shear)	UHPFRC mix; Use of strands or bars; Presence of shear reinforcement
Voo et al (2010)	I-girder (prestressed)	125-140	Straight steel fiber (Lf =15, 20, 25 mm, df=0.2 mm)	1 and 1.5	3-point loading (Shear)	Type and quantity of fibers; Shear span to depth ratio
Yang et al (2012)	I-beams	160-190	Straight steel fiber (Lf =13 mm, df=0.2 mm)	1, 1.5, and 2	3-point loading (Shear)	Shear span to depth ratio; Volume fraction of steel fibers; Presence of prestress
Bunje and Fehling (2004)	Rectangle	180-207	Straigth steel fiber (Lf =9 mm, df=0.15 mm)	2.5	4-point loading (Shear)	Reinforcement ratio; Presence of shear reinforcement
Pourbaba et al. (2018)	Rectangle	125-137	Straigth steel fiber (Lf =13 mm, df=0.2 mm)	2	4-point loading (Flexure-Shear)	Type of concrete (NSC or UHPFRC); Reinforcement ratio; Shear span to depth ratio
Xia et al (2011)	T- beams (deck strip)	193	-	2	3-point loading (Shear)	Longitudinal and shear reinforcement ratio

2.3.2 Numerical Studies

There are limited numerical studies on the structural behavior of UHPFRC beams. Some of the major studies are summarized in Table 2-5. Much of the reported numerical studies focused on applying sectional analysis approach to trace moment curvature response of UHPFRC beams under flexural loading [5,49,128]. Yang et al. [5], Yoo and Yoon [49], and Yoo et al [128] applied sectional analysis to predict flexural behavior of UHPFRC beams. In these studies, compressive response was modeled using linear stress-strain response till failure. For tensile response, results from 3-point bending test (Load-CMOD) were utilized to obtain tension softening curve using inverse analysis. For this purpose, relation between stress and CMOD was obtained from crack growth analysis based on a fictitious crack model. Then, stress and crack width was converted to stress-strain response using recommendations in AFGC [25] and JSCE [26]. Results from these studies showed that analytical approach was effective in evaluating moment-curvature response of UHPFRC beams. It should be noted that in these analytical approaches, strain hardening response of steel reinforcement was ignored and elastic perfect plastic response was considered. Further, Yao et al. [129] proposed an analytical model to predict flexural response of UHPFRC beams. The model is able to predict moment-curvature, load-deflection response of UHPFRC with different cross sectional configurations subjected to bending.

There are limited finite element based numerical studies that simulated the behavior of UHPFRC members. Mahmud et al [130] undertook two dimensional plane stress finite element analysis of unreinforced notched UHPFRC beams to study size effects on flexural capacity. The results showed that the size effect is negligible for beams up to 300 mm in depth. Tysmans et al. [131] simulated the behavior of high performance fiber reinforced concrete under biaxial tension. The authors inferred that finite element model incorporating concrete damage plasticity (CDP) material model can account for strain hardening behavior of UHPFRC in tension and thus can predict realistic load capacity of UHPFRC members. However, these studies relied upon small-scale specimens with no reinforcing bars for validating the model.

Singh et al [113] developed a finite element model for evaluating structural behavior of UHPFRC beams wherein the developed model was validated only under flexural and not under shear loading. The authors showed that the model was able to predict moment capacity of UHPFRC beam, and the variation with respect to experimental measurement were 5%.

Chen and Graybeal [62,132] focused on predicting load deflection (strain) response of UHPFRC I-girders and Pi-girders subjected to shear and flexure. The authors showed that finite element model adopting smeared cracking model produce a stiffer response as compared to concrete damage plasticity model. However, in this study strain hardening response of UHPFRC in tension was neglected.

Bahij et al. [133] developed a numerical model for tracing shear response of UHPFRC beams. The authors showed that mode of failure changes from shear to flexure with increasing shear span to depth ratio. However, strain hardening in steel and UHPFRC was not included in the developed model and therefore post-peak response of the beams was not captured. Also, shear contribution of concrete and stirrups was not quantified.

Baby et al. [134] applied modified compression field theory for predicting shear capacity of reinforced or prestressed UHPFRC girders. The model was validated against data generated from two sets of experiments, and predictions agreed well with experimental measured data. In this study, tensile response of UHPFRC was modeled as elastic-perfectly plastic stress strain response without considering strain hardening effect of UHPFRC. Also, the ultimate state was identified as the strain corresponding to crack localization on unnotched prisms tested under fourpoint bending, therefore the post crack localization and descending branch of structural response was not predicted.

Voo et al. [135,136] developed a model for predicting shear strength of steel fiber reinforced concrete beams based on plastic shear model (PSM) proposed by Zhang [137] and variable engagement model (VEM) proposed by Voo and Foster [138]. Voo et al. [123] modified VEM model for predicting shear capacity of UHPFRC beams. The authors reported that since steel fibers in concrete leads to plastic response after cracking, theory of concrete plasticity provides a good basis for shear design of UHPC beams. However, the proposed approaches are not simplified expressions for practical design purposes. In this study, test results of only 17 UHPC prestressed beams, from five test series of two research groups, were used for validation.

Table 2-5. Reported numerical studies on flexural and shear behavior of UHPFRC beams and girders

Reference	Analysis	Member	Loading Pattern	Studied Parameters	Main Findings
Yang et al (2011)	Sectional Analysis	Rectangular beam	Flexure	Tension softening curve	Bending strength of UHPFRC beams can be accurately predicted by employing sectional analysis.
Yoo and Yoon (2015)	Sectional Analysis	Rectangular beam	Flexure	Material model recommended by AFGC/SETRA	Sectional analyses incorporating AFGC/SETRA tension stiffening curves with fiber orientation factor of 1.25 predicted the flexural capacity of UHPFRC beams well.
Yao et al. (2020)	Analytical approach	Beams with different cross section	Flexure	Reinforcement and geometric characteristics	The developed analytical model can predict moment curvature and load deflection of UHPFRC beams.
Mahmud et al (2013)	FEA	Notched prism	Flexure	Size effect	Size effect on the beam nominal strength is little due to high ductility of UHPFRC.
Tysmans et al. (2015)	FEA	Cruciform specimen	Biaxial tension-tension	Biaxial stress state-strain distribution	CDP model can simulate strain hardening capacity after crack initiation in UHPFRC.
Singh et al (2017)	FEA	Rectangular beam	Flexure	Load displacement response; Moment capacity	CDP model can accurately predict the load/moment carrying capacities of the UHPFRC beams.
Chen and Graybeal (2011)	FEA	I-girder	Flexure and Shear	Applicability of CDP; Mesh sensitivity	CDP can replicate deflection and strain response of UHPC I-girders; The maximum tensile stress of UHPC played a significant role in the predicted FEM response.
Baby et al (2013)	Stress field approach	I-girder (prestressed)	Shear	Feasibility of applying modified compression field theory	Predictions of model agree well with test data.
Bahij et al. (2018)	FEA	Rectangular beam	Shear	Shear span to depth ratio; Volume fraction of steel fiber; reinforcement ratio; Stirrups spacing	The cracking pattern changes from flexural mode to shear mode with increasing *a/d*; Shear capacity increases linearly with increasing volume fraction of steel fibers and decreasing a/d.

2.4 Provisions in Design Standards and Codes

In the US, structural design criteria for UHPC have not been fully developed. There are limited provisions and recommendations for structural design of UHPC (FHWA [8], AFGC-SETRA [25], JSCE [26], and KCI [139]). These recommendations integrates knowledge and experience from first industrial applications and laboratory research.

AFGC [25] and JSCE [26] recommendations are categorized in three parts. First part deals with material characteristics of UHPC, and second part is about design and analysis of UHPC members. Finally, last part deals with durability properties of UHPC. In AFGC-SETRA[25], design strength is recommended based on mechanical properties of Ductal®[140], having compressive strength (f_{ck}) of 150-250 MPa, post cracking tensile strength (f_{tj}) of 8 MPa, and elastic modulus (E_c) of 55 GPA. In order to consider effect of fiber orientation on tensile response, fiber orientation coefficients is suggested in AFGC-SETRA[25]. Compressive model is also presented by a bilinear stress-strain response with design strength and strain of $\sigma_{bcu} = o.85 f_{ck}/\theta\gamma_b$ and $\varepsilon_u = 0.003$, respectively as shown in Figure 2-25. For tensile modeling according to in AFGC-SETRA [25], first load-CMOD obtained from flexural tests on prisms needs to be converted to stress-CMOD. Then, stress-CMOD can be converted to stress-strain using proposed relations. Strains at cracking stage, and at crack width of 0.3mm and 1% f beam height can be calculated using Eq. 2-15 to 2-17. It should be noted that these material models are not valid for different material characteristics including matrix strength, fiber type, and volume fraction.

$$\varepsilon_e = \frac{f_{tj}}{E_c} \tag{2-15}$$

$$\varepsilon_{0.3} = \frac{w_{0.3}}{l_c} + \frac{f_{tj}}{\gamma_{bf} E_c} \tag{2-16}$$

$$\varepsilon_{1\%} = \frac{w_{1\%}}{l_c} + \frac{f_{tj}}{\gamma_{bf} E_c} \tag{2-17}$$

where ε_e, $\varepsilon_{0.3}$, $\varepsilon_{1\%}$ are elastic strain, strain at crack width of 0.3 mm ($w_{0.3}$), and strain at crack width corresponding to 1% height ($0.01H$) of the specimen. The ultimate strain is defined by Eq. 2-18, in which L_f , l_c are length of fiber, characteristic length defined as $l_c = \frac{2}{3}h$, and h is beam height.

$$\varepsilon_{lim} = \frac{L_f}{4l_c} \tag{2-18}$$

Stresses at crack width of 0.3mm (f_{bt}) and 1% height of the beam height ($f_{1\%}$) can be calculated using Eq. 2-19 and 2-20. A partial safety factor is introduced to account for any manufacturing defects, γ_{bf}=1.3 in case of fundamental combinations, and γ_{bf}=1.05 in case of accident combinations. In addition, to account for fiber orientation effect on tensile response, fiber orientation coefficient (K) is considered as follows: K=1 for placement methods validated from test results of a representative model of actual structure, K=1.25 for all loading other than local effects, and K=1.75 for local effects.

$$f_{bt} = \frac{f(w_{0.3})}{K\gamma_{bf}} \tag{2-19}$$

$$f_{1\%} = \frac{f(w_{1\%})}{K\gamma_{bf}} \tag{2-20}$$

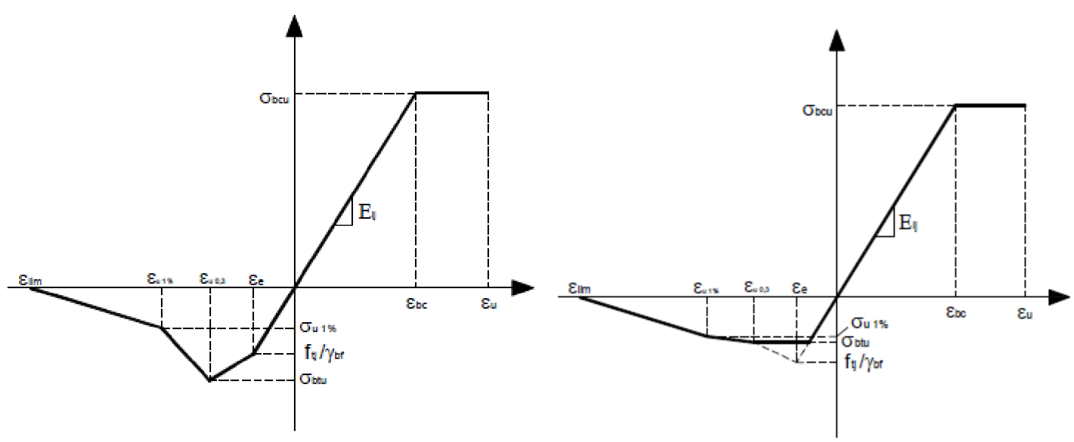

(a) Strain-hardening (b) Strain-softening

Figure 2-24. Stress-strain response of UHPFRC as specified in AFGC/SETRA [25]

Similarly, JSCE [26] provides recommendations for design strength based on Ductal® UHPFRC [140] with 2% fiber volume fraction (L_f=15mm, d_f=0.2mm), which is commercially available. JSCE suggests a bilinear stress-strain response under compression and tension (shown in Figure 2-25) with design strength parameters of f_c'=180 MPa, f_{crk}=8 MPa, f_{tk}=8.8 MPa, and E_c=50 GPa.

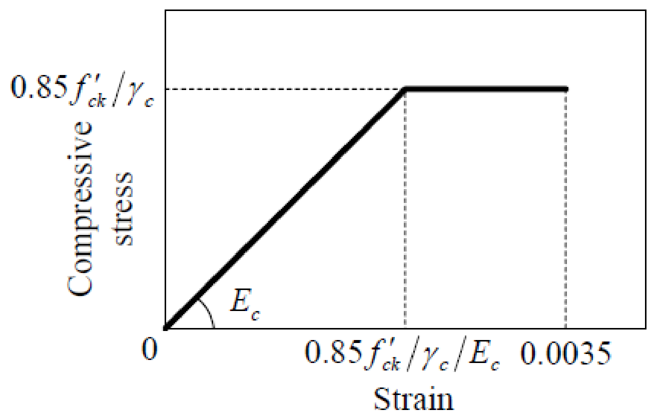

(a) Compressive stress-strain

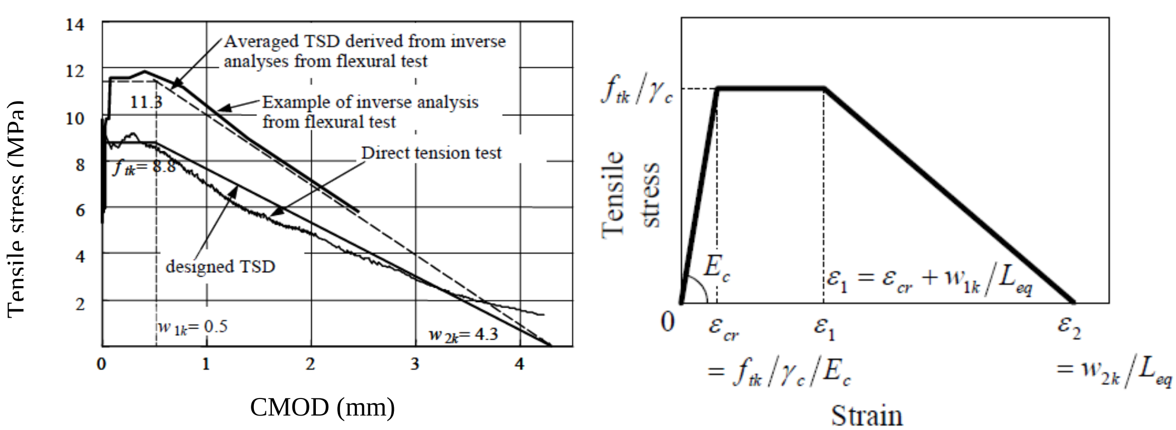

(a) Tensile stress-CMOD and tensile stress-strain

Figure 2-25. Stress-CMOD and stress-strain response of UHPFRC as specified in JSCE [26]

There is no design expressions for predicting ultimate moment capacity of flexural members or axial capacity of compression members made of UHPC in above mentioned international recommendations. Therefore, sectional analysis is to be performed adopting the suggested material models to design UHPC beams subjected to flexural loading. AFGC [25] and JSCE [26] recommended expressions for calculating shear capacity of UHPFRC beams consisting of contribution of concrete, fibers, and shear reinforcement. These recommended shear prediction expressions are summarized in Table 2-6. As per AFGC-SETRA [25] recommendations, since steel fibers contribute to shear strength of UHPFRC beams, there might be a possibility of dispensing with stirrups.

Table 2-6. Summary of shear prediction equations from literature

Reference	Shear strength models
AFGC [25]	$V_u = V_c + V_f + V_s$ $V_C = \frac{0.21}{\gamma_E \gamma_b} k\sqrt{f_c'}\, bd,\ \gamma_E \gamma_b = 1.5\ (for\ reinforced\ beams)$ $k = 1 + \frac{3\sigma_{cm}}{f_{tj}}\ (in\ compression);\ k = 1 - \frac{0.7\sigma_{tm}}{f_{tj}}\ (in\ tension)$ $V_C = \frac{0.24}{\gamma_E \gamma_b}\sqrt{f_c'}\, bz,\ \gamma_E \gamma_b = 1.5\ (for\ prestressed\ beams)$ $V_f = \frac{0.9 bd\sigma_p}{\gamma_{bf}\ tan\beta_u}$ $\sigma_p = \frac{1}{K}\frac{1}{w_{lim}}\int_0^{w_{lim}} \sigma(w)dw\,, w_{lim} = \max(w_{u,0.3\ mm})$ $V_s = 0.9\ d\ \frac{A_v}{S}\frac{f_{ys}}{\gamma_s}(sin\alpha + cos\alpha)$
JSCE [26]	$V_u = V_c + V_f + V_s,\ \ V_c = \frac{0.18}{\gamma_b}\sqrt{f_c'} bd,\ \gamma_b = 1.3$ $V_f = \frac{f_{vd}}{\gamma_b\ tan\beta_u} b_w \frac{d}{1.15},\ \ V_s = \emptyset_b d\ \frac{A_v f_{ys}}{S}(sin\alpha + cos\alpha)$ $f_{vd} = \frac{1}{w_{lim}}\int_0^{w_{lim}} \phi\ \sigma(w)dw\,,\ w_{lim} = \max(w_{u,0.3\ mm})\,, \phi = 0.8$

2.5 Field Applications of UHPC

UHPFRC, due to its excellent mechanical properties, has attracted attraction of engineers for field applications. In the US and other countries, several state departments of transportation are exploring UHPFRC in bridge projects, supported by research conducted by FHWA and universities [141]. Advanced properties of UHPC facilitate designing bridge structures having longer span, shallower depths, accompanied by improved durability. High tensile strength and ductility of UHPC can help to reduce longitudinal reinforcing area and eliminate shear reinforcement. Therefore, it reduces the fabrication costs and also mitigates corrosion degradation issues [142]. UHPC has been employed in a variety application from pedestrian bridges to architectural facades. Some examples of UHPFRC applications in architectural and civil structures in the US and other countries are presented here and are shown in Figure 2-26 and Figure 2-27.

A prestressed pedestrian bridge at Sherbrook in Canada, which was constructed in 1997, was the first application of UHPFRC [143]. The Bourg-les-Valence bridge built in France in 2001, was the first UHPFRC road bridge in the world. The bridge was made of five pi-shaped precast beams [144]. Seonyu Footbridge, built in 2002, is the longest footbridge made by UHPFRC with a single span of 120m and no central support as shown in Figure 2-26. It consists of a pi-shaped arch supporting a ribbed UHPFRC slab with a thickness of 30mm, and transverse prestressing was provided by monostrands. This bridge needed half of the amount of materials required for conventional concrete construction [145,146]. The U.S Federal Highway developed UHPC prestressed bridge girders for single span bridges spanning up to 135 ft. The developed pi-girder is double tee shaped bridge with an integral deck. The structural testing and initial deployment of this developed bridge is shown in Figure 2-26 (e) and (f). First UHPC cable stayed roadway bridge with span length of 100m was constructed in Korea [7,147]. This bridge consists of an O-shaped single steel pylon with diameter of 45m and a UHPC girder with width of 29.5m and height of 1.8m. Using UHPC in construction resulted in the girder being 33% lighter that conventional concrete girder. Therefore, the amount of stay cables and foundation was reduced and as a result it made the circular shaped pylon feasible.

(a) Prestressed pedestrian bridge in Sherbrooke [143]

(b) Bourg-les-Valence bridge in France [144]

(c) Seonyu bridge in South Korea [148]

(d) UHPC Cable Stayed Roadway Bridge [7,147]

(e) FHWA structural testing of Pi-girder [149]

(f) FHWA field deployment in Buchanan County, IA [142]

Figure 2-26. Examples of UHPC applications in bridge

Curved UHPFRC panels were applied in 2013 to a building named Atrium in Victoria, BC, Canada [150]. In this project UHPC was selected due to ability of UHPC to form monolithically tight curve that leads in energy efficiency of the building owing to eliminating openings. The museum of European and Mediterranean civilizations (MuCEM) in France, was the first building in the world that used UHPC extensively. In this structure shown in Figure 2-27, UHPC was used in tree-shaped columns, brackets and bridges decks of the footbridges, lattice style roof and facade, pedestrian footbridges with length of 115m and 69m [151,152]. Also, precast UHPFRC lattice-style facade system was built in Jean Bouin stadium in France. This facade system includes 23,000m^2 envelope containing a 12,000m^2 roof, which was built of 3600 self-supporting UHPFRC panels with 8-9m length, 2.5m width, and 45mm thickness [150,153]. Application of UHPC in building facade is increasing due to its high durability, and also possibility of producing complex forms with tight construction tolerances. UHPC was used to develop precast and prestressed thin shells in wastewater treatment plant in France. UHPC was chosen due to high strength resulting in structural slenderness, and more importantly superior durability especially in the aggressive environment of the project (high concentration of H_2S) [151]. There are other examples of UHPC applications such as facade at Terminal 1 of Rabat airport in Morocco [154], roof of the Olympic museum in Lausanne, Switzerland [155], cladding for Qatar National Museum [156].

(a) The Atrium in Canada [150,153]

(b) UHPC shells roofing over tanks [151]

(c) MUCEM in France [150,153]

(d) Stade Jean Bouin in France [150,153]

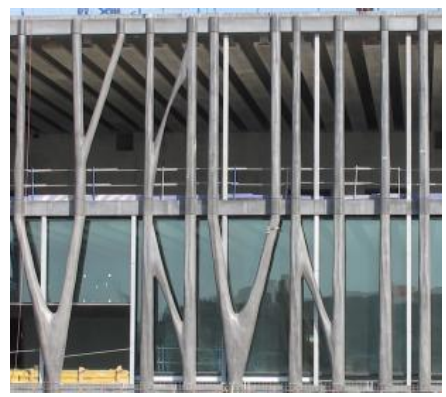

(e) Lattices in MuCEM and roof of Jean Bouin [157]

(f) Facade columns in MuCEM [158]

Figure 2-27. Building and architectural applications of UHPC

2.6 Summary

This chapter reviewed previous experimental and numerical studies on UHPFRC at material level and UHPFRC members at structural level. Previous material level studies focused on evaluating effect of number of parameters such as mix proportions, fiber type, fiber fraction, curing conditions etc. on mechanical properties of UHPFRC. At structural level, number of studies has been reported to characterize the response of UHPFRC beam with different configurations under different loading configurations using experiments and numerical modeling. Also, recommendations and provisions for UHPC members available in international codes and standards as well as field application of UHPFRC were review. This state-of-the-art review revealed that despite these research efforts over the past few decades there are some knowledge gaps as follows that further research is needed:

- Field production of UHPFRC using locally available raw materials that can be prepared in conventional ready-mix trucks has not been established.
- The conducted studies at structural level mostly focused on flexural response with only limited studies giving consideration to shear behavior of UHPFRC beams.
- There is lack of data on structural response of UHPFRC beams without stirrups.
- Numerical studies relied upon small-scale experiments for validation and focused on predicting load deflection response with no attention to local response such as crack propagation direction, and contribution of compression block, interfacial resistance, and stirrups to shear capacity.
- There is limited design methodology for UHFRC structural members in current codes and standards.

CHAPTER 3

3 EXPERIMENTAL STUDIES

As presented in Chapter 2, there is limited test data on the response of UHPC beams under dominant shear loading. To fill this gap, seven UHPFRC beams with different configurations were fabricated and tested under flexural and shear dominant loading. The test variables included sectional properties, longitudinal reinforcement ratio, presence of shear reinforcement, and type of loading (flexure and predominant shear). A UHPFRC mix containing coarse aggregates was utilized to fabricate these beams. In order to take advantage of high tensile, shear, and compressive strength offered by UHPFRC, five beams were designed without shear and compression reinforcement. The other two beams were provided with stirrups to study effects of removing shear reinforcement in the beams. Response parameters measured during tests, including load-deflection response, crack propagation, failure patterns, and failure loads were utilized to evaluate structural response of UHPFRC beams under flexural and dominant shear loading [159,160].

3.1 Design of UHPFRC Beams

All seven UHPFRC beams were of rectangular cross section and were designated as U-B3 to U-B9. The sectional dimentions of these beams were of 180 mm in width, 270 mm and 450 mm in depth. The length of the beams were selected to be 4000 mm which was dictated by the loading equipment available in MSU civil infrastructure laboratory. Since there is no specific coded provisions for UHPC members, the beams were designed based on best practices availabe as per recent research findings [5,49,61,128,153]. The rebars spacing, arrangment, and shear reinforcement were designed as per ACI-318 requirements for NSC beams [161].

To take advantage of high compressive and high tensile strength offered by UHPFRC, no compression and shear reinforcement were provided in beams U-B3 to U-B6. Sectional details and reinforcemenet configuration of fabricated UHPFRC beams are illustrated in Figure 3-1 and Table 3-1. In addition, after testing these beam to failure, the undamged part of beams U-B4, U-B5, U-B6, U-B7, and U-B9 were retested with span of 1830 mm, to evaluate effect of shear span to depth ratio and span length. These beams are named as U-B4(2), U-B5(2), U-B6(2), U-B7(2), and U-B9(2).

Table 3-1. Sectional dimensions and reinforcement of UHPFRC beams

Beam Designation	Span (mm)	Width (mm)	Depth (mm)	Tensile Reinforcement	ρ_t(%)	ρ_v(%)	Concrete cover (mm)	Concrete batch mix
U-B3	3658	180	270	3-Ø13mm	0.90	-	35	1
U-B4	3658	180	270	3-Ø13mm	0.90	-	35	1
U-B5	3658	180	270	4-Ø13mm	1.20	-	35	1
U-B6	3658	180	270	4-Ø13mm	1.20	-	35	1
U-B7	3658	180	270	4-Ø13mm	1.20	0.79	35	2
U-B8	3658	180	450	6-Ø19mm	2.48	-	45	2
U-B9	3658	180	450	6-Ø19mm	2.48	0.40	45	2
U-B4(2)	1830	180	270	3-Ø13mm	0.90	-	35	1
U-B6(2)	1830	180	270	4-Ø13mm	1.20	-	35	1
U-B7(2)	1830	180	270	4-Ø13mm	1.20	0.79	35	2
U-B9(2)	1830	180	450	6-Ø19mm	2.48	0.40	45	2

ρ_t: Tensile reinforcement ratio, ρ_v: Shear reinforcement ratio

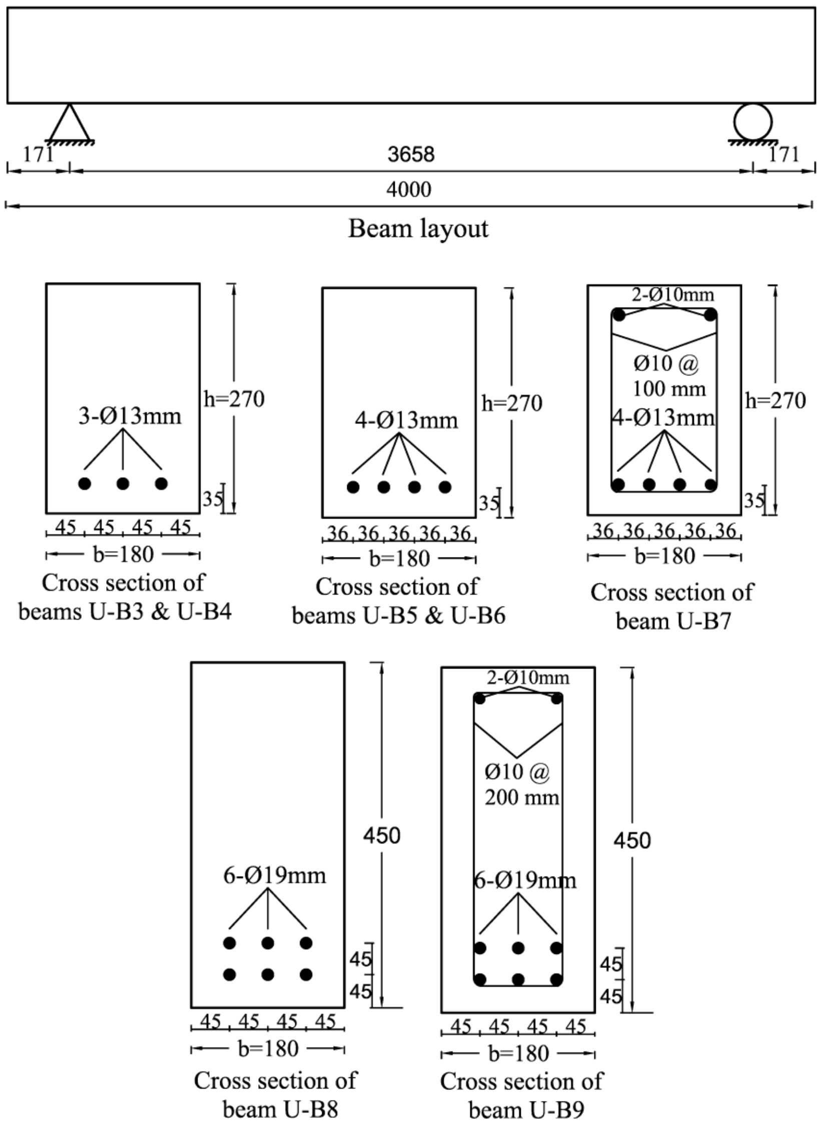

Figure 3-1. Layout and cross section of UHPFRC beams (All units are in mm)

3.2 Mix Design

The use of UHPC in structural applications is still limited and this is mainly due to high cost of UHPC and lack of design specifications for batch mix proportioning as well as structural design of members in codes and standards [49,162]. Conventional UHPC mix designs do not contain coarse aggregates, and rely heavily on specially graded fine aggregates, silica fume, and high volume of superplasticizers. Such conventional UHPC mixes have a relatively high packing density owing to micro/nanoparticles, and require considerable high energy and also specialized equipment for mixing. In addition, UHPC performance characteristics are more sensitive to properties of raw material and composition, mixing procedure, casting and curing. The specialized equipment and raw materials are not readily available in most concrete production plants in the current scenario. Therefore, an improved batch mix proportions and innovative procedure for preparing UHPC was adopted in which coarse aggregates were used so as to reduce the dosage of cementitious material and thus the cost of UHPC. This mix can be prepared in a conventional ready-mix truck, and at relatively lower cost, which in turn can facilitates its market acceptance. This designed mix can be prepared using the drum and pan mixers commonly used by concrete industry [41].

This specially designed UHPFRC mix is adopted for preparing two batches of concrete from which seven beams were casted. Four beams (U-B3 to U-B6) were fabricated using Batch 1 mix and three beams (U-B7 to U-B9) using Batch 2 mix. The UHPFRC mix comprised of coarse aggregate (limestone 29A with maximum size of 12.7 mm), fine aggregate (silica sand, flat Rock Bagging # 52), binder (including cement-type I, silica fume, slag, and limestone powder), water, superplasticizer, and steel fibres. UHPFRC batch mix proportions are given in Table 3-2. The desired strength and durability properties of UHPC are achieved by using very low water-cement ratio, high cementitious content and high packing density, especially of the fine grains. Workability of the mix is one of the key concerns in casting UHPC members. In order to obtain desired flowability of UHPFRC, a high range water reducer (HRWR), which is a polycarboxylate based superplasticizer (Chryso 150), was added to the batch mix [41,163]. This ensured sufficient workability is achieved in the mix. Slump test was conducted in the field according to the ASTM C143 [164] and height of the slump was measured to be about 250 mm as shown in Figure 3-4. Steel fibers, 1.5% of volume fraction, was added to the mix. The steel fibers are of straight type (without hooks) with 0.2 mm diameter and 13 mm length (aspect ratio of 65) as shown in Figure 3-2 and had tensile strength in the range of 690 to 1000 MPa and a modulus of elasticity of about 210,000 MPa.

Table 3-2. Batch proportions for UHPFRC mix

Ingredient	Batch 1 (Kg/m^3)	Batch 2 (Kg/m^3)
Beams	U-B3,U-B4, U-B5, U-B6	U-B7,U-B8, U-B9
Coarse Aggregate	478	517
Natural sand	504	544
Silica sand	277	299
Cement	472	510
Silica fume	208	224
Slag	94	102
Limestone powder	170	184
Water	136	121
HWRA (28%) Chryso 150	43	48
Steel fibers (1.5% volume fraction)	118	127
Water to binder ratio	0.15	0.14
Slump	250mm	260mm

Figure 3-2. Brass coated steel fiber utilized in the UHPFRC mix

The UHPC mixing sequence is crucial for attaining uniform and workable mix without fiber and cement balling. For the first batch, 80% of total water was added to the truck followed by superplasticizer. Then, fine aggregate (silica sand), silica fume, slag and limestone powder were manually loaded to the truck. Also, cement and coarse aggregate were added using the automated system in the plant. Then, the rest of the water was added. Fast mixing was done (about 70 revolutions within 5–7 min) and transported to the field approximately 10 miles away. However, fiber balling and cement balling was observed in this batch. Therefore, a new mixing procedure was adopted for second batch.

For the second batch, the coarse and fine aggregates were first dry mixed. This was followed by manually addition of binders in the following order: silica fume, slag, limestone powder, and cement. One-third amount of the total water was manually added in the form of ice, for slowing the reaction time. Remaining water and superplasticizer (HWRA Chryso) were mixed together and 90% of this solution is added to the dry ingredients in the mix truck. All the ingredients in the concrete supply truck was mixed at high speed (1 revolution per 4 seconds) for 5 minutes, followed by reversing the mixing bowl of the truck in order to bring the settled ingredients from the bottom to the top, to ensure uniformity in the mix. Steel fibers were sprinkled in the mix and mixed at high speed for 5 minutes, followed by reversing of the mixing bowl. The mix appeared to be dry at this point, which indicated non-uniform mixing. Hence, the steps of high speed revolution with bowl reversal was repeated again and the slump test conducted at this point was satisfactory. Then the UHPFRC was poured into three beams (U-B7, U-B8 and U-B9) and specimens. The mixing procedure adopted for the second batch and adding a portion of water (1/3 of the total water) in form of ice improved the workability of the mix. Figure 3-5 shows the surface of a UHPFRC beam from second batch as compared to a beam from first batch. The surface of the beam fabricated with second batch has a very smooth surface without any surface treatment and finishing.

(a) (b)

Figure 3-3. Loading of materials to the concrete mixing truck

Figure 3-4. Fresh mix slump test

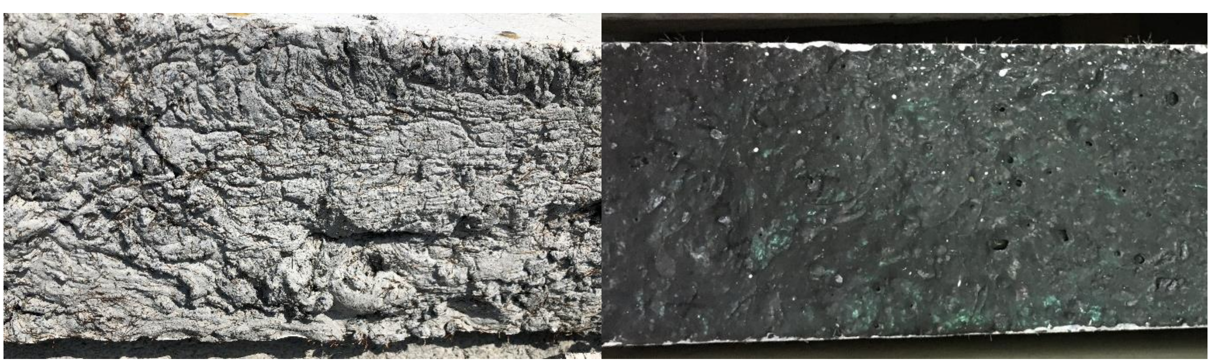

(a) UHPFRC beam from first batch (b) UHPFRC beam from second batch

Figure 3-5. Surface of the cured beams fabricated using two UHPFRC batch mixes

3.3 Fabrication Details

The designed beams were fabricated using UHPFRC mixes prepared in two batches. The first batch was prepared in a ready-mix truck and poured at a field site on Michigan State University campus. The second batch was prepared in a mix truck at Civil Infrastructure Laboratory (CIL). Plywood forms were designed and assembled to achieve required internal dimensions in beams. In order to achieve in-situ high temperature curing, rigid Styrofoam insulation of 50 mm thickness, was installed on two interior sides of the framework. Bottom side of the framework was provided with rigid Styrofoam of 100 mm thickness as shown in Figure 3-6. Then reinforcing bars were assembled and placed in the plywood forms. Concrete was cast from one end and gradually moved to other end of the framework, as illustrated in Figure 3-7(a). Beams covered with insulation as shown in Figure 3-7(b), and were kept at MSU Civil and Infrastructure Laboratory for curing and were demolded after 50 days. In addition to the beams, seventy cylinders and prisms were also cast for measuring mechanical properties of UHPFRC.

Figure 3-6. Preparation of wood forms and reinforcement for fabrication of UHPFRC beams

(a) Concrete pouring (b) Curing using insulation

Figure 3-7. Fabrication of UHPFRC beams

3.4 Instrumentation

Instrumentation mounted on the beams included thermocouples, strain gauges, string pots, and Linear Variable Displacement Transducers (LVDTs). In order to monitor progression of temperatures in beams during curing, type-K chromel-alumel thermocouples (0.91 mm thick) thermocouples were installed at mid-span and quarter-span of beams U-B3, U-B4, and U-B8 at four different depths (quarter, half, three-quarter, and near surface) as shown in Figure 3-8. Strain gauges were installed on corner and middle rebars at mid-span section and point load section of the beams. In addition, strain gauges were installed on shear reinforcements in shear span as shown in Figure 3-9. Strain gauges, of 60 mm length, were installed on the side surface of beams, to monitor strains along depth of critical section of the beams. These strain gauges were bonded with epoxy after the concrete surface was ground. In addition to strain gauges, LVDTs were placed on side surface of the beams to calculate average curvature of critical section of the beams. Installed LVDTs and strain gauges on side surface of one UHPFRC beam are shown in Figure 3-11. String pots (LVDTs) were also installed at mid-span and loading points of the beams to measure beam deflections during the tests. Figure 3-10 illustrates location of LVDTs and strain gauges on side and bottom surface of UHPFRC beams. In addition, LVDTs forming a rosette were installed on side surface of beam U-B7, U-B8 and U-B9, prior to testing to measure principal strains in shear span. The rods for these rosette LVDTs were placed in beams before casting. Details of the rosette LVDTs are shown in Figure 3-12.

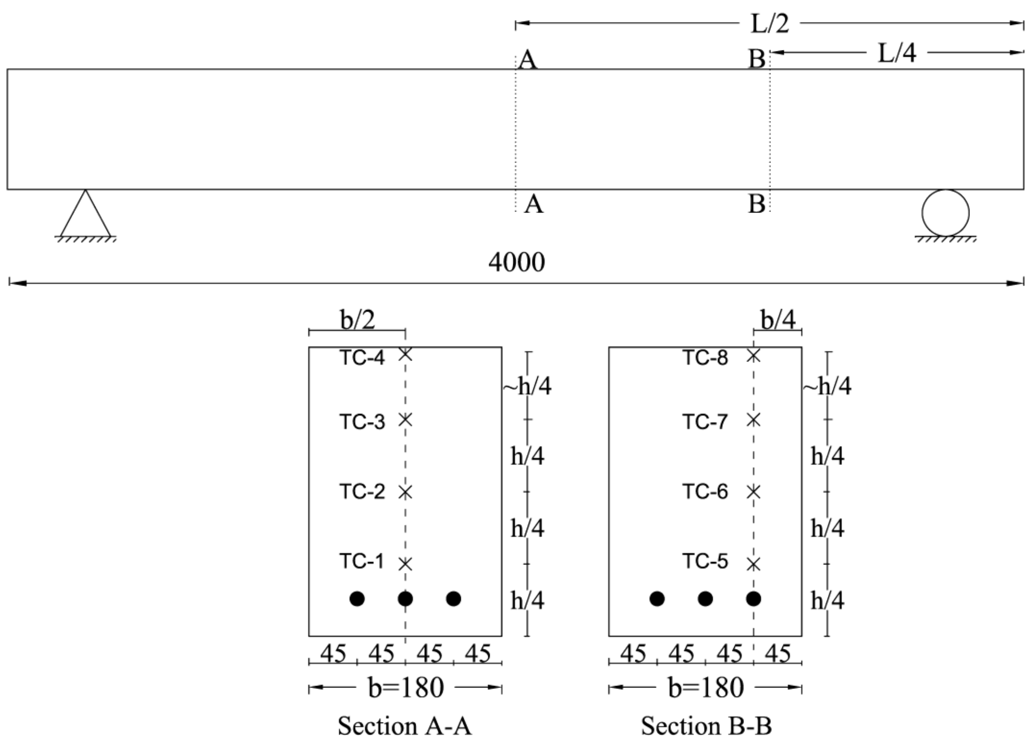

Figure 3-8. Location of thermocouples in beams U-B3, U-B4 and U-B8 at mid-span and quarter-span sections (All units are in mm)

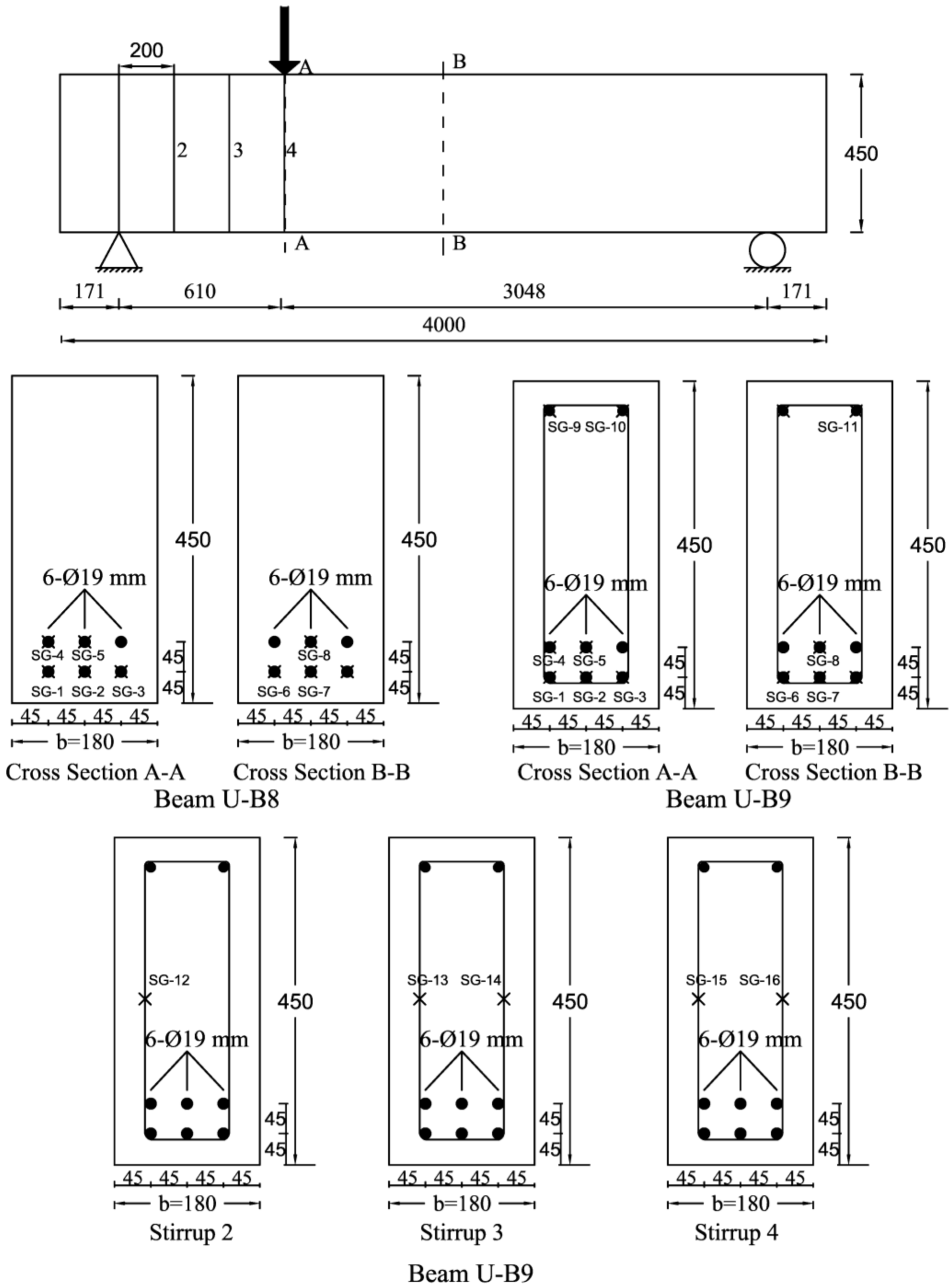

Figure 3-9. Location of strain gauges on longitudinal bars in beams U-B8 and U-B9 (All units are in mm)

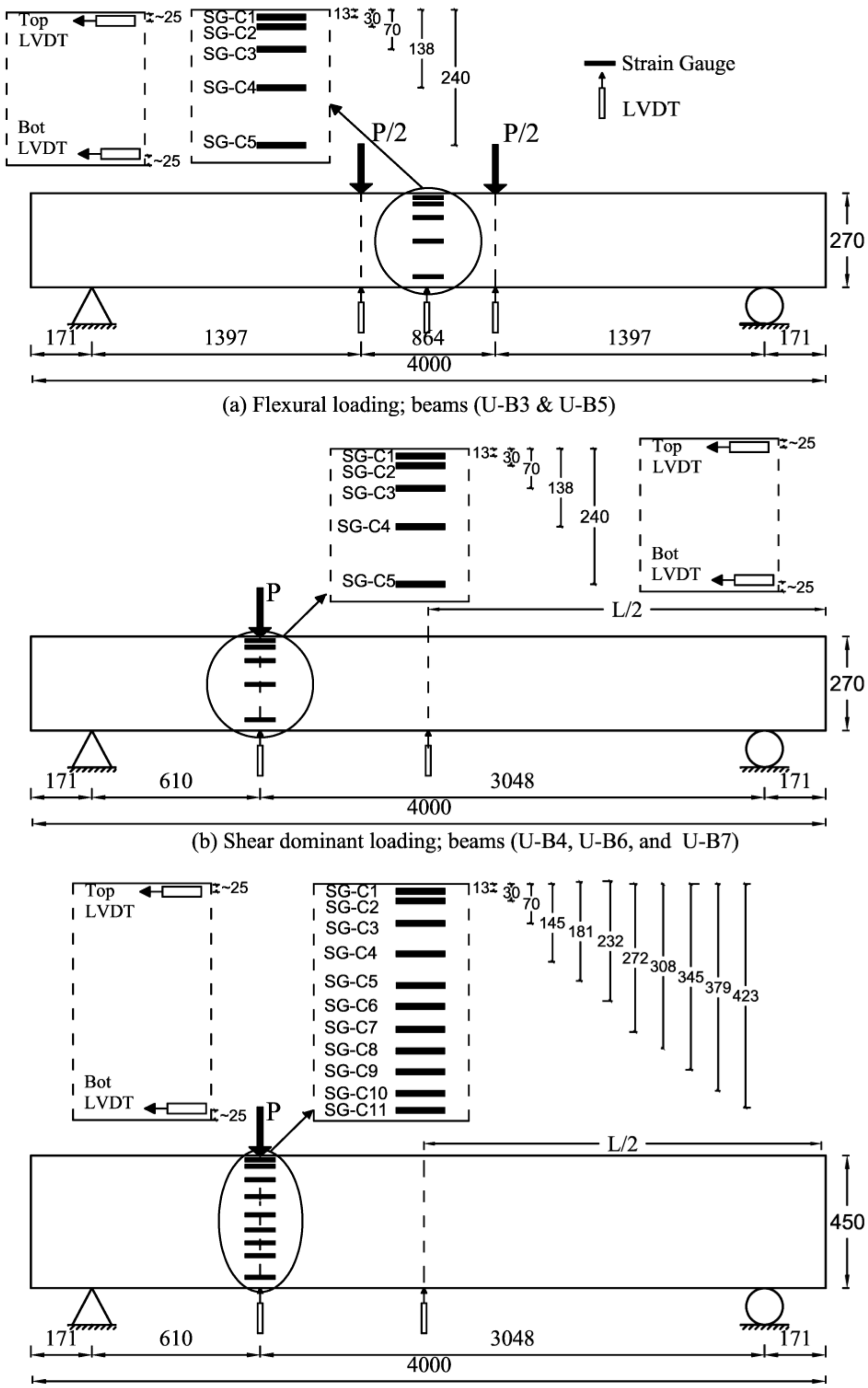

(a) Flexural loading; beams (U-B3 & U-B5)

(b) Shear dominant loading; beams (U-B4, U-B6, and U-B7)

(c) Shear dominant loading; beams (U-B8 and U-B9)

Figure 3-10. Location of strain gauges and LVDTs on side surface of the beams (All units are in mm)

(a) (b)

Figure 3-11. (a) Strain gauges and LVDTs on side surface of the beams, (c) String pots (LVDTs) on bottom face of the beams

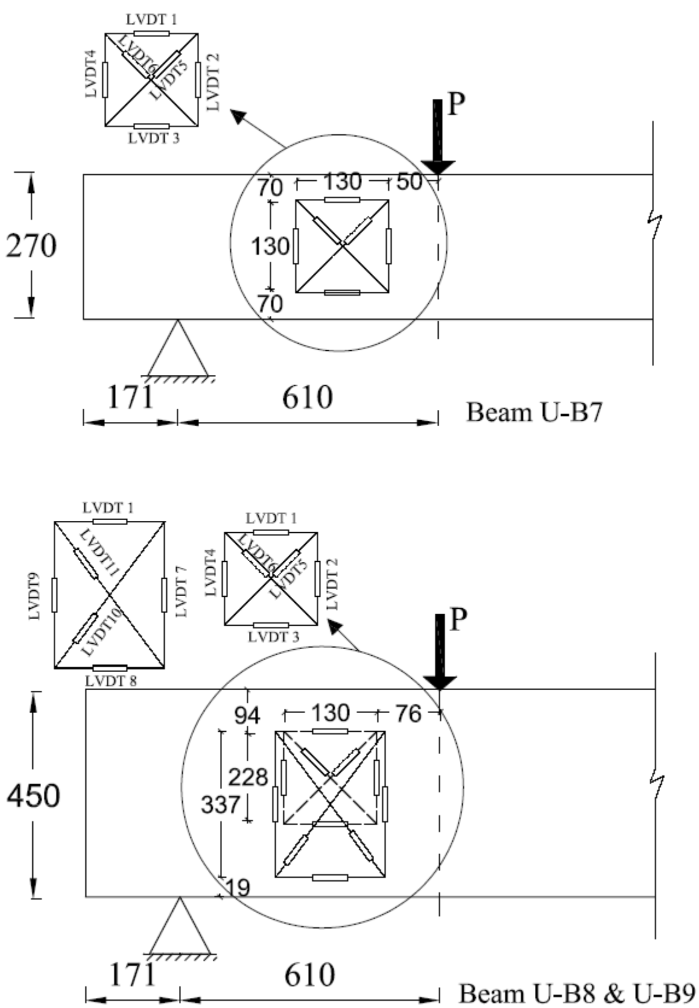

Figure 3-12. Rosette LVDTs mounted on side surface of beams U-B7, U-B8, and U-B9 (All units are in mm)

3.5 Curing

For curing, high temperature or steam conditions is essential for obtaining highly packed microstructure and low drying shrinkage of UHPC [49,75,165,166]. Compressive strength of UHPC gets enhanced by as much as 60% through steam curing as compared to standard curing at room temperature [33,167]. UHPC cylinders and prisms were kept at room temperature for 24 hours and then were cured in hot water (90^{o}C) and steam for 48 hours for first and second batch, respectively. Similar high temperature treatment can be applied to full-scale structures by preventing loss of heat generated during hydration of the cementitious binder in UHPC to the environment using insulating (curing) blankets and lining formwork with insulation [168].

In order to achieve in-situ high temperature curing, from heat of hydration of the cementitious matrix, adequate insulation (with R-value>20) was provided in the beams formwork using a combination of rigid Styrofoam and mineral wool as shown in Figure 3-6. In addition, a layer of fiber glass batt insulation was placed outside the formwork and on top face of the beams after casting (see Figure 3-7). Insulation in the formwork was utilized to facilitate effective use of heat of hydration of the cementitious binder in UHPC towards field thermal curing. Such insulation also helps to maintain relatively uniform temperatures within the cast beams. Otherwise, temperature distribution can be extremely non-uniform with much higher temperatures within the concrete core as compared to layers closer to external surface of the beams. Therefore, insulation provided in the formwork is critical for preventing early age cracking within the concrete resulting from high thermal gradients [169,170].

During curing, temperature rise in beams U-B3, U-B4, and U-B8 was monitored at four different depths (quarter, half, three-quarter, and near surface) in mid-span and quarter-span sections through mounting type-K thermocouples (see Figure 3-8). The temperature variation in beams U-B3 and U-B4 at different depths in mid-span section is shown in Figure 3-13. A sustained rise in temperatures is seen within about 25 hours of curing time when temperatures attain a peak value of 75°C. It is also important to note that this temperature rise was similar across the depth of the beams. Such uniform temperature profile in the beams indicates the effectiveness of provided insulation in restricting the heat of hydration of cementitious components of UHPFRC during curing from escaping into outside environment. Temperatures within the beams began to decay after 25 hours and gradually reverted back to ambient temperature after about 300 hours (12 days) of curing.

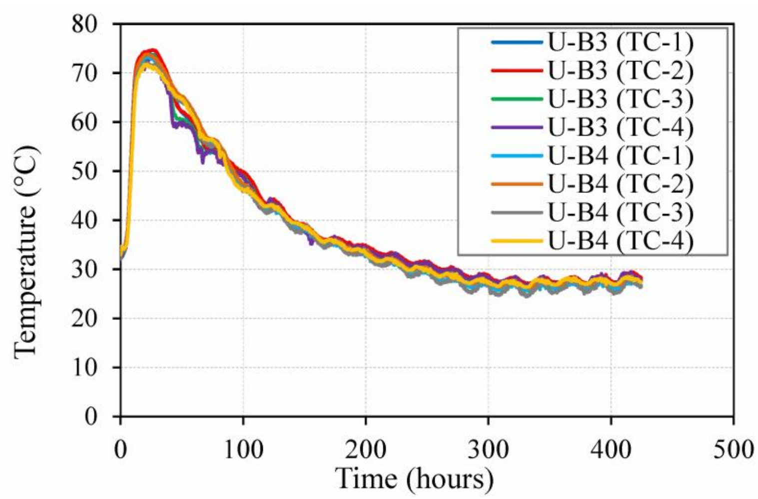

Figure 3-13. Heat of hydration during curing of the beams U-B3 and U-B4

3.6 Strength Tests on UHPFRC

During fabrication of the beams, cylinders and prisms were also cast from two batch mixes for evaluating compressive strength, tensile strength, and flexural strength of UHPFRC. UHPFRC cylinders were tested at different ages under compression as per ASTM C39 specifications [19]. In these compression tests, a uniaxial loading was applied with loading rate of 0.25±0.05 MPa per second using Forney strength test machine shown in Figure 3-14. This machine is a load controlled test machine which allows to manually controlled rate of loading during the test. Average compressive strengths from tests on cylinders from two batches at different ages of 7 days, 14 days, 28 days, and 90 days are summarized in Table 3-3. It can be seen that UHPFRC from batch 2, cured in steam, reached its maximum compressive strength after 7 days of curing. In addition to cylinders cast while fabrication of the UHPFRC beams, two cores were drilled out of beams U-B3 to U-B6 after testing the beams to assess the compressive strength at the time of testing. The cores were drilled from stress free zones extending beyond the clear span of the beams to ensure that no damage was sustained at the drilling locations during testing. Average compressive strength of first and second batch of UHPFRC at 90 days was measured to be 167 MPa and 174 MPa, respectively. UHPFRC cylinders failed under compression tests are shown in Figure 3-14.

Table 3-3. Compressive and splitting tensile strength of UHPFRC cylinders

Age (days)	Batch 1			Batch 2		
	Density (kg/m³)	Compressive strength (MPa)	Splitting tensile strength (MPa)	Density (kg/m³)	Compressive strength (MPa)	Splitting tensile strength (MPa)
7	2570	-	-	-	182.4	13.5
14	2573	136	14	-	167.9	13.7
28	2573	145	14.2	-	171.9	17.5
90	2573	167	15.3	2565	174.2	17.9

Density of cast UHPFRC was evaluated at different ages of 1, 4, 7, 14, 28, and 90 days of casting. For this purpose, mass and volume (dimensions) of UHPFRC specimens were measured at different ages. Average calculated densities at ages of 7, 14, 28 and 90 days are presented in Table 3-3. UHPFRC specimens from the first batch had average density of 2538 kg/m³ and 2570 kg/m³ at age of 1 day and 4 days, respectively. There was only very small increase in density from day 1 to day 4, and density remained invariant after 4 days of casting. The results show that the effect of age on density of UHPFRC is not significant. The average density of UHPFRC specimens from batch 1 and batch 2 at 90 days after casting were measured to be 2573 kg/m^3 and 2565 kg/m^3, respectively.

(a) (b)

Figure 3-14. (a) Compression test set-up, (b) Cylinders failed under compression

In addition to compression tests, splitting tensile tests were also carried out on cylinders according to ASTM C496 specifications [171] with a loading rate of 0.7 to 1.4 MPa per minute. Maximum loads applied on the specimens were used to calculate the split tensile strength utilizing the Eq. (3-1).

$$T = \frac{2P}{\pi l d} \qquad (3\text{-}1)$$

where, T is the split tensile strength; P is the maximum applied load; l is the length of the specimen; and d is the diameter of the specimen. The average splitting tensile strength of UHPFRC from batch 1 was 14.2 MPa at 28th day of casting. UHPFRC cylinders from second batch attained a splitting tensile strength of 17.5 MPa after 28 days of casting (see Table 3-3). The test set-up and cylinders failed under splitting tensile test is shown in Figure 3-23.

(a) (b)

Figure 3-15. (a) Splitting tensile test set-up, (b) Cylinders failed under splitting

Further, direct tension tests were conducted on dog bone specimens. Prior to tests, 10 mm depth notches were cut at both sides of the specimen at the center. The tests were conducted using universal testing machine with a loading rate of 0.2 mm/min [172]. The test set-up and dog bone specimens tested under direct tensile test are shown in Figure 3-16. During the tests, strains and crack opening was measured using clip gages placed on two opposite sides of the specimens. Stress-strain response of three UHPFRC specimens under direct tension is shown in Figure 3-17. All specimens exhibited strain hardening after cracking, and ductile response even under direct tensile test due to fiber bridging at the crack surfaces.

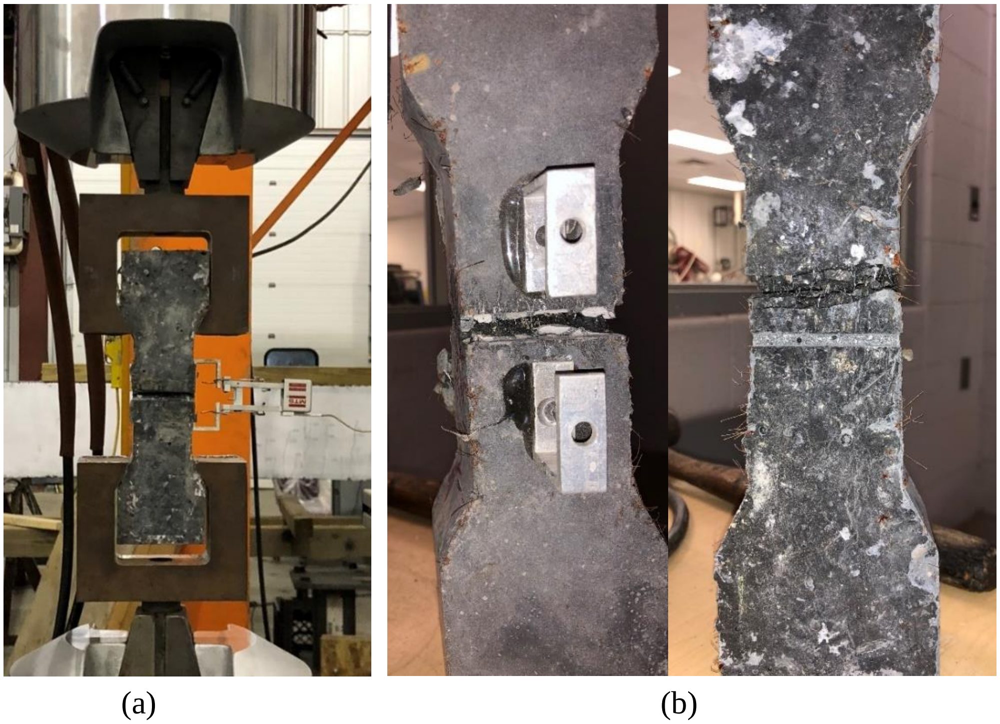

Figure 3-16. (a) Direct tensile test set-up, (b) Dog bone specimens failed under direct tension

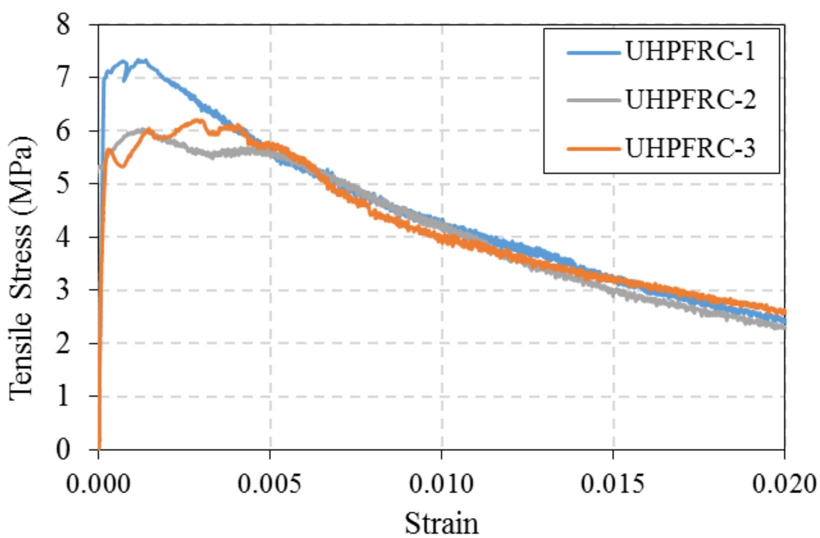

Figure 3-17. Stress-strain response of UHPFRC dog bone specimens under direct tension

Flexural tests were also conducted on prisms as per JCI-S-002–2003 [173]. The prism specimens were 100 mm high, 100 mm wide, 400 mm long, and with a span of 300 mm. In prism specimens, a notch with a depth of 30 mm (0.3 times the beam depth) and width of 4 mm was cut into the tension face. Each prism was turned 90° from the casting surface and then sawn through its width at mid-span. A uniaxial load was applied using a UTM with a maximum capacity of 3000 kN under displacement control as shown in Figure 3-18. A clip gauge was installed at the midspan notch to measure the crack mouth opening displacement (CMOD). The load-crack mouth opening displacement for prisms made of UHPC with no fibers, and UHPFRC with steel fibers (1.5% volume fraction) are plotted in Figure 3-19. UHPC exhibited brittle behavior with abrupt failure after reaching the peak load of 7 kN, as opposed to UHPFRC which exhibited ductile behavior. The maximum load carrying capacity of prism made of UHPFRC with steel fibers was measured to be 18 kN. The flexural strength of the notched UHPFRC and UHPC prisms were calculated using Eq. (3-2) to be 21.3 MPa and 6.9 MPa, respectively.

$$f = \frac{3PL}{2b(h-a_0)^2} \tag{3-2}$$

where, P is the maximum applied load, L is the span length, b is the beam width, h is the beam depth, and a_0 is the notch depth.

(a) (b)

Figure 3-18. (a) Three-point flexure test set-up, (b) Notched UHPFRC prism failed under bending

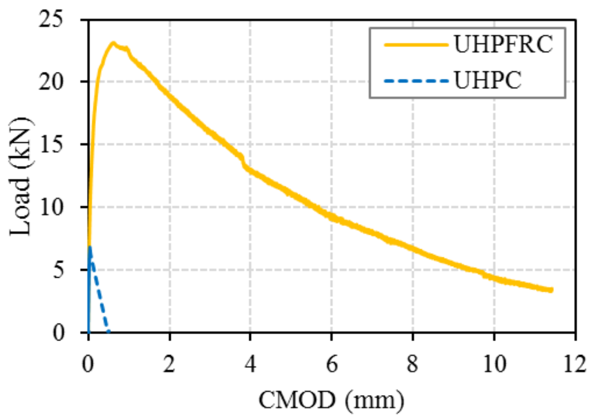

(a) Load-CMOD response

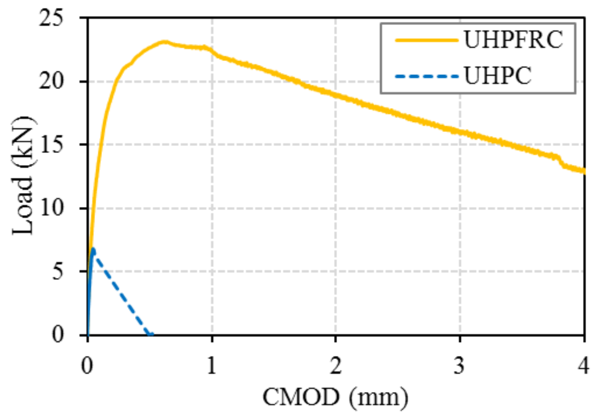

(b) Zoomed in Load-CMOD response

Figure 3-19. Load-crack mouth opening displacement response of UHPC and UHPFRC

3.7 Strength Tests on Steel Bars

Tensile strength tests were also undertaken on steel bars used as tensile reinforcement in UHPFRC beams. The steel coupons for these tests were 812 mm. Tensile strength tests were carried out using MTS-810 test machine with 250 kN loading capacity shown in Figure 3-20. Displacement control loading was applied at a displacement rate of 0.002 mm/sec up to yielding and then the rate of displacement was raised to 0.021 mm/sec up to rapture of the steel specimen. The displacement recorded at incrementing load levels, during strength tests, is utilized to generate stress-strain response of rebars and these are plotted in Figure 3-21. It can be seen in this figure that the general trend of stress-strain curve is linear-elastic up to yielding of steel and then response follows nonlinear trend. Well-defined yield plateau is recorded at yielding. Past the yielding plateau, steel undergoes plastic deformation with stress increasing with strain up to reaching ultimate (stress) point. Once the ultimate stress is reached, rapture of rebar occurs as it is illustrated in Figure 3-20. The yield strength, ultimate strength, and ultimate strain were found to be about 436 MPa, 696 MPa and 0.122, respectively.

(a) (b)

Figure 3-20. (a) Tensile test on steel bars using MTS machine, (b) Tensile failure (rupture) of bars

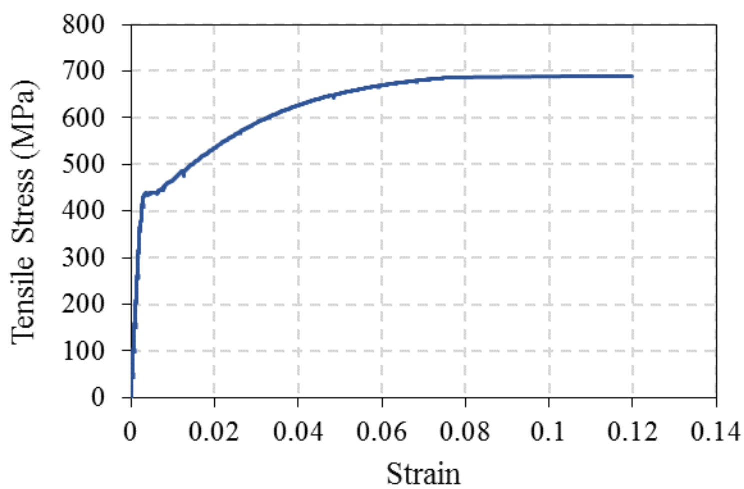

Figure 3-21. Stress-strain response of tensile reinforcement used in UHPC beams

3.8 UHPFRC Beam Tests

Two UHPFRC beams (U-B3 and U-B5 from batch 1) were tested under flexural loading. Remaining five UHPFRC beams (U-B4 and U-B6 from batch 1, U-B7 to U-B9 from batch 2) were tested under dominant shear loading. Results from these tests are discussed in following sections.

3.8.1 Preparation of the Beams for Tests

In order to install instrumentation (strain gauges and LVDTs) on side-faces of the beams, and as well as to trace crack patterns, the surface of the beams were cleaned and sanded thoroughly. Then, strain gauges and LVDTs were bonded to surfaces of the beam using an epoxy adhesive. For tracing crack propagation, a thin layer of white paint was applied to the prepared surface of the beams before testing. After installing instrumentation, the beams were transferred to the test setup and aligned in place with the help of a laser tracker.

3.8.2 Test Set-up and Procedure

The tests on UHPFRC beams were conducted using a displacement controlled technique at a rate of 1 mm per min. During each test, load was increased monotonically in predefined steps, and at each increment the loading was maintained at constant level for certain period for marking crack formation and propagation. Strains, deflections, and crack propagation were measured and recorded continuously as the applied load increased in increments, throughout the duration of the tests.

In order to evaluate flexural behavior of UHPFRC beams, a four-point specialized loading set-up was designed as shown in Figure 3-22 (a) and Figure 3-23(a). In this set-up, two point loads were applied on the top face of each beam (U-B3 and U-B5) through a displacement controlled actuator (MTS machine with a capacity of 1500 kN). Point loads were applied at a distance of 432 mm on either side of mid-span (see Figure 3-22). This setup ensured that the critical span (mid-span) was subjected to pure flexure and no shear. For dominant shear loading, UHPFRC beams (U-B4, U-B6, U-B7, U-B8, and U-B9) were tested under a three-point loading set-up. This test setup was designed to subject the beams to dominant shear loading. A point load was applied on the top face of the beams, at a distance of 610 mm from support (1/6 of span), through a displacement controlled actuator as shown in Figure 3-22 (b) and Figure 3-23(b). This test setup led to shear span to effective depth of 2.6 and 1.6 for beams with depth of 270 mm and 450 mm tested under dominant shear loading.

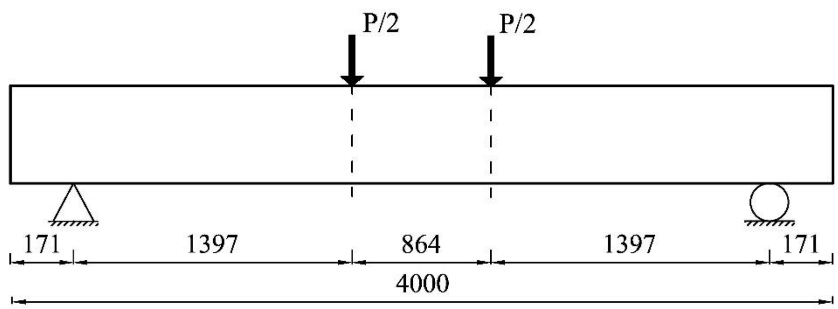

(a) Four-point flexural loading

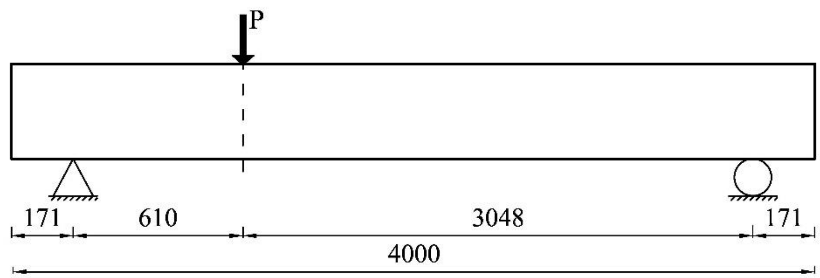

(b) Three-point shear loading

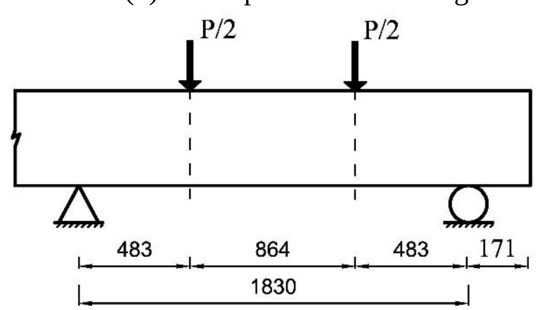

(c) Four-point loading for retesting beams

Figure 3-22. Test setup of UHPFRC beams

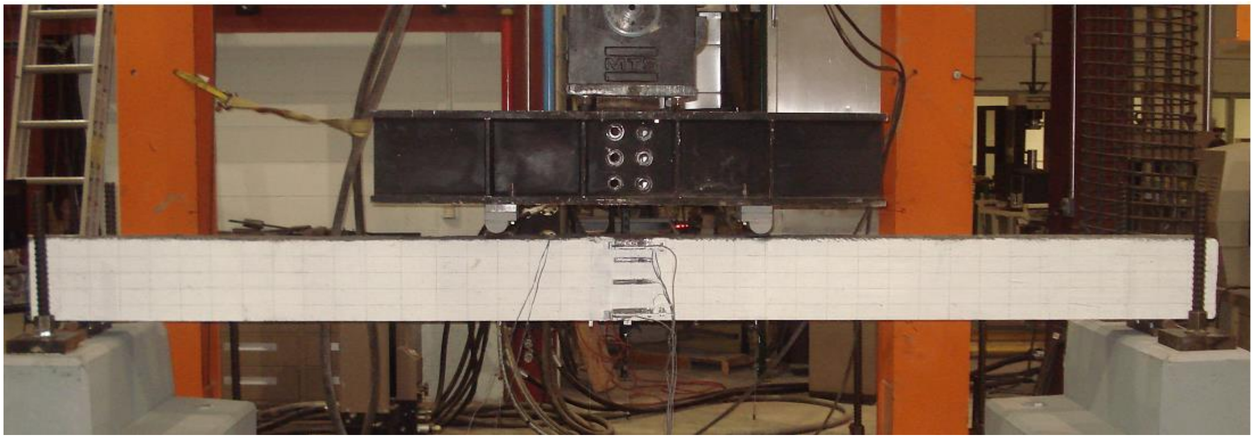

(a) Four-point flexural loading

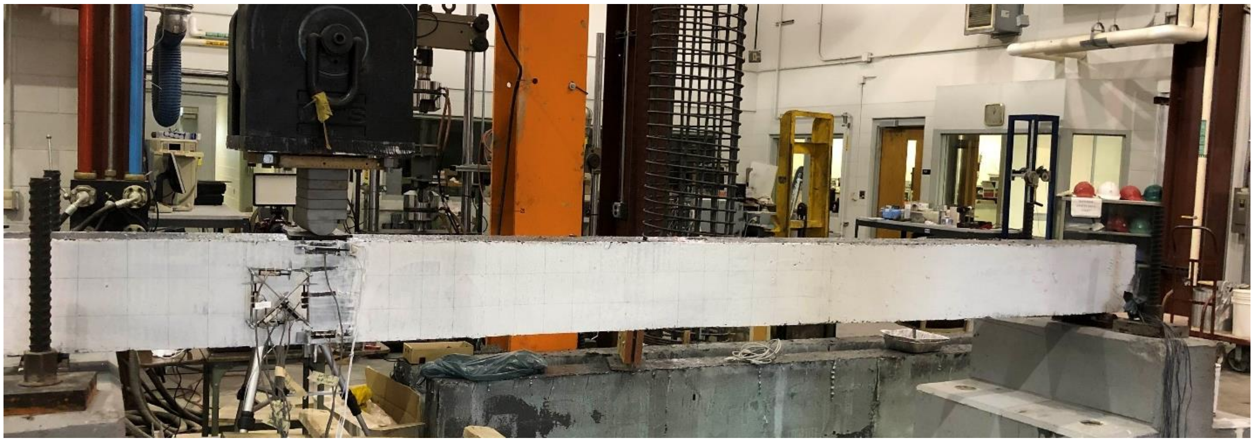

(b) Three-point shear loading

(c) Four-point loading for retesting beams

Figure 3-23. Test setup of UHPFRC beams

In addition, the beams tested under shear loading were retested with smaller span. Since the load point were close to support in the case shear dominant loading, the undamaged part of the beams were utilized to conduct experiments on beams with smaller span. For testing theses beams two point loads were applied at a distance of 432 mm on either side of mid-span resulting in shear span to effective depth of 2.06 and 1.26 in beams with depth of 270 mm and 450 mm, respectively. This test set up is shown in Figure 3-22 (c) and Figure 3-23(c).

3.8.3 Results from Experiments

Data generated from tests is utilized to evaluate the comparative response of UHPFRC beams under flexural and dominant shear loading.

3.8.3.1 Load Deflection Response

The deflection at critical section of the beams was measured at each load increment using LVDTs installed on bottom surface of the beams. Load-deflection response at mid span of beams U-B3 and U-B5, tested under flexural loading, is plotted in Figure 3-24 for the entire range of loading till failure. The beams exhibited four distinct stages of response i.e., linear elastic stage until initiation of tensile cracking (zone OA), post-cracking stage with enhanced cracking and their progression (zone AB), onset of yielding in steel reinforcement (corresponding to point B), and plastic deformation stage till peak load (zone BC), followed by attainment of failure (at point D).

A change in slope in the load-deflection plot indicates the onset of tensile cracking in the UHPFRC beams (at point A). Tensile cracking in beams U-B3 and U-B5, with reinforcement ratios of 0.90% and 1.20%, developed at load level of 26.2 kN and 28.4 kN, respectively. As the load increased further, stiffness in both beams decreased due to increased macro cracking and progression of these cracks. The strain in reinforcing steel at the critical section was monitored to note yielding of tensile reinforcement. The steel reinforcement yielded (point B in Figure 3-24) at a load level of 81.1 kN and 104.7 kN in beams U-B3 and U-B5, beyond which deformation in the beams become predominantly plastic. The yielding of steel was followed by strain hardening phase (zone BC). This deformation phase in the beams is beyond yielding of steel reinforcement wherein the beam exhibits sustained increase in load carrying capacity, due to strain hardening in both tensile reinforcement and UHPFRC, until peak load is reached (corresponding to point C in Figure 3-24). Finally, the beams could not sustain any increment in load, and entered unloading phase wherein beams continued to deform in a plastic fashion until failure (at point D). While the load level at which first cracking developed was similar in both beams, beam U-B5, had a 30% higher load carrying capacity than beam U-B3, mainly resulting from 33% increase in tensile reinforcement area.

Load-deflection response of beams U-B4 and U-B6 tested under dominant shear loading is also plotted in Figure 3-25. As in flexural loaded beams, distinct stages of response; linear elastic until initiation of tensile cracking, post-cracking stage, onset of yielding in steel, and strain hardening stage till peak load and softening zone till failure were also observed under dominant shear loading in these beams (U-B4 and U-B6). Tensile cracks in beams U-B4 and U-B6, with reinforcement ratios of 0.90% and 1.20%, developed at load level of 39.1 kN and 38.8 kN, respectively. Beam U-B6, with a higher reinforcement ratio, exhibited higher load at reinforcement yielding, peak phase, and ultimate phase by 18%, 25%, and 36% respectively than beam U-B4.

The applied loading and corresponding deflection at various stages of loading for beams U-B3 to U-B6 are summarized in Table 3-4. Load levels corresponding to initial cracking, reinforcement yielding, peak and ultimate failure were greater by 36%-49%, 43%-56%, 40%-46% and 47%-49% for the beams tested under dominant shear loading (U-B4 and U-B6) as compared to identical beams tested under flexural loading (U-B3 and U-B5). This variation in behavior indicates that beams tested under shear loading exhibited stiffer response as compared to beams tested under flexural loading. A review of load deflection response plotted in Figure 3-24 and

Figure 3-25 indicate that all four UHPFRC beams (tested under dominant shear and flexural loading), displayed ductile behavior and underwent significant plastic deformation even after yielding of steel reinforcement. This ductile behavior is owing to presence of steel fibers which facilitated fiber bridging at crack surfaces in UHPFRC.

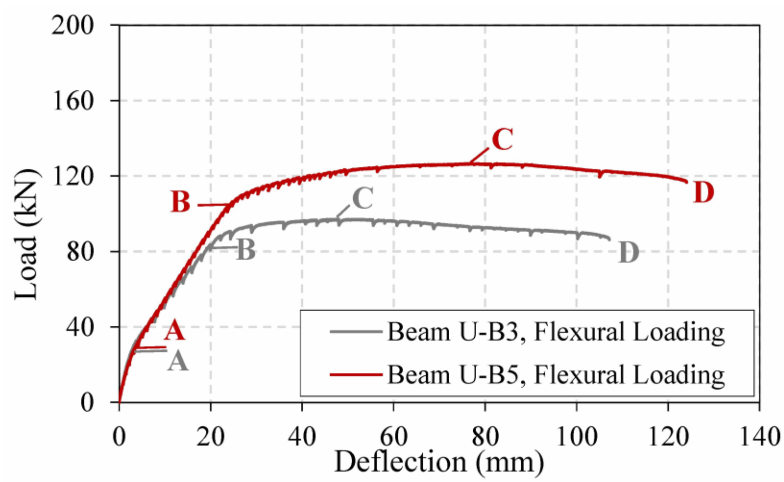

Figure 3-24. Load-deflection of beams U-B3 and U-B5 tested under flexural loading

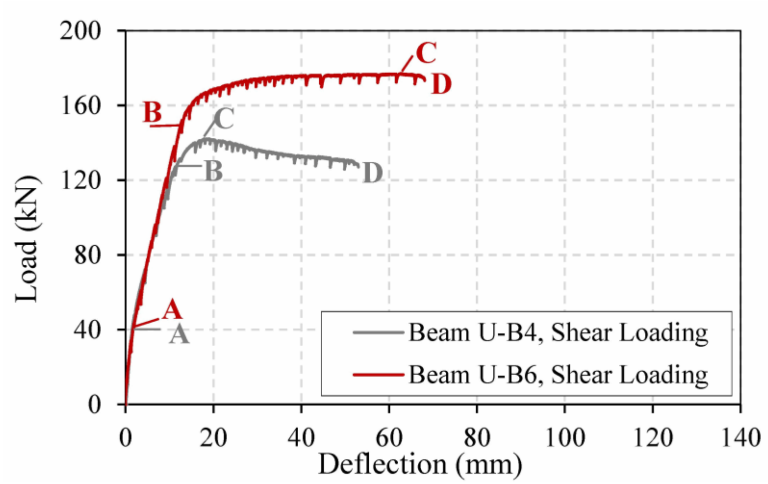

Figure 3-25. Load-deflection of beams U-B4 and U-B6 tested under predominant shear loading

Post-peak response of UHPFRC beams is mainly influenced by the level of reinforcement ratio. Beams U-B5 and U-B6 with higher reinforcement ratio remained at peak load for a sustained period as compared to beams U-B3 and U-B4 (having lower reinforcement ratio) which exhibited softening soon after attaining peak load carrying capacity. This indicates that post peak load deflection response in beams U-B5 and U-B6 was dominated by strain hardening of steel reinforcing bars. However, in beams U-B3 and U-B4 (lower reinforcement ratio), concrete (UHPFRC) dominated post peak response, which is characterized by a drop in applied load with increasing deflections, in accordance with tensile response of UHPFRC.

Moment-curvature response of beams U-B4 and U-B6, tested under shear loading, is compared to that of beams U-B3 and U-B5, tested under flexural loading, in Figure 3-26 and Figure 3-27. The moment curvature response of these beams was evaluated knowing the measured strains at different load levels and through applying linear elastic theory [49]. Interestingly, the beams under dominant shear loading exhibit similar moment curvature response as beams under flexural loading. This indicates that shear deformation was negligible and did not affect overall deflection response of UHPFRC beams. This is due to high shear stiffness of UHPFRC and this response is in contrast to beams fabricated using conventional concrete mixes [50]. Moment curvature response plots also show that UHPFRC beams U-B4 and U-B6 (without shear reinforcement) subjected to dominant shear loading did not fail in a brittle fashion and reached their ultimate moment capacity.

Load deflection response of beams U-B7, U-B8, and U-B9, subjected to dominant shear, is presented in Figure 3-28 and Figure 3-29 for the entire range of loading till failure. These beams also exhibited four distinct stages of response i.e., linear elastic stage, post-cracking stage, onset of yielding in steel reinforcement, and plastic deformation stage till peak load, followed by failure. However, in the case of deeper beams (U-B8 and U-B9) no significant reduction in stiffness was observed after first cracking, i.e. the slope of load deflection did not change after cracking.

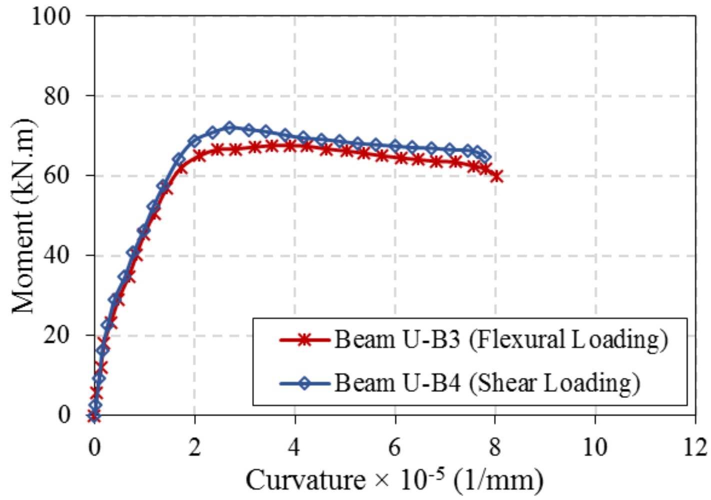

Figure 3-26. Moment curvature response of beams U-B3 and U-B4 with ρ_t=0.90%

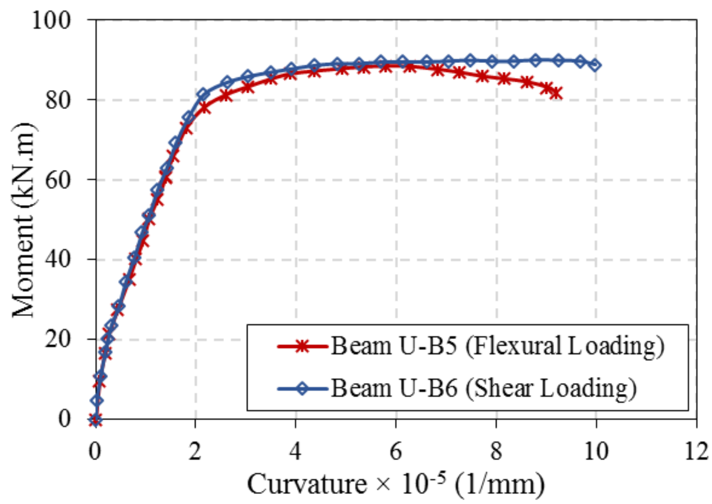

Figure 3-27. Moment curvature response of beams U-B5 and U-B6 with ρ_t=1.20%

Comparison of load deflection response of UHPFRC beams U-B6 and U-B7 is also presented in Figure 3-28. Beams U-B6 and U-B7 had same cross sectional and longitudinal tensile reinforcing details except for shear reinforcement. Beam U-B7 was provided with shear reinforcement (ρ_v = 0.79%), however beam U-B6 was provided with no stirrups (ρ_v = 0%). Load and deflection of beams U-B6 (ρ_v = 0%) and U-B7 (ρ_v = 0.79%) at different stages of cracking, rebar yielding, peak, and ultimate state are also summarized in Table 3-4. The results indicate that load and deflection response of beams U-B6 ($\rho_v = 0\%$) and U-B7 ($\rho_v = 0.79\%$) are comparable and removing stirrups did not result in reduction of ductility and load carrying capacity of the beams.

Load deflection response of beams U-B8 ($\rho_v = 0\%$) and U-B9 ($\rho_v = 0.40\%$) are also compared in Figure 3-29. Further, load and deflection of these beams at different stages are summarized in Table 3-4. Beam U-B8 and U-B9 were of 180 mm width and 450 mm depth with longitudinal tensile reinforcement ratio of 2.48%. Beam U-B8 did not have any stirrups, while Beam U-B9 was provided with shear reinforcement with ratio of 0.40%. Beam U-B8 ($\rho_v = 0\%$) had higher stiffness compared to beam U-B9 ($\rho_v = 0.40\%$) and reached maximum load carrying capacity of 790.1 kN. Beam U-B8 ($\rho_v = 0\%$) exhibited similar ductility but 6% lower load carrying capacity as compared to beam U-B9 ($\rho_v = 0.40\%$). It should be noted that during test of beam U-B9 actuator stopped working at load level of 719 kN and corresponding deflection of 16.5 mm. Therefore, the load setup was changed from a plate to a half sphere steel plate, and a sharp increase was observed in load deflection response of beam after using the new setup. Therefore, the increase in load carrying capacity of beam U-B9 compared to beam U-B8 can be attributed to change of loading plate as the loading point was moved slightly.

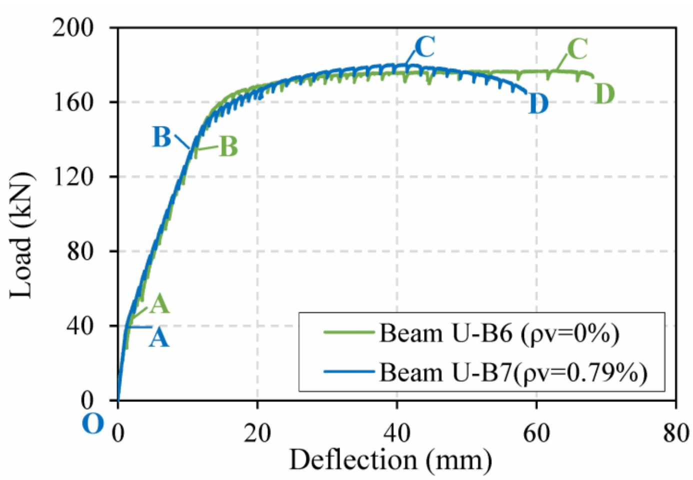

Figure 3-28. Load deflection response of beam U-B6 and U-B7

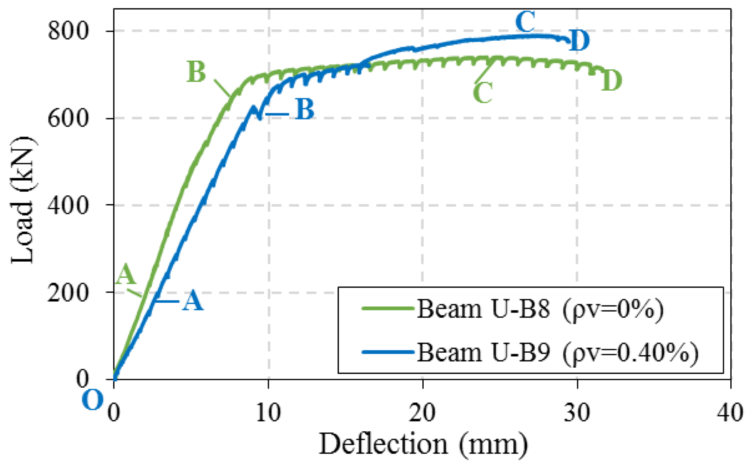

Figure 3-29. Load deflection response of beam U-B8 and U-B9

The beams tested under three-point dominate shear loading (U-B4, U-B6, U-B7, and U-B9) were retested under four-point loading to evaluate structural response of these beam with smaller span length and shear span to depth ratio (see Figure 3-22). The load deflection of beam U-B9 is plotted in Figure 3-30. The beam was only tested up to yielding of steel reinforcement due to issues in load actuator. The results shows that beam U-B9(2) exhibited stiffer response as compared to same beam with longer span and higher shear span to depth ratio.

The comparison of load deflection of beams U-B6(2) and U-B7(2) is shown in Figure 3-32. As can be seen in this figure, Beam U-B7(2) exhibited significant strain hardening after rebar yielding and reached maximum load carrying capacity of 453.7 kN. Due to issues with test set-up faced during experiment, test on beam U-B6(2) was stopped before attaining failure. However, the beam U-B6(2) reached maximum load level of 423.6 kN before stopping the test. This maximum load level attained confirms that removing stirrups in this beam tested with shear span to depth ratio of 2.06, did not result in significant reduction of shear capacity.

Load deflection response of beam U-B6(2) confirms higher load carrying capacity by 33% as compared to beam U-B4(2) with lower reinforcement ratio. This observation is similar to beams

U-B4 and U-B6, where beam U-B6 obtained load carrying capacity of 177.1 kN being 25% higher than that in beam U-B4.

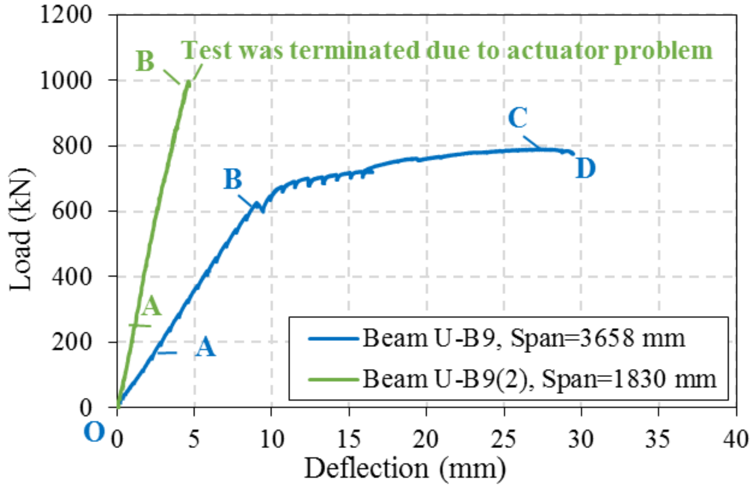

Figure 3-30. Load deflection response of beam U-B9(2)

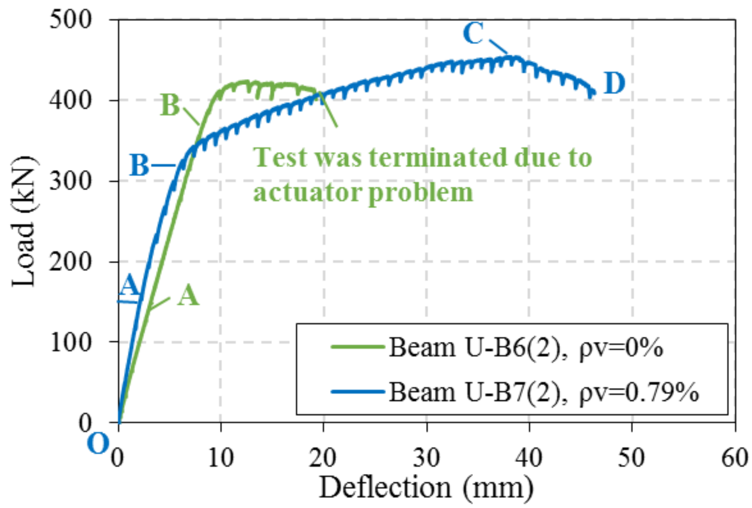

Figure 3-31. Load deflection response of beam U-B6(2) and U-B7(2)

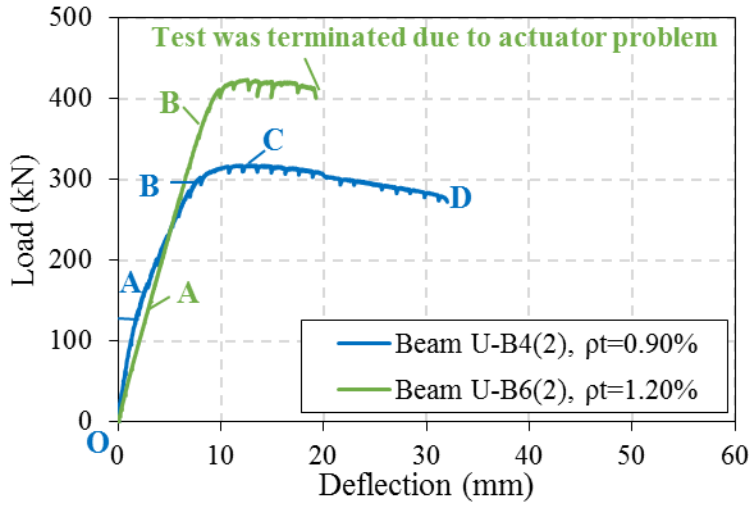

Figure 3-32. Load deflection response of beam U-B4(2) and U-B6(2)

Table 3-4. Load-deflection values at various stages of loading on beams U-B6 to U-B9

Beam	Initial Cracking (A)		Rebar Yielding (B)		Peak Phase (C)		Ultimate Phase (D)	
	Load (kN)	Deflection (mm)	Load (kN)	Deflection (mm)	Load (kN)	Deflection (mm)	Load (kN)	Deflection (mm)
Flexural loading								
U-B3	26.2	2.5	81.1	19.1	97.1	47.6	86.2	107.2
U-B5	28.4	3.4	104.7	24.3	126.6	76.2	116.6	124.0
Shear loading								
U-B4	39.1	1.4	126.7	11.3	142.1	17.9	126.9	52.9
U-B6	38.8	1.6	149.9	12.6	177.1	62.9	173.2	68.1
U-B7	39.4	1.2	144.8	12.1	180.3	41.2	164.8	58.5
U-B8	176	1.9	663.7	8.0	740	24.8	707.3	31.7
U-B9	155	2.2	610.1	8.8	790.1	27.1	774.9	29.5
Flexural-shear loading (retesting undamaged part of the beams)								
U-B4(2)	124.8	1.7	294.6	7.5	317.6	12.6	271.9	32
U-B6(2)	140.4	2.9	365.1	8.1	-	-	-	-
U-B7(2)	150.1	2.1	335.8	6.9	453.7	37.9	408.4	46.3
U-B9(2)	224.4	1.1	982.5	4.7	-	-	-	-

The comparison of shear force-deflection and moment curvature under loading point in beams U-B4 and U-B4(2) is shown in Figure 3-33 and Figure 3-34. Beam U-B4 with span of 3658 mm were tested using three-point loading set up shown in with shear span to depth ratio of 2.6. The undamaged part of this beam (U-B4(2)) was tested under four-point loading setup that led to shear span to depth ratio of 2.06. As illustrated in Figure 3-33 and Figure 3-34, the beam with smaller span (U-B4(2)) exhibited 6% increase in moment capacity. Therefore, span and loading configuration did not significantly affect moment capacity of these beams. However, decreasing shear span to depth ratio, and length of the span resulted in 34% increase in shear capacity of the beam U-B4(2).

Similarly, comparison of shear force-deflection and moment-curvature under point load in beams U-B7 and U-B7(2) is presented in Figure 3-35 and Figure 3-36. These comparison show improvement of shear capacity in beam U-B7(2) by 51% with decreasing shear span to depth ratio from 2.6 to 2.06. Also, moment capacity in beam UB-7(2) with decreasing span increased by 19.6% as compared to U-B7 which was not as significant as shear resistance improvement. Further, the results of shear resistance (load)-deflection of beams U-B4(2) and U-B7(2) illustrate significant increase in post cracking stiffness as compared to same beams with longer span.

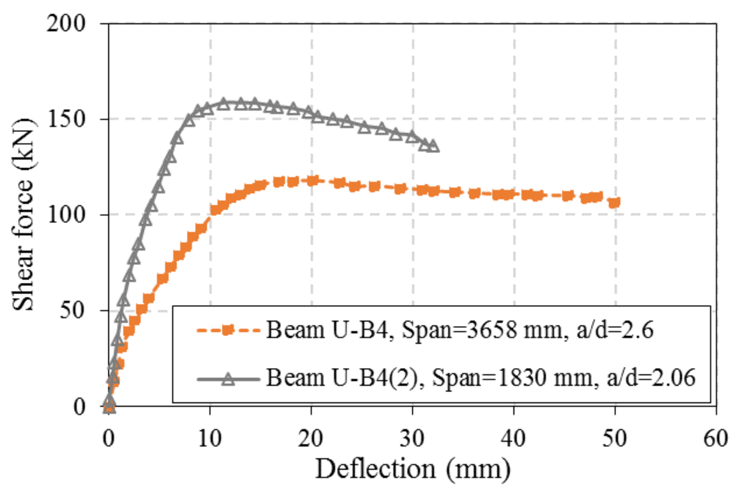

Figure 3-33. Comparison of shear force-deflection response of beams U-B4 and U-B4(2)

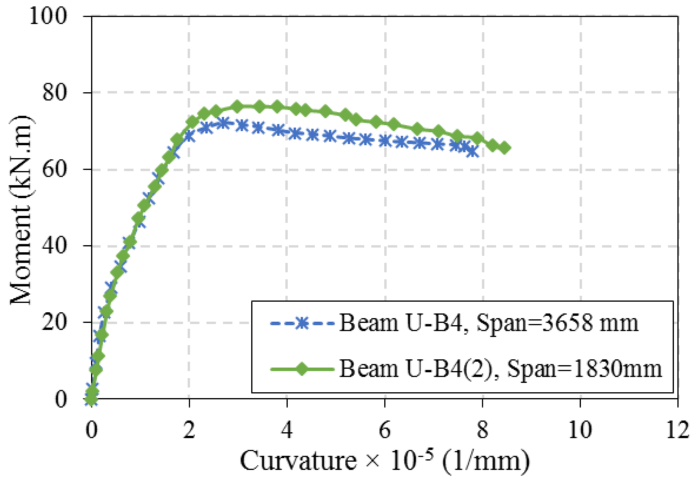

Figure 3-34. Comparison of moment-curvature response of beams U-B4 and U-B4(2)

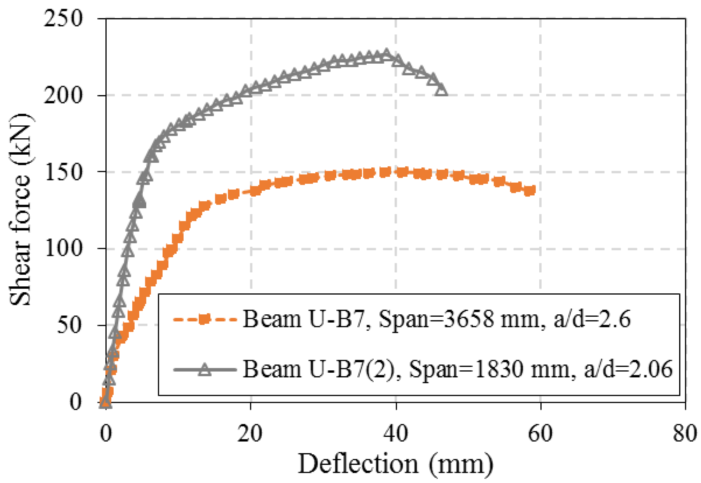

Figure 3-35. Comparison of shear force-deflection response of beams U-B7 and U-B7(2)

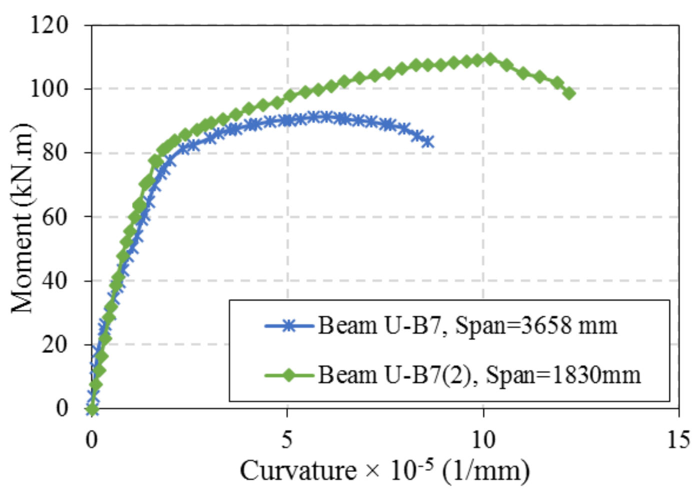

Figure 3-36. Comparison of moment-curvature response of beams U-B7 and U-B7(2)

3.8.3.2 Load Strain Response

Strain gauges mounted on reinforcing bar and concrete at critical section of the beams were utilized to record strains over the full range of loading on these beams. The typical load-strain response of beams U-B4 (under shear loading) and U-B5 (under flexural loading) is shown in Figure 3-37. Negative values (strain) indicate compressive state and positive values (strain) indicate tensile state at the corresponding depths. Strain gauges SG-C1 and SG-C2 which were located in the vicinity of extreme compression fiber (see Figure 3-10), recorded compressive (negative) strains throughout the loading. Strain gauges SG-C4 and SG-C5 (see Figure 3-10) recorded increasing tensile (positive) strains during loading. Shifting of strains from compressive to tensile state was observed in SG-C3 (located at a distance of 70 mm from top face of the beams) in UHPFRC beams. This shifting of strains from compressive to tensile state indicates shifting (movement) of neutral axis. This shift in neutral axis depth was also confirmed by the propagation of cracks towards compression zone with increased loading on the beams. Beams U-B3 and U-B6 exhibited similar load-strain response, as in corresponding beams U-B4 and U-B5.

Load-strain response of beam U-B9 recorded by strain gauges placed at critical section of the beam is also plotted in Figure 3-38. It should be noted that strain gauges SG-C1 and SG-C6 in beam U-B8 did not record strains reliably. SG-C1, SG-C2, SG-C3, SG-C4 (mounted at a distance of 13mm, 30 mm, 70 mm, and 145mm from top surface of beams), recorded change in strains from compressive to tensile strain indicating moving neutral axis upward. Shifting of strains from compressive to tension in SG-C1 (located at distance of 13 mm from top surface of beams), confirms propagation of cracks toward extreme compression fiber. Strain gauges SG-C5 to SG-C11 recorded increasing tensile strains with increasing applied load. In this beam, strain of about 0.055 was recorded close to failure by SG-C11 located at 27 mm from bottom surface of the beam.

The strain gauges located in the tensile zone of the UHPFRC beams, did not show abrupt change in strain values after initiation of cracking. This behavior in UHPFRC beams is attributed to resistance and bridging effects of steel fibers under tensile forces.

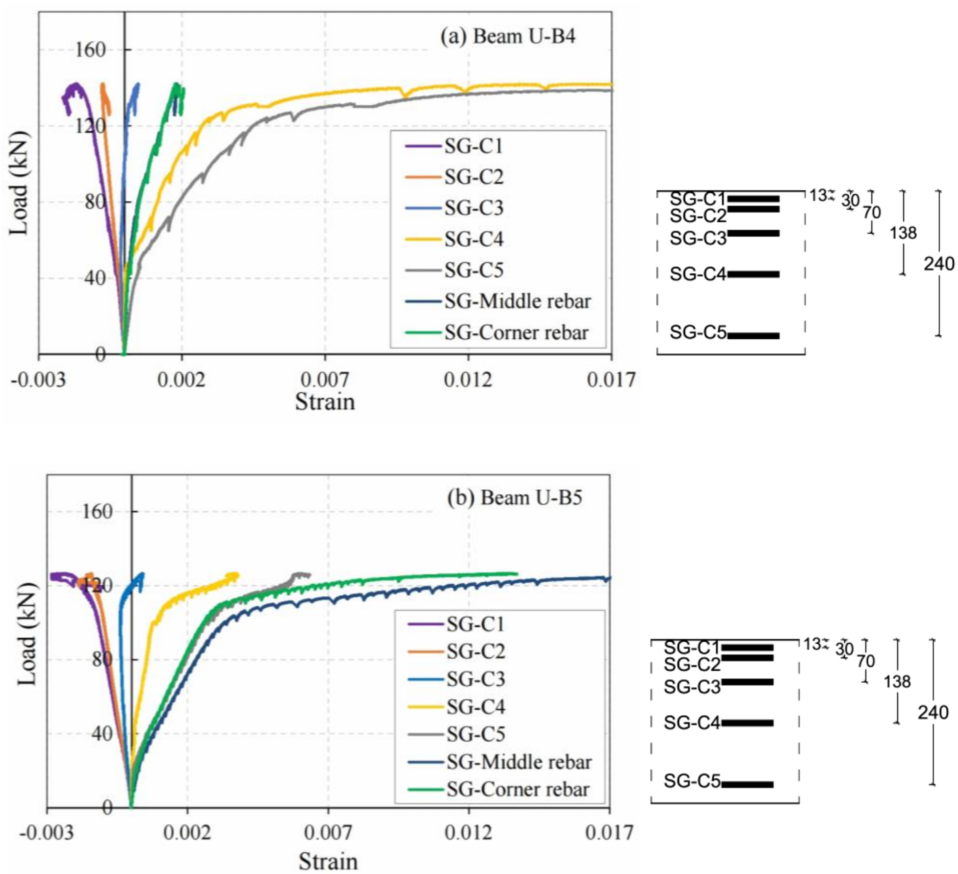

Figure 3-37. Load strain response of UHPFRC beams, (a) beam U-B4, (b) beam U-B5

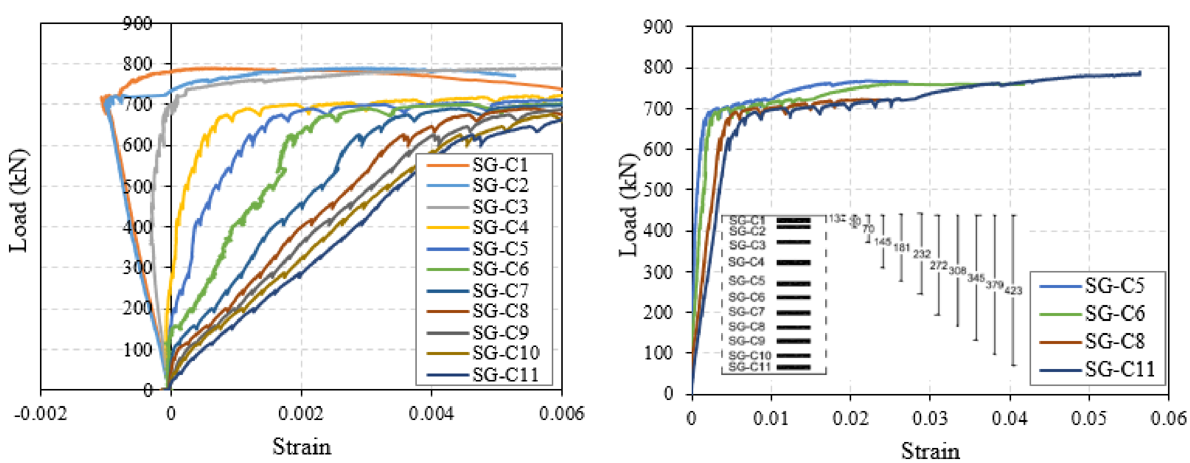

Figure 3-38. Load strain response of beam U-B9 tested under shear dominant loading

The strains developed with increasing load in longitudinal reinforcement at critical section (under loading point) and stirrups in shear span of beam U-B9 is plotted in Figure 3-39. It can be seen that tensile reinforcement yielded before yielding in shear reinforcement, confirming high shear resistance of UHPFR. Strain measurements show that strain in a shear reinforcement reached yielding strain before failure of the beams.

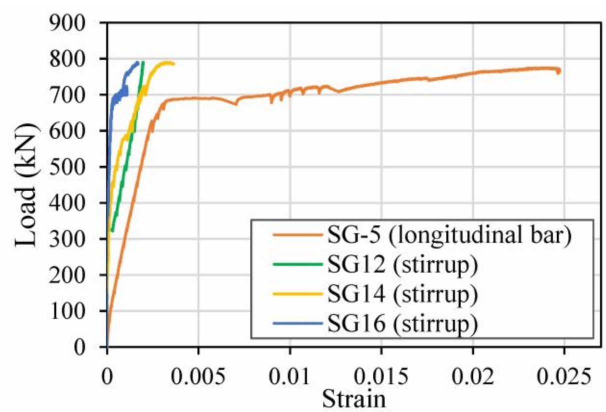

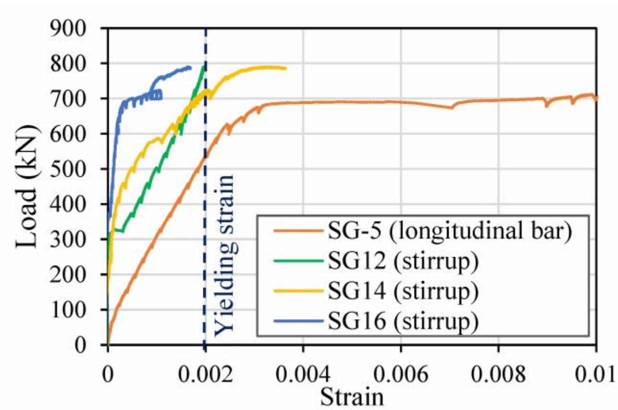

Figure 3-39. Load strain response of beam U-B9 tested under shear dominant loading

3.8.3.3 Crack Propagation and Failure Pattern

The crack patterns and their propagation are crucial in understanding behavior of tested beams, including nature of stresses, movement of neutral axis location, and energy dissipation [174]. The difference in response of beams under flexural and shear loading can be explained by comparing crack propagation in beams U-B3 and U-B5 (under flexural loading) and beams U-B4 and U-B6 (under shear loading). Crack propagation patterns at different stages in beams U-B5 and U-B6 are shown in Figure 3-40.

In beams U-B3 and U-B5, tested under four-point flexural loading, first cracks initiated between load points, in the pure bending zone, when the load level was 26.2 kN and 28.4 kN, corresponding to bending moment of 18.3 kN.m and 19.8 kN.m, respectively. Vertical cracks extending from the bottom (tensile) face of the beams towards the top (compressive) face formed in the critical section as a result of flexural stress. At increased load levels, more cracks formed with little increase in width of existing cracks. Owing to bridging of steel fibers, magnitude of maximum crack width remained low until peak load was attained in the tested beams. For instance, the maximum crack width in beam U-B3 reached around 1.2 mm at peak load. This pattern of multiple cracks with small crack width can be attributed to the ability of UHPFRC in undergoing stress re-distribution resulting from the bridging effect facilitated by the presence of fibers, and this is quite different from the cracking pattern that develops in conventional concrete beams [61]. As the load increased further, the cracks widened to dissipate the increased energy generated by the applied loading. After reaching the peak load, one of the cracks (60 mm from center of the beam UB3, 20 mm from center of the beam UB5) widened more than other cracks in the beams and fibers at these sections pulled out as shown in Figure 3-41. Furthermore, the cracks propagated towards compression zone with further increment in load. Beam U-B5, with higher reinforcement ratio, developed larger number of cracks at a closer spacing compared to beam U-B3.

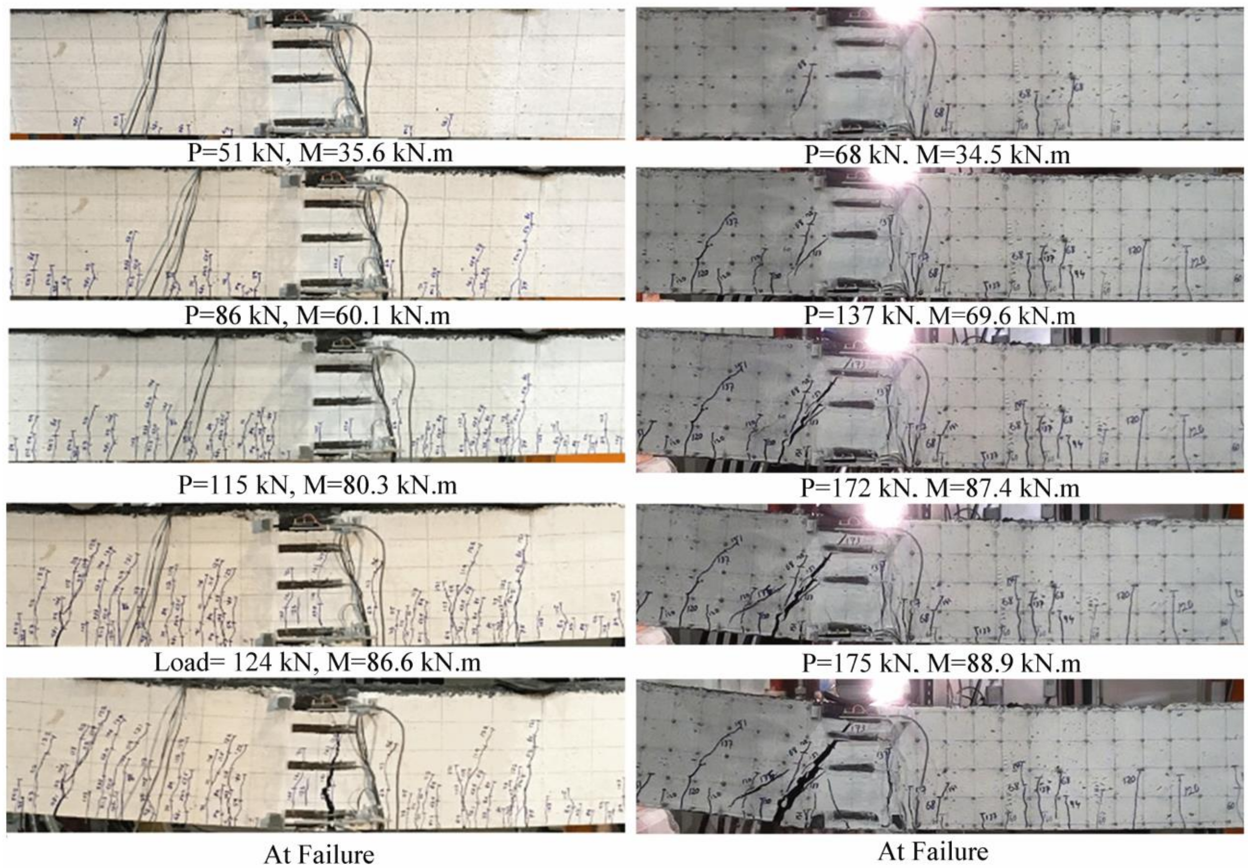

(a) U-B5 (under flexural loading) (b) U-B6 (under predominant shear loading)

Figure 3-40. Comparative crack pattern in UHPFRC beams at various load levels

In beams U-B4 and U-B6, which did not have any stirrups and that were tested under dominant shear loading, flexural cracks initiated between load point and mid-span location at a load level of 39.1 kN and 38.8 kN, corresponding to bending moment of 19.9 kN.m and 19.7 kN.m, respectively. This pattern was similar to that as in beams under flexural loading. The number of flexural cracks in shear span and between shear span and mid-span continued to grow with increase in loading. First diagonal crack initiated in shear span of the beams U-B4 and U-B6 at load level of 94.4 kN and 68.6 kN, corresponding to bending moment of 47.9 kN.m and 34.8 kN.m, respectively. More diagonal cracks developed in the shear span of the beams U-B4 and U-B6 at higher load levels as shown in Figure 3-40. Due to relatively short length of steel fibers used in the present UHPFRC mix, failure occurred through a single macro-crack once fibers began to pull-out at that location. One of the diagonal cracks in shear span of beams U-B4 and U-B6, initiated at a distance of 23 mm and 149 mm from load point, widened more as applied load increased due to progressive pull-out of fibers and eventually caused failure in beams U-B4 and U-B6 (see Figure 3-40 and Figure 3-41).

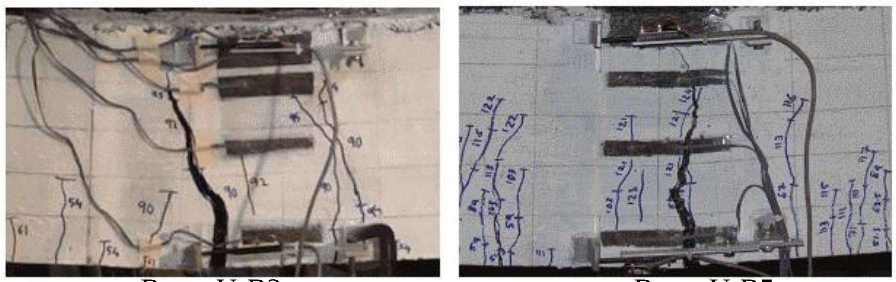

Beam U-B3 Beam U-B5

Flexural loading

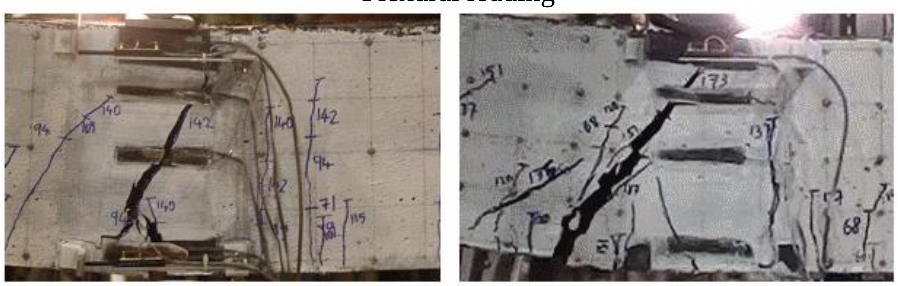

Beam U-B4 Beam U-B6

Shear dominant loading

Figure 3-41. Widening of specific crack in UHPFRC beams with increasing loads

Crack propagation at different stages in beam U-B7 is also shown in Figure 3-42. At early stages of loading, flexural cracks initiated in the beams, between loading point and midspan at load level of 39.4 kN. With increasing load level, number of cracks in shear span and between shear span and midspan increased, and cracks propagated towards compression zone. At higher load levels one major crack widened more than other cracks, and failure occurred due to propagation of the major crack through the depth of the beam as shown in Figure 3-42. In the case of the beam U-B6 ($\rho_v = 0\%$), major crack was a diagonal crack in shear span as shown in Figure 3-40 and

Figure 3-41. However, in beam U-B7 ($\rho_v = 0.79\%$), the major crack was a flexural crack under the point load as shown in Figure 3-42. Comparison of structural response of beams U-B6 and U-B7 indicates that removing stirrups in beam U-B6 did not result in reduction of ductility and load carrying capacity, but it changed the failure mode.

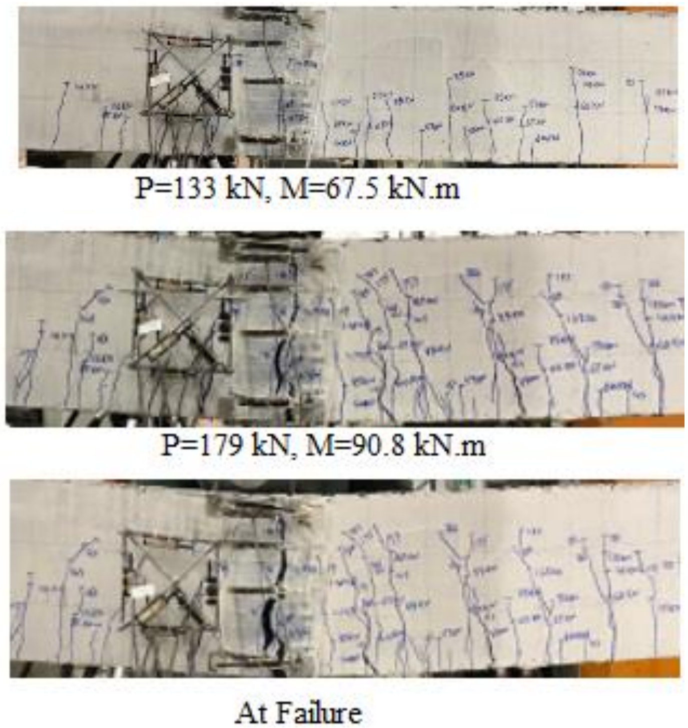

Figure 3-42. Crack pattern in beam U-B7 ($\rho_v = 0.79\%$) at various load levels

Cracking pattern in deep beams U-B8 and U-B9 are also presented in Figure 3-43. First flexural crack developed in zone between loading point and midspan at load level of 176 kN and 155 kN in beams U-B8 and U-B9, respectively. With increasing load levels, more cracks developed in between loading point and midspan and diagonal cracks also propagated in shear span of the beams. At higher load levels, one major crack widened more compared to other cracks and this major crack propagated towards compression fiber. These major cracks were developed at critical section of the beams, i.e under point load in both beams. However in beam U-B8 ($\rho_v = 0\%$), the major crack widened more as compared to beam U-B9 ($\rho_v = 0.40\%$) as shown in Figure

3-44. Maximum crack width close to failure was measured to be 9mm, 5mm in beam U-B8 and U-B9, respectively. Therefore, stirrups provided restraint against cracking in beam U-B9 and resulted in smaller crack width. However, beam U-B8 without stirrups, reached ultimate load capacity and ductility as compared to beam U-B9. In other words, beam U-B8 without stirrups exhibited high shear capacity same as beam U-B9, but the crack width was higher. Moreover, in beam U-B8 (with no stirrups), cracks propagated in unrestrained fashion towards compression zone as shown in Figure 3-44 and Figure 3-45. In beam U-B8 without stirrups, concrete crushing was also observed under point load indicating shear compression failure (see Figure 3-46).

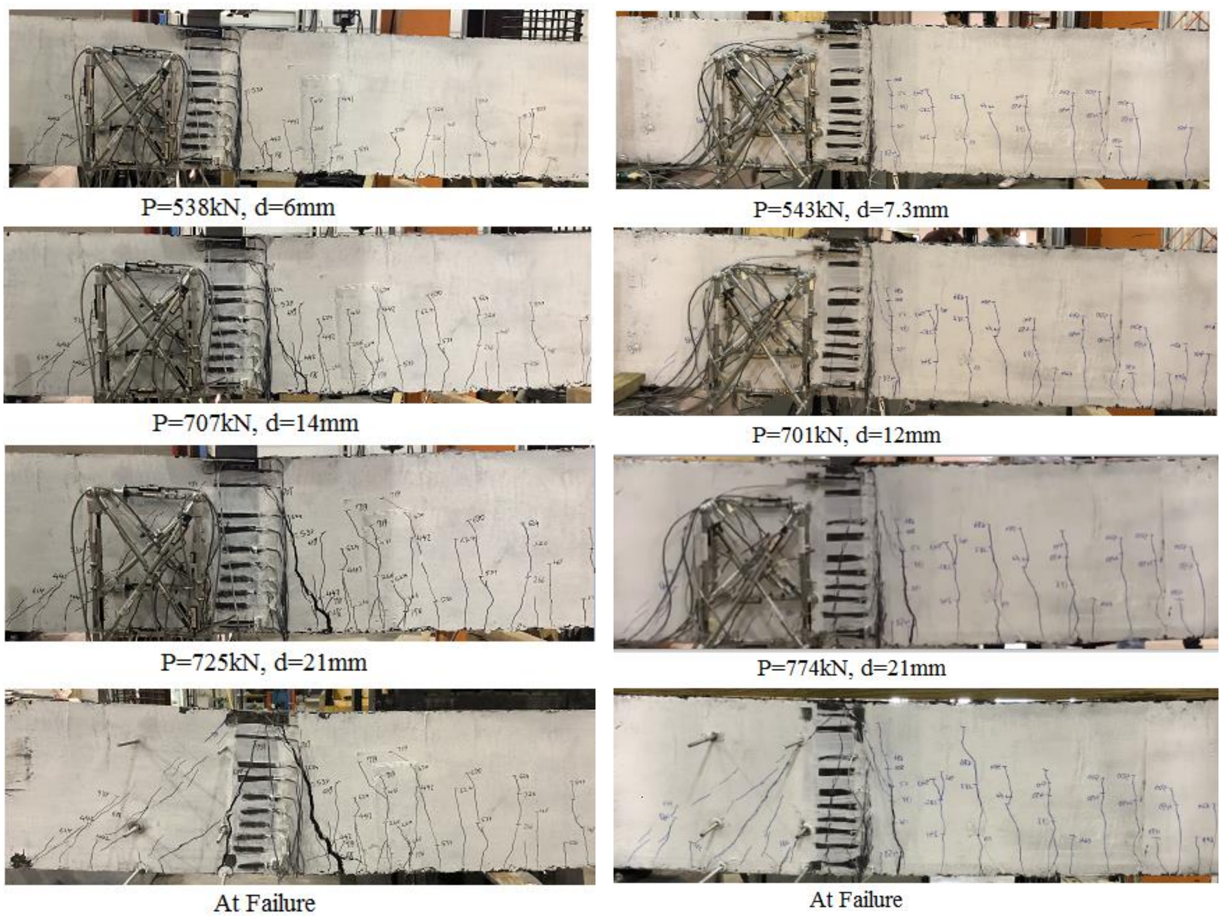

(a) Beam U-B8 (b) Beam U-B9

Figure 3-43. Crack pattern in beams, (a) U-B8 ($\rho_v = 0.0\%$), (b) U-B9 ($\rho_v = 0.40\%$) at various load levels

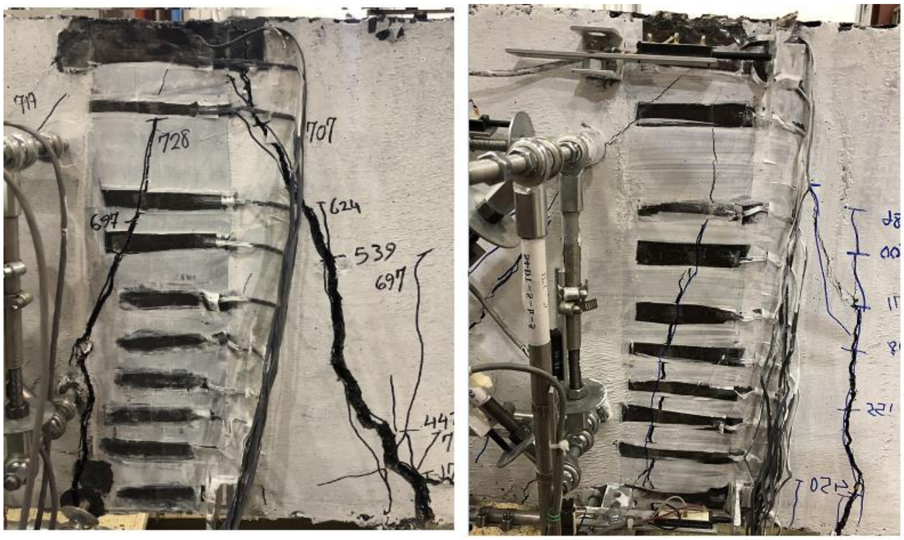

(a) Beam U-B8 (b) Beam U-B9

Figure 3-44. Major cracks at failure in front side of the beams (a) U-B8, (b) U-B9

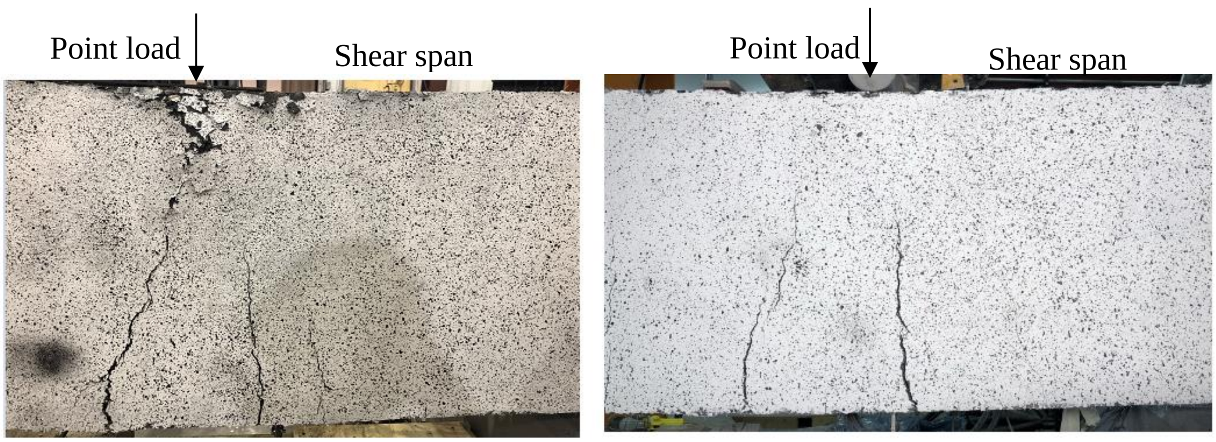

(a) Beam U-B8 (b) Beam U-B9

Figure 3-45. Crack propagation at failure in back side of the beams (a) U-B8, (b) U-B9

(a) Front side of the beam (b) Back side of the beam

Figure 3-46. Zoomed view of compression zone under point load in beam U-B8

The UHPFRC beams exhibited significant shear resistance arising from three mechanisms i.e. shear resistance of the uncracked portion of concrete, vertical component of the interface shear force (due to aggregate interlock and presence of steel fibers), and dowel action in the tension reinforcement [175,176]. The subsequent behavior in shear, including failure pattern and ultimate strength in shear depends on the evolution of these mechanisms with increasing load. Results from experiments showed that UHPFRC beams under dominant shear loading, continued to resist increasing loads until ultimate moment capacity was attained and the cracks extended along the entire depth of the beams. Such behavior is different from beams fabricated using conventional normal strength concrete (NSC) or high strength concrete (HSC) mixes which fail through diagonal tension well before maximum moment capacity is reached, unless shear reinforcement (stirrups) are in place [175,176]. Conventional concrete beams without stirrups fail suddenly with appearance of a single shear crack [177]. This improvement in overall shear performance is a consequence of larger compressive strength, as well as enhanced interface shear force resistance facilitated by steel fibers (through fiber bridging) in UHPFRC.

Variation of maximum crack width with increasing moment in beams U-B4, U-B6, and U-B7 (under shear loading) is plotted in Figure 3-47. The trends plotted in this figure show that presence of steel fibers in UHPFRC contributed in controlling crack width in UHPFRC beams as the maximum crack width was measured to be 0.05 mm at nearly 70% of peak load which are relatively lower than conventional concrete beams having similar dimensions and reinforcement ratio [178–180]. At load level of 168.9 kN corresponding to moment of 85.8 kN.m, maximum diagonal crack width of the beam U-B6 was measured to be 1 mm (as shown in Figure 3-47), and this low crack width is mainly due to bridging effect facilitated by steel fibers in UHPFRC beams. Moreover, increase in the width of specific cracks in these beams was gradual (or ductile) instead of being abrupt (or brittle) as is the case of beams made of conventional concrete without fiber. Maximum crack width at failure in beams U-B4, U-B6, and U-B7 was recorded to be 10.8 mm, 15.8 mm, and 14.5 mm, respectively. Measured maximum crack widths at failure was comparable to the length of the steel fibers in UHPFRC. This is an indirect indication of the extent of fiber bridging that occurs in UHPFRC prior to failure.

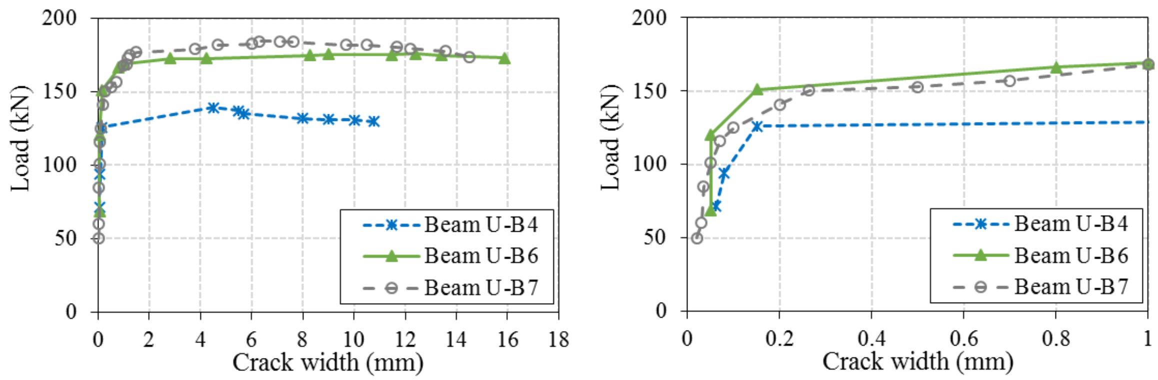

Figure 3-47. Variation of main diagonal crack width with increasing moment in beams U-B4 and U-B6

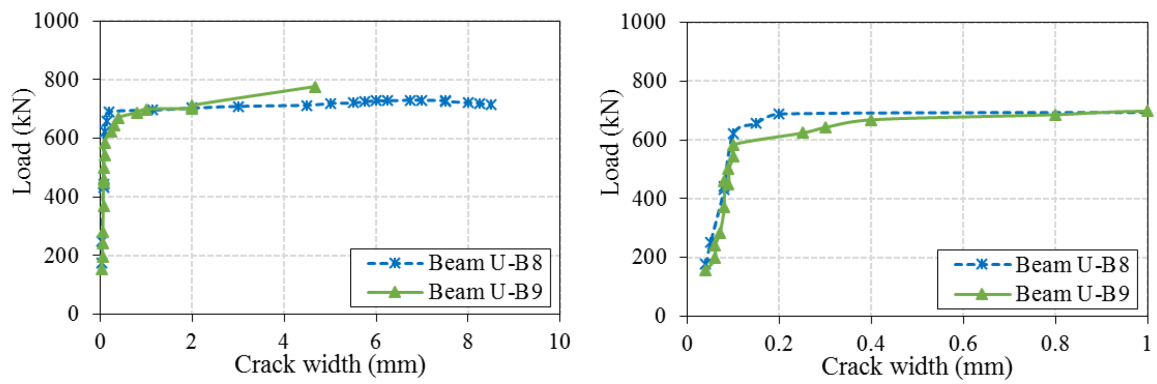

(a) Crack width (b) Zoomed view of crack width in 0 to 1 mm range

Figure 3-48. Variation of main diagonal crack width with increasing moment in beams U-B8 and U-B9

3.8.3.4 Ductility

Ductility is a measure of energy absorption capacity of a structural member and can be expressed as resistance to deformability during transition from elastic stage to plastic stage leading to failure [61]. Deflection ductility index [181,182], curvature ductility index [183,184], or rotational ductility index [181] can be utilized to measure ductility in a reinforced concrete flexural member. Ductility of the beams evaluated base on deflection index, was compared for various UHPFRC beams. Deflection index (μ) is expressed as the ratio of deflection at the peak load (Δ_p) to deflection at yielding of steel reinforcing bar (Δ_y) as follows [61]:

$$\mu_P = \frac{\Delta_P}{\Delta_y} \tag{3-3}$$

Computing ductility using deflection at the ultimate phase (Eq. (3-4)) instead of deflection at peak loading point leads to improved estimation of post yielding response of RC beams [25]. The ultimate phase, point D in load-deflection response, is when the load level dropped abruptly and the beams could not sustain any more increase in loading.

$$\mu_u = \frac{\Delta_u}{\Delta_y} \tag{3-4}$$

The ductility indices of beams U-B3 to U-B9 calculated using both peak and ultimate deflection criterion are summarized in Table 3-5. For the beams tested under dominant shear loading, comparable ductility could be achieved as in the case of similar beams tested under flexure. These ductility indices $(\mu_p \ and \ \mu_u)$ were 2.49 and 5.61 for beam U-B3, 3.14 and 5.10 for beam U-B5, 1.58 and 4.68 for beam U-B4, and 4.99 and 5.40 for beam U-B6. These are comparable to the ductility indices reported in literature [182,185] for both NSC and HSC beams having stirrups (ranged from 1.1 to 5.4) under a variety of loading conditions and reinforcement ratios (see Table 3-5).

Increase in longitudinal reinforcement ratio resulted in increasing of ductility index (μ_p) of UHPFRC beams. This is in accordance with the observation that peak load carrying capacity was sustained in UHPFRC beams with higher reinforcement ratio and did not exhibit reduction. However, ductility index (μ_u) in beam U-B5 with higher reinforcement ratio decreased as compared to beam U-B3. The results indicate that there was no significant reduction in ductility even when either of the UHPFRC beams (without stirrups) failed in shear, as opposed to NSC and HSC beams which experience significant reduction in ductility under shear failure [175]. Further, comparison of ductility indices in beam U-B7 and U-B6, and U-B8 and U-B9 shows that removing stirrups did not result in reduction of ductility indices. It should be noted that beams made with conventional concrete (normal strength concrete) can fail in a brittle fashion even when reinforcement has a yield plateau due to shear-compression failure prior to yielding of reinforcement.

Table 3-5. Ductility indices of the UHPFRC beams tested under different loading configurations

Beam	$\boldsymbol{\rho_t}$**(%)**	**Loading type**	$\boldsymbol{\rho_v}$**(%)**	**Peak state ductility index** $(\frac{\Delta_p}{\Delta_y})$	**Ultimate state ductility index** $(\frac{\Delta_u}{\Delta_y})$
U-B3	0.90	Flexure	None	2.49	5.61
U-B5	1.20	Flexure	None	3.14	5.10
U-B4	0.90	Dominant shear	None	1.58	4.68
U-B6	1.20	Dominant shear	None	4.99	5.40
U-B7	1.20	Dominant shear	10mm@100	3.40	4.83
U-B8	2.48	Dominant shear	None	3.10	3.96
U-B9	2.48	Dominant shear	10mm@200	3.08	3.35
U-B4(2)	0.90	Flexure-shear	None	2.54	4.27
U-B6(2)	1.20	Flexure-shear	None	-	-
U-B7(2)	1.20	Flexure-shear	10mm@100	5.49	6.71
U-B9(2)	2.48	Flexure-shear	10mm@200	-	-
HSC [182]	1.4- 3.6	Flexure	6mm@80	-	1.31 - 2.89
HSC [185]	1.9-5.8	Flexure	8mm@100	1.1 - 1.8	1.2-5.4
NSC [185]	1.1-3.5	Flexure	8mm@100	1.2 – 3.3	2.5-4.7

ρ_t: Longitudinal reinforcement ratio; ρ_v: Shear reinforcement ratio

3.8.4 Digital Image Processing

In order to trace cracking pattern in the beams, Digital Image Correlation (DIC) technique was employed. DIC is an optical method and utilizes mathematical correlation analysis to measure strains and displacements. This technique captures consecutive images with a digital camera during the deformation process and evaluates change in surface characteristics [186]. DIC provides a contour map of strains and deformations of specimen surface subjected to mechanical loading and this data can be utilized to identify cracks on the surface of specimens [187]. In addition, different strain components can be extracted at any point within the viewing field.

For using DIC, the surface of specimen must have a random gray intensity distribution by the application of a random dot pattern (random speckle pattern). This speckle pattern can be natural texture of the specimen surface or made by spray paint [186,188]. In the current study, a thin layer of white paint was applied on the surface of the beams and a random speckle pattern was obtained through spraying black paint. The resulting speckle pattern is shown in Figure 3-49.

The basic principle of DIC is in tracking of the same points (or pixels) between consecutive images (i.e. before and after loading). A rectangular subset can be selected for matching rather than an individual pixel, since subset comprises a wider variation in gray levels and can be more uniquely identified in the deformed images [188]. In this technique, intensity patterns in images after deformation are compared to reference image in order to match subsets. Once the locations of the subsets in the deformed images are found, the displacements of the subsets can be determined [189].

Figure 3-49. Speckle patterns in UHPFRC beams for monitoring cracks through DIC

A two-dimensional image correlation procedure using a 24.1 megapixel NIKON D3200 and iPhone camera placed at 1 meter from the monitoring surface was utilized in the present study. For this purpose, a picture (reference image) was taken prior to loading and this was followed by a series of pictures taken during each load increment. GOM correlation software was used to apply DIC principles and analyze the images in order to map UHPFRC beams surface deformation and strains. Maximum principal strain contours at critical section of beams U-B4, U-B6, and U-B7 captured utilizing DIC technique at different load levels are shown in Figure 3-50 to Figure 3-52. These figures clearly indicate that DIC measurements can be utilized to map zones of strain localization and crack propagation in the beams at different stages of loading. As seen through visual observation, multiple micro cracks formed in the beams during initial stages of loading followed by formation of a single macrocrack close to failure.

Furthermore, Figure 3-53((a) and (b)) show a comparison between maximum principal strains measured using DIC at the same locations as SG-C1 (compression) and SG-C5 (tension). Significant oscillation can be seen in measured strain values using DIC technique. This can be attributed to the heterogeneous nature of UHPFRC which results in non-uniform local deformation (strain) at the target points. Also, the accuracy of DIC measurements is closely related to the quality of the speckle pattern on the specimen surface, out of plane displacement, noise in the recorded images (i.e. shot noise, thermal noise and cut-off noise), changes in lighting conditions, sensor integration time (exposure time) variation, and lens distortion [186,188]. Nonetheless, the measured strains using DIC exhibited similar trend, as compared to values measured using stain gauges. Thus, the present DIC measurement set-up for UHPFRC beams is effective in monitoring crack pattern formation and propagation, but needs further refinement for accurately capturing strain values during testing.

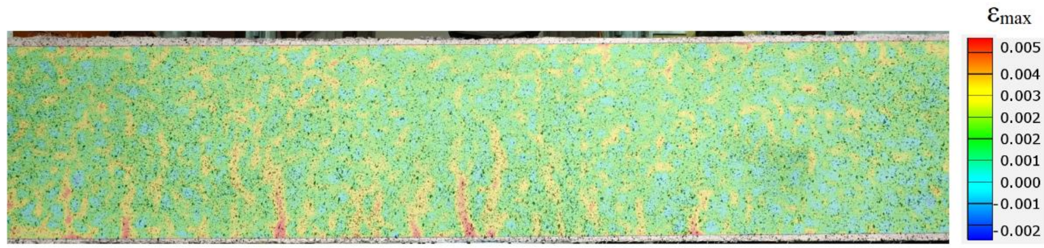

Load= 71 kN

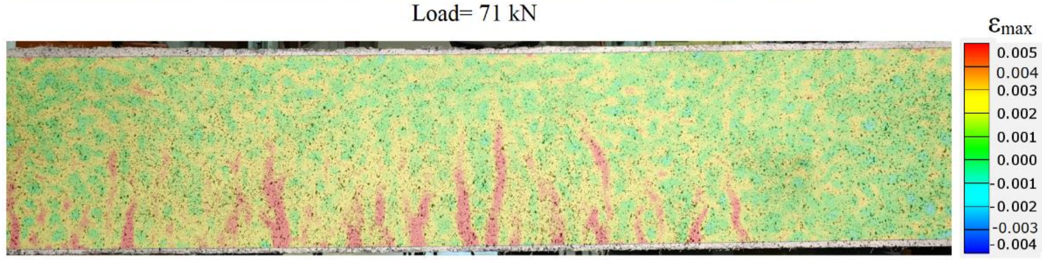

Load= 109 kN

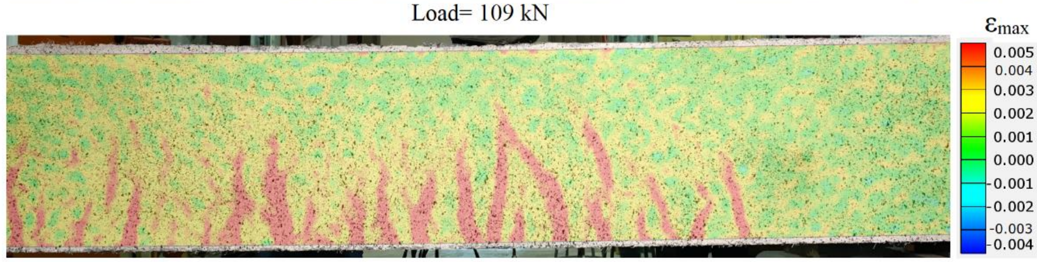

Load= 126 kN

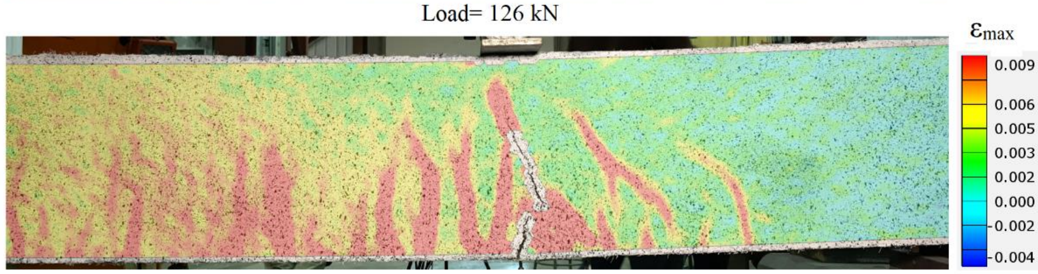

Load= 137 kN

Figure 3-50. Maximum principal strain contours in beam U-B4 obtained by DIC at different stages of loading

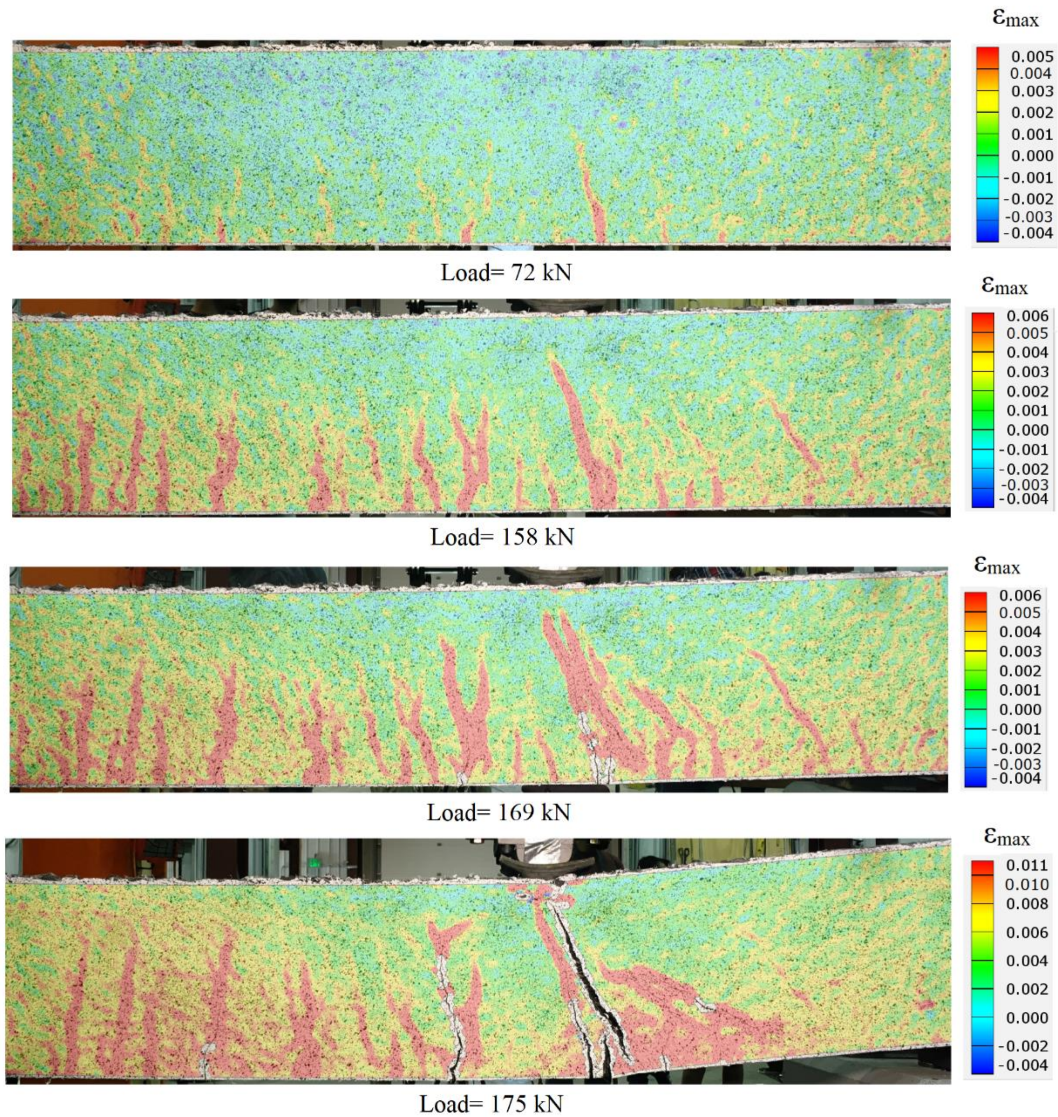

Figure 3-51. Maximum principal strain contours in beam U-B6 obtained by DIC at different stages of loading

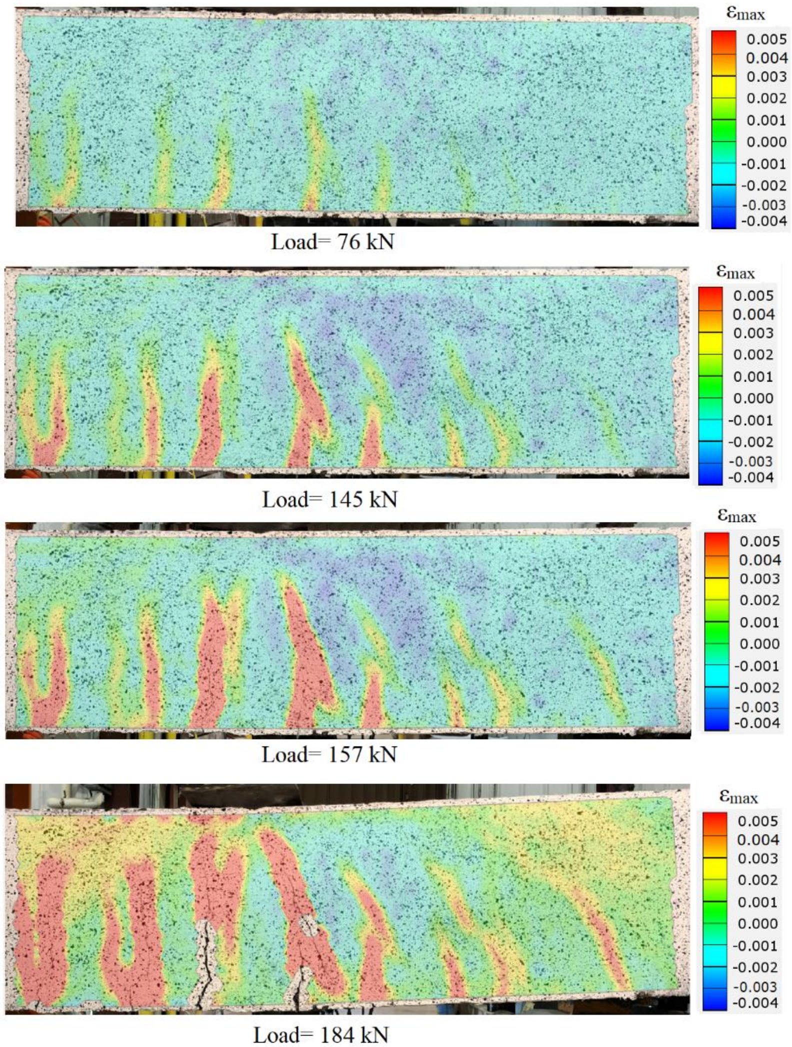

Figure 3-52. Maximum principal strain contours in beam U-B7 obtained by DIC at different stages of loading

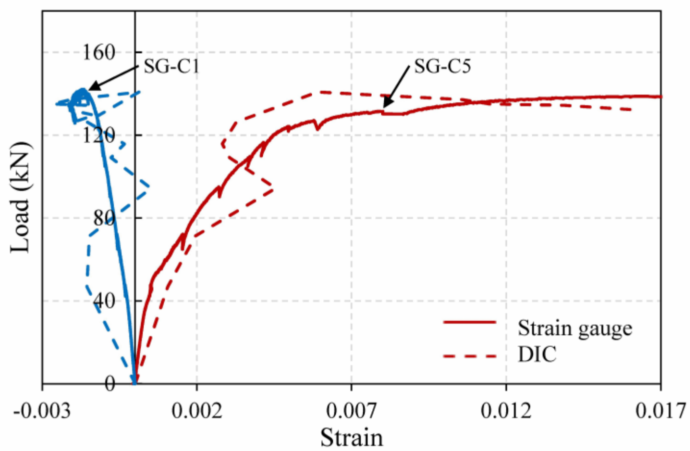

(a) Beam U-B4

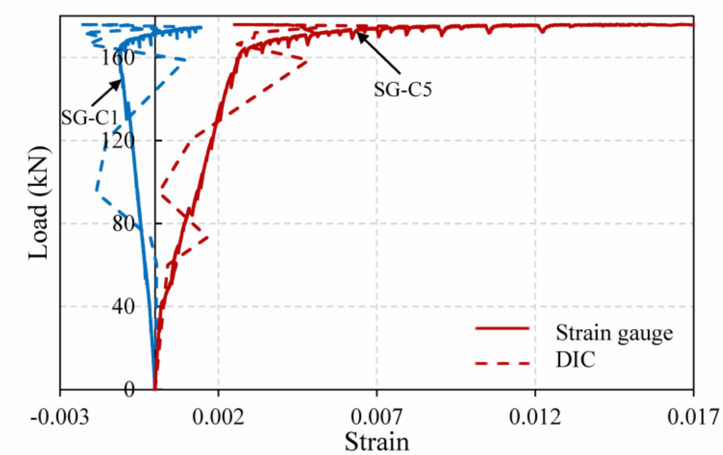

(b) Beam U-B6

Figure 3-53. Comparison of strain measurements using strain gauges and DIC in beams, (a) U-B4, (b) U-B6

3.9 Summary

For evaluating structural response of UHPFRC beams, seven beams were fabricated and tested as part of this study. The beams were tested under flexural and dominant shear loading with test variables of loading configuration, sectional properties, and shear span to depth ratio, longitudinal reinforcement ratio, and presence of shear reinforcement. Results from these experiments can be utilized to draw the following conclusions:

- The adopted improved mix design and procedure for preparing and curing UHPFRC with coarse aggregates is successful to attain desired workability and strength characteristics.

The mix can be prepared in a conventional ready-mix truck utilizing locally available materials, and at relatively lower cost, which in turn can facilitates UHPFRC market acceptance.

- Combination of Styrofoam in the formworks and insulating blanket is effective to eliminate thermal gradients within concrete block leading to early age cracking. Also, it can facilitate effective use of heat of hydration of the cementitious binder in UHPFRC towards field thermal curing.
- UHPFRC beams exhibit a cracking pattern characterized by formation of multiple microcracks at initial stages, followed by propagation of a singular macrocrack at the critical section leading to failure. This cracking response in UHPFRC beams is attributed to bridging effect facilitated by the presence of steel fibers in UHPFRC.
- UHPFRC beams possess significant ductility under both flexure and shear dominant loading. The ductility indices of UHPFRC beams tested under flexural and dominant shear loading ranges from 5.10 to 5.61, and 3.35 to 5.40, respectively.
- UHPFRC beams can attain 10-30% increase in load carrying capacity following yielding of steel reinforcement and this is facilitated from strain hardening effect in both tensile steel reinforcement and UHPFRC.
- UHPFRC beams possess high shear resistance due to high tensile and compressive strength of UHPFRC, combined with bridging effect at crack surfaces and high ultimate tensile strength, facilitated by presence of steel fibers and thus can be designed without shear reinforcement.
- Absence of shear reinforcement in UHPFRC beams does not lead to any reduction in either ductility or load carrying capacity of the beams even under dominant shear loading.

Further, UHPFRC beams subjected to dominant shear loading exhibit similar moment-curvature response, as that under flexural loading, indicating shear deformations to be negligible and this response is mainly due to high shear stiffness of UHPFRC.

CHAPTER 4

4 NUMERICAL MODELING

As discussed in Chapter 2, number of numerical studies have been undertaken to evaluate structural behavior of UHPFRC beams. Much of these studies applied sectional analysis approach and traced moment curvature response of UHPFRC beams under predominant flexural loading [5,49,128]. In these studies, the strain hardening in UHPFRC as well as reinforcing bars was not considered in the analysis.

Also, finite element based numerical models were applied to simulate the behavior of UHPFRC members. However some of these models [130,131] were validated against data from small-scale specimens with no reinforcing bars. Also, majority of previous studies focused on global response of UHPFRC structural members with no attention to local response (such as crack propagation direction, contribution of concrete and stirrups to shear capacity) and strain hardening in UHPFRC under tension was neglected. Further, developed numerical models were not fully validated for tracing shear behavior of UHPFRC beams.

To address some of the noted issues, a sectional analysis was applied to evaluate moment curvature response of UHPFRC beams. This sectional analysis accounted for high tensile strength and ultimate strain of UHPFRC as well as strain hardening effects in UHPFRC and steel. In addition, a finite element based numerical model was developed in ABAQUS to trace comprehensive structural response of UHPC and UHPFRC beams in the entire range of loading from initial loading to collapse of member. The model specifically accounts for stress-strain response of UHPC (or UHPFRC) in compression and tension, strain hardening of reinforcing bars, and the level of bond that develops between concrete and bars. The developed model was validated against measured response parameters from full scale tests on UHPFRC beams under flexural and shear loading [53,190].

4.1 Analytical Approach for Predicting Flexural Response

Flexural response of RC beams, is often established by evaluating moment-curvature relations at critical sections. The flexural response of UHPFRC beams was evaluated by undertaking an analytical method based on cross-sectional analysis and strain compatibility principles. For this cross-sectional analysis, the cross section of the member is discretized into number of layers and classical beam theory [191] is applied to evaluate forces and moment (M) in the cross section for a given curvature ($\emptyset$). Further, the complete moment-curvature response of a section is obtained by calculating strains and forces in layers, and the moment in the section while incrementing the curvature of the section until failure is obtained. The procedure applied in the analysis together with validation of the approach are presented in the following sections.

4.1.1 Modeling Assumptions

The following assumptions have been made in calculation of the moment-curvature response of the UHPFRC beams:

- Plane sections remain plane before and after bending, i.e., shear stresses are negligible.
- The strain distribution across the depth of the section is assumed to be linear.
- No slip occurs between steel reinforcement and concrete, implying that total strain in the reinforcement is the same as that in concrete.
- The strain hardening response of UHPFRC after tensile cracking due to fiber bridging is considered through tensile stress-strain curve.

4.1.2 Analysis Procedure

The sectional analysis procedure is implemented in MATLAB and the various steps needed for tracing moment-curvature relations is shown in Figure 4-1. The critical cross section of the beam is divided into a predefined number of layers (strips) along the depth of the cross section, as depicted in Figure 4-2. Assuming (knowing) curvature of the section, strain in each layer can be calculated in terms of the sectional curvature (ϕ) and depth of the neutral axis (c). Thus, strain at top and bottom faces are given by

$$\varepsilon_{top} = \phi c \tag{4-1}$$

$$\varepsilon_{bottom} = \phi(h-c) \tag{4-2}$$

For an assumed value of curvature (ϕ) and depth of neutral axis (c), the strains at the top and bottom faces of the cross section can be determined using Eqs. (4-1) and (4-2). After the strains in the extreme fibers of the cross-section are known, the strain in each layer along the height of the cross-section can be determined. Strain in steel rebars are considered to be as the strain in the concrete at the same layer of rebars. Subsequently, stress at each of these layers is calculated using predefined stress-strain relationships for concrete and reinforcing steel. These stresses are then multiplied with the corresponding area of each strip to get compressive (Fc) and tensile forces (Ft). Summing the forces in each of the strips above neutral axis will give total compressive force acting in the section. Similarly, summing the forces in all of the strips below neutral axis will give tensile force acting in the section. The compressive and tensile forces acting in concrete is calculated as;

$$Fc = \sum \frac{(\sigma c_{i+1} + \sigma c_i)}{2} A_i \tag{4-3}$$

$$Ft = \sum \frac{(\sigma t_{i+1} + \sigma t_i)}{2} A_i \tag{4-4}$$

where A_i is the area of the strip and is given as:

$$A_i = b(h_{i+1} - h_i) \tag{4-5}$$

Similarly, tensile force developed in rebars (Fs) is calculated as:

$$Fs = \sigma_s A_s \tag{4-6}$$

where, h_i is the position of the i^{th} layer of the cross section; σc_i is compressive stress at a given layer in compression zone, σt_i is tensile stress at a given layer at tensile zone, A_s is rebar area, and σ_s is tensile stress developed in rebars.

Finally, the forces across the section need to satisfy static equilibrium, giving rise to the following condition:

$$Fc = Ft + Fs \tag{4-7}$$

where Fs is tensile force developed in rebars. Fc and Ft are summation of the forces in concrete strips at compression zone and tension zone, respectively.

To obtain neutral axis depth for a given curvature, iterative calculations are performed by changing the depth of the neutral axis (c) until the equilibrium condition (Eq. (4-7)) is satisfied. Once the neutral axis depth is defined, the total bending moment at a given curvature can be calculated by taking moments of various forces acting on the section:

$$M = \sum \frac{(\sigma c_{i+1} + \sigma c_i)}{2} A_i \left(\frac{h_{i+1} + h_i}{2} - c\right) + \sum \frac{(\sigma t_{i+1} + \sigma t_i)}{2} A_i \left(\frac{h_{i+1} + h_i}{2} - c\right) + Fs(h_s - c) \tag{4-8}$$

This established one point on moment-curvature response. The curvature is incremented and the above procedure is repeated at the next strain level to generate moment and corresponding curvature at that strain. This process of incrementing curvature continues till concrete or steel reach their ultimate strain. This way moment-curvature points are generated until ultimate capacity of the beam cross-section is reached.

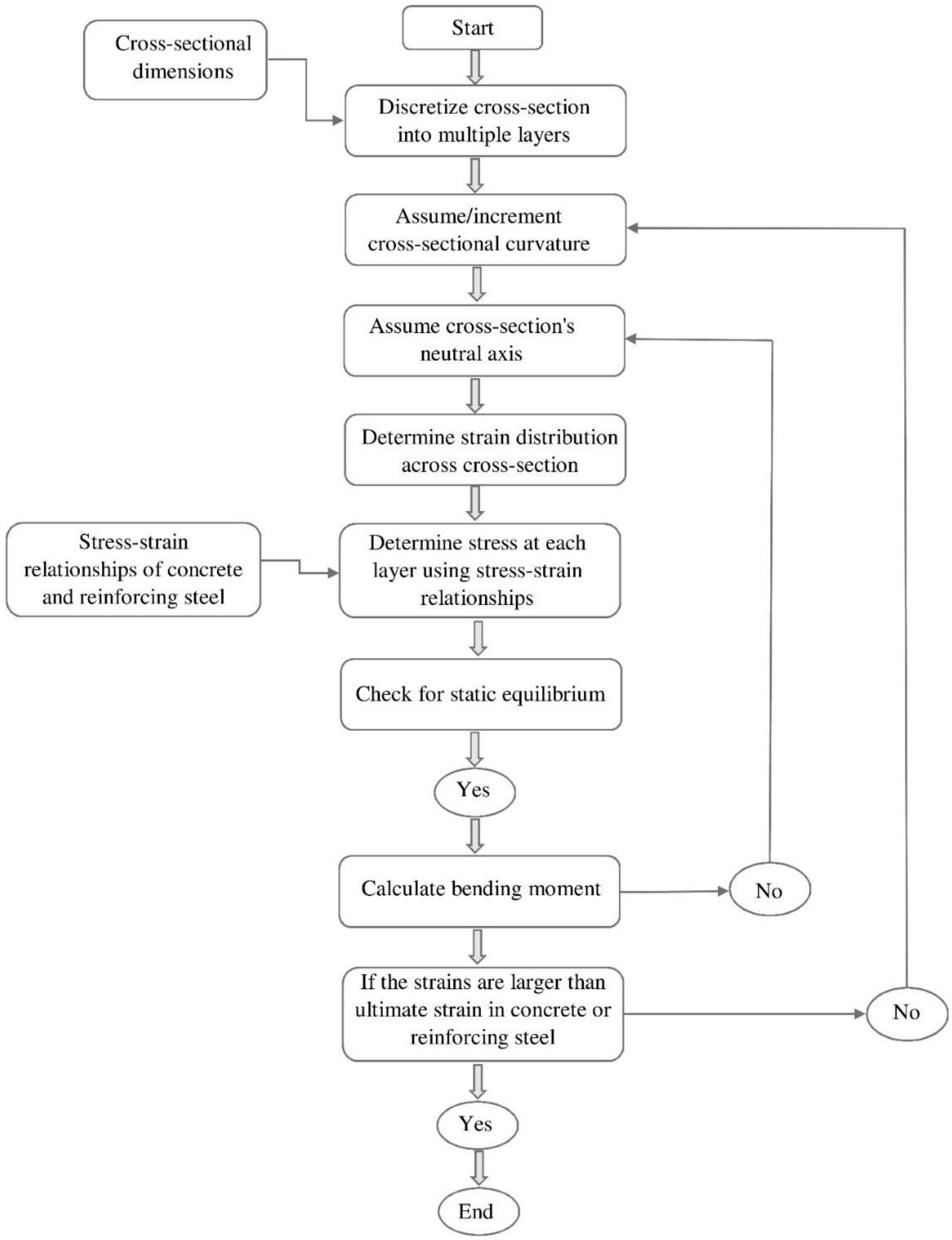

Figure 4-1. Flow chart illustrating the various steps involved in calculating moment-curvature response in a UHPFRC beam

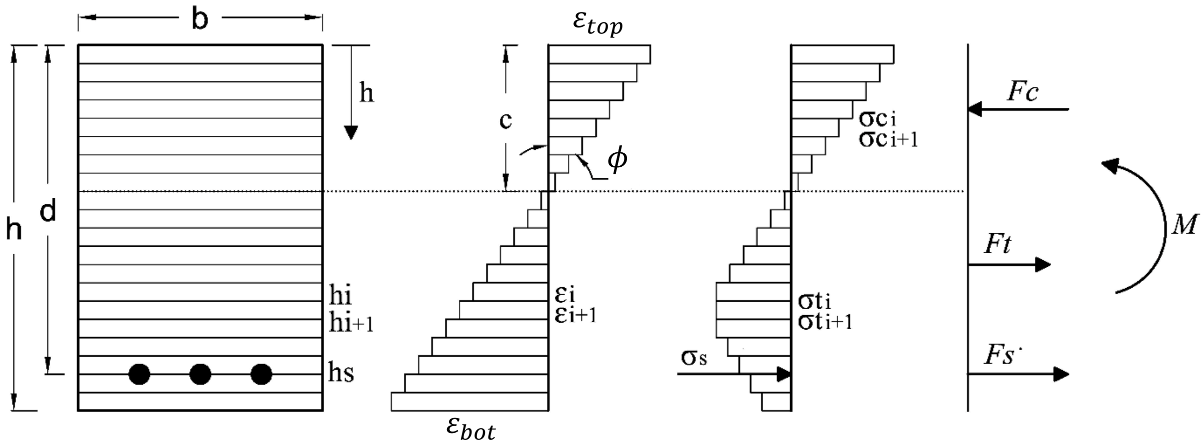

Figure 4-2. Schematic description of strain and stress distribution in cross-section of beams

4.1.3 Material Properties

For generating moment-curvature response compressive and tensile stress-strain relations of concrete and steel needs to be input in the model. Tensile fracture properties of UHPFRC, particularly post crack strain hardening and fiber bridging are to be given due consideration for reliable assessment of moment curvature response. The strain hardening behavior in UHPFRC under tension and also that of steel reinforcement is taken into account in the analyses. The details of the adopted material models are presented in sections 4.2.4 to 4.2.6. Stress-strain response of UHPFRC obtained from uniaxial compression tests, and direct tension tests or flexural tests along with inverse analysis was utilized for modeling response of UHPFRC in compression and tension, respectively. Also, stress-strain response of steel reinforcement under tension and compression consisting of three phases of linear elastic, yield plateau, and strain hardening zone was input to the model.

4.1.4 Validation of Analytical Approach

To undertake validation of the above developed sectional analysis model in predicting flexural response of UHPFRC beams, UHPFRC beams tested under flexure (U-B3 and U-B5) were analyzed and predicted response are compared against measured test data.

The predicted sectional moment curvature response of beams U-B3 and U-B5 with different reinforcement ratios along with measured experimental data is shown in Figure 4-3. The predicted and measured moment-curvature response exhibits four distinct stages i.e. linear elastic response, onset of flexural cracking along with crack propagation, yielding of steel reinforcement, followed by plastic deformation and attaining failure. It can be seen that moment-curvature response is linear up to a curvature (bending moment) of 0.22×10^{-5} per mm (28.3 kN-m) and 0.23×10^{-5} per mm (28.8 kN-m) for beams U-B3 and U-B5, respectively. The applied moment continues to increase monotonically beyond initial cracking and becomes nonlinear till the onset of rebar yielding. Subsequently, plastic deformation (curvature) increases until failure is attained. Overall, the predictions from the model compares well with those measured in tests.

In addition to above beams, UHPFRC beams tested by other researchers [49,61] having different types and geometry of fibers were analyzed utilizing the developed analytical model. The comparison of the results from tests and model is shown in Figure 4-4. There is a good agreement between predicted values from the numerical model and measured data obtained through experiments. The slight difference between numerical and experimental results can be attributed to slight variations arising from material models (properties), which might be different from actual properties. Ratio of moment capacity predicted by the model to that of experimental results is in the range of 0.90 to 1.10 for the analyzed beams. This shows that moment capacity of UHPFRC beams can be well predicted using the numerical model based on sectional analysis developed as part of this study.

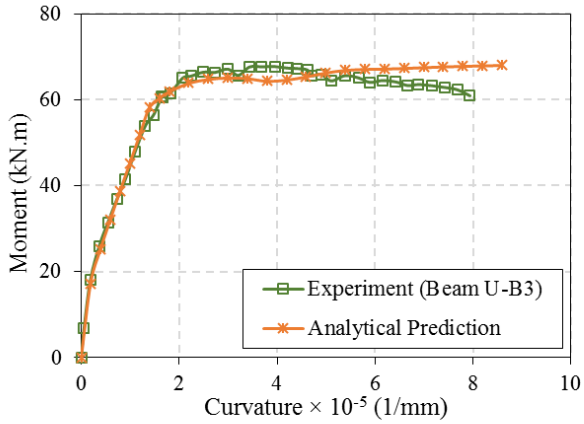

(a) Beam U-B3 (ρ=0.90%)

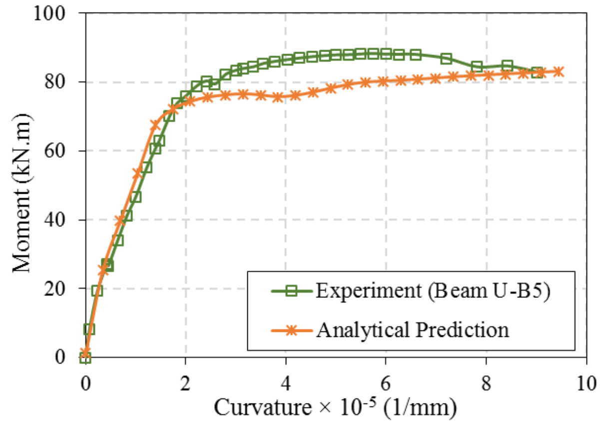

(b) Beam U-B5 (ρ=1.20%)

Figure 4-3. Comparison of moment-curvature response obtained by analytical approach and conducted tests on beams U-B3 and U-B5

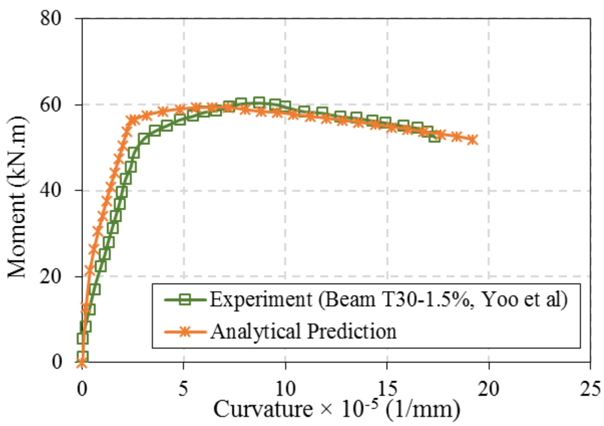

(a) Beam T30-1.5% [49]

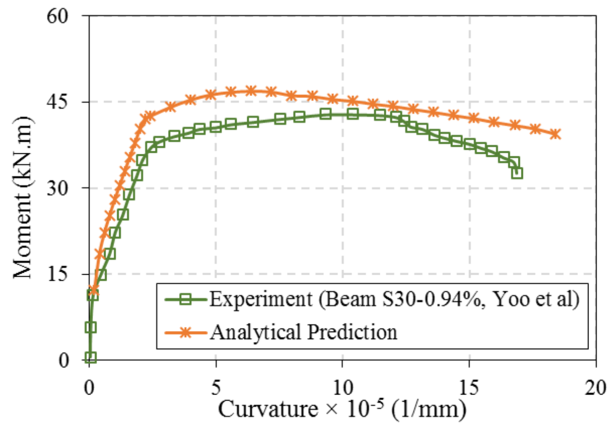

(b) Beam S30-0.94% [49]

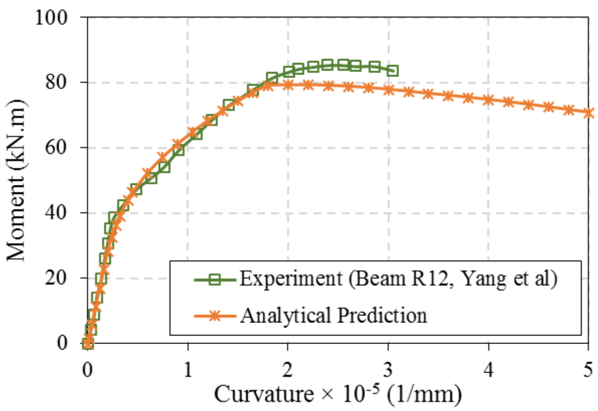

(c) Beam R12 [61]

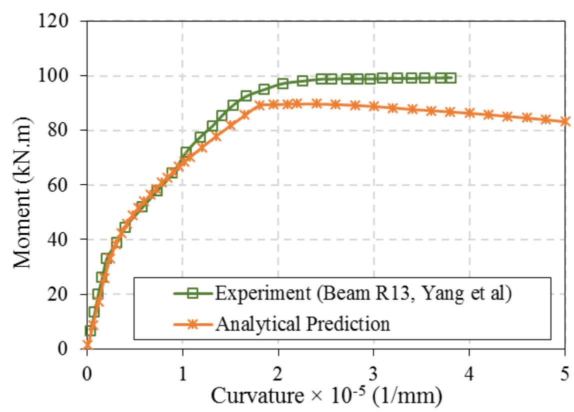

(d) Beam R13 [61]

Figure 4-4. Comparison of moment-curvature response obtained by analytical approach and conducted tests in literature

Table 4-1. Comparison of moment capacity of UHPFRC beams as predicted by analytical approach with test data

Beam	Moment Capacity (kN.m)		Ratio (1)/(2)
	Analytical Result (1)	Test Data (2)	
U-B3	68.0	67.9	1.00
U-B5	83.1	88.4	0.94
T30-1.5% [49]	59.3	60.4	0.98
S30-0.94%	46.9	42.9	1.10
R12 [61]	79.2	85.3	0.93
R13 [61]	89.7	99.3	0.90

4.2 Finite Element Model

In lieu of above presented sectional analysis approach, finite element based models can be utilized for tracing detailed structural behavior of an entire beam (not just at one section). For this purpose, a finite element based numerical model was developed in ABAQUS. A displacement controlled technique was utilized to trace softening response of the beams wherein displacement (instead of load) incremented at the nodes located under load points in steps till failure is attained. Details of the numerical model development including discretization details and material models are described below [53,190].

4.2.1 Discretization of the Beam

In a given UHPC (or UHPFRC) beam, concrete mass is discretized with brick elements (C3D8) while reinforcing steel is modeled as link elements (T3D2). C3D8 element is of eight nodes with three degrees of freedom in directions of x, y, and z. This element is capable of modeling concrete behavior in 3D and accounts for cracking in tension, crushing in compression, and large strains [192].

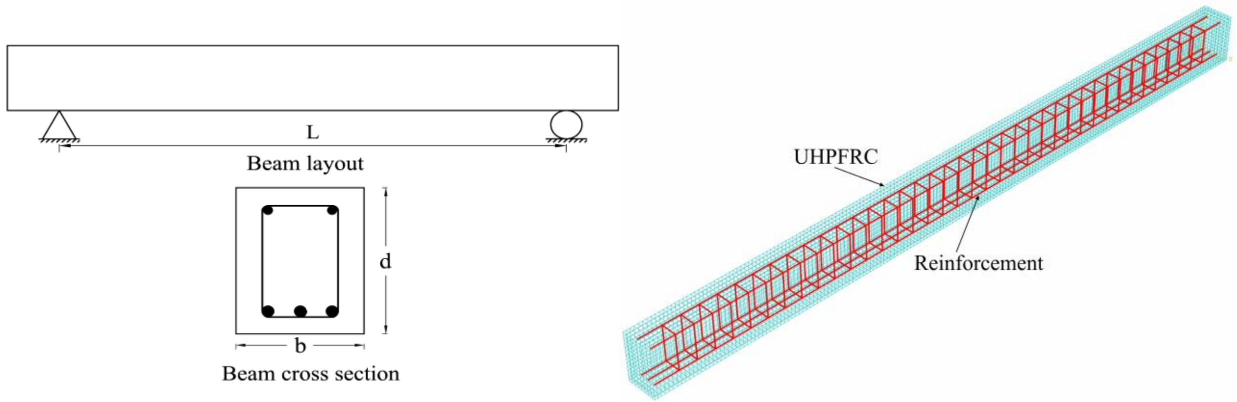

(a) Typical beam (b) Discretization of a beam

Figure 4-5. Discretization of a beam in ABAQUS for finite element analysis

The steel reinforcing bars were modeled using truss elements (T3D2), with the cross section of each bar defined within 3D solid. T3D2 are two noded elements and are used to model one-dimensional reinforcing bars that are assumed to deform by axial stretching only. The bond between concrete and reinforcement is modeled by using bond-link element approach [192,193]. Figure 4-5 illustrates discretization of a typical UHPFRC beam.

4.2.2 Material Models for UHPC

A damage based concrete plasticity model, available in ABAQUS, is utilized to model the nonlinear material behavior of UHPC (and UHPFRC). The Concrete Damage Plasticity model (CDP) is a smeared crack material model and is based on theory of plastic flow [131]. The yield surface in CDP model is based on the yield surface proposed by Lubliner et al [194] along with modifications proposed by Lee and Fenves [195] to account for different evolution laws of the strength under tension and compression. Yield surface of CDP model under plane stress condition is illustrated in Figure 4-6.

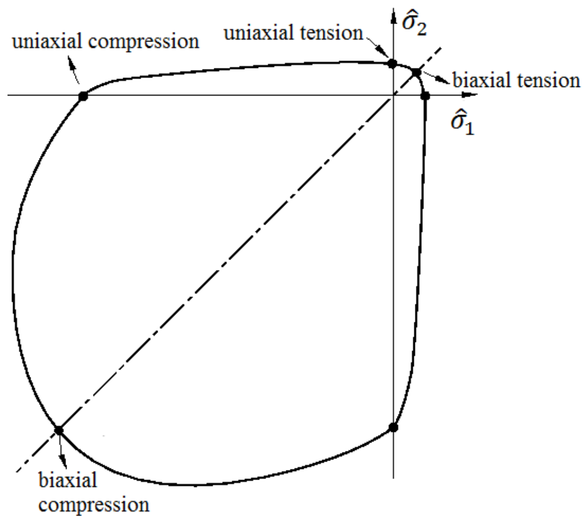

Figure 4-6. Yield surface under plane stress condition [192]

CDP model consists of combination of isotropic damage evolution and isotropic tensile and compressive plasticity to simulate inelastic behavior of concrete. It allows to incorporate strain hardening in compression, strain stiffening in tension, and uncoupled damage initiation and accumulation in tension and compression. CDP uses a non-associated flow rule with the help of a plastic potential. CDP model assumes two main failure mechanisms; tensile cracking and compressive crushing of concrete. The evolution of yield (or failure) surface is controlled by two hardening parameters (equivalent plastic strains), which are linked to failure mechanisms under tension and compression loading, respectively. In order to define CDP model, a set of material properties including compression hardening, tension stiffening, elastic modulus, poison's ratio, and density needs to be input for analysis [113,130,131,192]. These parameters can be determined through various material property tests.

4.2.3 Parameters for Modeling UHPC Behavior

Five parameters relating to plasticity response in UHPC, namely σ_{b0}/σ_{c0}, k_c, ψ, ξ, μ, are required to define CDP model. Two parameters of σ_{b0}/σ_{c0} and k_c modify the yield surface. σ_{b0}/σ_{c0} is the ratio of biaxial compressive strength to uniaxial compressive strength which influences the yield surface in a plane stress state and the parameter k_c is the ratio between distances measured from the hydrostatic axis to tensile and compressive meridians and is used to define the shape of the failure surface in deviatoric plane. The other two parameters, ψ and ξ modify the non-associated potential flow. ψ is the dilation angle which describes the angle of inclination of the failure surface towards the hydrostatic axis measured in the meridional plane. ξ is an eccentricity parameter which controls the deviation of the hyperbolic plastic potential from its asymptote. μ is the viscosity parameter which is used for the visco-plastic regularization of the concrete constitutive equations [62,130,131,192]. These five parameters, $\sigma_{b0}/\sigma_{c0}, k_c, \psi, \xi, \mu,$ are selected to be 1.05, 2/3, 30, 0.1, 1E-4, respectively, according to the literature and sensitivity analysis in this study as shown in Table 4-2 [62,131,196,197]. In addition, poison ratio of UHPC (or UHPFRC) were considered to be 0.2 according to AFGC [25]. Density of UHPC (or UHPFRC) was measured to be $2565 kg/m^3$ [159].

Table 4-2. Parameters to define damage plasticity model for UHPC

Parameter	Value
ψ	30
σ_{b0}/σ_{c0}	1.05
k_c	2/3
ξ	0.1
μ	1E-4

CDP model adopted for UHPC and UHPFRC accounts for tension and compression stiffness degradation which is given in terms of scalar degradation variables. The degradation variables are increasing functions of the plastic strains which get more pronounced with increase in plastic strain. These variables capture degradation in material stiffness with increased loading, which are zero for an undamaged state and unity (=1) for a complete damage state.

The damage parameter in tension is assumed to get activated after reaching peak tensile strength. Therefore, damage contours replicate tensile cracking and the extent of damage increases with increase in strain at higher load levels (crack widening). In order to account for reduction in stiffness due to cracking, tension damage parameter (Eq. (4-9)) is incorporated in the finite element model. This assumes that the tension damage variable is a function of the plastic strain which is zero (no damage) at zero plastic strain. The stiffness degradation in compression is also included in the CDP model as Eq. (4-10) [62,113,130].

$$d_t = 1 - \frac{\sigma_t}{f_t} \tag{4-9}$$

$$d_c = 1 - \left[\frac{\sigma_c/E}{0.2\varepsilon_c^{in} + \sigma_c/E}\right] \tag{4-10}$$

wherein σ_t, f_t, σ_c, E, and σ_c are tensile stress, tensile strength, elastic modulus, and compressive stress, respectively.

4.2.4 Compressive Behavior of UHPC

There is limited test data and associated relations for tracing uniaxial compressive stress-strain behavior of UHPC and UHPFRC. A material model that can relate stress-strain behavior of UHPC (or UHPFRC) to compressive strength and modulus of elasticity is developed for undertaking detailed analysis of UHPC and UHPFRC structures.

The uniaxial stress-strain response of UHPFRC can be approximated with a quad-part model that include softening branch as well. A schematic representation of the proposed model of stress-strain response of UHPFRC under compression is shown in Figure 4-7(a). UHPFRC under compression, unlike conventional concrete, exhibits nearly linear behaviour up to almost 70% of their compressive strength [72] (point 2 in Figure 4-7(a)). Compressive strength of UHPFRC which varies depending on fibre content and type, curing regime, mix design, etc. is to be determined by uniaxial compression test. The stress-strain response in this linear part can be defined by elastic modulus using Eq. (4-11). The linear part of stress strain response is followed by a nonlinear phase until peak stress is reached and can be represented using Eq. (4-12), which relates strain to stress by modulus and a reduction factor (α). This reduction factor (Eq. (4-13)), defines reduction of stress from linear elastic stress [72].

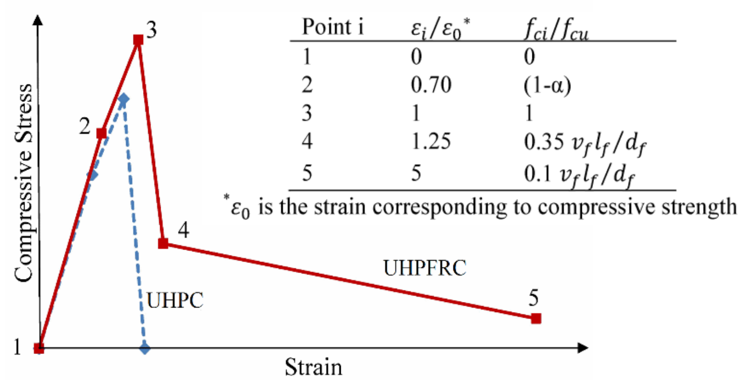

(a)

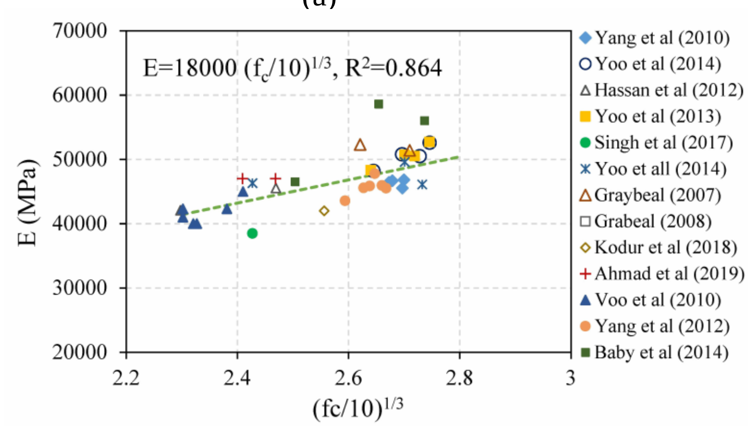

(b)

Figure 4-7. (a) Approximation for compressive stress-strain behavior of UHPC and UHPFRC, (b) Comparison of proposed equation for elastic modulus with test results

$$f_c = E\varepsilon \qquad for\ 0 < f_c < 0.70 f_c' \tag{4-11}$$

$$f_c = E\varepsilon(1-\alpha) \qquad for\ 0.70 f_c' < f_c < f_c' \tag{4-12}$$

in which α the reduction factor is given as:

$$\alpha = 0.001 e^{\frac{E\varepsilon}{0.243\, f_c'}} \tag{4-13}$$

where ε, E, f'_c, and α are compressive strain, elastic modulus, compressive strength, and reduction factor, respectively. Using data from literature [4,46,51,56,61,72,73,75,77,113,198], elastic modulus of UHPFRC is plotted as a function of $(\frac{f'_c}{10})^{(\frac{1}{3})}$ in Figure 4-7(b) and an empirical relation available in literature for calculating elastic modulus of high strength concrete [199] is modified for UHPFRC as:

$$E = 18000(\frac{f'_c}{10})^{(\frac{1}{3})} \tag{4-14}$$

The ascending branch of compressive stress strain response (1-2, and 2-3) is calculated using Eqs. (4-11) to (4-14). The descending branch (3-4, and 4-5), is obtained based on empirically derived parameters generated in experiments by Empelmann [3]. The relations to calculate these five key points based on fiber content (by volume) and fiber size (aspect ratio) are given in Figure 4-7(a). Where ε_0 is the strain corresponding to compressive strength and v_f, l_f, and d_f are fiber volume fraction, fiber length and diameter, respectively. Behavior of UHPC with no fibers is also linear up to 70% of compressive strength and it fails in brittle manner under compression (explosive) [200] as shown in Figure 4-7(a). Stress-strain response of UHPFRC based on parameters generated from two different experiments is plotted along with experimental stress-strain response in Figure 4-8. It shows a good agreement between predicted stress-strain response using proposed model and test data especially in ascending branch of response.

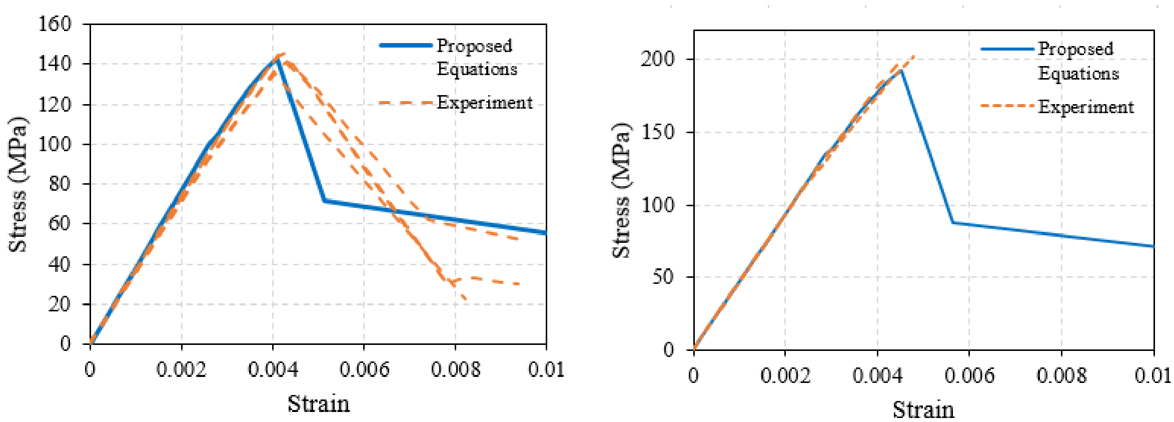

(a) Singh et al experiments [113] (b) this study

Figure 4-8. Comparison of the proposed compressive stress-strain approximation with test results

4.2.5 Tensile Behavior of UHPC

To fully capture the beneficial effects of UHPFRC, tensile behavior of UHPFRC needs to be properly modelled in pre and post cracking zones. For this, uniaxial stress strain response in tension is required to evaluate the hardening/softening behavior of the concrete.

Behavior of UHPC without fibers under tension after cracking is brittle and does not exhibit strain hardening and a significant descending branch [200] as shown in Figure 4-9(a). However, the fibers present in UHPFRC induce significant bridging stress between open crack faces. This bridging stress between opened cracks faces leads to a relatively higher fracture toughness and ductility in UHPFRC. Therefore, it is essential that this fiber bridging mechanism is effectively incorporated in modeling tensile fracture of UHPFRC through stress-strain response in tension. Typical stress strain behavior of UHPFRC is idealized into three stages as shown in Figure 4-9(a) [88]. The initial part is linear elastic up to cracking stress of UHPFRC, which is followed by strain hardening part accompanied by initiation of multiple cracking facilitated by fiber bridging. This is further followed by softening branch that presents crack opening with fiber bridging.

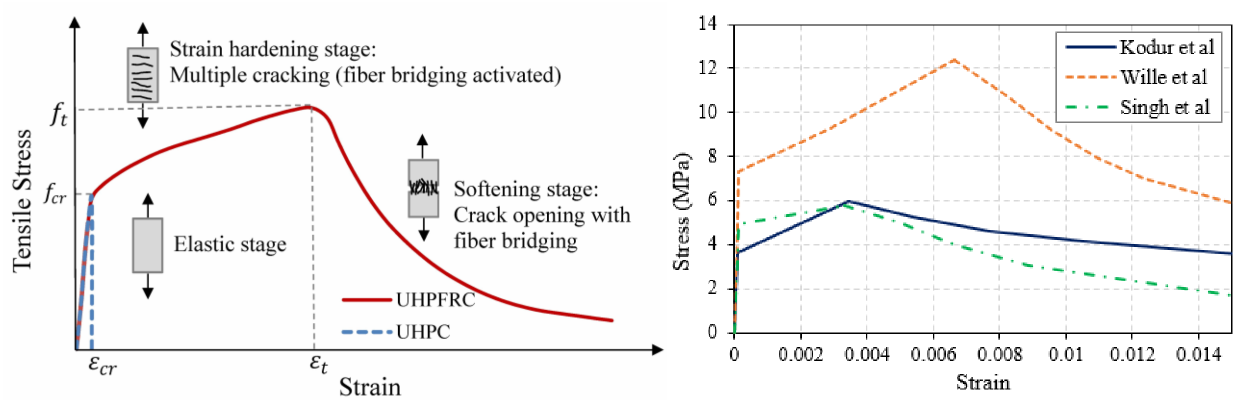

(a) Typical σ-ε response (b) σ-ε response from test data

Figure 4-9. Tensile stress strain response of UHPFRC

Tensile behavior of UHPFRC specimens cast as part of this study [159] as well as test data of UHPFRC specimens by Sing et al [113] and Wille et al [88] under direct tension is presented in Figure 4-9(b). It can be seen that there is significant variation in tensile stress-strain response of UHPFRC with different mix, fiber type, volume fraction, and distribution. Since the shape of tensile stress-strain response of UHPFRC is highly influenced by various factors such as characteristic strength of the concrete matrix, fiber type, orientation and distribution of fibers, fiber aspect-ratio and fiber content (by volume). The key points of stress strain response, namely cracking, peak, and ultimate points are to be evaluated from direct tension tests. In addition, uniaxial tensile strength can be calculated through flexural tests on concrete prisms. However, flexural capacity alone cannot be utilized to describe the complete fracture mechanism. Therefore, inverse analysis is to be conducted to develop a tensile fracture model for UHPFRC from flexural tests [1,2,4,51,85].

4.2.6 Material Model for Steel reinforcement

A metal plasticity model that utilizes Mises yield surface with associated plastic flow and isotropic hardening available in ABAQUS [192] was adopted for the constitutive modelling of reinforcing steel. The stress strain response of steel reinforcement under tension and compression consisting of three phases of linear elastic, yield plateau, and strain hardening as shown in Figure 4-10 was incorporated in the model. The strain hardening part of stress strain curve can be calculated using Eq. (4-15) [201].

$$f = fy\left[\frac{f_u}{fy} - 0.5\left(\frac{\varepsilon_u - \varepsilon}{\varepsilon_u - \varepsilon_{sh}}\right)^2\right] \tag{4-15}$$

where f_y, f_u, ε_{sh}, and ε_u are yield stress, ultimate stress, strain at end of plateau part, and ultimate strain, respectively.

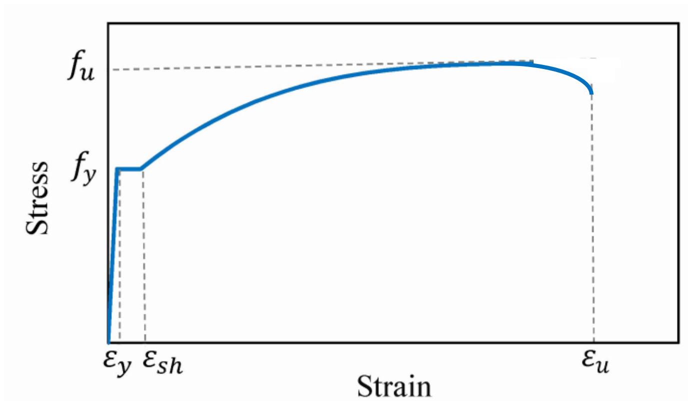

Figure 4-10. Stress-strain response of reinforcing steel bar

4.2.7 Bond-Slip Behavior of UHPC

Number of researchers have investigated bond behavior of steel reinforcement with UHPC. These authors reported that the average bond strength of steel bars embedded in UHPC to be about 10 times higher than that of steel bars placed in conventional concrete [56,153]. UHPFRC provides a strain hardening behavior in concrete after first cracking and enhances post-cracking behavior. This improved tensile behavior generates high and quasi-uniform tensile stresses in concrete surrounding reinforcing that efficiently counterbalance the radial bursting pressure. Therefore, it provides better bond performance as compared to conventional concrete.

The modified CMR [202] model proposed by Yoo et al [56] for UHPC and UHPFRC with varying fiber content was utilized to define bond behavior of steel bars embedded in concrete to incorporate local bond effects in numerical models for tracing response of UHPFRC beams. The CMR model is defined in Eqs. (4-16) and (4-17), where τ and τ_{max} are bond stress and bond strength respectively. s_r and β are the coefficients based on curve fitting of experimental results on UHPC and UHPFRC which were adopted as 0.07, and 0.8, respectively.

$$\tau = \tau_{max}(1 - e^{-s/s_r})^{\beta} \tag{4-16}$$

$$\tau_{max} = 5.0\, f_c'^{0.5} \tag{4-17}$$

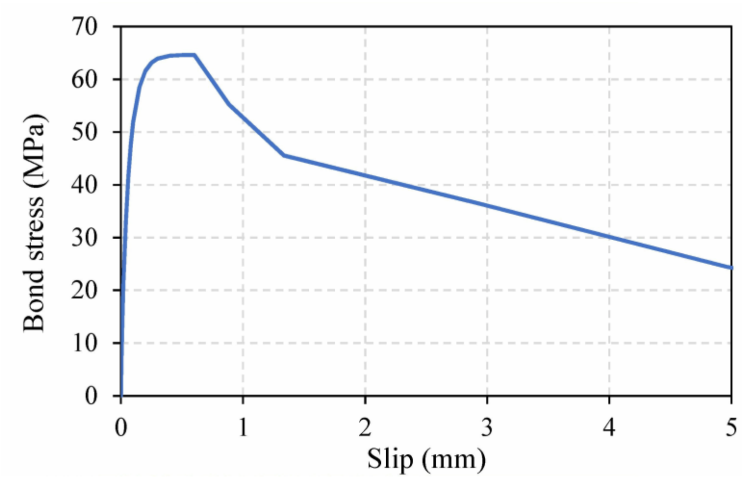

Figure 4-11. Bond stress-slip response of steel reinforcement in UHPFRC

4.3 Analysis Details

Since UHPFRC beams, owing to high ductility, undergo large deflections (as compared to beams made of conventional concrete or plain UHPC), the effect of geometric non-linearity is to be given due consideration in the analysis. This is accounted for in the numerical model through updated Lagrangian method [192]. Newton–Raphson solution technique is adopted and a tolerance limit of 0.5% of average force specified to meet convergence criterion at each load increment [203]. The analysis is carried out in small displacement increments, which are automatically chosen by ABAQUS. An optimum mesh size was arrived by carrying out a parametric study with different mesh sizes and a mesh size of 25mm was able to predict good post yield response in the beams selected for validation.

4.4 Modeling Interfacial Bond between Rebar and Concrete

The interfacial bond between reinforcement and concrete can be accounted for through explicit modeling of both reinforcement ribs and the concrete lugs [204]. Alternatively, local bond-slip can be modeled as bond-link elements which provides a reasonable compromise between accuracy and computational efficiency [193].

In bond-link element approach, the concrete and the reinforcing steel are represented by two different sets of elements, and node pairs at the interface are connected using interfacial spring elements. Three spring elements are modeled at each node pair, wherein one spring represents shear bond behavior according to a bond-slip relationship. This bond-slip is related to longitudinal axis direction. The other two springs represent the bond behavior in the normal directions which are assumed to be rigid by assigning large spring stiffness to the normal springs [193]. It is assumed that the slip between reinforcing steel and concrete is related only to the longitudinal axis direction. The bond force (F) between the concrete and reinforcing steel bar for the bond element is obtained by multiplying contact area between reinforcing bar and concrete (A), and average bond stress between concrete and steel reinforcement (τ). Contact area of rebar and concrete can be calculated using equation where P is perimeter of the steel reinforcing bar and L is length of rebar between nodes connected to bond elements (see Eqs. 4-18 and 4-19).

$$F = A\tau \tag{4-18}$$

$$A = PL \tag{4-19}$$

The bond stress-slip response of streel bars in UHPFRC in this study is shown in Figure 4-11. The bond force between the concrete and reinforcing steel bar for the bond element is obtained by multiplying contact area between reinforcing bar and concrete and average bond stress developed at the concrete and steel reinforcement interface.

4.5 Model Validation

The above developed finite element model is validated by analyzing a set of UHPC and UHPFRC beams tested in the laboratory [5,49,61,113,159]. In order to gauge efficacy of the model in predicting detailed structural behavior of UHPC and UHPFRC beams, predictions from the model, including load-deflection response, load-strain response, load capacity, and tensile damage (cracking), are compared with experimental results and test observations.

4.5.1 Selected Beams for Validation

Seven UHPFRC beams, designated as U-B3 to U-B9 were fabricated and tested for tracing flexural and shear response of beams. Two of these beams (U-B3 and U-B5) were tested under two point loads to simulate pure bending between points of load application as shown in Figure 4-12. Five other beams (U-B4 to U-B9) were subjected to dominant shear loading through applying a single point load at the distance of 610 mm from support (see Figure 4-12). Details of these beams are given in Chapter 3.

In addition, data from tests on UHPC and UHPFRC beams conducted by Yoo and Yoon [49], Yang et al. [5], and Singh et al [113] were utilized to validate the model. Details of these beams are presented in Figure 4-12. Additional details on experiments, including arrangement of reinforcing bars, loading set-up, and material properties can be found in relevant references [49,61,113,159]. The compressive strength of UHPC and UHPFRC cylinders reported by authors were used to define compressive stress strain response as proposed in section 4.2.4. Properties of concrete in tension were based on results of the tests conducted under direct tension. Stress strain response of reinforcement bars were calculated using Eq. (4-15) based on reported yield and ultimate stress of the reinforcement.

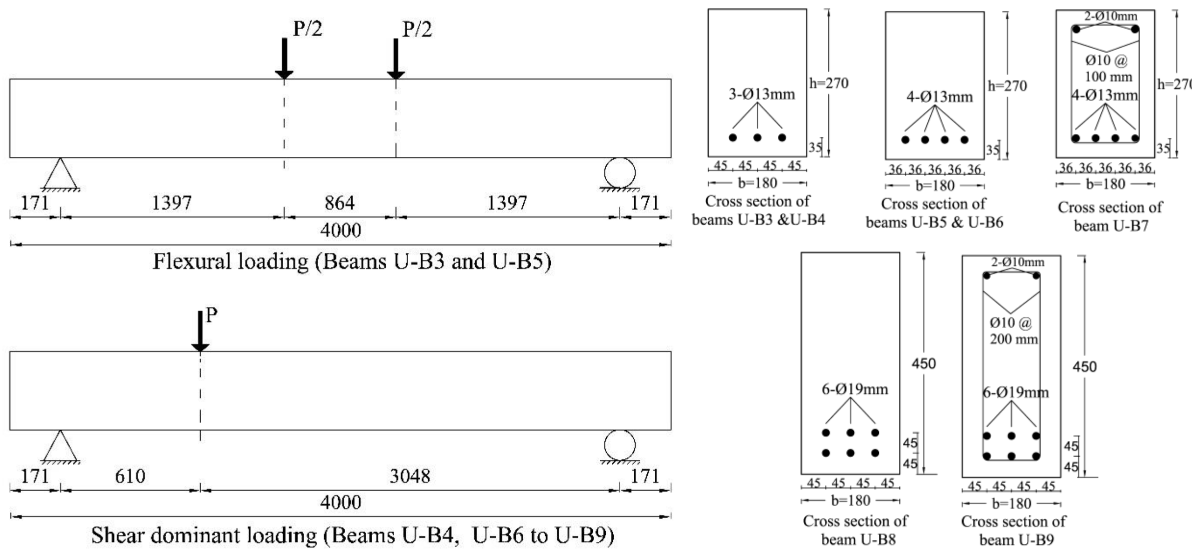

Figure 4-12. Loading conditions, layout and cross section of tested UHPFRC beams

Table 4-3. Details of the beams used for validation and comparison of load carrying capacity of UHPC beams as predicted by FEA with test data

Beams	Vf (%)	Width (mm)	Depth (mm)	Span (mm)	ρt (%)	ρc (%)	ρv (%)	Loading condition	Peak load (kN)		Ratio (1)/(2)
									FEA (1)	Test (2)	
U-B3	1.5	180	270	3658	0.90	0	0	4-point	94.9	97.1	0.98
U-B4	1.5	180	270	3658	0.90	0	0	3-point	140.1	142.1	0.99
U-B5	1.5	180	270	3658	1.20	0	0	4-point	121.6	126.6	0.96
U-B6	1.5	180	270	3658	1.20	0	0	3-point	163.5	177.1	0.92
U-B7	1.5	180	270	3658	1.20	0.34	0.79	3-point	163.2	180.3	0.91
U-B8	1.5	180	450	3658	2.48	0	0	3-point	664.9	740.7	0.90
U-B9	1.5	180	450	3658	2.48	0.21	0.40	3-point	724.9	790.1	0.92
B15-1	2.25	150	150	1350	2.31	2.31	0.42	3-point	95.9	106.4	0.90
B25	2.25	250	250	3250	1.80	0.30	0.70	4-point	163.3	171.7	0.95
R13	2	180	270	2700	0.90	0	0	4-point	190.4	188.9	1.01
R14	2	180	270	2700	1.20	0	0	4-point	210.5	205.2	1.03
ρ0.94%-S13	2	150	220	2200	0.94	0.59	1.31	4-point	82.5	86.5	0.95
ρ0.94%-NF	0	150	220	2200	1.50	0.59	1.31	4-point	64.0	62.6	1.02

ρ_t, ρ_c, and ρ_v are longitudinal tensile, longitudinal compressive, and shear reinforcement

4.5.2 Comparison of Response Parameters

4.5.2.1 Load-Deflection Response

To establish the validity of the model, a number of tested UHPC and UHPFRC beams, as listed in Table 4-3, with different geometric, material, and loading characteristics, were analyzed and predicted load-deflection response of the beams are compared with measured data from experiments. Figure 4-13(a and b) show load-deflection response of beams U-B4 and U-B5 [159] with different reinforcement ratios tested under different loading configurations (dominant shear and flexure), while Figure 4-13(c and d) shows load deflection of beams ρ0.94%-NF and B25 [49,113] with different fiber volume fractions (0, and 2.25%). It can be seen from the overall trends that the predictions from the numerical model compares well with measured data in all four stages i.e., linear elastic stage until initiation of tensile cracking, post-cracking stage with progression of enhanced cracking, onset of yielding in steel reinforcement, and plastic deformation stage including softening till failure in both cases of UHPC and UHPFRC beams. It should be noted that similar comparisons were made for other beams tested by various researchers and very good comparisons were obtained (see Table 4-3). However, the figures showing comparative load-deflection response are not included due to space limitations.

Moreover, the developed model predicts response well for both UHPC and UHPFRC beams under different loading conditions i.e. flexural and dominant shear loading. Only, in post cracking stage, model predictions are slightly stiffer than experimental results. This difference can be attributed to possible cracks developing in concrete due to dry shrinkage and environmental effects, which resulted in softer response in tests. Also, UHPFRC beams with higher reinforcement ratio as compared to similar beams with lower reinforcement ratio (beams U-B5 and U-B6 as compared to beams U-B3 and U-B4), exhibited higher strain hardening in experiments as compared to finite element model predictions. This can be attributed to slight variations in the stress-strain curve adopted for reinforcing steel, which gets more pronounced in load-deflection response at higher reinforcement ratios.

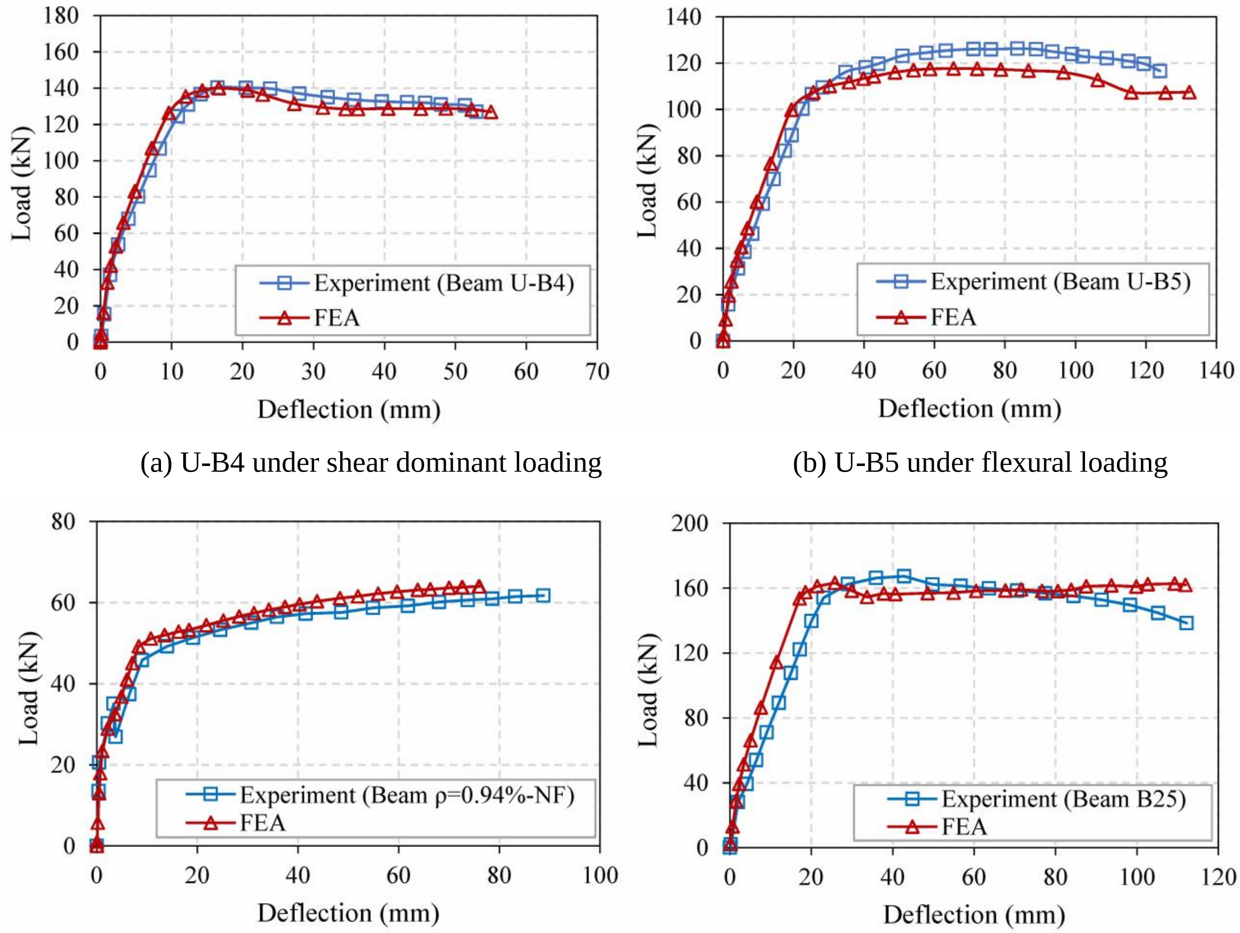

(a) U-B4 under shear dominant loading

(b) U-B5 under flexural loading

(c) UHPC beam (ρ=0.94%-NF) [49]

(d) UHPFRC beam (B25) [113]

Figure 4-13. Comparison of load deflection response of UHPFRC beams under different loading conditions and with different fiber volume fractions

In addition to load-deflection response, the failure load of the beams, as predicted from FEA, is compared with measured peak loads from experiments in Table 4-3. A ratio of unity (=1) indicates perfect agreement, while less than unity and higher than unity are conservative and unconservative predictions, respectively. Ratio of total load carrying capacity (P) from model to that of measured values in tests ranges from 0.90 to 1.03 for analyzed UHPC and UHPFRC beams, indicating good capability of the model to capture failure load.

The model is also capable of evaluating the bond developed at rebar interface at different stages of loading. The bond developed between steel reinforcement and concrete in beams U-B5 and U-B6 (subjected to flexural and dominant shear loading) is plotted in Figure 4-14. It can be seen that the bond stress increased from about 0.4 MPa, just prior to cracking initiated in the beams, to a stress of about 5.5 MPa at failure. The maximum bond stress in beams U-B5 and U-B6 developed at critical section of the beams i.e. under load points.

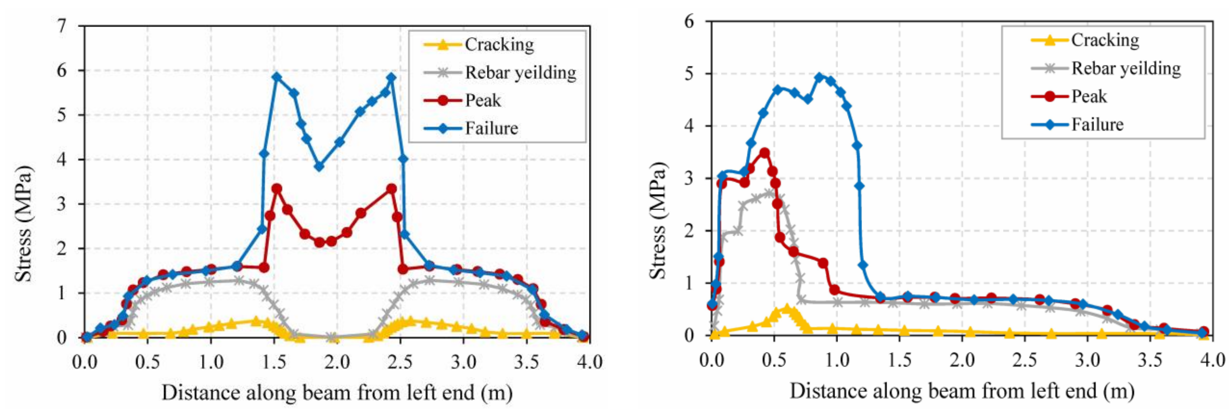

(a) Beam U-B5 (b) Beam U-B6

Figure 4-14. Level of bond stress developed in beams U-B5 and U-B6 along the beam length

4.5.2.2 Load-Strain Response

To illustrate the capability of model in capturing the local behavior of UHPFRC beams, predicted load-longitudinal strains on reinforcing bar and concrete layers at critical section of beams U-B3 and U-B4 [159] are compared with measured strains from tests in Figure 4-15. A negative strain in the figure indicates that the material is in compressive state while positive strain indicates the presence of tensile state. Strain predictions are plotted until strain gauges stopped recording strains reliably due to cracks developing at the location of strain gauge. The trends in the plots show that predicted strains from the model are in good agreement with measured strains from tests. However strain response in post cracking regions is stiffer from the model as compared to measured values. This difference between numerical predictions and measured data in tests can be attributed to slight variations arising from difference in the material models, as well as any experimental discrepancies arising from level of bonding between strain gauges and concrete or reinforcing bars.

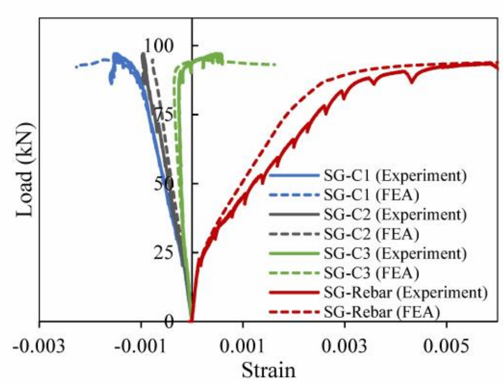

(a) Beam U-B3

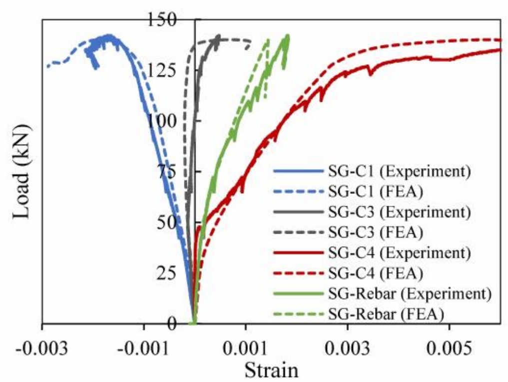

(b) Beam U-B4

Figure 4-15. Comparison of load-strain response in bars and concrete at critical section of beams, as obtained from FEA and tests

4.5.2.3 Crack Propagation and Failure Mode

The developed numerical model is also capable of capturing crack propagation through tracing scalar tensile damage parameter. This damage parameter in tension gets activated after concrete attains its peak tensile strength. Therefore, damage contours replicate tensile cracking and the extent of damage increases with increase in strain resulting at higher load levels (crack widening). In other words, tensile damage parameter of 0 (zero) represents no tension damage, while a value of 1 (unity) represents complete damage state. Direction of cracking can be represented using direction of principal strain being perpendicular to crack direction.

Tensile damage contours and crack direction obtained through FEA along with experimental results are illustrated in Figure 4-16 for beams U-B5 and U-B6, subjected to different loading configurations. In beam U-B5, under flexural loading, flexural cracks initiated at load level of 28 kN at extreme tension fibers of the beam. These flexural cracks developed at the zone between loading points which is under pure bending. At a load level of 86 kN, this tensile damage propagated towards compression zone (till mid depth of the beam) as shown in Figure 4-16(a). Direction of principal strain generated from the model confirms propagation of flexural cracks. This type of cracking behavior was observed in the experiment, also can be seen in Figure 4-16(a). With increasing load, at P=108 kN which is close to failure load, greater depth of the beam was subjected to tensile damage. This clearly infers propagation of cracking towards compression zone with increasing load levels as observed in the tests (Figure 4-16(a)). The tension damage contour generated through FEA indicate that maximum tension damage, close to failure, is concentrated at the critical section of the beam which matches with the progression of macro crack as seen during the test. It should be noted that a higher value of the tensile damage parameter indicates a greater level of tensile damage (cracking).

In the case of UHPFRC beam U-B6, under dominant shear loading, tensile damage got initiated at extreme tension fibers at a load level of 40 kN and this resulted from tensile stress exceeding the tensile strength of concrete. This initial tensile damage (cracking) was confined to zone between the load point and mid-span and was mainly in the form of flexural cracks in lower depth of the beam. When the load on the beam increased to 137 kN, these flexural cracks propagated towards compression zone (upper depth). Further, additional flexural-shear cracks developed in the shear span as shown in Figure 4-16(b). The tensile damage contour and principal direction shown in Figure 4-16(b) match well with crack pattern observed during tests. As the load increased further to 155 kN (just prior to failure), shear stresses in the shear span increased significantly and shear cracks became much more predominant. In other words, maximum principal stresses in shear span exceeded tensile capacity of UHPFRC. Model predictions also show that as the load level approached failure load, tensile damage further propagated towards compression zone and more cracks got initiated and propagated further into the shear span. The predicted tensile damage and principal direction in the shear span of the beam U-B6 (between left support and loading point) close to failure and cracking pattern observed in experiment are compared in Figure 4-16(b). The predicted direction of principal strains in shear span matches well with direction of the major diagonal tension crack (which is perpendicular to principal direction) observed in the experiment.

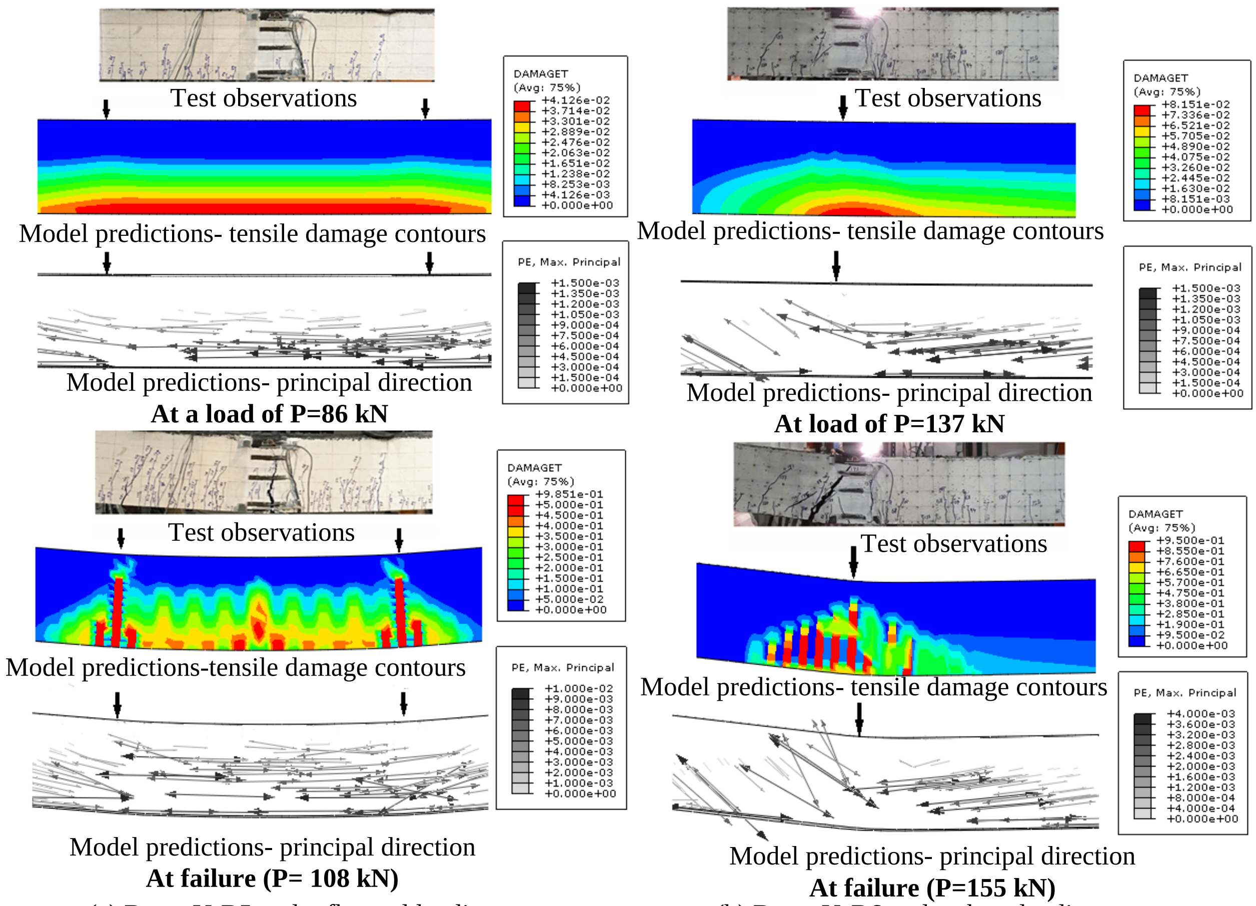

(a) Beam U-B5 under flexural loading

(b) Beam U-B6 under shear loading

Figure 4-16. Comparison of tensile damage contours and principal strain direction as predicted by FEA with test data

4.6 Concrete and Stirrups Contribution to Shear Capacity

Flexural resistance of UHPFRC beams that comes from tensile resistance of steel bars and concrete compressive and tensile resistance can be evaluated using sectional analysis approach. UHPFRC possesses high tensile strength and ductile characteristics (high ultimate tensile strain), and this can be utilized to realize high shear capacity in UHPFRC beams. This high shear resistance of UHPFRC beams mainly arises from shear resistance of uncracked concrete, and vertical component of the interface shear resistance (due to aggregate interlock and presence of steel fibers). The developed model can be applied to gauge contribution of different components of the shear resistance in the beams and also to explore the feasibility of removing shear reinforcement in UHPFRC beams.

Behavior of tested UHPFRC beams U-B4 and U-B6, provided with shear reinforcement, were analyzed under dominant shear loading using the above developed numerical model. Moreover, for comparative study, NSC beams with the same cross sectional details as U-B4 and U-B6, as shown in Figure 4-12, were modeled under dominant shear loading. The material model for NSC recommended in ABAQUS documentation [192] were incorporated into the model for analyzing NSC beams.

Predicted load-deflection response of NSC beams, with different longitudinal tensile reinforcement ratios (i.e. ρ_t=0.90% and ρ_t=1.20%) with and without stirrups, is shown Figure 4-17(a and b). As can be seen in the figure, the load carrying capacity in the NSC beams, with tensile reinforcement ratio of 0.90% and 1.20%, reduces by 14% and 15% when the stirrups are removed. In addition, NSC beams without shear reinforcement, exhibited significant reduction of stiffness after reaching peak load, as compared to the beams provided by stirrups.

Also, stress distribution developed along the tensile reinforcement bars in NSC beams, with and without stirrups, at peak load level is shown in Figure 4-18(a and b). The comparative trends indicate that reinforcing bars in NSC beam, provided with stirrups, yielded as opposed to NSC beam with no stirrups; in other words, the beam with stirrups reached its ultimate moment capacity. However NSC beam without stirrups failed in shear before reaching ultimate moment capacity (see Figure 4-18 a and b).

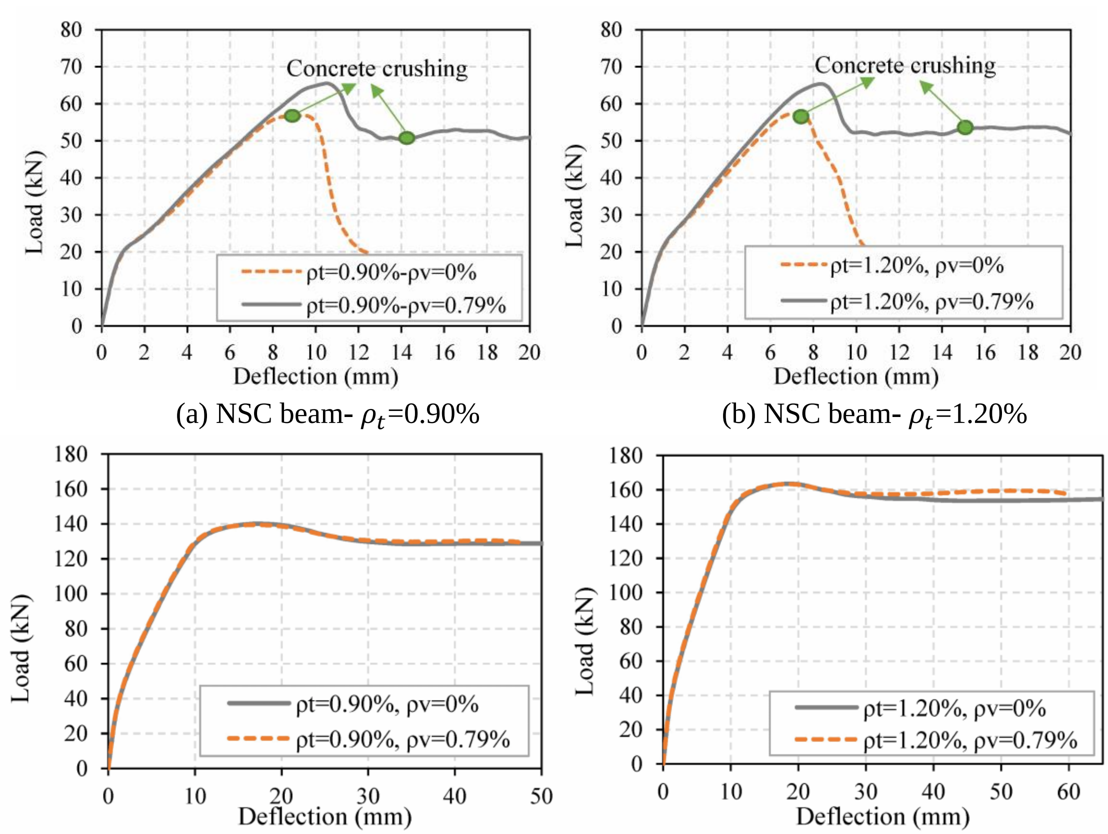

(a) NSC beam- ρ_t=0.90%   (b) NSC beam- ρ_t=1.20%

(c) UHPFRC beam-ρ_t=0.90%   (d) UHPFRC beam-ρ_t=1.20%

Figure 4-17. Load deflection response of NSC and UHPFRC beams (with cross section similar to U-B4 and U-B6) with reinforcement ratios of 0.90% and 1.20% with and without stirrups

The behavior of UHPFRC beams having same configurations as that of U-B4 and U-B6 were analyzed under two cases; one with stirrups and the other one without stirrups. The load-deflection response of UHPFRC beams with and without shear reinforcement are compared in Figure 4-17(c and d). It can be seen that removing stirrups did not affect overall structural response of the beams in terms of load carrying capacity and ductility. This was also confirmed with experimental data generated from tests on beams U-B3 to U-B6. Beams U-B4 and U-B6, with no shear reinforcement reached their ultimate moment capacity under dominant shear loading.

The stress developed in longitudinal bars in UHPFRC beam (similar to U-B4) with and without stirrups is presented in Figure 4-18(c and d). In both cases, UHPFRC beam with and without stirrups, bars yielded. In other words, unlike NSC beams, UHPFRC beams without stirrups, do not experience abrupt failure before yielding in the reinforcing bars and this is owing to higher tensile strength and ultimate strain of UHPFRC that develops due to bridging effect facilitated by presence of steel fibers.

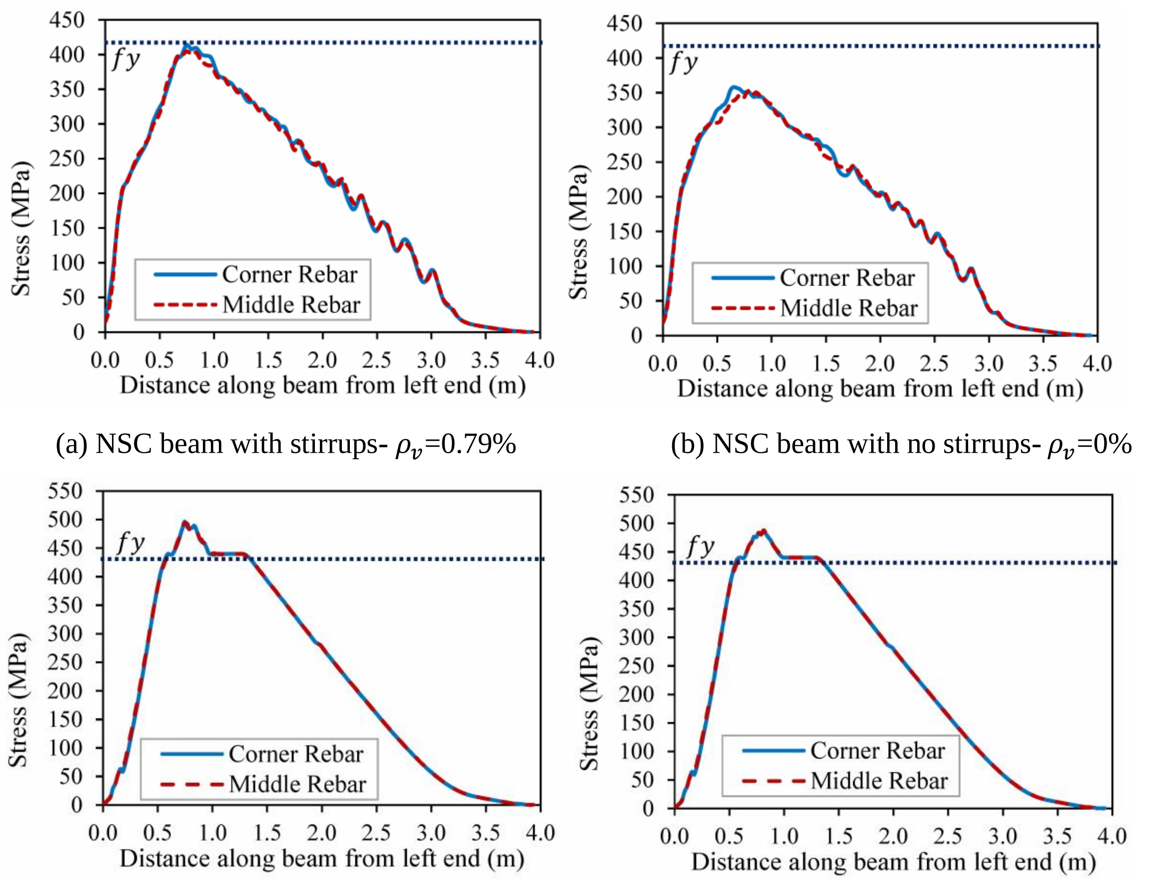

(a) NSC beam with stirrups- ρ_v=0.79%

(b) NSC beam with no stirrups- ρ_v=0%

(c) UHPFRC beam with stirrups- ρ_v=0.79%

(d) UHPFRC beam with no stirrups- ρ_v=0%

Figure 4-18. Stress distribution in longitudinal reinforcing bars in NSC and UHPFRC beams (with cross section similar to U-B4- ρ_t=0.90%) along the beam length

The contribution of different components to shear capacity of NSC and UHPFRC beams was quantified to determine the extent of contribution from UHPFRC and stirrups. For this purpose, the stirrups crossing crack surface, which were in tension as compared to other stirrups, were identified. The contribution of stirrups to shear strength (Vs) was calculated using the tensile stress developed in the stirrups of two NSC and UHPFRC beams. In the case of a NSC beam contribution of stirrups to shear resistance, which was small till cracking, increased after first cracking and reached to about 90% of total shear capacity at peak state. However, in the case of a UHPFRC beam, shear resistance of the beam resulted mostly from contribution of concrete (Vc) and stirrups did not contribute to shear capacity of the beam as shown in Figure 4-19.

Contribution of concrete to shear strength comprises of contribution of uncracked concrete in compression (from compression block of concrete), and resistance arising from fiber bridging and aggregate interlock across cracked concrete. It should be noted that in the case of slender steel fiber reinforced concrete beams without stirrups, and underreinforced beams, dowel action contribution can be neglected [205].

Therefore, to quantify the contribution of uncracked concrete (Vcc) to shear resistance, model prediction is used to identify the region above the neutral axis which is in compression (see Figure 4-20). This region (compression block) is subjected to normal compressive and shear stresses. Therefore, the contribution of concrete to shear strength arising from compression block can be evaluated utilizing predicted shear stress in region above neutral axis. Once the contribution of uncracked concrete to shear capacity is determined, the remaining shear strength of concrete is attributed to interfacial shear resistance (Vi) which arises from aggregate interlock and fiber bridging as shown in Figure 4-20 [205].

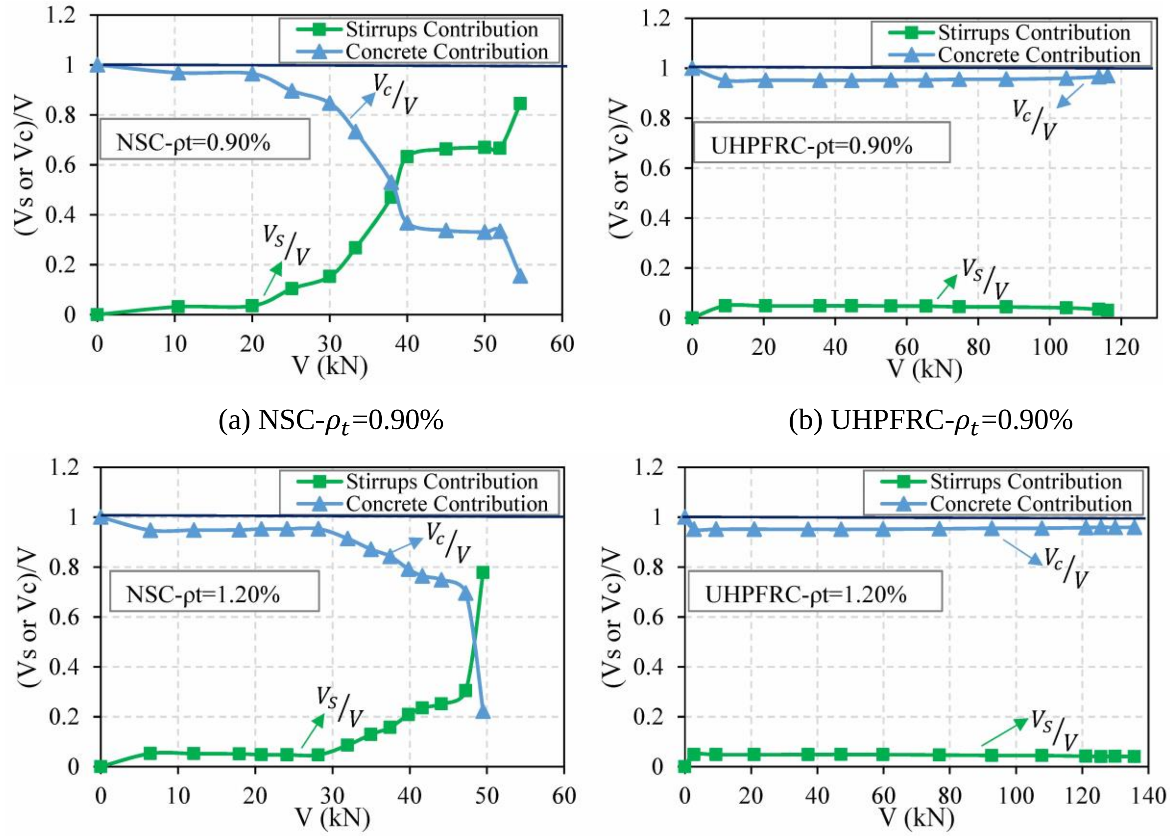

(a) NSC-ρ_t=0.90% (b) UHPFRC-ρ_t=0.90%

(c) NSC-ρ_t=1.20% (d) UHPFRC-ρ_t=1.20%

Figure 4-19. Concrete and stirrups contribution to shear capacity of NSC and UHPFRC beam with different reinforcement ratios (ρ_t=0.90% and ρ_t=1.20%)

In two UHPFRC beams without stirrups, U-B4 and U-B6, subjected to dominant shear loading, shear strength contribution from compression block (Vcc) and fiber bridging and aggregate interlock (Vi) is evaluated and presented in Table 4-3. The results show that 67% and 65% of shear capacity of these beams (U-B4 and U-B6) came from compression block (Vcc) at initial cracking stage. With increasing load level (at peak and failure load levels), cracks propagated more towards compression zone. Therefore, the contribution of compression block to shear capacity decreased as smaller depth of concrete was in compression. As can be seen in Table 4-4, with decreasing contribution of compression block (Vcc/V), interfacial shear resistance (Vi/V) which is due to fiber bridging and aggregate interlock at cracks surfaces increased. The reduction in contribution of compression block to shear resistance was higher in case of beam U-B6 as compared to beam U-B4. This is attributed to higher applied load in beam U-B6 as compared to beam U-B4 due to higher reinforcement ratio. Therefore, cracks propagated more towards compression zone in beam U-B6, and smaller depth of the beam was uncracked (in compression).

In addition, contribution of compression block and aggregate interlock to shear strength of NSC beams, having the same cross sectional details as beams U-B4 and U-B6 is quantified (see Table 4-4). The results show that NSC beams did not exhibit significant reduction in compression block contribution to shear strength (Vcc/V) with increasing load till peak state. In other words, contribution of interfacial shear resistance to shear capacity (Vi/V) did not increase, as opposed to UHPFRC beams wherein interfacial shear resistance (Vi/V) increased due to activation of fiber bridging.

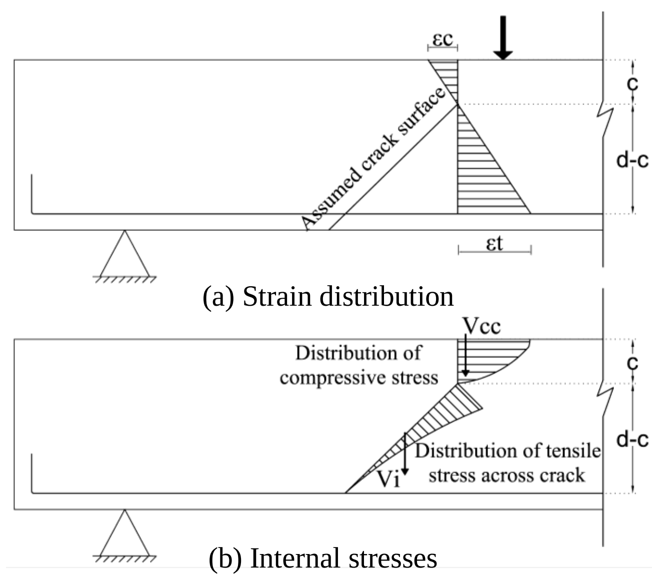

Figure 4-20. Schematic of an assumed strain distribution and internal stresses in shear span of a beam [205]

These analyses illustrate the usefulness of the developed model in determining the contribution of concrete and stirrups to shear capacity of beams. In UHPFRC beams, due to high tensile and compression strength of UHPFRC, concrete contribution to shear capacity is quite significant and until final stages of loading, stirrups do not play major role in resisting shear. Therefore, stirrups can be eliminated in many cases. This is in contrast to shear response of NSC beams wherein contribution of concrete to shear capacity decreases after the onset of cracks in beams, and thus the presence of stirrups are critical in resisting shear beyond cracking load levels.

Table 4-4. Contribution of compression block and interface resistance to shear strength

Beam	First Cracking			Peak state			Ultimate state (before failure)		
	V (kN)	Vcc/V	Vi/V	V (kN)	Vcc/V	Vi/V	V (kN)	Vcc/V	Vi/V
U-B4 (ρt=0.90%)	35.2	0.67	0.33	116.7	0.65	0.35	105.7	0.54	0.46
U-B6 (ρt=1.20%)	36.6	0.65	0.35	163.5	0.54	0.46	155.0	0.32	0.68
NSC (ρt=0.90%)	17.1	0.67	0.33	47.3	0.61	0.39	30.9	0.55	0.45
NSC (ρt=1.20%)	17.3	0.69	0.31	47.8	0.74	0.26	33.3	0.64	0.36

4.7 Summary

In order to predict moment curvature response of UHPFRC beams, an analytical approach was developed and the predictions were compared with experimental data. In addition, a finite element based numerical model was developed and validated against experimental data for tracing structural response of UHPFRC beams. Based on the results presented in this chapter the following conclusions can be drawn:

- An analytical method based on cross sectional analysis and strain compatibility using multi-layer approach can be used to predict flexural response of UHPFRC beams. A good agreement is achieved between the predicted and experimentally measured response parameters by incorporating strain hardening of UHPFRC and steel.
- UHPFRC exhibits significantly different mechanical properties as compared to conventional concrete. The proposed numerical model utilizing concrete damage

plasticity model with adjusted parameters is capable of adequately tracing the response of UHPFRC beams in the entire range of loading; from precracking stage till failure. The model predictions at global level (load-deflection response) and local level (load-strain response) of UHPFRC beams agree well with experimental data.

- The developed numerical model can accommodate various configurations in beams, including different loading patterns (flexure or shear), and different material characteristics such as presence of fibers, fibers volume fraction, and presence of shear reinforcement. Also, the model is capable of predicting contribution of stirrups and concrete (including compression block and interfacial shear strength) to shear capacity of UHPFRC beams. The model will be applied to undertake a set of parametric studies to evaluate the influence of various parameters on the response of UHPFRC beams.
- Tensile damage contour predictions along with principal direction, is an effective response parameter for tracing crack propagation zone and failure modes in UHPFRC beams.
- Removing stirrups does not result in reduction of ductility or load carrying capacity of UHPFRC beams. In other words, UHPFRC beams without shear reinforcement, subjected to dominant shear loading, can attain ultimate moment capacity, without experiencing brittle failure before rebar yielding. This behavior is in contrast to similar normal strength beams, which attain failure in shear mode well before reaching ultimate moment capacity. Also, stirrups do not contribute to shear capacity of UHPFRC beams unlike similar NSC beams that contribution of stirrups to shear resistance increases after first cracking.

CHAPTER 5

5 PARAMETRIC STUDIES

The developed finite element model was applied to undertake a set of parametric studies to evaluate different factors influencing response of UHPFRC beams. The varied parameters included fiber volume fraction in UHPFRC, longitudinal reinforcement ratio, loading type, and shear span to depth ratio. High shear resistance of UHPFRC due to high tensile strength, strain hardening after cracking, and fiber bridging makes it possible to eliminate stirrups in design of UHPFRC beams. Therefore, in addition to mentioned variables, effect of presence of shear reinforcement and also its spacing was studied. Further, predictions from the model was used to evaluate shear resisting mechanisms of arch and beam action in UHPFRC beams. Also, the developed moment curvature analytical model was utilized to evaluate effect of the noted parameters on flexural capacity of UHPFRC beams.

5.1 Selection of Beams and Range of Parameters

The structural response of UHPC beams is influenced by a number of factors such as fiber volume fraction, longitudinal reinforcement ratio, presence of shear reinforcement, and shear span to depth ratio. In this study, rectangular beams with width and depth of 150 mm and 300 mm were selected based on best practice documents and these beams were analyzed using developed model. The clear span of the beams were selected to be 5000 mm as shown in Figure 4-5. The variables for this parametric studies were the governing factors of shear span to depth ratio, fiber volume fraction, longitudinal reinforcement ratio, and shear reinforcement ratio (or spacing). The beams were provided with different reinforcement ratios as shown in Table 5-1 to study the effect of longitudinal reinforcement ratio (ρ_t) on structural response of UHPC beams. The reinforcement ratio varied from 1.4 to 7.2%. It should be noted that the reinforcement ratio was increased upto 7.2% in order to induce shear failure in the beams. Shear reinforcement ratio (ρ_v) was varied from 0% to 1.32% with stirrups spacing (S) of 0.3d, 0.5d, and 0.75d. The rebars spacing, arrangment, and shear reinforcement were designed as per ACI-318 requirements for NSC beams [161].

Further, for each beam with different reinforcement ratio, UHPC with different fiber volume fractions (V_f) of 0, 1, 2, and 3 was considered to study the influence of presence and volume fraction of steel fibers. In this study, fibers were considered to be straight and with length and diameter of 13 mm and 0.2 mm, respectively. The material properties of UHPC with different fiber volume fractions were selected based on experiments and empirical expressions in literature [4,88].

The beams with mentioned variables were analyzed under dominant shear loading with different shear span to depth ratios of 1.5, 2, and 3. For applying shear dominant loading, as shown in Figure 4-5, a point load was applied on top surface of the beams at different distances (a) from the support. Also, flexural capacity of the beams were evaluated utilizing the developed moment-curvature analytical approach. All the variables considered in the parametric studies and their range are summarized in Table 5-1.

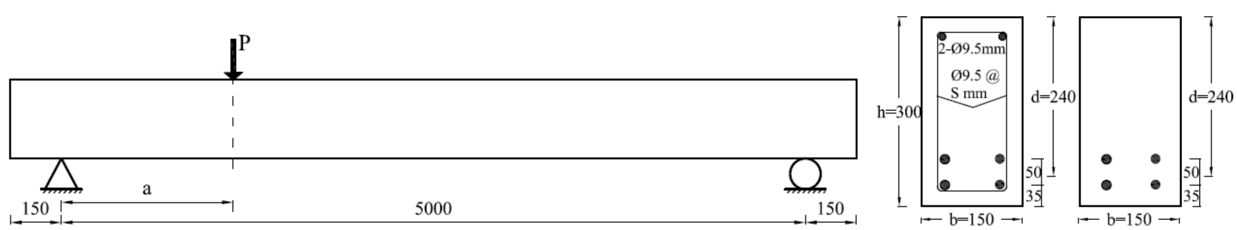

Figure 5-1. Details of the beams selected for parametric studies

Table 5-1. Range of parameters considered in parametric studies

Tensile bars	$\rho_t(\%)$	S	$\rho_v(\%)$	$V_f(\%)$	a/d
4 ϕ13	1.4	0.3d, 0.5d, 0.75d	0, 0.53, 0.79, 1.32	0, 1, 2, 3	1.5, 2, 3
4 ϕ15	2.2	0.3d, 0.5d, 0.75d	0, 0.53, 0.79, 1.32	0, 1, 2, 3	1.5, 2, 3
4 ϕ19	3.2	0.3d, 0.5d, 0.75d	0, 0.53, 0.79, 1.32	0, 1, 2, 3	1.5, 2, 3
4 ϕ22	4.3	0.3d, 0.5d, 0.75d	0, 0.53, 0.79, 1.32	0, 1, 2, 3	1.5, 2, 3
4 ϕ25	5.6	0.3d, 0.5d, 0.75d	0, 0.53, 0.79, 1.32	0, 1, 2, 3	1.5, 2, 3
6 ϕ28	7.2	0.3d, 0.5d, 0.75d	0, 0.53, 0.79, 1.32	0, 1, 2, 3	1.5, 2, 3

5.2 Analysis Details

As discussed in Chapter 4, the effect of geometric non-linearity was given consideration in the analysis since UHPFRC beams experience large deflections owing to high ductility. This was accounted for in the numerical model through updated Lagrangian method [192]. The Newton–Raphson solution technique was adopted and a tolerance limit of 0.5% of average force was applied to achieve convergence to a solution [203,206]. The optimum mesh size was selected by conducting set of parametric studies with different mesh sizes for beams utilized for validation.

The primary outputs generated at different stages of analyses are displacements (strains), applied load, and stresses. Shear and flexural capacity of the beams are evaluated using the maximum load predicted from the analyses. In addition, generated damage parameter contours, principal strain contours, and principal strain directions are utilized to predict cracking zone and direction, and failure modes in the analyzed beams. Also, the stresses developed in shear reinforcement are used to quantify contribution of stirrups to shear resistance. Finally, stresses developed in concrete and reinforcing bars are utilized to evaluate shear mechanisms (i.e. beam action and arch action) in the beams.

5.3 Effect of Longitudinal Reinforcement Ratio

First, flexural response of the beams in terms of moment curvature with different reinforcement ratios and fiber volume fractions were evaluated and the results are shown in Figure 5-2. Also, variation of maximum moment capacity of UHPC beams with different fiber volume fractions and longitudinal reinforcement ratio is also shown in Figure 5-3. As can be seen with increasing reinforcement ratio from 1.4% to 7.2%, moment capacity of the beams increases linearly. As an example, beam with fiber volume fraction of 2% and tensile bars ratio of 7.2% exhibits increased moment capacity by 150% as compared to beam with reinforcement ratio of 1.4%. The enhancement of moment capacity with increasing reinforcing bar ratio decreases with increasing fiber volume fraction. It should be noted that, in all the beams even with high reinforcement ratios, rebar yielding happens before concrete crushing confirming that the beams are not over reinforced.

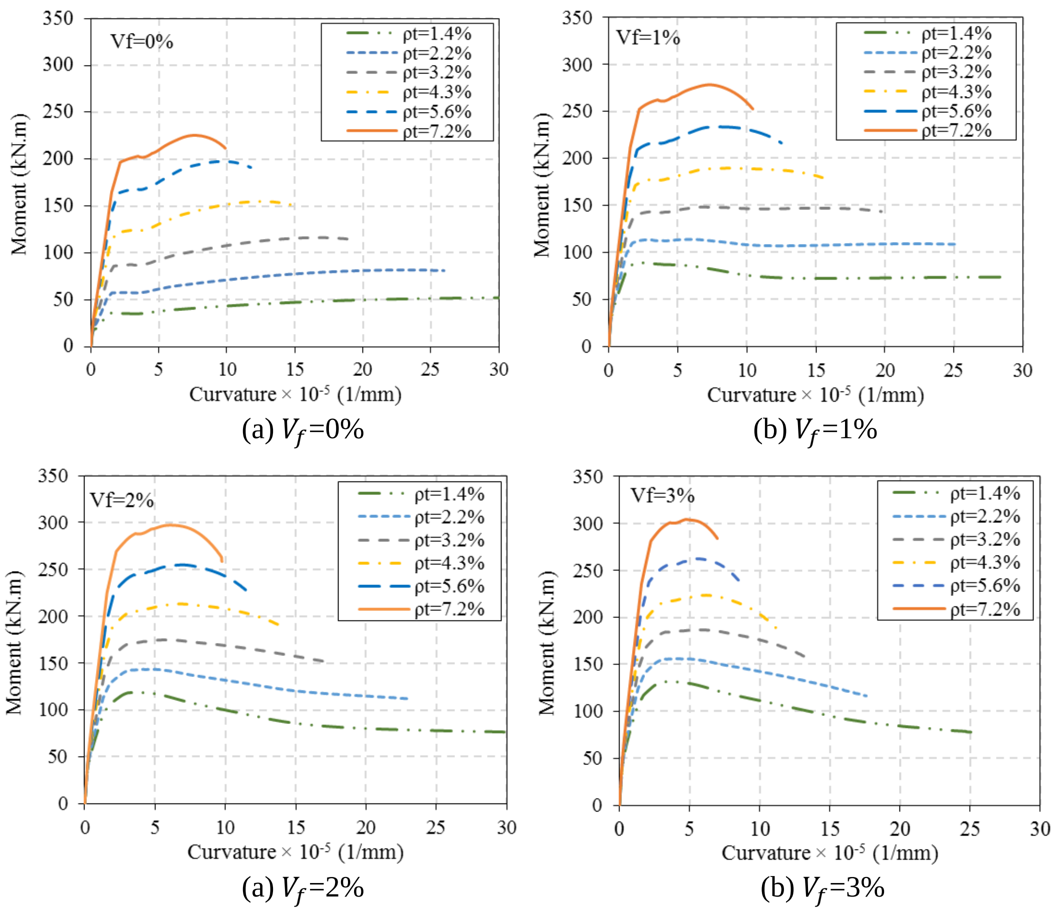

Figure 5-2. Moment curvature response of UHPC beams with different reinforcing bar ratios

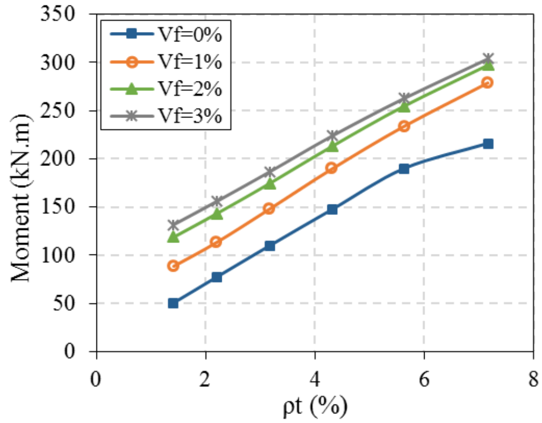

Figure 5-3. Variation of moment capacity with reinforcement ratio for beams with different V_f

Representative load-deflection response predicted at critical section (under point load) of the UHPFRC beams with different fiber volume fractions, subjected to dominant shear loading with different shear span to depth ratios are shown in Figure 5-4 and Figure 5-5. As shown in these figures, the load corresponding to initial cracking in beams with different reinforcement ratios is similar. However, with increasing the reinforcement ratio, post cracking stiffness and load carrying capacity of the beams increase in all beams with different fiber volume fractions and shear span to depth ratios. The variation of shear capacity with reinforcement ratio for beams with different fiber volume fraction and shear span to depth ratio is shown in Figure 5-6(a) to (d). It can be seen from these figures that shear capacity of the beams increases with increasing reinforcement ratio. This increase in shear capacity can be attributed to dowel action and enhanced control of flexural cracking due to higher reinforcement ratio [207], therefore higher flexural capacity and as a consequence higher shear capacity is achieved.

The results also show that shear capacity of the beams increases linearly with increasing reinforcement ratio upto 4.3%. With increasing reinforcement ratio beyond 4.3%, shear capacity improvement is not significant. In other words, maximum shear capacity of the concrete section is attained in beams with reinforcement ratio of 4.3%. The small increase in shear capacity of the beams with reinforcement ratios beyond 4.3% is attributed to dowel action mechanism. This is unlike moment capacity of the beams which increases linearly with increasing reinforcement ratio upto 7.2%. This linear increase in moment capacity with tensile reinforcement ratio upto 7.2% is attributed to high compressive strength of UHPFRC that can balance increased tensile resistance provided by steel bars. However, in these beams with high reinforcement ratio, flexural capacity is higher than shear capacity resulting in dominant shear failure before reaching ultimate moment capacity.

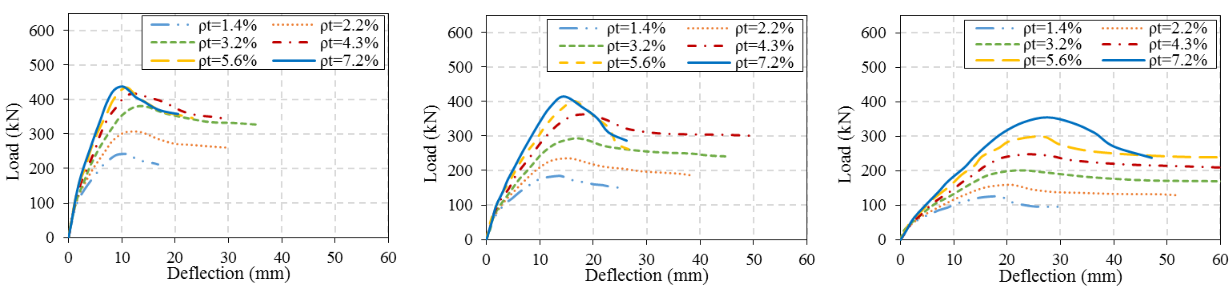

(a) V_f=1%, $^a/_d$ = 1.5 (b) V_f=1%, $^a/_d$ = 2 (c) V_f=1%, $^a/_d$ = 3

Figure 5-4. Load deflection response of UHPC beams under shear dominant loading with different $^a/_d$

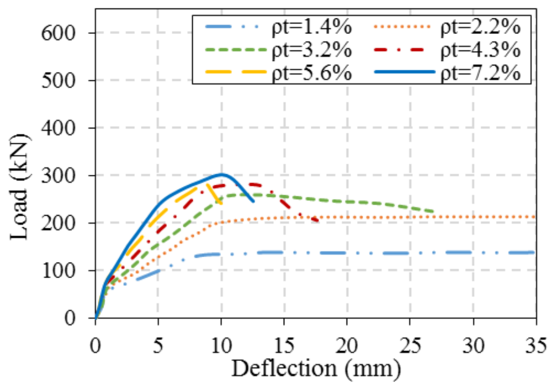

(a) V_f=0%, $^a/_d = 1.5$

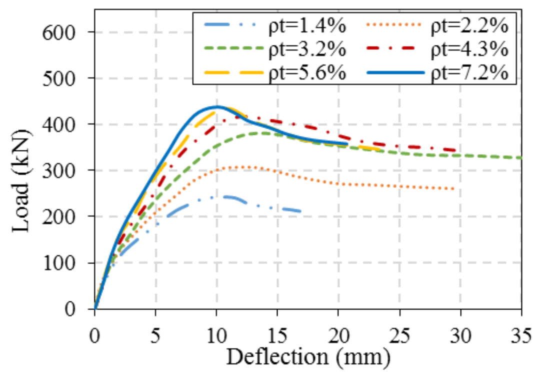

(b) V_f=1%, $^a/_d = 1.5$

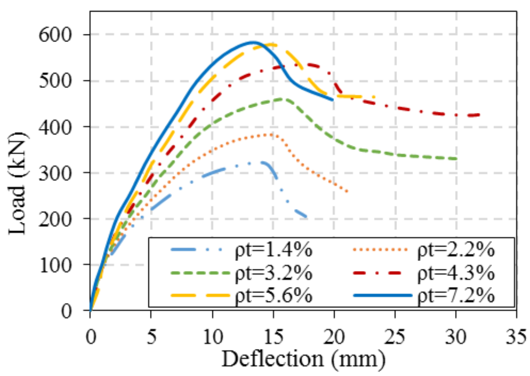

(c) V_f=2%, $^a/_d = 1.5$

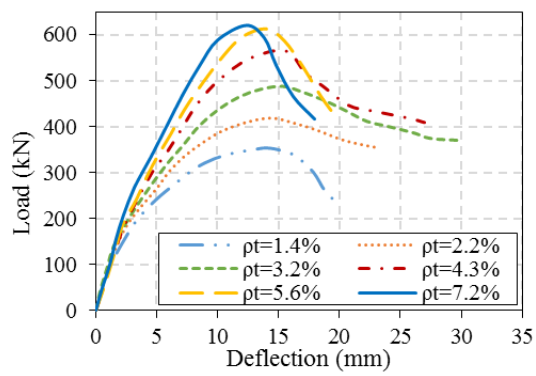

(d) V_f=3%, $^a/_d = 1.5$

Figure 5-5. Load deflection response of UHPC beams under shear dominant loading with different V_f=1%

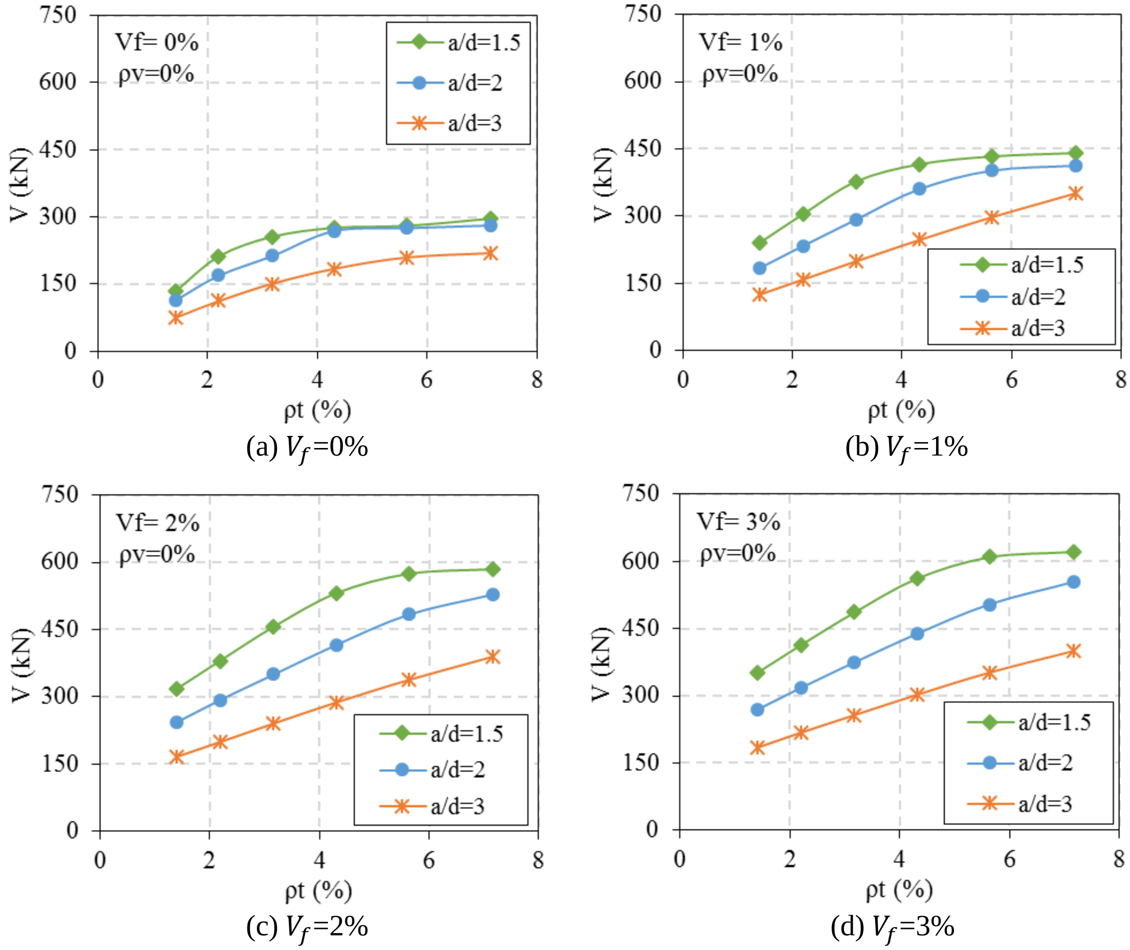

(a) V_f=0% (b) V_f=1%

(c) V_f=2% (d) V_f=3%

Figure 5-6. Variation of shear capacity of UHPC beams with reinforcing bar ratio

5.4 Effect of Steel Fibers Volume Fraction

To study how fiber volume fraction affect the response of the beams, UHPC with different fiber volume fractions of 0%, 1%, 2%, 3% were considered in this study. The developed model was utilized to analyze the effect of presence and volume fraction of steel fibers in beams with different reinforcement ratios and with different shear span to depth ratios. Material models for UHPC and UHPFRC with different volume fractions, based on material property tests conducted by Wille et al. [85] were utilized.

Load-deflection response of beams with different steel reinforcing ratios and with different steel fiber volume fractions is presented in Figure 5-7 and Figure 5-8 under two loading conditions with shear span to depth ratio ($\frac{a}{d}$) of 1.5 and 3. The change in slope in load deflection response indicates development of cracks in the beams. As can be seen in these figures, the cracking load does not change with presence of steel fibers. However, when steel fibers are present in the concrete, post-cracking stiffness increases due to bridging effects facilitated by steel fibers. The improvement of post-cracking stiffness and tensile strength due to presence of steel fibers results in higher load carrying capacity in the beams as shown in Figure 5-7 and Figure 5-8. It should be noted that with inclusion of 3% steel fibers (by volume), no noticeable difference in the load carrying capacity and post-cracking stiffness is observed as compared to inclusion of 2% steel fibers (by volume).

It is interesting to note that in beams with lower reinforcement ratios, higher ductility is obtained where no steel fibers (V_f=0%) are present. In other words, in beams with low reinforcement ratio exhibiting flexural failure mode, including steel fibers results in lower ductility. This can be attributed to cracking pattern in UHPFRC beams, which is different from cracking pattern in UHPC beams. UHPFRC, due to development of fiber bridging at crack surfaces, undergoes multiple cracks followed by the growth of a single macro crack. These macro cracks widen more as compared to other cracks and fibers pull out at the crack surface and this widening of a specific crack leads the failure. This distinct cracking pattern results in localization of the deformation in longitudinal steel reinforcements at the point where the single macro crack widens. Therefore, steel bars yield at a relatively smaller deflection resulting in lower ductility as compared to UHPC beams without fibers. This different cracking pattern in UHPC and UHPFRC is shown in Figure 5-9 and Figure 5-10 for beams with different reinforcement ratios of 1.4% and 2.2%. However, in beams with higher reinforcement ratio, since the failure is dominantly through shear mode, addition of steel fibers improves the ductility of the beams.

As shown in Figure 5-7 and Figure 5-8, UHPC beams (V_f=0%) remain at peak load with increasing deflection for a sustained period as compared to UHPFRC beams which exhibit softening after attaining peak load. This indicates that load-deflection response in UHPC beams (without fibers) is dominated by strain hardening in steel reinforcing bars, while tensile response of UHPFRC dominates load-deflection response of UHPFRC beams.

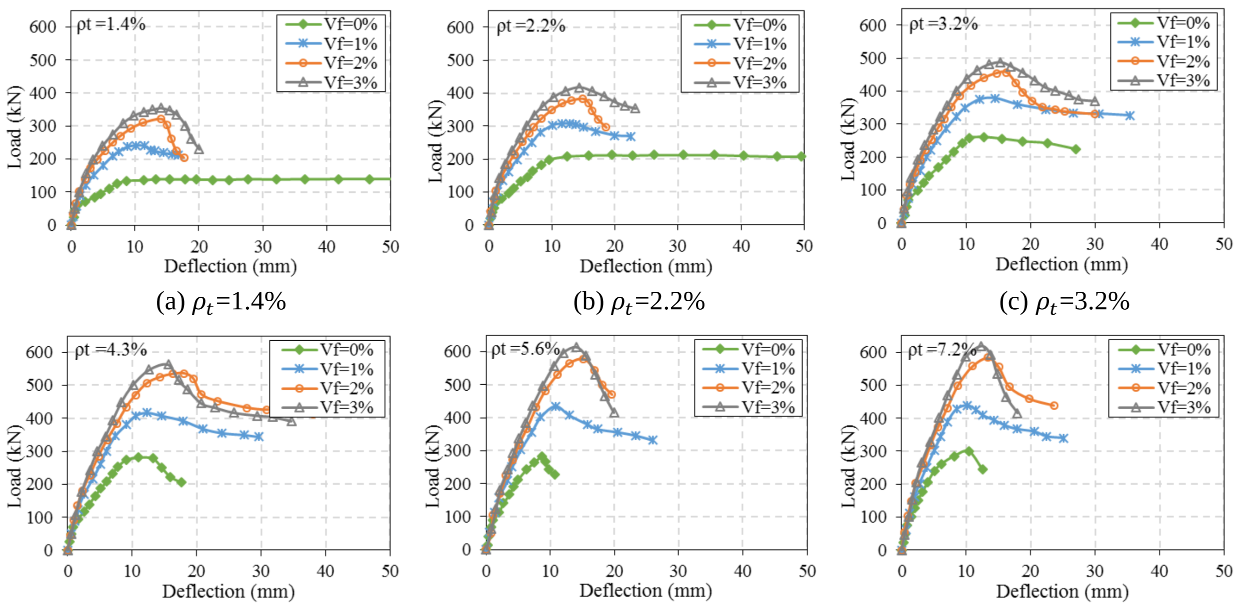

(a) ρ_t=1.4% (b) ρ_t=2.2% (c) ρ_t=3.2%

(d) ρ_t=4.3% (e) ρ_t=5.6% (f) ρ_t=7.2%

Figure 5-7. Load deflection response of beams with different reinforcement ratios and fiber volume fractions with shear span to depth ratio of 1.5

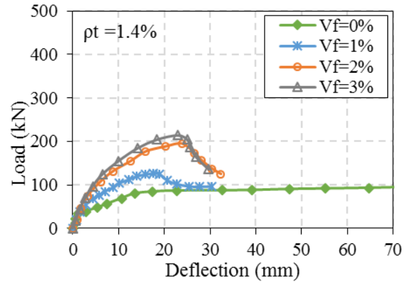

(a) ρ_t=1.4%

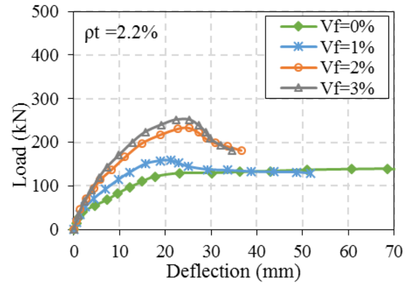

(b) ρ_t=2.2%

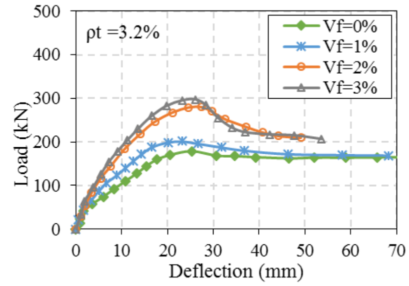

(c) ρ_t=3.2%

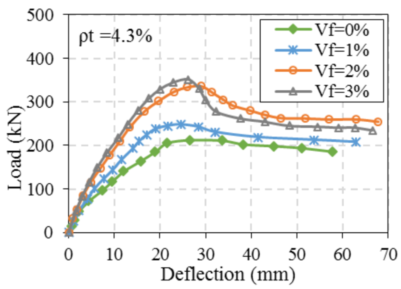

(d) ρ_t=4.3%

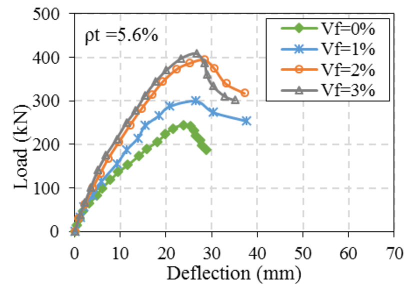

(e) ρ_t=5.6%

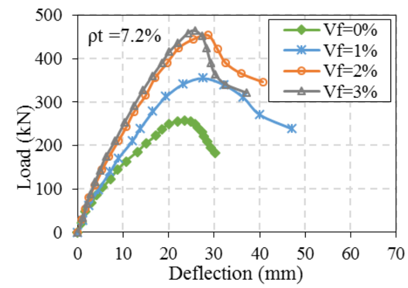

(f) ρ_t=7.2%

Figure 5-8. Load deflection response of beams with different reinforcement ratios and fiber volume fractions with shear span to depth ratio of 3

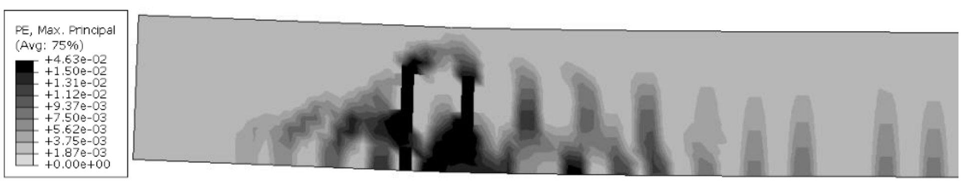

(a) ρ_t=1.4%

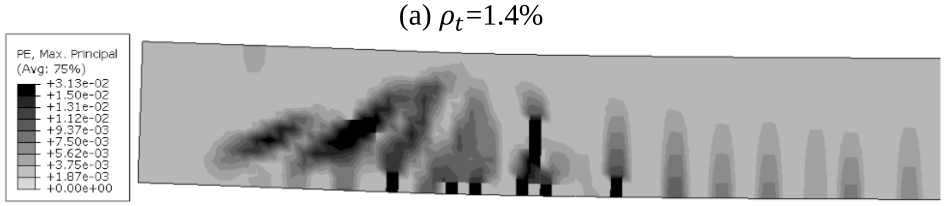

(b) ρ_t=2.2%

Figure 5-9. Cracking patterns in UHPC beams without fibers with $\frac{a}{d} = 2$ under dominant flexural failure

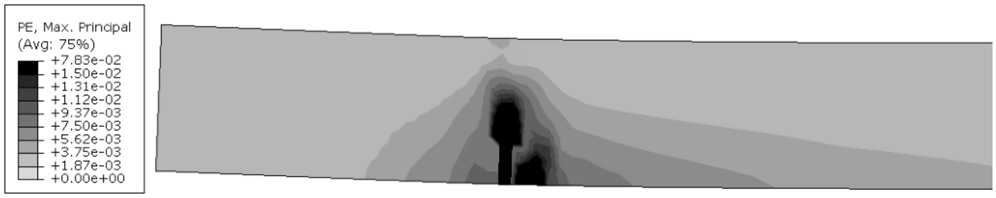

(a) ρ_t=1.4%

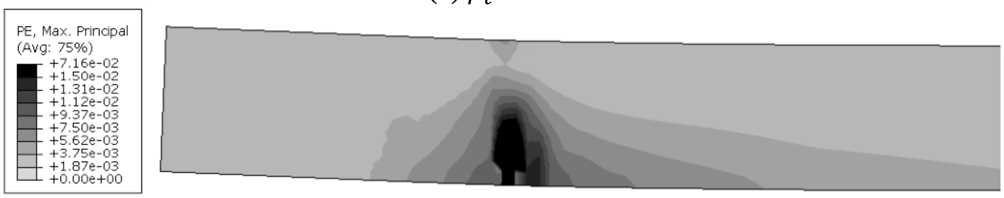

(b) ρ_t=2.2%

Figure 5-10. Cracking patterns in UHPFRC beams with V_f=2% and $\frac{a}{d}$=2 under dominant flexural failure

Variation of shear capacity in the beams with different reinforcement ratios having different fiber volume fractions of 0%, 1%, 2%, and 3% is summarized in Figure 5-11. As can be seen, with including 1% volume fraction of steel fibers, 33% to 73% higher shear capacity is obtained in the beams subjected to dominant shear loading with shear span to depth ratio of 1.5, 2, and 3. Also, results infer that including 2% volume fraction of fibers in UHPFRC, leads to higher improvement in shear capacity (about 54% to 133%) in the UHPFRC beams as compared to UHPC beams without fibers. However, further increase of fiber volume fraction from 2% to 3% does not significantly enhance shear capacity of the beams.

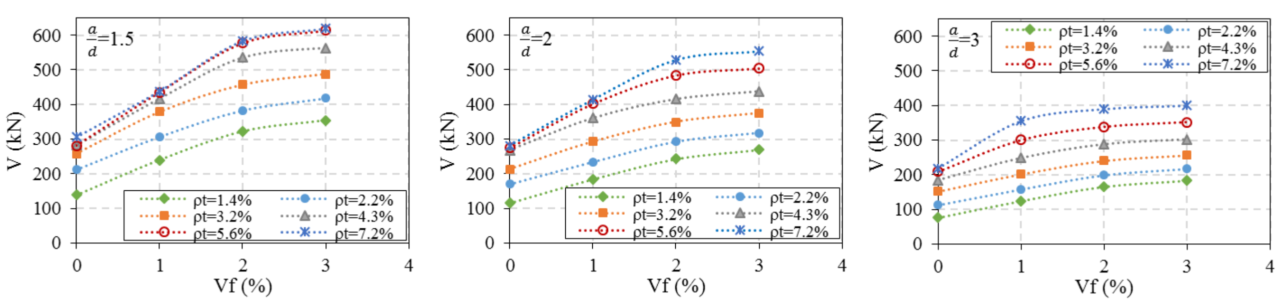

(a) $\frac{a}{d}=1.5$ (b) $\frac{a}{d}=2$ (c) $\frac{a}{d}=3$

Figure 5-11. Variation of shear capacity of UHPC beams with steel fiber volume fraction

5.5 Effect of Shear Reinforcement

As part of this parametric study, the feasibility of removing shear reinforcement (stirrups) in UHPFRC beams was evaluated. To do this, the beams with different reinforcement ratios and fiber volume fractions were analyzed with and without shear reinforcement. The shear reinforcements consisted of stirrups with 9.5 mm bars spaced at 0.3d (72 mm), 0.5d (120 mm), and 0.75d (180 mm).

Load-deflection response of all the analyzed beams with and without stirrups are compared to evaluate effectiveness of shear reinforcement. The results are summarized in Figure 5-12 to show the cases that stirrups can be eliminated since removing stirrups does not lead to reduction of load capacity and ductility. In this figure, shear stress ($v_u = \frac{V_u}{bd}$) is plotted versus reinforcement ratio for beams subjected to dominant shear loading with different shear span to depth ratios. As can be seen, in UHPC beams with tensile reinforcement ratio larger than 2%, stirrups are needed to attain ultimate capacity before failure. This is attributed to brittle response of UHPC without fibers. In UHPFRC beams with different fiber volume fractions, stirrups could be removed without reduction of ductility and load capacity. This is due to the fact that in these beams, the load corresponding to shear capacity of UHPFRC section is higher than the load corresponding to flexural capacity of the section. This high shear resistance of UHPFRC beams without stirrups is due to inclusion of steel fibers that leads to fiber bridging at the crack surfaces and as a result strain hardening after tensile cracking. Therefore, in these beams failure happens when flexural capacity is achieved, and the failure load is less than the load corresponding to shear capacity of the section. However, in UHPFRC beams with high tensile reinforcement ratio, removing stirrups results in reduction of capacity and ductility of the beams. With increasing tensile reinforcing area, moment capacity of the beams increases and thus higher load levels can be applied leading to higher shear stresses in the beams. These shear stresses are higher than capacity of the UHPFRC beam section, therefore stirrups resist the increased shear stresses.

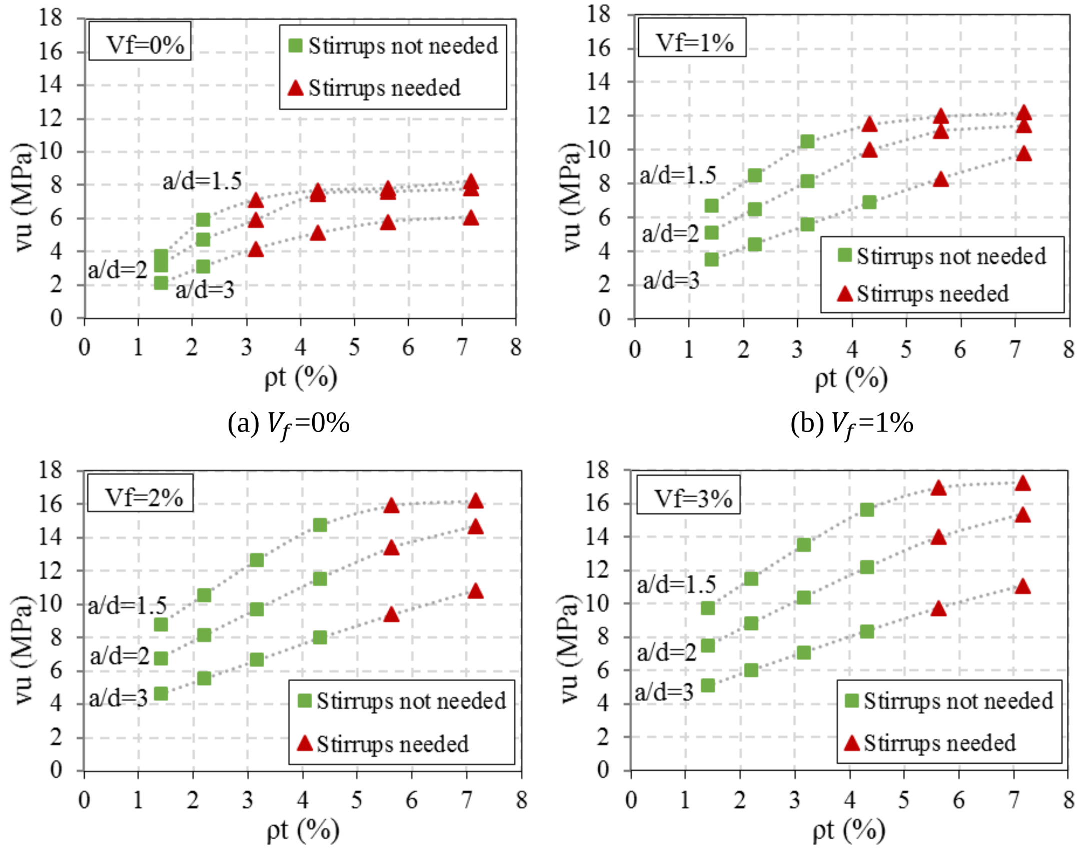

(a) V_f=0% (b) V_f=1%

(c) V_f=2% (d) V_f=3%

Figure 5-12. Effectiveness of stirrups in shear response of UHPC beams

According to ACI-318 provisions [161], steel fibers can be used as shear reinforcement (i.e. minimum stirrups can be eliminated) in FRC beams with 0.75% deformed steel fibers (by volume), if the shear force does not exceed shear strength of concrete. FRC beams with volume fraction of steel fibers equal or larger than 0.75%, have shown to exhibit shear strength greater than $0.29\sqrt{f_c'}b_w d$ [208]. In order to find this boundary for UHPFRC beams, normalized shear strength $(v_u/\sqrt{f_c'})$ defined as shear stress divided by square root of compressive strength of concrete is calculated for the analyzed beams. Figure 5-13 illustrates the normalized shear strength for all the analyzed beams without stirrups with different fiber volume fractions. As can be seen in the case of shear span to depth ratio of 1.5 where the shear was more dominant, the lower boundary of shear strength was $0.48\sqrt{f_c'}$, $0.62\sqrt{f_c'}$, and $0.68\sqrt{f_c'}$ for UHPFRC beams with volume fiber fractions of 1%, 2%, and 3%, respectively. Also, upper boundary of shear strength of UHPFRC beams is analyzed to be $1.2\sqrt{f_c'}$. Further, in the case of UHPC without fibers shear strength is calculated to be from $0.28\sqrt{f_c'}$ to $0.62\sqrt{f_c'}$.

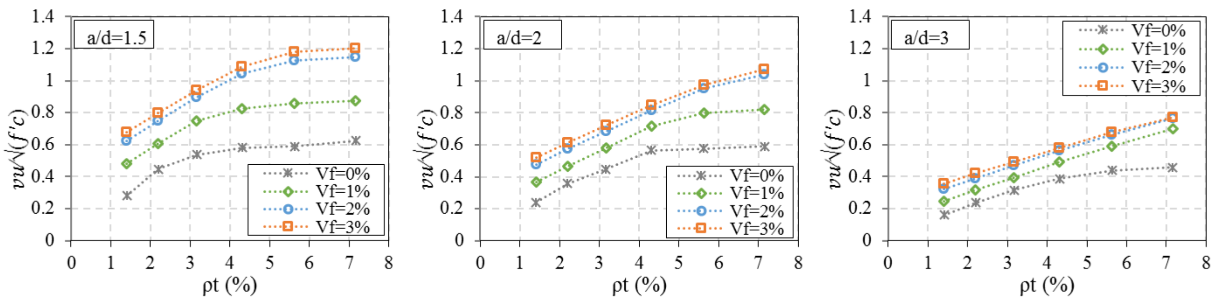

(a) $\frac{a}{d} = 1.5$ (b) $\frac{a}{d} = 2$ (c) $\frac{a}{d} = 3$

Figure 5-13. Normalized shear strength for UHPC beams

To investigate whether removing stirrups in UHPFRC beams results in failure before attaining ultimate moment capacity, flexural capacity of the beams were evaluated utilizing the developed analytical approach. Ultimate moment capacity of the beams obtained from moment-curvature analysis is compared to moment corresponding to maximum load carrying capacity predicted by FE model in beams under shear dominant loading with different shear span to depth ratios (see Figure 5-14 to Figure 5-17). As can be seen in Figure 5-14, UHPC beams (V_f=0%) without stirrups and with reinforcement ratio larger than 2.2% fail before attaining ultimate moment capacity. This confirms that stirrups are needed in UHPC beams (with $\rho_t \geq 2\%$) under shear dominant loading to attain ultimate moment capacity and ductility. It should be noted that with increasing shear span to depth ratio, shear stresses decreases thus, the reduction in capacity due to shear failure decreases.

In the case of UHPFRC beams with fiber volume fraction of 1% with shear span to depth ratio of 1.5 and 2, beams with reinforcement ratio above 4% require shear reinforcement to obtain ultimate capacity. Similar results are observed for beams with fiber volume fraction of 2% and 3%, however the reduction of capacity due to shear failure is less as compared to UHPFRC beams with fiber volume fraction of 1%. The results show that with increasing shear span to depth ratio ($\frac{a}{d}$=3), UHPFRC beams without stirrups even with high reinforcement ratios can attain their ultimate moment capacity before failure due to decreased shear stresses.

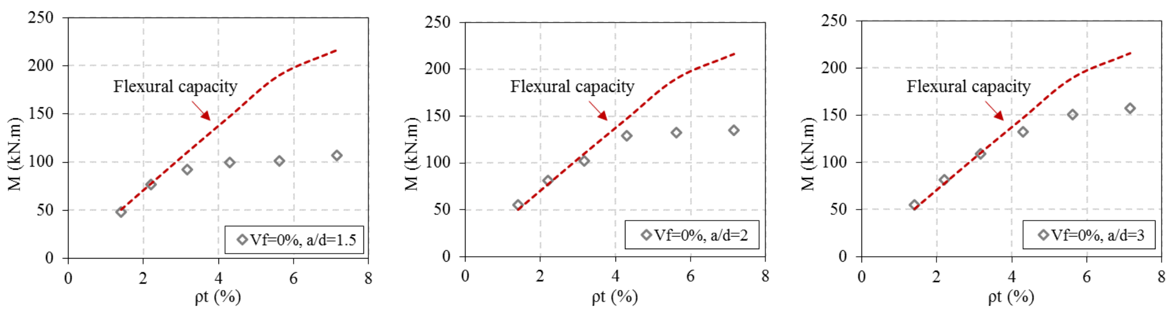

a) V_f=0%, $\frac{a}{d}$=1.5 (b) V_f=0%, $\frac{a}{d}$=2 (c) V_f=0%, $\frac{a}{d}$=3

Figure 5-14. Comparison of nominal moment capacity of UHPFRC beams (V_f=0%) with maximum moment obtained under shear dominant loading

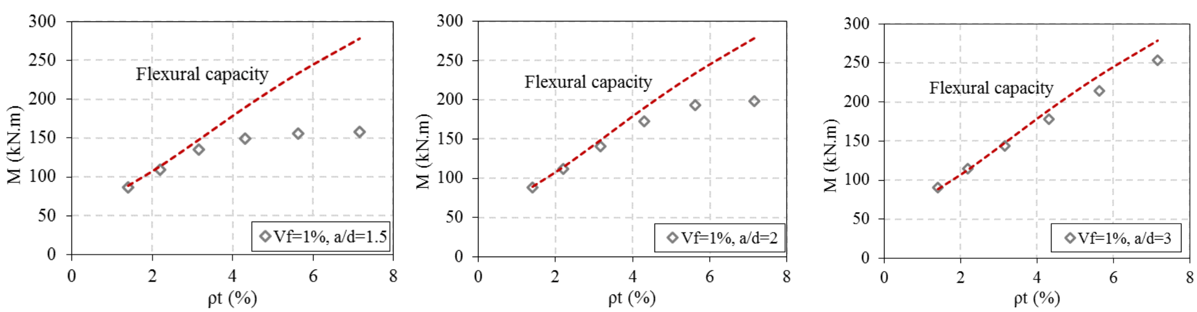

(a) V_f=1%, $\frac{a}{d}$=1.5 (b) V_f=1%, $\frac{a}{d}$=2 (c) V_f=1%, $\frac{a}{d}$=3

Figure 5-15. Comparison of nominal moment capacity of UHPFRC beams (V_f=1%) with maximum moment obtained under shear dominant loading

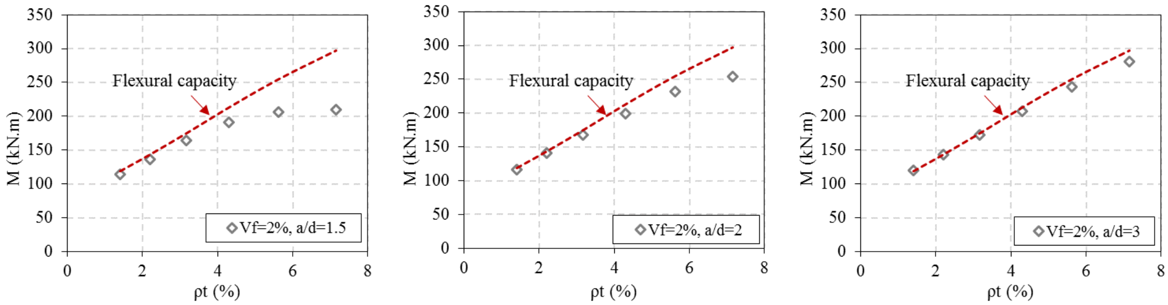

(a) V_f=2%, $\frac{a}{d}$=1.5 (b) V_f=2%, $\frac{a}{d}$=2 (c) V_f=2%, $\frac{a}{d}$=3

Figure 5-16. Comparison of nominal moment capacity of UHPFRC beams (V_f=2%) with maximum moment obtained under shear dominant loading

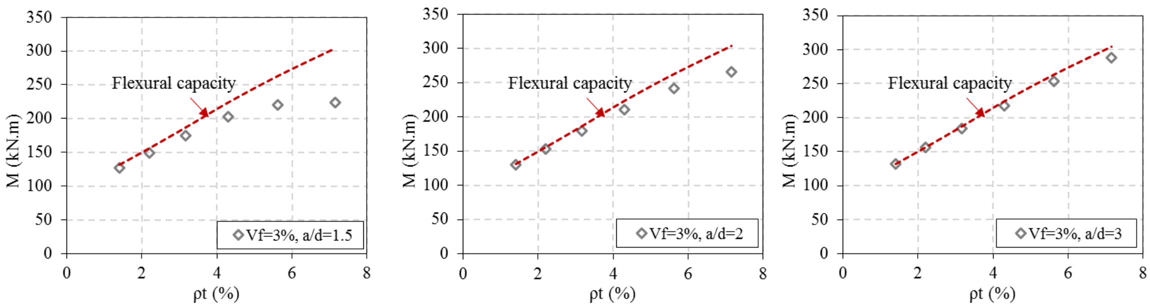

(a) V_f=3%, $\frac{a}{d}$=1.5 (b) V_f=3%, $\frac{a}{d}$=2 (c) V_f=3%, $\frac{a}{d}$=3

Figure 5-17. Comparison of nominal moment capacity of UHPFRC beams (V_f=3%) with maximum moment obtained under shear dominant loading

To quantify effect of stirrup spacing, shear capacity of the beams with varying fiber volume fraction, reinforcement ratios, and shear span to depth ratio, having different shear reinforcement ratio (spacing), are compared in Figure 5-18 to Figure 5-21. In UHPC beams with ρ_t= 4.3% and $\frac{a}{d}$= 1.5, having stirrups at 0.75d, 0.5d, and 0.3d spacing results in higher shear capacity by 14%, 38% and 39%, respectively. This increase in shear capacity of UHPC beams with including stirrups is more significant in beams with higher tensile reinforcement ratio. In UHPC beams with ρ_t= 7.2%, including stirrups with spacing of 0.75d, 0.5d, and 0.3d leads to higher shear capacity by 33%, 47%, and 71%, respectively (see Figure 5-18(a)). This enhancement in shear capacity in UHPC beams with stirrups decreases when the beam are subjected to shear loading with higher shear span to depth ratio due to decrease in shear stresses.

In UHPFRC beams with 1% fiber volume fraction with ρ_t= 7.2% and $\frac{a}{d}$= 1.5, having stirrups with spacing of 0.75d, 0.5d, and 0.3d could enhance the shear capacity of the beams by 12%, 19%, and 33%, respectively. However, with increasing fiber volume fraction or shear span to depth ratio, spacing of the stirrups has negligible effects on shear capacity of the beams.

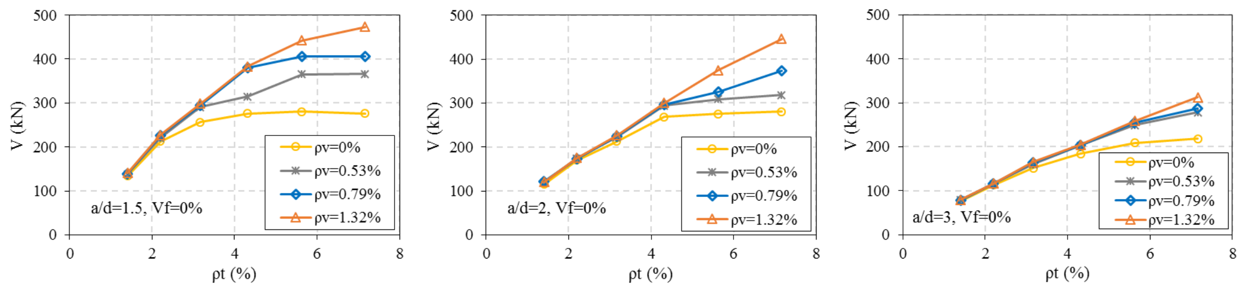

(a) V_f=0%, $\frac{a}{d}$=1.5 (b) V_f=0%, $\frac{a}{d}$=2 (c) V_f=0%, $\frac{a}{d}$=3

Figure 5-18. Effect of varying shear reinforcement ratio on shear capacity of UHPFRC beams (V_f=0%)

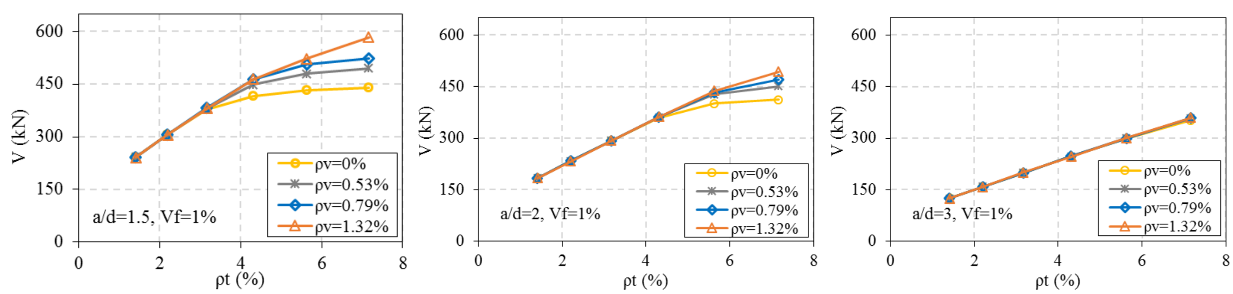

(a) V_f=1%, $\frac{a}{d}$=1.5 (b) V_f=1%, $\frac{a}{d}$=2 (c) V_f=1%, $\frac{a}{d}$=3

Figure 5-19. Effect of varying shear reinforcement ratio on shear capacity of UHPFRC beams (V_f=1%)

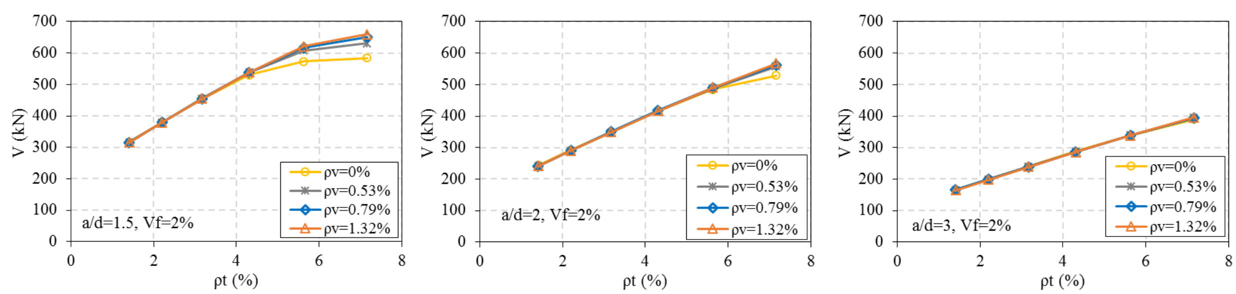

(a) V_f=2%, $\frac{a}{d}$=1.5 (b) V_f=2%, $\frac{a}{d}$=2 (c) V_f=2%, $\frac{a}{d}$=3

Figure 5-20. Effect of varying shear reinforcement ratio on shear capacity of UHPFRC beams (V_f=2%)

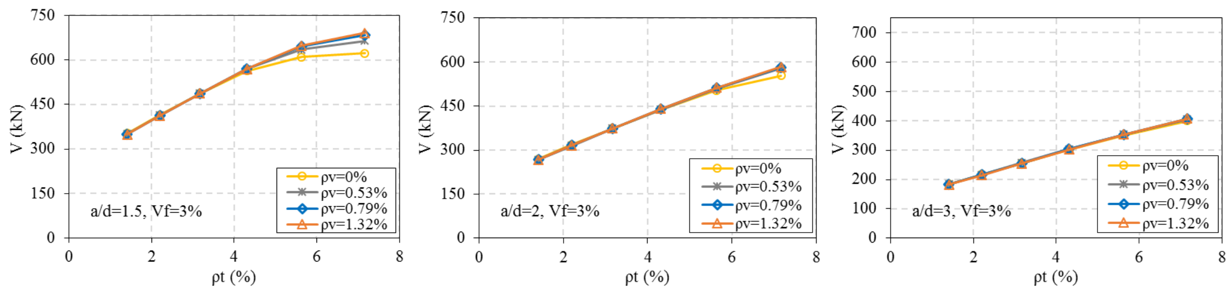

(a) V_f=3%, $\frac{a}{d}$=1.5 (b) V_f=3%, $\frac{a}{d}$=2 (c) V_f=3%, $\frac{a}{d}$=3

Figure 5-21. Effect of varying shear reinforcement ratio on shear capacity of UHPFRC beams (V_f=3%)

ACI-318 [161] provisions requires designers to provide minimum shear reinforcement, even when the contribution of concrete itself to shear capacity is sufficient. According to ACI, minimum shear reinforcement is to be provided in the beams if the factored shear force (V_u) from loading exceeds half concrete shear resistance ($\frac{1}{2}\emptyset V_c$). However, the results from this study show that minimum shear reinforcement can be removed in UHPFRC beam with minimum fiber volume fraction of 1%.

Also, ACI-318 section 9.7.6.2.2 [161] specifies limiting spacing of shear reinforcement. According to ACI, spacing of shear reinforcement along the length of the beams should not exceed $\frac{d}{2}$ or 600 mm where the contribution of stirrups to shear capacity is less than $0.33\sqrt{f_c'}b_w d$. Results from this study show that stirrups spacing of 0.75d is effective in UHPFRC beams with shear dominant failure to attain ultimate capacity and ductility. Therefore, limiting spacing of shear reinforcement specified in ACI 318 can be increased in case of UHPFRC beams.

In order to quantify the contribution of stirrups to shear capacity at different stages of loading, first the stirrups crossing diagonal crack that are stressed as compared to other stirrups need to be identified as discussed in Chapter 4. Then, the stress developed in the identified stirrups crossing major diagonal cracks is used to calculate the stirrups contribution by multiplying the stresses by stirrups cross sectional area. As an example the contribution of stirrups to shear capacity in

UHPFRC beams with steel fiber volume fraction of 1% is quantified at different stages of loading. The stirrups crossing major diagonal cracks in UHPFRC beams with fiber volume fraction of 1%, and reinforcement ratio of 5.6% with different stirrups spacing of 0.3d and 0.5d are shown in Figure 5-22. As shown in this figure, two stirrups are tensioned in the shear span, illustrating the location of the major cracks in shear span.

Figure 5-34(a) shows that in beam with volume fiber fraction of 1% and reinforcement ratio of 2.2%, stirrups do not contribute to shear capacity as the strength of concrete itself is sufficient. In this figure, the stress developed in longitudinal bars at critical section and stirrups as well as concrete contribution and stirrups contribution to capacity is illustrated. It can be seen that even though flexure bars yield and enter the hardening phase, the level of stress in stirrups is not significant. With increasing reinforcement ratio in beams leading to dominant shear failure, stirrups contribution to shear capacity increases as shown in in Figure 5-34(b) to (d). Stresses developed in stirrups increase with increasing loading on the beams and reach yielding stress. Also, the results indicate that in UHPFRC beams even when the beams fail under shear, contribution of stirrups is negligible till almost 70% of shear capacity is attained. This is in contrast to conventional concrete beams, where contribution of stirrups to shear resistance increases immediately after initial cracking.

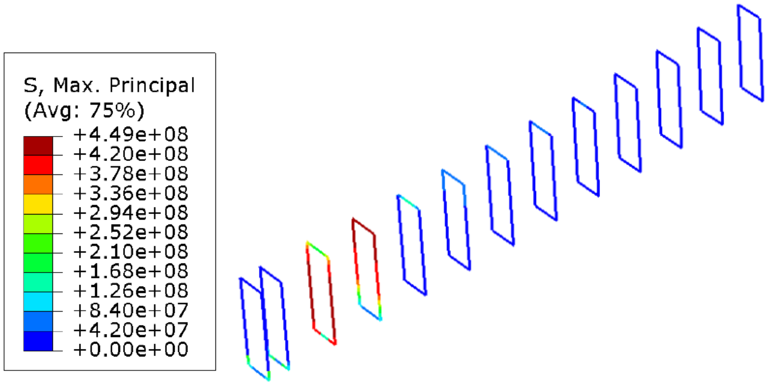

(a) V_f=1%, $\frac{a}{d}$=1.5, ρ=5.6%, S=0.5d

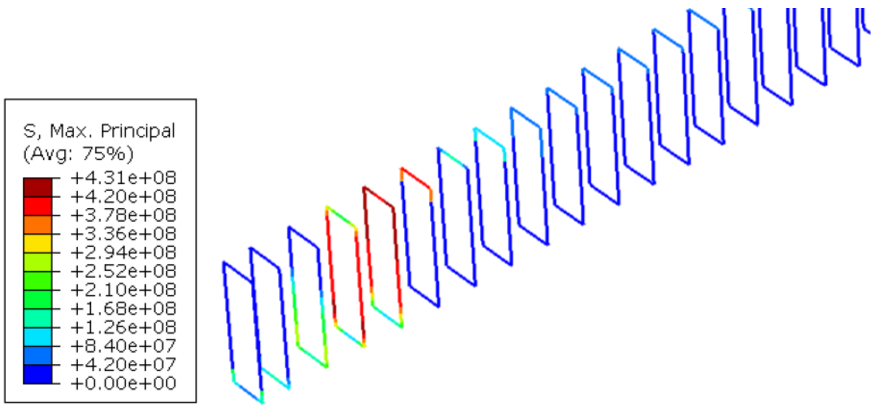

(b) V_f=1%, $\frac{a}{d}$=1.5, ρ=5.6%, S=0.3d

Figure 5-22. Stirrups crossing diagonal shear crack in shear span

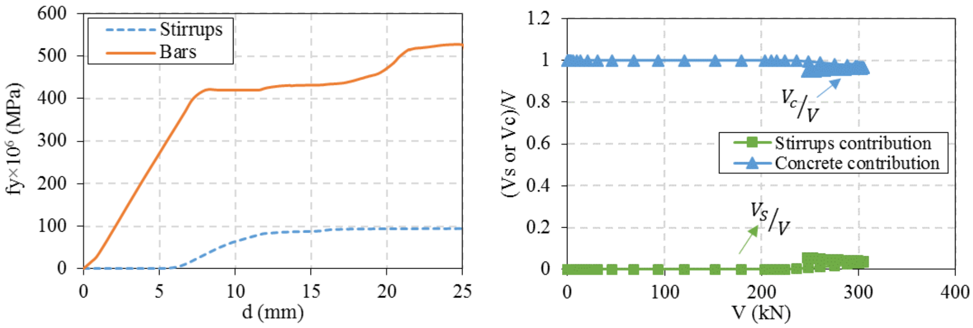

(a) V_f=1%, $\frac{a}{d}$=1.5, ρ=2.2%, S=0.5d

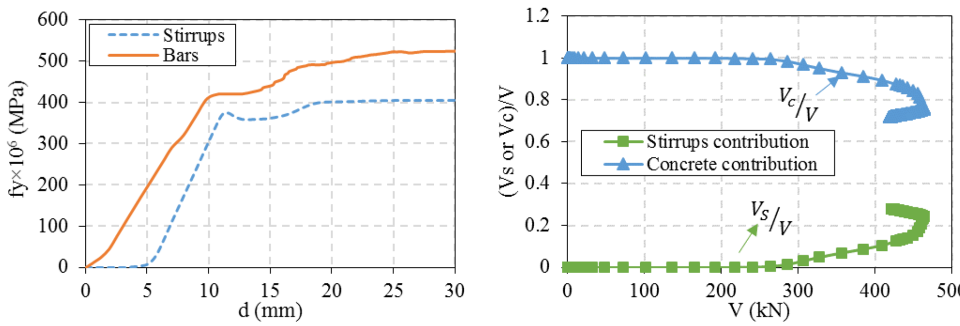

(b) V_f=1%, $\frac{a}{d}$=1.5, ρ=4.3%, S=0.5d

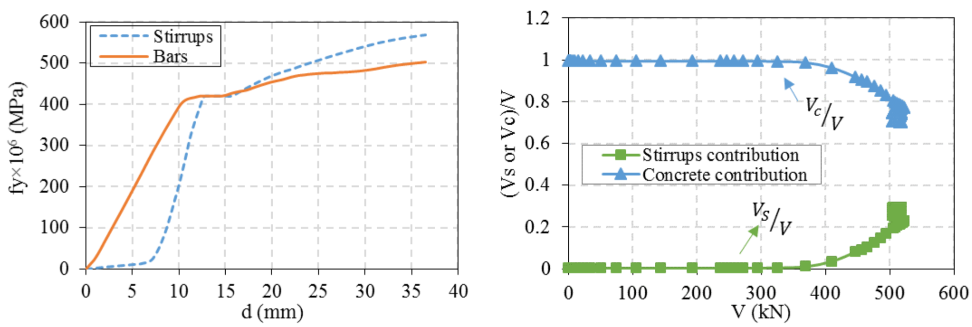

(c) V_f=1%, $\frac{a}{d}$=1.5, ρ=5.6%, S=0.3d

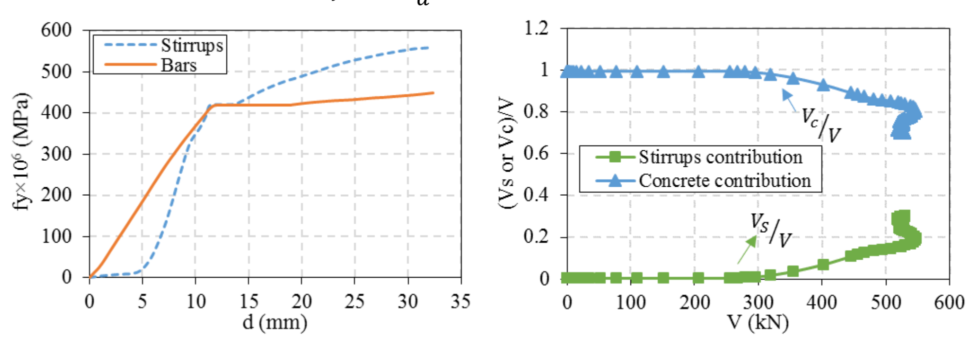

(d) V_f=1%, $\frac{a}{d}$=1.5, ρ=7.2%, S=0.3d

Figure 5-23. Stresses developed in longitudinal bars and stirrups, and contribution of stirrups and concrete to shear capacity

5.6 Mode of Failure

Principal strain contours and the direction of principal strains (being perpendicular to cracks) obtained from numerical model were utilized to evaluate failure mode in the beams. As an example, the principal strains direction and contours in beams with fiber volume fraction of 2% with different reinforcement ratios subjected to dominant shear loading with shear span to depth ratio of 1.5 is shown in Figure 5-24 to Figure 5-29. These figures show the change in mode of failure from flexure to flexure-shear and shear with increasing steel reinforcing ratio.

Maximum principal strain contour in beam with ρ=1.4% is concentrated at critical section of the beam under the point load as shown in Figure 5-24(a) indicating the macro crack leading to failure. Direction of principal strains (being perpendicular to cracks) shown in Figure 5-24(b) indicates flexural failure mode. Beams with ρ=2.2% and 3.2% exhibit similar response with flexural failure mode as can be seen in Figure 5-25. With increasing reinforcement ratio and thus flexural capacity of the beams, higher load levels can be applied on the beams before failure. Therefore, shear stresses increase in shear span and this increase in shear stresses results in diagonal cracking in shear span. In the case of beam with ρ=4.3%, the beam exhibit flexure-shear failure mode since localized plastic strains (crack) is flexural crack under the point load and diagonal tension crack in the shear span (as shown in Figure 5-26). At higher reinforcement ratio of 5.6% and 7.2%, major crack leading to failure is propagated in shear span. Also, the direction of principal strains illustrates propagation of diagonal crack confirming shear failure mode.

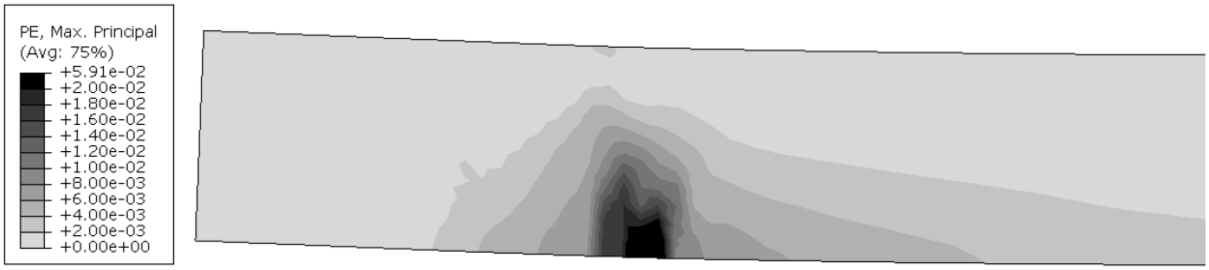

(a) Maximum pricipal strain contour

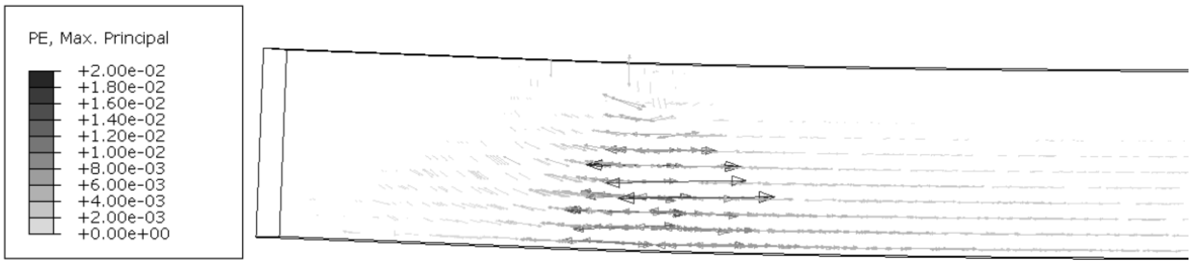

(b) Maximum principal strain direction

Figure 5-24. Principal strain contour and direction in beam without stirrups with V_f=2%, ρ_t=1.4%, and $\frac{a}{d}$=1.5 at P= 290 kN, d=15mm

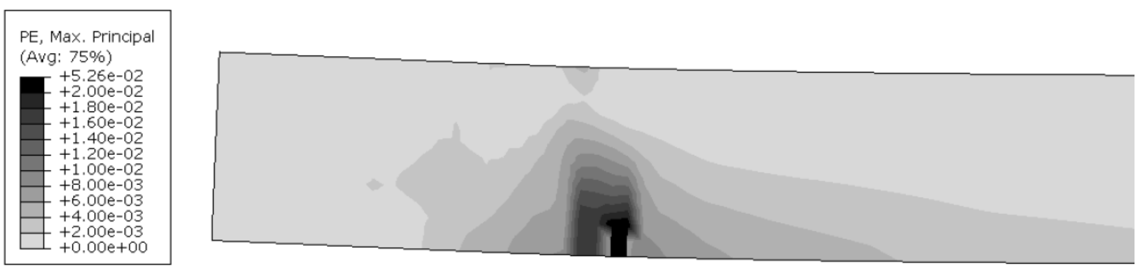

(a) Maximum pricipal strain contour

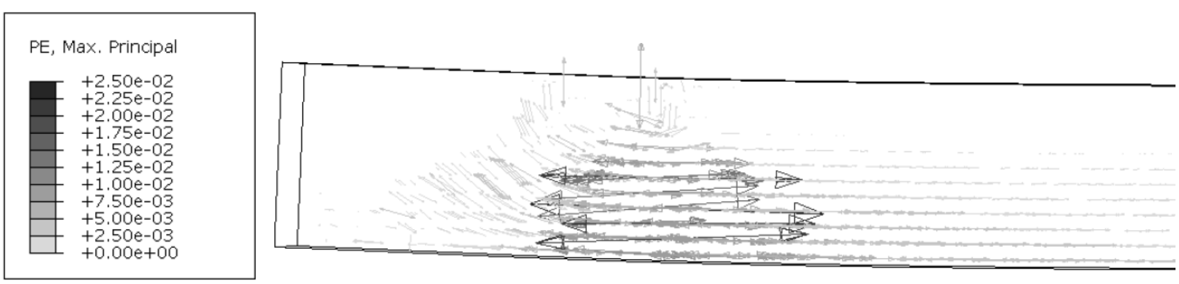

(b) Maximum principal strain direction

Figure 5-25. Principal strain contour and direction in beam without stirrups with V_f=2%, ρ_t=2.2%, and $\frac{a}{d}$=1.5 at P=363 kN, d=16mm

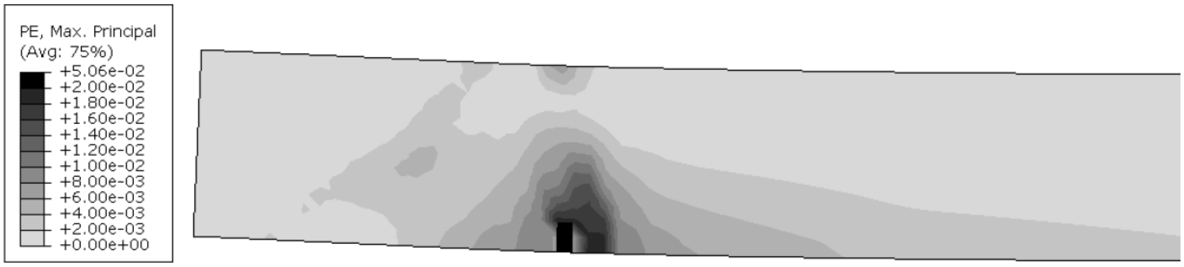

(a) Maximum pricipal strain contour

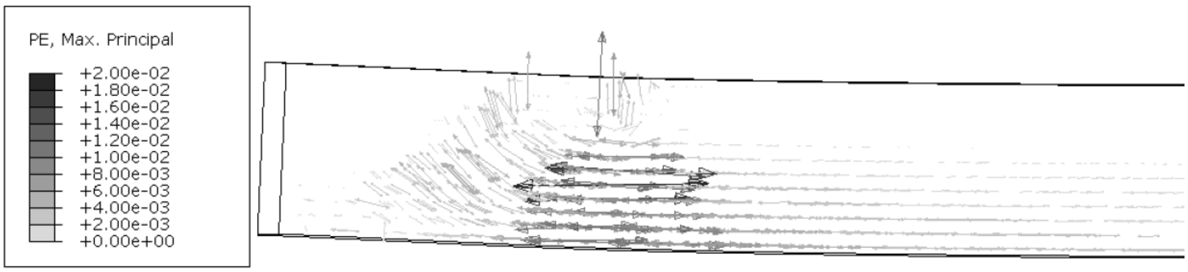

(b) Maximum principal strain direction

Figure 5-26. Principal strain contour and direction in beam without stirrups with V_f=2%, ρ_t=3.2%, and $\frac{a}{d}$=1.5 at P=447 kN, d=17mm

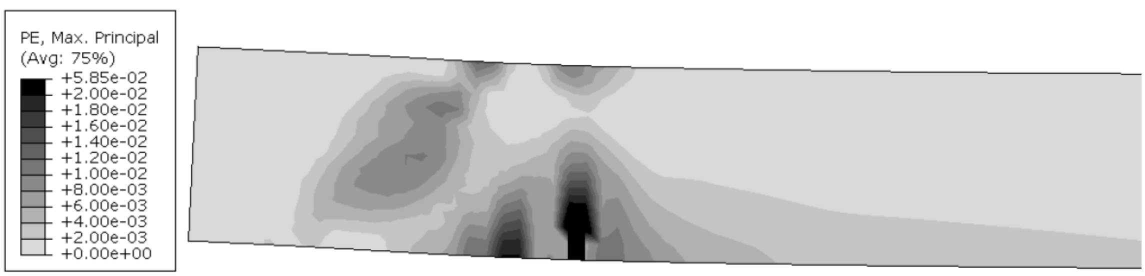

(a) Maximum pricipal strain contour

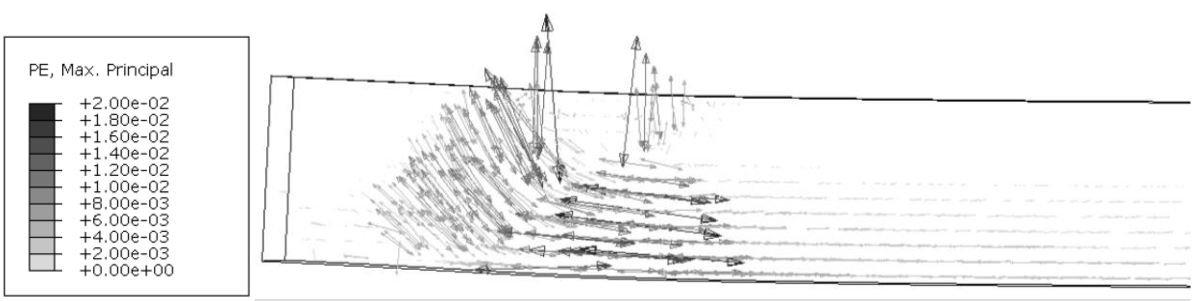

(b) Maximum principal strain direction

Figure 5-27. Principal strain contour and direction in beam without stirrups with V_f=2%, ρ_t=4.3%, and $\frac{a}{d}$=1.5 at P= 509 kN, d= 20.5 mm

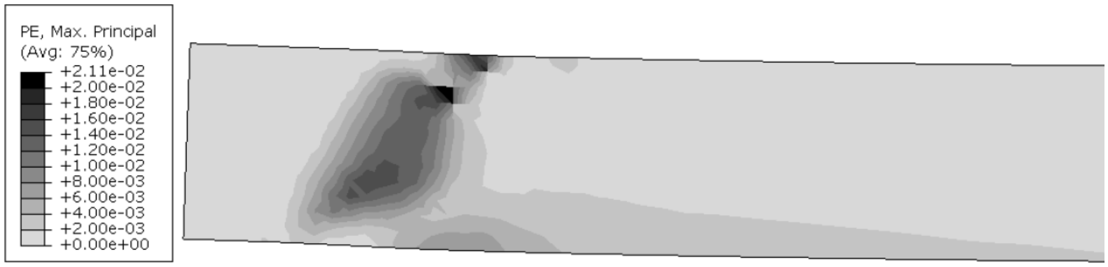

(a) Maximum pricipal strain contour

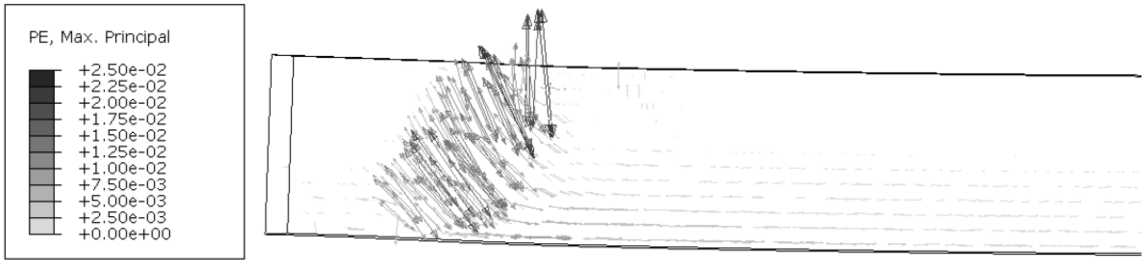

(b) Maximum principal strain direction

Figure 5-28. Principal strain contour and direction in beam without stirrups with V_f=2%, ρ_t=5.6%, and $\frac{a}{d}$=1.5 at P=611 kN, d=16mm

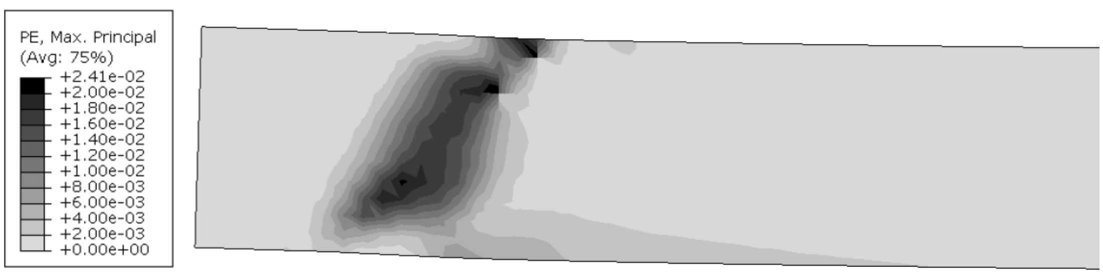

(a) Maximum pricipal strain contour

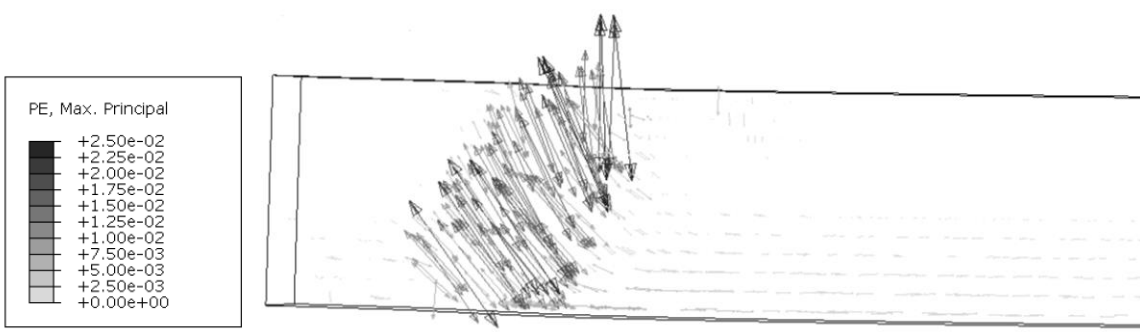

(b) Maximum principal strain direction

Figure 5-29. Principal strain contour and direction in beam without stirrups with V_f=2%, ρ_t=7.2%, and $\frac{a}{d}$=1.5 at P=610 kN, d=14.5mm

The principal strain contour predictions along with principal direction was utilized to identify the failure mode in all analyzed beams. The domain for shear, flexure-shear, and flexure failure modes as $\frac{a}{d}$ versus ρ is illustrated in Figure 5-30. Also, Figure 5-31 shows the domain for observed failure modes as ρ_t versus V_f. As can be seen in these figures, with increasing shear span to depth ratio or fiber volume fraction, mode of failure changes from shear to flexure-shear and pure flexure. Since addition of steel fibers results in bridging at the crack surfaces and improves post cracking stiffness and tensile strength of concrete and therefore transforms failure mode from shear to flexure (more ductile). Also, with longer shear spans, shear stresses decrease leading to dominant flexural stresses and thus flexural failure mode. Figure 5-32 shows variation of failure mode for beams with reinforcement ratio of 4.3% and shear span to depth ratio of 2 with different fiber volume fraction of 0% 1%, 2%, and 3%. As can be seen, mode of failure changes from shear to flexure with increasing fiber volume fraction. The results also show that for a given fiber volume fraction and shear span to depth ratio, with increasing reinforcement ratio failure mode changes from flexure to shear due to increase in shear stresses (see Figure 5-30 and Figure 5-31).

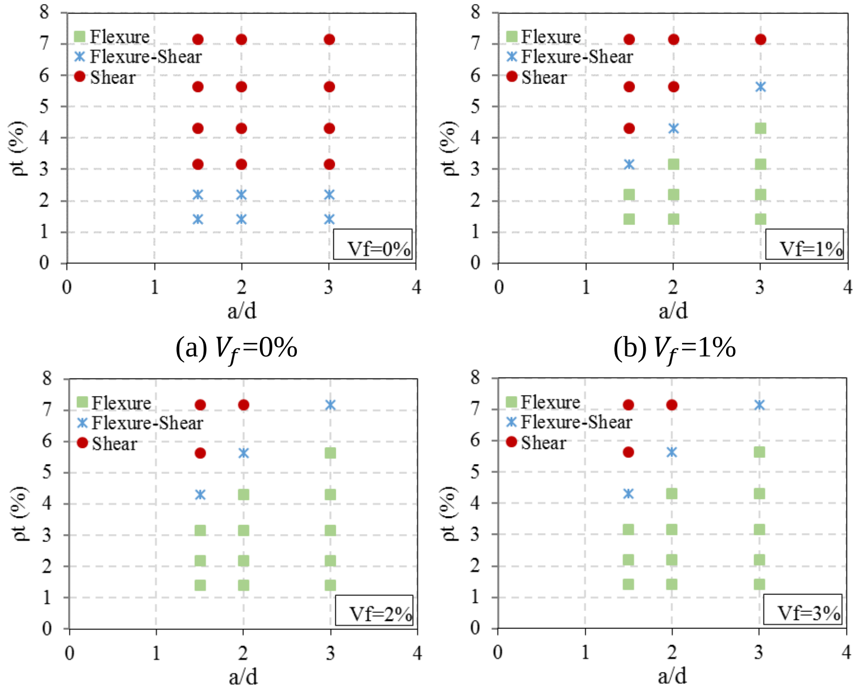

(a) V_f=0% (b) V_f=1%

(a) V_f=2% (b) V_f=3%

Figure 5-30. Classification of failure mode in beams with different fiber volume fractions

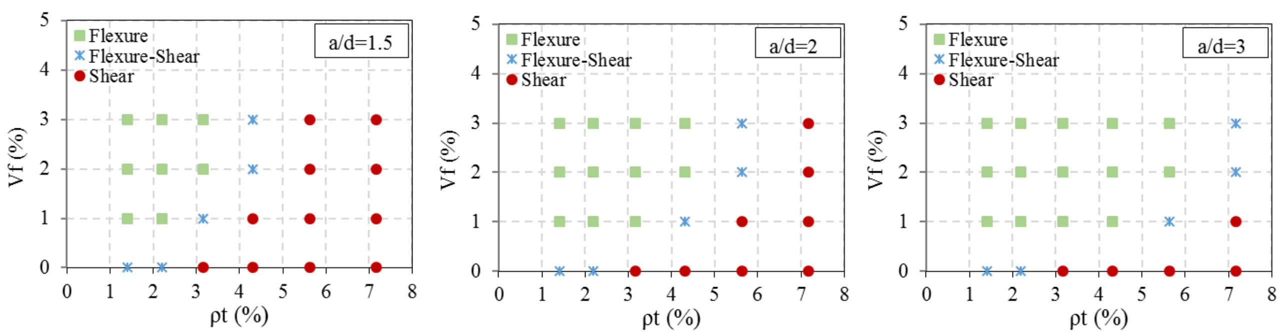

(a) $\frac{a}{d}$=1.5 (b) $\frac{a}{d}$=2 (c) $\frac{a}{d}$=3

Figure 5-31. Classification of failure mode in beams with different shear span to depth ratios

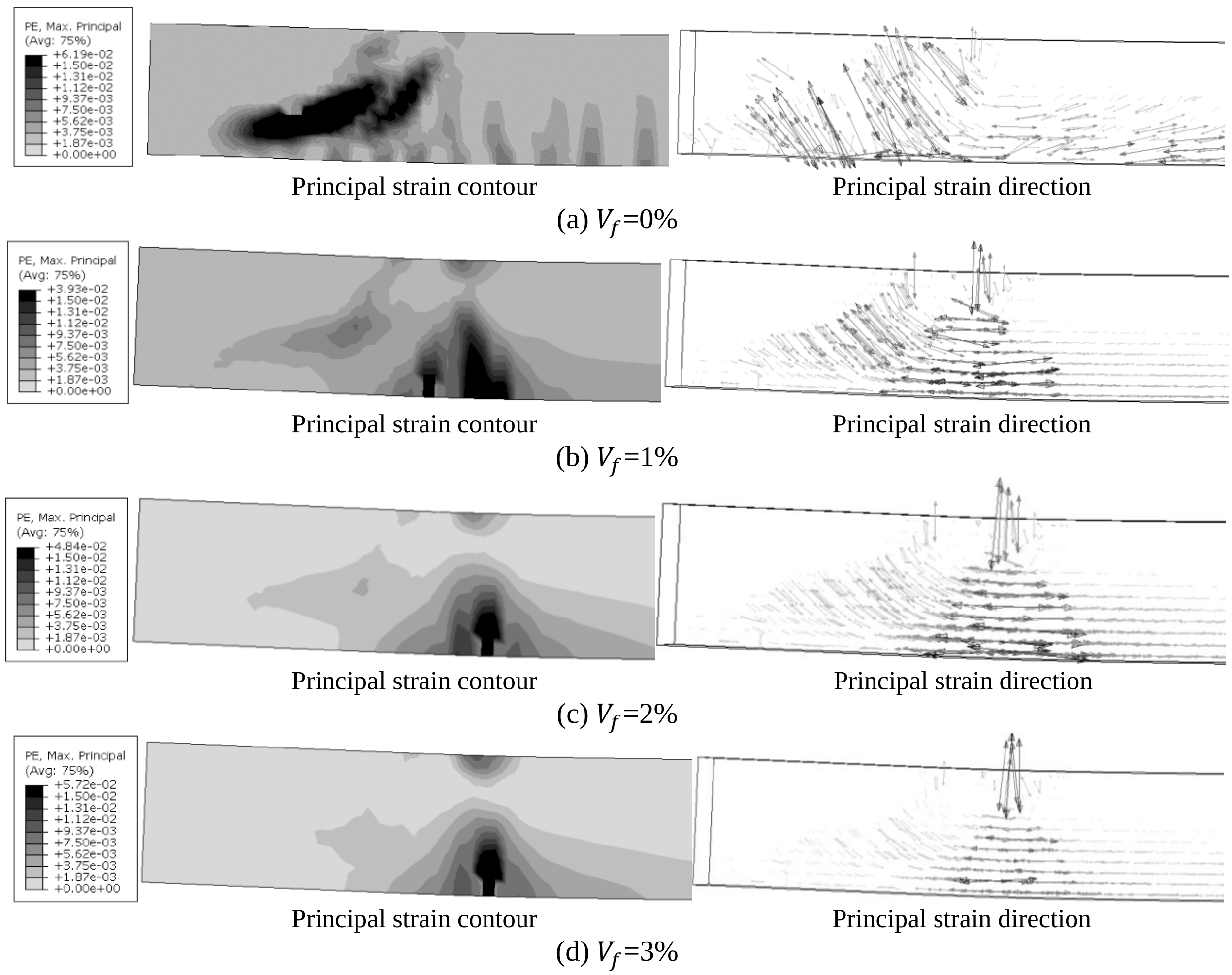

Figure 5-32. Variation of failure mode from shear to flexure with increasing fiber volume fraction in beam with ρ_t=4.3%, and $\frac{a}{d}$=2 at peak state

5.7 Factors Contributing to Shear Resistance

The developed model can be applied to quantify the factors (mechanisms) that help in achieving shear resistance in the beams. Shear resistance of reinforced concrete beams develops through a combination of arch action and beam action [209]. In order to develop better understanding on shear resistance mechanism in UHPC beams, beam action and arch action contribution to shear resistance was evaluated in the analyzed beams.

Park et al [209] developed an approach for decomposing shear strength into two mechanisms of arch action and beam action. A shear span of a beam, over that, the shear force is constant is illustrated in Figure 5-33(a). Also, the internal forces and external forces maintaining equilibrium are shown in this figure. As can be seen, the external shear force can be resisted by a shear force across the uncracked concrete in compression zone (V_c), and a dowel force transmitted by longitudinal bars across the crack (V_d), and also the vertical component of shear resistance across the crack (V_a) [209]. The moment of the resistance of the beam is expressed as:

$$M = xV = jd\ (T + V_d\ cot\alpha) \tag{5-1}$$

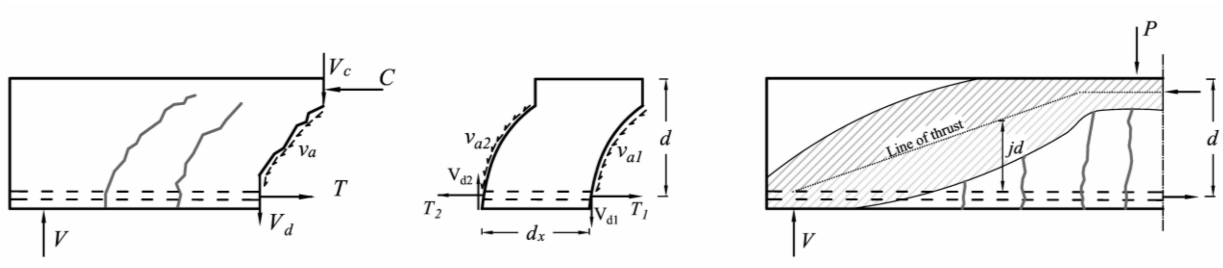

(a) Part of a beam with constant shear (b) Beam action (c) Arch action

Figure 5-33. Shear mechanism in shear span of a beam [209]

If the contribution of the dowel action to flexural resistance is neglected, the moment of resistance simplifies to Eq. (5-2) which illustrates the relation between internal and external moments. The shear resistance expressed by rate of change in bending moment along the beam is shown in Eq. (5-3) [209].

$$M = Tjd \tag{5-2}$$

$$V = \frac{dM}{dx} = \frac{d}{dx}(Tjd) = jd\left(\frac{dT}{dx}\right) + T\,\frac{d(jd)}{dx} \tag{5-3}$$

In shear resistance mechanism (Eq. (5-3)), the term $jd\left(\frac{dT}{dx}\right)$ being the resistance due to change of internal tensile force (T) with constant lever arm (jd), defines beam action mechanism. Beam action is the resistance provided by aggregate interlock, interfacial resistance, dowel action and stirrups. Therefore, if the lever arm remains constant, the perfect beam action is obtained. The second term $T\frac{d(jd)}{dx}$ being the resistance due to change in lever arm is referred to as arch action. Arch action is the concrete contribution through the arch shaped compressive stress developed in uncracked concrete zone as shown in Figure 5-33. Therefore, if the variation of the tensile force in shear span of a beam subjected to shear loading is determined, the contribution of arch action and beam action can be evaluated. For this purpose, first the tensile force (T) at different adjacent sections of the beam need to be determined at different load levels. Then, the lever arm length can be calculated at each section using Eq. (5-4) [210].

$$jd = \frac{M}{T} = \frac{V\,x}{T} \tag{5-4}$$

where x is distance of each section from support, and V is the applied shear force. Then shear resistance arising from beam action and arch action at different sections along the shear span can be calculated using Eqs. (5-5) and (5-6). For each section, *T* and *jd* are the average between 2 points of each section. Then, the shear resistance mechanism (beam and arch action) in a beam can be quantified at every shear force level by averaging calculated arch and beam action contribution to shear resistance in all the selected sections in the shear span [210].

$$(V_{beam})_{each\,section} = jd\left(\frac{dT}{dx}\right) = \frac{jd_i + jd_{i+1}}{2}\,\frac{T_{i+1} - T_i}{x_{i+1} - x_i} \tag{5-5}$$

$$(V_{arch})_{each\,section} = T\left(\frac{djd}{dx}\right) = \frac{T_{i+1} + T_i}{2}\,\frac{jd_{i+1} - jd_i}{x_{i+1} - x_i} \tag{5-6}$$

Fu et al. [211] and Nakamura et al. [212] estimated beam and arch action with use of local stresses predicted by numerical model to investigate shear mechanism of RC members. On the basis of their work, mechanical equilibrium of cross section of RC beam as shown in Figure 5-34 can be expressed by Eq. (5-7).

$$M = (T_s + C_s)\frac{j_s}{2} + C_c j_{C_c} + T_c j_{T_c} \tag{5-7}$$

where T_s and C_s are tensile and compressive forces developed in reinforcing bars, and T_c and C_c are resultant tensile force and compressive force resisted by concrete. j_{C_c} and j_{T_c} are the distance between beam axis and the centroid of concrete compression block and resultant concrete tensile force, respectively. j_s is also the distance between compression bars and tensile bars. If the expression in Eq. (5-7) is differentiated over small cross sections in shear span, the contribution of beam action and arch action can be calculated by Eqs. (5-8) and (5-9).

$$V_{beam} = \left(\frac{dT_s}{dx} + \frac{dC_s}{dx}\right)\frac{j_s}{2} + \frac{dC_c}{dx} j_{C_c} + \frac{dT_c}{dx} j_{T_c} \tag{5-8}$$

$$V_{arch} = C_c \frac{dj_{C_c}}{dx} + T_c \frac{dj_{T_c}}{dx} \tag{5-9}$$

Therefore, the stresses and their centroids can be determined from the numerical model results at different adjacent sections (elements) across the shear span. This incremental change of stresses and their centroids can be utilized to quantify contribution of arch action and beam action to shear strength in the beams.

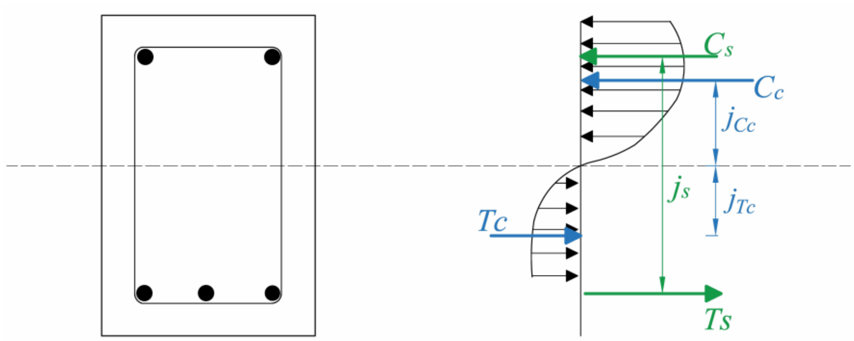

Figure 5-34. Stresses in a beam cross section; stresses in reinforcing bars and concrete [212]

The stress and strain predictions from the numerical analyses was used to evaluate shear resistance mechanism in UHPFRC beams. Variation of contribution of arch actin and beam action to shear capacity, for beams with different reinforcement ratios with different fiber volume fractions were calculated at different stages of loading. Figure 5-35 shows the results for the case of beams with fiber volume fraction of 1% and shear span to depth ratio of 1.5 with different reinforcement ratios. As can be seen, prior to cracking the entire applied shear is resisted through beam action mechanism. Results show that beam action contribution increases even after cracking as opposed to conventional concrete beams without stirrups where shear resistance is nearly completely provided by arch action after cracking. With further increasing load levels (external shear), beam action contribution starts to decrease after reaching its peak values. With reducing the beam action contribution, arch action contribution becomes more dominant.

Also, the results show that in beams with lower reinforcement ratio, the applied shear is significantly resisted by beam action. With increasing longitudinal reinforcement ratio in beams, the contribution of arch action to shear strength increases. As can be seen in Figure 5-35, in beams with longitudinal reinforcement ratio higher than 3.2%, the arch action becomes more dominant and beam action starts to decrease after cracking stages. It can be seen that at higher reinforcement ratios of 5.6% and 7.2%, shear load is entirely sustained by arch action and beam action had no effect on shear resistance. This is due to high shear stresses at higher reinforcement ratios resulting in more widening of the cracks and more propagation of the cracks towards compression zone. Therefore, shear resistance as a result of beam action (aggregate interlock and fiber bridging) decreases and shear is resisted mainly through arch action mechanism. It should be noted that this high contribution of arch action is attributed to high compressive strength offered by UHPFRC.

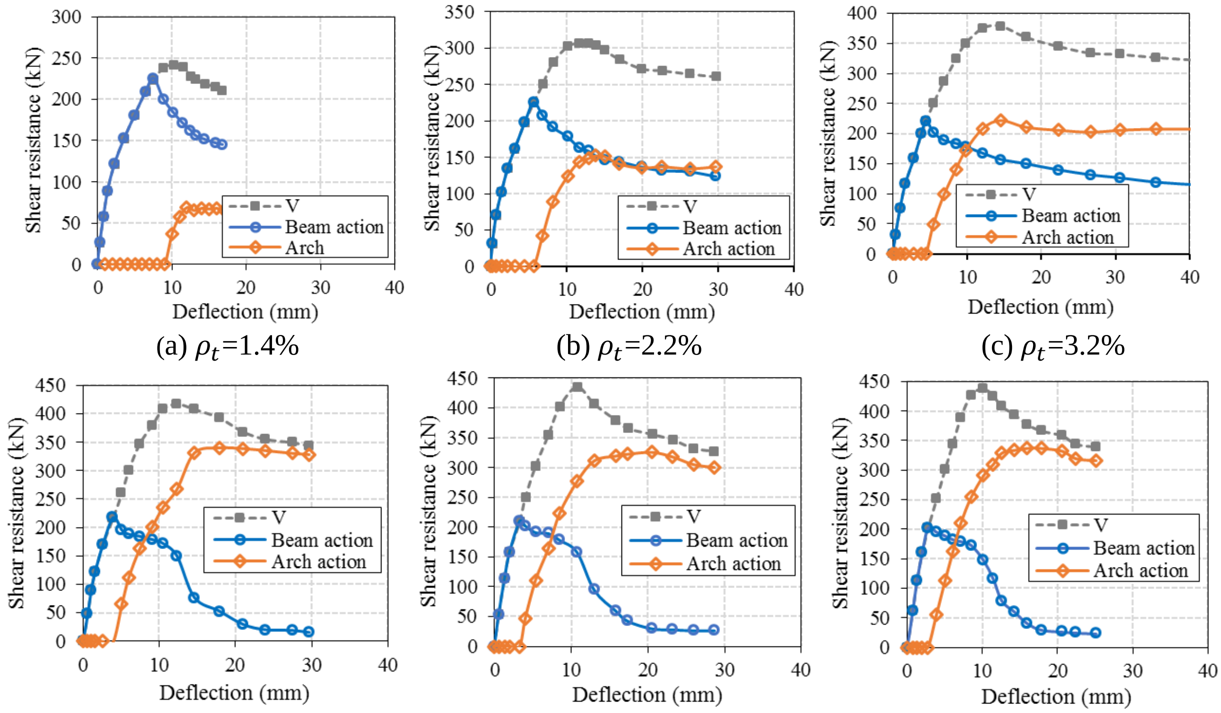

(a) ρ_t=1.4% (b) ρ_t=2.2% (c) ρ_t=3.2%

(d) ρ_t=4.3% (e) ρ_t=5.6% (f) ρ_t=7.2%

Figure 5-35. Beam action and arch action developed in UHPFRC beams (V_f=1%) with $\frac{a}{d}$=1.5 with different reinforcement ratios

Contribution of beam action and arch action in UHPFRC beams with 1% fiber volume fraction with shear span to depth ratios of 2 and 3 were also evaluated and the results are presented in Figure 5-36 and Figure 5-37. Comparison of beams with volume fiber fraction of 1% with shear span to depth ratio of 1, 2, and 3 shows that with increasing length of shear span, the arch action contribution decreases significantly, and beam action becomes dominant mechanism in developing shear resistance. Also, results show that contribution from arch action in beams with smaller reinforcement ratio is negligible and it increases with increasing reinforcement ratios. Similar results are observed for beams with 2% and 3% fiber volume fraction.

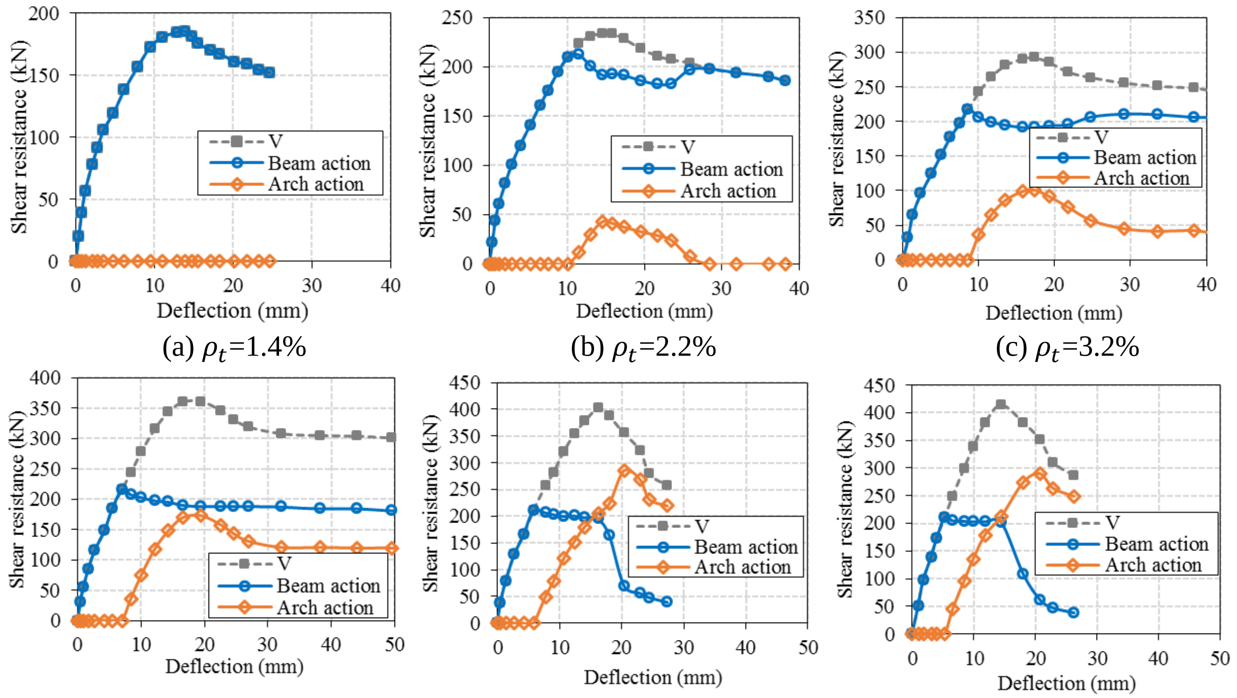

(a) ρ_t=1.4% (b) ρ_t=2.2% (c) ρ_t=3.2%

(d) ρ_t=4.3% (e) ρ_t=5.6% (f) ρ_t=7.2%

Figure 5-36. Beam action and arch action developed in UHPFRC beams (V_f=1%) with $\frac{a}{d}$=2 with different reinforcement ratios

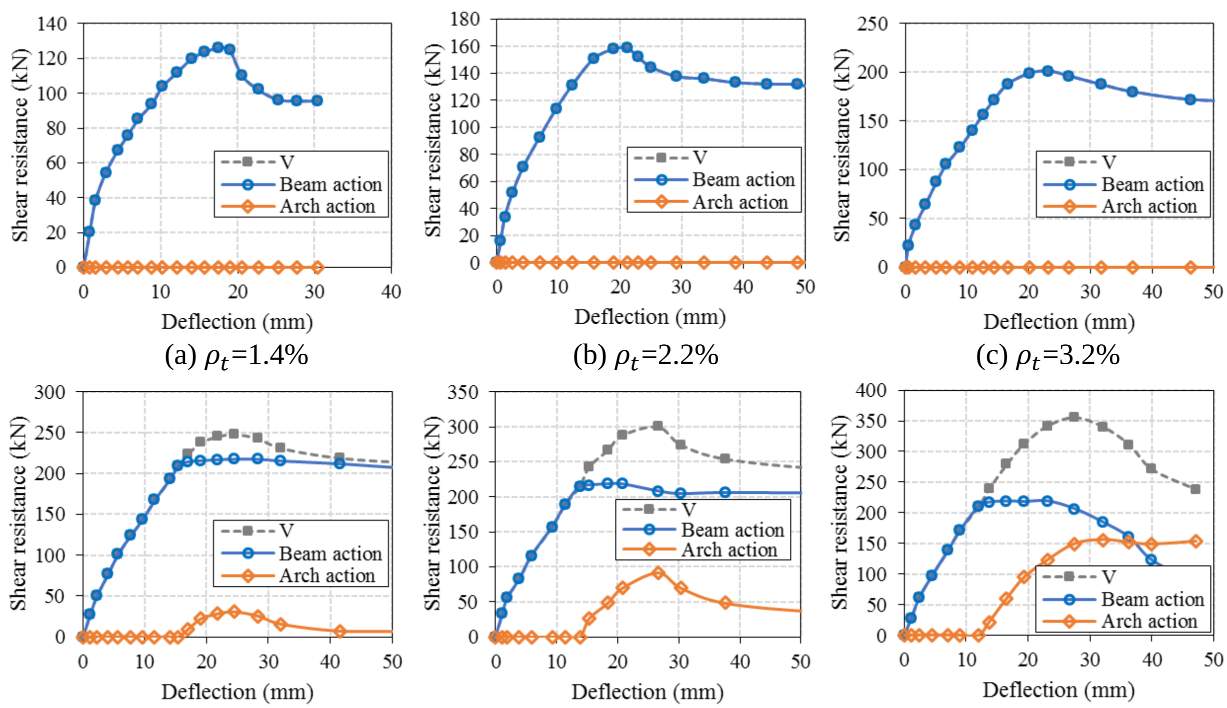

(a) ρ_t=1.4% (b) ρ_t=2.2% (c) ρ_t=3.2%

(d) ρ_t=4.3% (e) ρ_t=5.6% (f) ρ_t=7.2%

Figure 5-37. Beam action and arch action developed in UHPFRC beams (V_f=1%) with $\frac{a}{d}$=3 with different reinforcement ratios

These analyses were also conducted for UHPC beams without fibers and the results for beams with different reinforcement ratios are illustrated in Figure 5-38. The results from these analyses show that in the case of UHPC beams (V_f=0%) beam action starts to decrease significantly after initiation of cracking and arch action increases with a constant rate until peak capacity is attained. In other words, after developing the cracks in UHPC beams, beam action drops to zero, and shear capacity of UHPC beams is mainly through arch action mechanism. This response is due to absence of fibers that results in reduction of interfacial shear resistance (fiber bridging). Also, with increasing the reinforcement ratio, the contribution of arch action increases. This increasing contribution of arch action is attributed to high compressive strength of UHPC as presence of steel fibers has small effect on compressive strength.

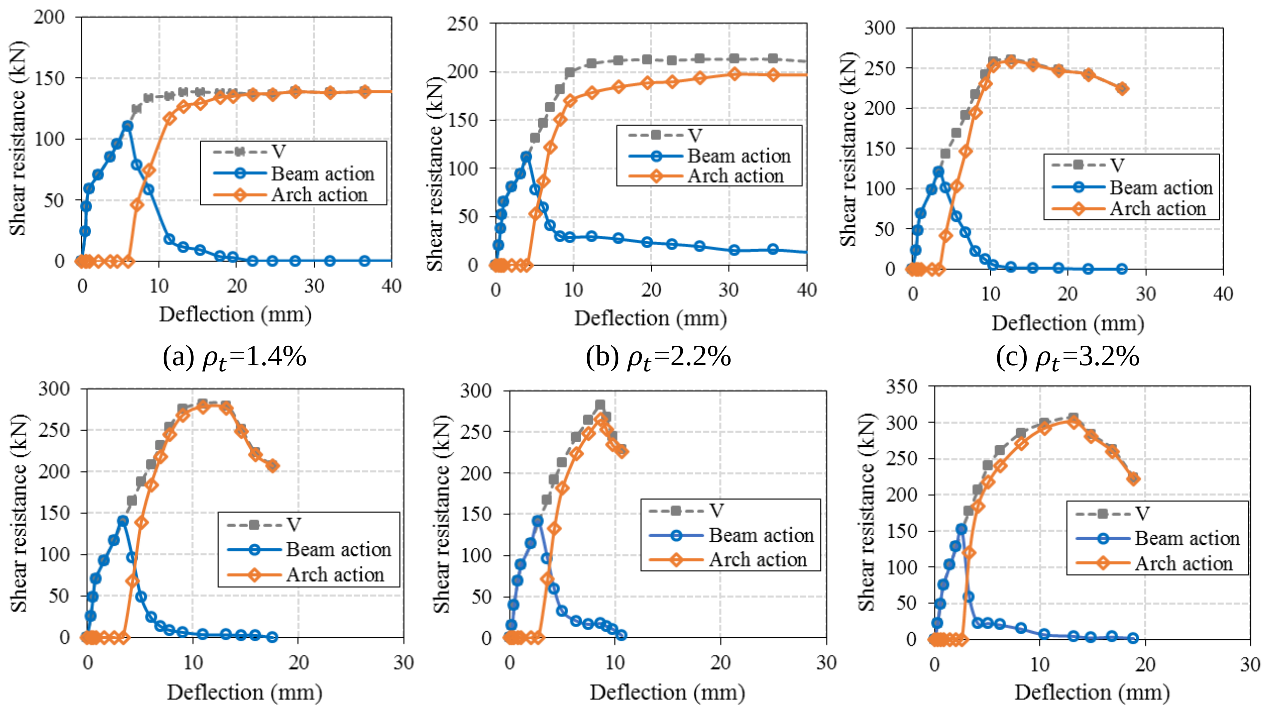

(a) ρ_t=1.4% (b) ρ_t=2.2% (c) ρ_t=3.2%

(d) ρ_t=4.3% (e) ρ_t=5.6% (f) ρ_t=7.2%

Figure 5-38. Beam action and arch action developed in UHPC beams (V_f=0%) with $\frac{a}{d}$=1.5 with different reinforcement ratios

It should be noted that the combined resistances (calculated beam and arc actions) are equivalent to external shear load demonstrating the reliability of the approach. The results of these analyses are summarized in Figure 5-39. This figure illustrates variation of the ratio of arch action contribution to total shear capacity at peak state with reinforcement ratio and shear span to depth ratio. It can be seen that with increasing reinforcement ratio arch action contribution to shear strength increases. Since with increasing reinforcement ratio, and consequently with increasing load carrying capacity, tensile and shear stresses increase leading to more widening of the cracks. This results in less loads and stresses that can be transferred by the mechanism of aggregate interlock and fiber bridging on the crack surfaces. Also, decreasing shear span to depth ratio results to higher contribution of arch action to shear resistance as shorter arch structure is stronger than slender arch structure [210].

Further, Figure 5-39(b) shows that in UHPC beams without stirrups arch action mainly sustain the shear loading in the beams. Adding steel fibers results in reduction of the ratio of arch action contribution to shear resistance as fiber bridging effects gets activated after cracking and results in higher concrete contribution to shear strength due to beam action.

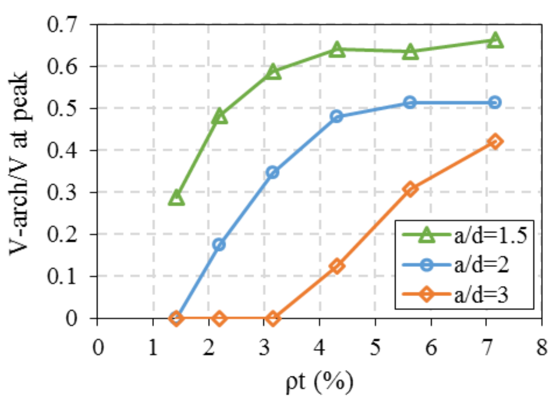

(a) Beams with V_f=1%

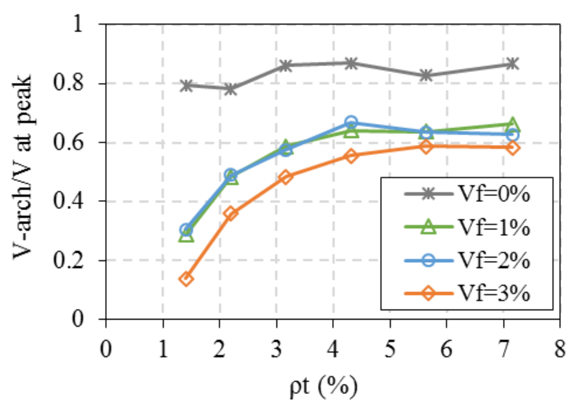

(b) Beams with $\frac{a}{d}$=1.5

Figure 5-39. Variation of ratio of arch action contribution to shear strength in UHPFRC beams with different V_f and $\frac{a}{d}$

Moreover, beam action and arch action resistance for beams with different reinforcement ratios with shear span to depth ratio of 1.5 at peak state is shown in Figure 5-40. As can be seen, the arch action resistance is almost the same for different fiber volume fractions. However, beam action resistance at peak load increases linearly with increasing fiber volume fraction. Therefore, the increase in shear strength of UHPFRC beams with increasing fiber volume fraction is due to increase in beam action contribution arising from ability of fibers in controlling the crack widths.

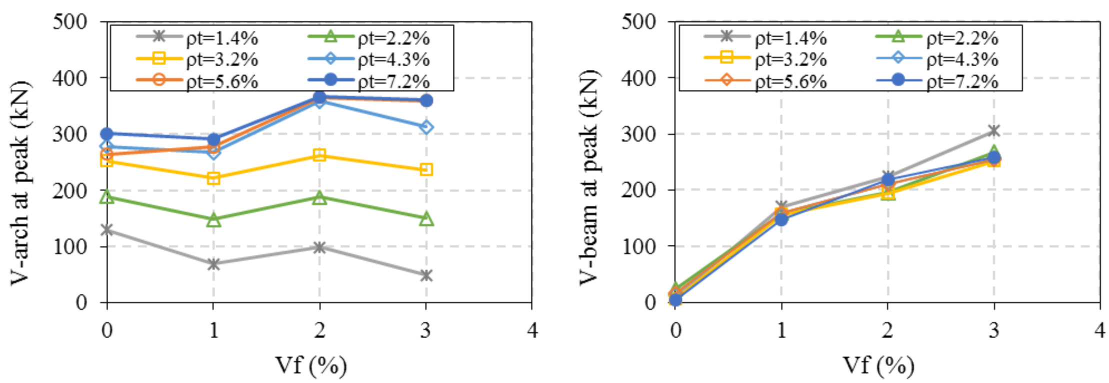

(a) Arch contribution (b) Beam contribution

Figure 5-40. Contribution of arch action and beam action to shear strength of UHPC beams with $\frac{a}{d}$=1.5 at peak load

Effect of shear reinforcement in shear resistance mechanism is shown for three beams with different fiber volume fractions in Figure 5-41. In these beams shear failure is the dominant failure mode and removing stirrups results in reduction of load carrying capacity and ductility of the beams (see section 5.5). In these beams without stirrups beam action resistance drops significantly after reaching its peak resistance. However, in the same beams but with shear reinforcement, beam action contribution is sustained after reaching peak load, and therefore the beams exhibit higher shear capacity. This increase in beam action is due to ability of stirrups in limiting the opening of diagonal cracks, therefore it enhances stress transfer between crack surfaces. Also, stirrups increase the arch action contribution, which can be attributed to confinement effect that can enhance the compression strength.

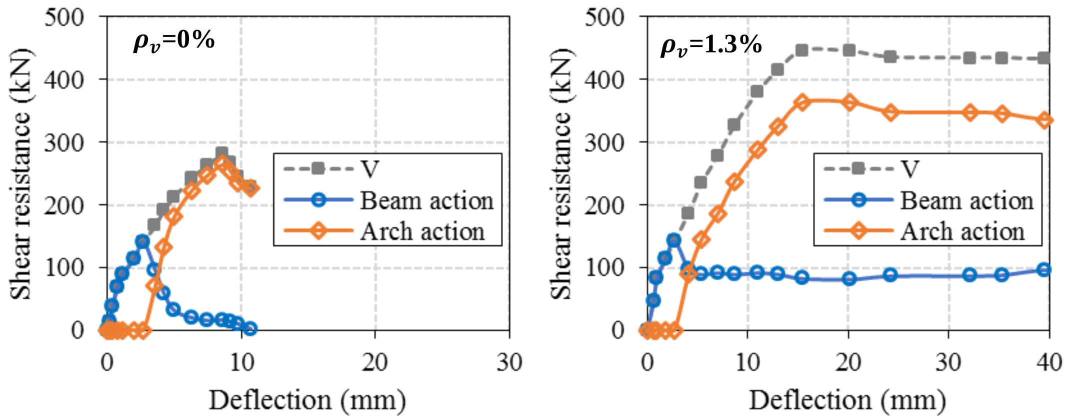

(a) V_f=0%, $\frac{a}{d}$=1.5, ρ_t=5.6%

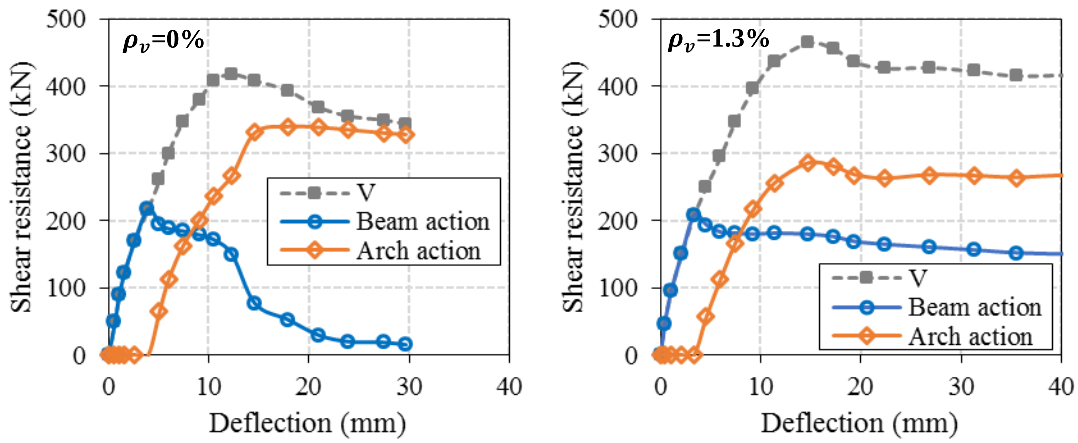

(b) V_f=1%, $\frac{a}{d}$=1.5, ρ_t=4.3%

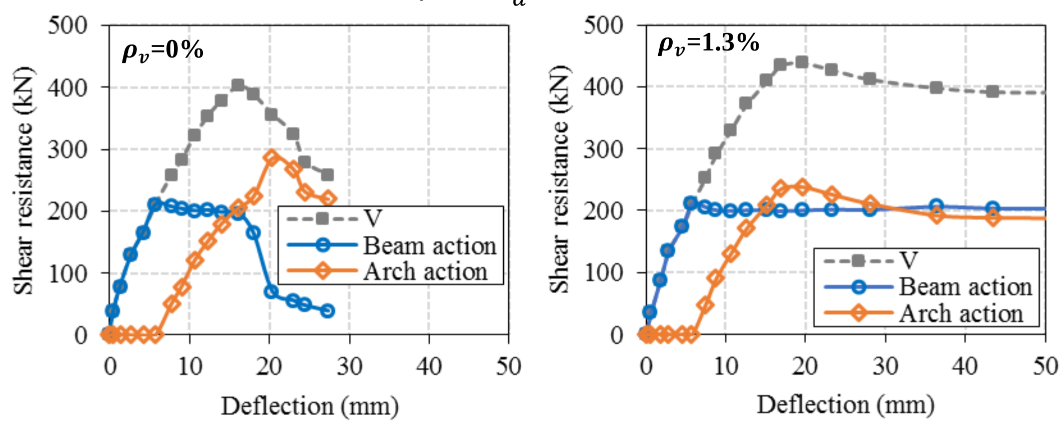

(c) V_f=1%, $\frac{a}{d}$=2, ρ_t=5.6%

Figure 5-41. Effect of presence of shear reinforcement in beam action resistance

5.8 Cost Effectiveness of UHPC

UHPC has emerged as a promising material for infrastructural applications owing to its superior strength properties, improved post cracking and ductility properties, accompanied with enhanced durability. UHPC makes it possible to design precast multi story buildings with column-free bays as large as 60 ft by 60 ft, and also to design bridges with long spans well beyond the current limits on precast prestressed concrete (about 200 ft) [141]. However, initial cost of UHPC is higher than conventional concrete due to high volume of cement and steel fiber. The cost of UHPC in North America is estimated to be $2000 per cubic yard [213,214], as compared to $100 per cubic yard for conventional normal strength concrete of 35 MPa. The cost of fibers depending on the volume fraction is between $250 and $500 per cubic yard [213]. The cost of UHPC in Europe is about $760 per cubic yard due to increased applications as compared to US [28,215].

The initial cost of UHPC can be offset with improved mix design, fabrication procedure, optimized structural design, and long term durability benefits. Number of precasters sponsored by Precast/Prestressed Concrete Institute (PCI) have developed UHPC mixes with reduced cost of about $600 to $800 per cubic yard. Further, in this study an improved batch mix proportions and innovative procedure for preparing and curing UHPC, as developed by Metna Company in which coarse aggregates were used so as to reduce the dosage of cementitious material, can lower the cost of UHPC. This batch mix can be prepared using locally available materials in a conventional ready-mix truck, which can reduce the cost of UHPC [41].

Although initial cost of UHPC is higher than conventional concrete, UHPC structures can be cost effective when other factors are taken into consideration. The improved mechanical properties of UHPC allows the design of members with smaller sizes and smaller reinforcement area for carrying same level of loading as compared to conventional concrete as shown in Figure 5-42

[28,216,217]. The reduced size of the UHPC members results in reduced weight leading to lower design loads on the structures and thus more cost-effective construction [28,218,219]. Also, as shown in this study, shear reinforcement can be eliminated in beams leading to more economical constructions. Further, high durability of UHPC results in long service life arising from improved permeability resistance of UHPC to water and chemicals and lesser susceptibility to corrosion in rebars, which in turn reduces cost for maintenance, repair, rehabilitation, and re-construction activities. In addition, the concrete cover required to resist weathering effects and harsh environments is smaller in UHPC members as compared to NSC [28,216]. Such reduced cover can enhance sectional moment capacity especially in prestressed members. Improved permeability resistance and freeze and thaw performance of UHPC yield in achieving more than 100 year design life even in the aggressive environment [218].

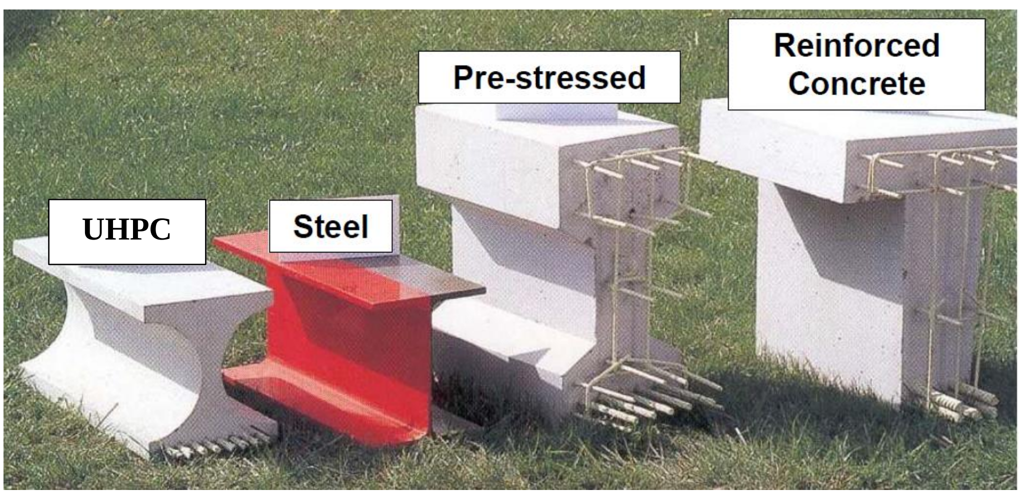

W (kg/m):	140	112	467	530
h (mm):	355	355	710	710

Figure 5-42. Comparison of size and weight of beams made with UHPC, steel, and conventional concrete with same load carrying capacity [220,221]

Moreover, UHPC can lead to lower environmental impact as compared to conventional construction materials. Due to very low water to binder ratio in UHPC, only part of cement hydrates during curing. Therefore, up to 40% of volume of cement in UHPC can be replaced by crushed quartz, blast furnace slag, or fly ash without reducing compressive strength that can reduce the energy consumption and greenhouse gas emissions associated with cement usage [28,31–33,216,222].

Number of cost comparisons have been made by taking into consideration size of members and volume/weight of utilized concrete in construction. One example is the bridge girder and deck design by PCI shown in Figure 5-43. Use of UHPC resulted in reduction of concrete volume by 45% and also reduced the number of required strands in girder and complete removal of shear reinforcement [216]. The expansion of Haneda Airport Runway D, made with UHPC precast slab, is another example of how weight reduction and durability properties make UHPC an economical construction material. Application of UHPC to deck slabs resulted in 56% reduction of self-weight of the structure. The size and weight of the slabs using conventional concrete and UHPC is compared in Figure 5-44 [223]. Also, improved durability and freeze and thaw performance of UHPC reduces life-cycle cost of the project [217–219].

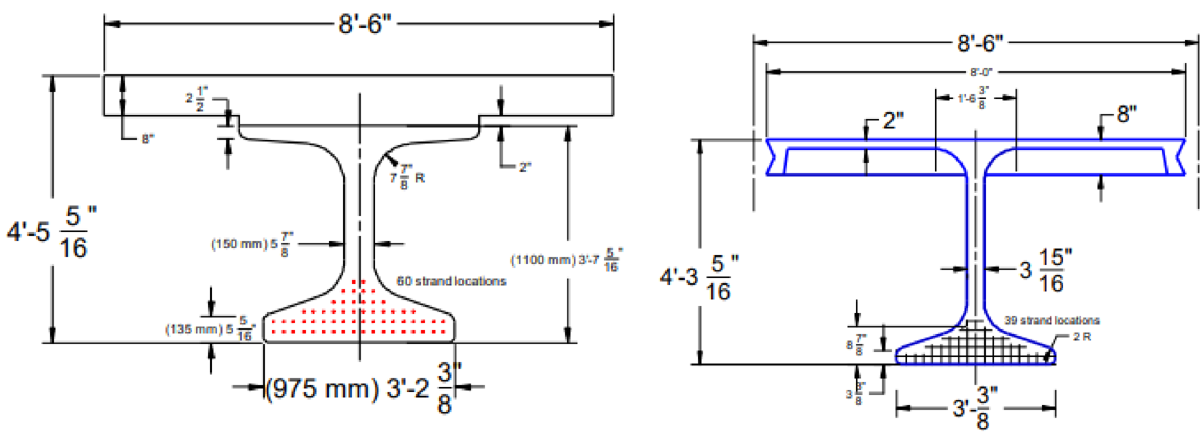

(a) (b)

Figure 5-43. Comparison of the designed cross sections for a 110 ft bridge using (a) conventional concrete, (b) UHPFRC [216]

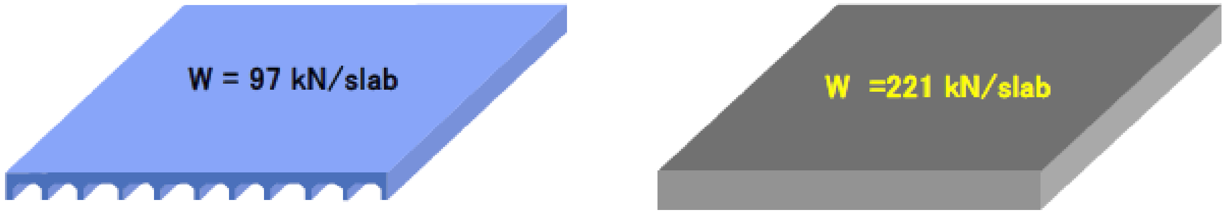

(a) UHPC slab (a) NSC slab
(Average thickness: 135 mm; Unit dead load: 3.83 kN/m^2) (Average thickness: 320 mm; Unit dead load: 7.84 kN/ m^2)

Figure 5-44. Comparison of UHPC and conventional concrete slab in Haneda Airport [223]

In the first world's UHPC cable roadway bridge, UHPC girder with width of 29.5m and height of 1.8 was designed. UHPC girder resulted in 33% lighter structure as compared to conventional concrete girder as shown in Figure 5-45. Therefore, the required stay cables and size and cost of the foundation was reduced [147]. Another example is a Japanese footbridge (Sakata Mirai) that its self-weight is only 20% of that of a conventional concrete bridge. This decreased self-weight of the bridge resulted in reduction of the costs of the foundations. The final cost of this UHPC bridge was 10% lower than that of a comparable bridge made with conventional concrete [217,223].

Although it is hard to put a dollar figure on comparative cost between UHPC and conventional concrete construction, UHPC construction can be cost effective considering its initial and long term benefits. UHPC members can be designed with smaller section, less reinforcement area, and without shear reinforcement. Moreover, UHPC is a solution for sustainable construction due to its improved strength properties, improved durability, and low porosity leading to excellent resistance against aggressive environment. Improved durability of UHPC results in long service life with reduced maintenance cost. Further, UHPC construction results in lower environmental impact, less energy consumption and greenhouse gas emissions. It should be noted that this cost benefit of UHPC is considering the current design and construction practices. With increasing interest in UHPC applications and research studies, and improvement of design specifications for batch mix proportioning as well as structural design, cost of UHPC structures will continue to decrease in the near future.

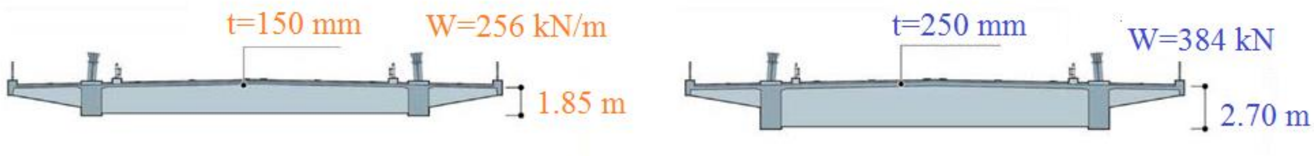

(a) UHPC (b) NSC

Figure 5-45. Comparison of the designed UHPC and conventional concrete girder in first UHPC cable stayed roadway bridge (W denotes weight)

5.9 Summary

In order to evaluate effect of different parameters on structural response of UHPFRC beams, a set of parametric studies was conducted utilizing the developed finite element based model and analytical sectional analysis approach. The varied parameters included fiber volume fraction in UHPFRC, longitudinal reinforcement ratio, loading type, shear span to depth ratio, and presence of stirrups. Further, predictions from the model was used to evaluate shear resisting mechanisms of arch and beam action in UHPFRC beams. Based on the results from this parametric studies, the following conclusions are drawn:

- Addition of steel fibers significantly improves the load carrying capacity and post-cracking stiffness in UHPFRC beams as compared to UHPC beams due to fiber bridging at the crack surfaces resulting in strain hardening in UHPFRC. However, including fibers decreases the ductility in beams with flexural failure mode. This reduction of ductility is attributed to cracking pattern in UHPFRC beams that undergoes widening of a single macro crack leading to localization of the deformation in longitudinal steel reinforcements at major crack surface. Therefore, steel bars yield at a relatively smaller deflection resulting in lower ductility.

- Removing stirrups does not result in reduction of load carrying capacity and ductility of UHPFRC beams subjected to dominant shear loading except for UHPFRC beams with high reinforcement ratio ($\rho_t \geq 5\%$) that need stirrups to obtain their ultimate moment capacity before shear failure.
- In UHPFRC beams with high reinforcement ratio and shear failure mode, contribution of stirrups is negligible till almost 70% of shear capacity is attained. This is in contrast to conventional concrete beams, where contribution of stirrups to shear resistance increases immediately after initial cracking.
- Increasing shear span to depth ratio or fiber volume fraction change mode of failure from shear to flexure-shear and pure flexure. Since addition of steel fiber improves post cracking stiffness and tensile strength of concrete and therefore transforms failure from shear to flexure (more ductile). Also, with longer shear spans, shear stresses decrease leading to dominant flexural stresses and purely flexural failure mode.
- Beam action contribution to shear capacity in UHPFRC beams increases even after cracking as opposed to conventional concrete beams without stirrups where shear resistance after cracking is mainly provided by arch action. Further, contribution of beam action to shear resistance increases linearly with increasing fiber volume fraction. Therefore, the increase in shear strength of UHPFRC beams with increasing fiber volume fraction is due to increase in beam action contribution arising from ability of fibers in controlling the crack width.

- With increasing reinforcement ratio in UHPFRC beams, arch action contribution to shear strength increases as the increased load capacity results in higher levels of tensile and shear stresses and more widening of the cracks. This leads to less loads and stresses that can be transferred by the mechanism of aggregate interlock and fiber bridging on the crack surfaces. Also, decreasing shear span to depth ratio results to higher contribution of arch action to shear resistance as shorter arch is stronger than slender arch.

CHAPTER 6

6 MACHINE LEARNING FRAMEWORK FOR PREDICTION OF FAILURE MODE AND CAPACITY OF UHPC BEAMS

6.1 General

Despite number of research investigations on evaluating structural response of UHPC members, there are limited provisions in international codes, standards as well as best practice documents for structural design of UHPC beams [25,26,139,224]. This clearly highlights the need for simplified provisions for the design of UHPC beams.

The developed finite element based model and analytical approach can predict structural response of UHPC beams in the entire range of loading. However, these models are complex to apply for practical design purposes. Further, these models require detailed material models, whose accuracy depends on numerous parameters and thus there can be large variability in material properties of UHPC. As such, to promote the applicability of UHPC in concrete structures, it is essential to develop simplified design methodologies that can optimize the superior range of properties offered by this new class of material.

Artificial intelligence (AI) is an efficient alternative approach to traditional modeling techniques, which offer advantages to overcome problems associated with large variability and interdependency of parameters. Further, AI is an effective and powerful aid to predict response parameters when testing and numerical modeling are not effective and can result in significant savings in terms of human time and effort spent in experiments and modeling [225].

Recently, AI and machine learning (ML) based techniques are being extended to structural engineering applications such as structural health monitoring [226–239], predictive material models [240–247], earthquake engineering [248–251], etc. Numerous ML algorithms have been adopted to develop data driven intelligent models for predicting the mechanical and structural properties of concrete [241,242,247,252–254]. For example, a model employing least squares support vector machine (LS-SVM) was developed by Vu and Hoang [252] to predict punching shear capacity of FRP-reinforced concrete slab. The applicability of support vector machine (SVM) for forecasting the elastic modulus of normal and high strength concrete was assessed by Yan and Shi [240]. Also, a computational model was developed by Lee et al [253] using artificial neural network (ANN) for prediction of shear strength of slender fiber reinforced concrete beams and it was shown that the ANN-based model performed better as compared to use of conventional empirical expressions.

Similarly, genetic programming (GP) is being extended to applications in concrete materials and structures [255,256]. Special attention was paid to high performance concrete (HPC), wherein Castelli et al. [257] applied GP to predict compressive strength of HPC with success. Kara [258] also used GP to evaluate shear strength of FRP-reinforced concrete beams without stirrups. Kara found that the GP-proposed model yielded better shear capacity predictions in FRP-reinforced concrete beams as opposed to predictions based on equations in current design codes. Ahmadi et al. (2020) used a hybrid approach wherein ANN was used in combination to GP to arrive at formulae capable of predicting shear capacity of steel fiber-reinforced concrete (FRC) beams without stirrups.

In this chapter, a computational framework employing AI and ML was developed to predict mode of failure, flexural and shear capacity of UHPC beams [259]. The main components of this framework consist of data collection, failure mode classification, and capacity prediction. Following sections present the details of these three steps.

6.2 Proposed Machine Learning Framework for Response Prediction

Machine learning (ML) deals with the study, design, and development of algorithms, which can learn from available set of data (observations) on certain systems and apply this to make predictions on the behavior of systems. ML methods are being increasingly applied over the last decade for various structural engineering applications [225,260]. In this study ML and pattern recognition/classification was applied to predict the failure mode of UHPC beams and then to evaluate flexural and shear capacity of these beams.

The proposed ML framework shown in Figure 6-1 comprises of three steps; namely, data collection, failure mode classification, and capacity prediction of UHPC beams. As part of data collection step, a large set of experimental data on UHPC beams was compiled (section 6.2.1). Then, critical parameters governing response of UHPC beams were identified using feature selection techniques, and these parameters were considered as pattern features. That is, each pattern represents a beam with its corresponding critical parameters. These patterns were then used as input to the failure mode classification step, in which different ML algorithms were utilized to classify the failure mode i.e., shear, or flexure-shear, or flexure. In the final step, based on the mode of failure, flexural or shear capacity of UHPC beams were predicted. The data from UHPC beams failed under flexure was utilized to predict flexural capacity of the beams utilizing support vector machine (SVM) regression algorithm. Also, the data from beams with shear failure mode was used to apply genetic programming (GP) algorithm to predict shear capacity of the beams and to develop simplified expressions for capacity prediction. A detailed description of the aforenoted steps is provided in the following subsections.

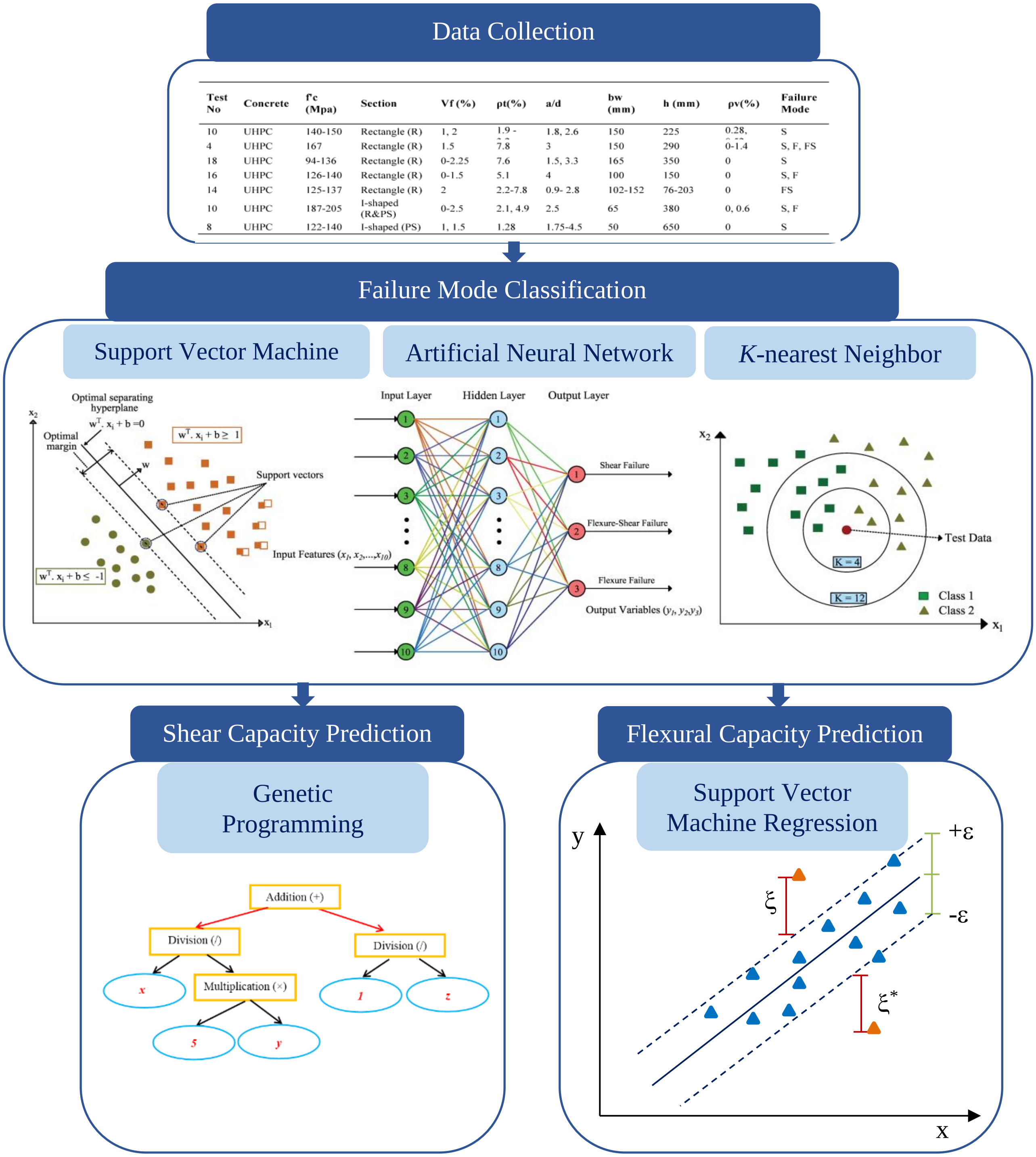

Figure 6-1. Schematic of the proposed ML framework for failure mode and flexural and shear capacity prediction of UHPC beams

6.2.1 Database Development

For use of ML approach to any problem, large set of data on the behavior of such problem is needed. A detailed literature review was undertaken to collect data from experiments conducted on beams fabricated with UHPC, high performance concrete (HPC), and reactive powder concrete (RPC) beams. The beams had varying features with regard to cross sectional shapes (rectangular, T-shaped, and I-shaped), cross sectional size, span length, longitudinal reinforcement ratio, shear reinforcement ratio (i.e. stirrups), prestressing level, loading set-up and fiber characteristics. It should be noted that the results from numerical studies in literature were not included in the data set, since numerical results are highly dependent upon the adopted material models, meshing practices, as well as other assumptions used in modeling.

A summary of the selected experimental programs with selected design variables, with their range and statistical analysis (mean, maximum, minimum, and standard deviation of each feature), along with observed failure mode is provided in Table 6-1. In addition, distribution of selected variables in dataset, such as beams configuration (rectangular or flanged, reinforced or prestressed), compressive strength (f_c'), width (b_w), effective depth (d), tensile reinforcement ratio or prestressing strand ratio (ρ_t), shear reinforcement ratio (ρ_v), shear span to depth ratio ($\frac{a}{d}$), volume fiber fraction (V_f), fiber aspect ratio (ratio of fiber length to fiber dimeter: $\frac{L_f}{d_f}$), and prestressing level (σ_p) with respect to their frequencies is shown in Figure 6-2. In this figure, frequency indicates the number of times that each specific value (or range) of the variables appeared in the dataset. Figure 6-2(a) illustrates number of data from tests on different beams configurations such as rectangular-reinforced (R), flanged beams- reinforced (R), and flanged beams- prestressed (PR). Figure 6-2((b) to (i)) show the number of data for different values or ranges of variables in the collected dataset. Additional details on the experiments, from which the data was generated, can be found in the relevant references [49,52,61,78,113,123,124,126–128,136,159,198,261–297].

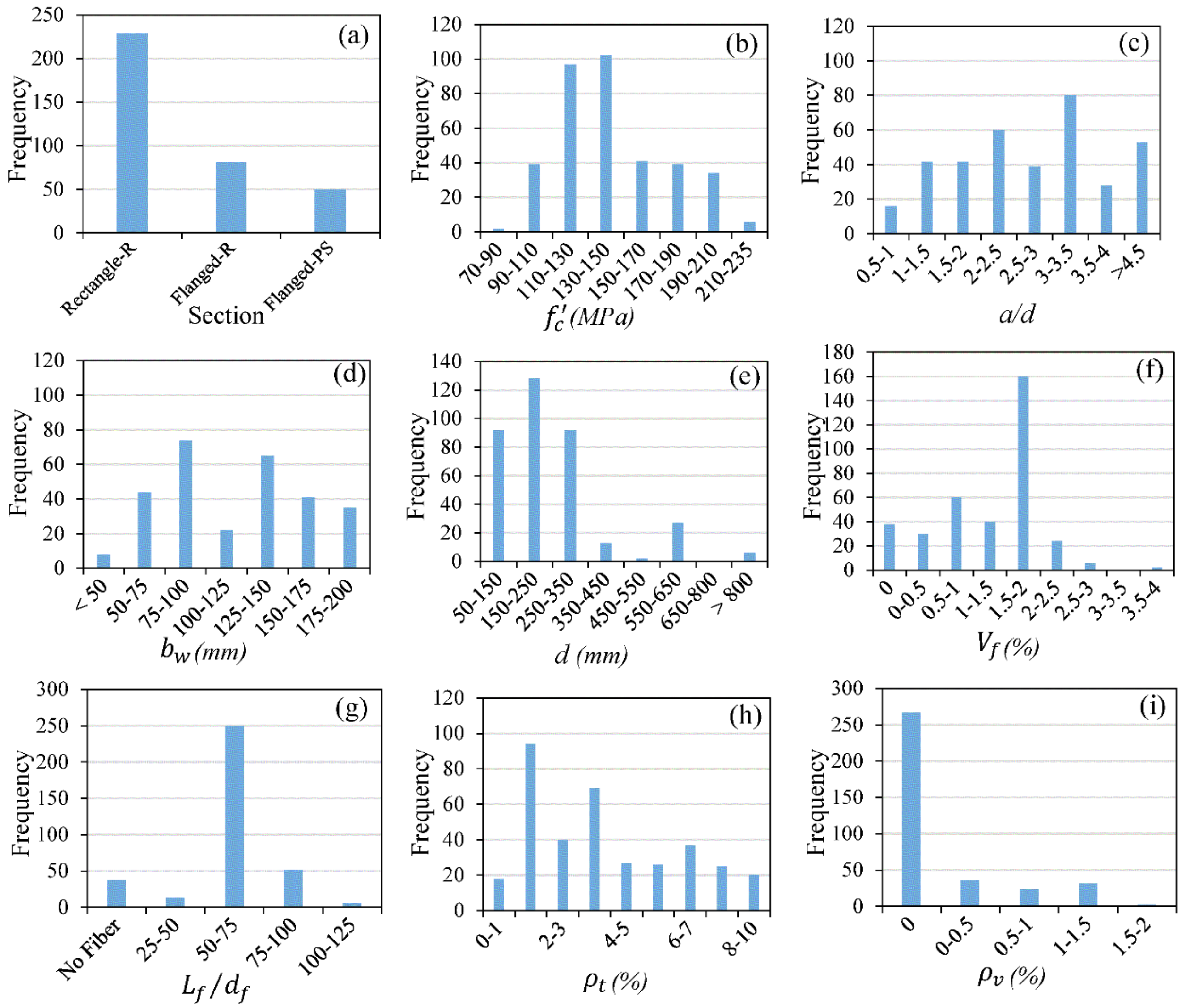

Figure 6-2. Distribution of the variables in the experimental dataset

Table 6-1. Summary of data collected from tests on UHPC beams

Ref.	Test No	Concrete	f'_c (Mpa)	Section	$\frac{L_f}{d_f}$	V_f (%)	ρ_t (%)	*a/d*	b_w (mm)	$\sigma_p (MPa)$	*d* (mm)	ρ_v (%)	Failure Mode
[198]	10	UHPC	140-150	Rec.-R	59.1	1, 2	1.9 -3.2	1.8, 2.6	150	0	183	0.28-2	S
[261]	4	UHPC	167	Rec.-R	87.5	1.5	7.8	3	150	0	220	0-1.4	S, F, FS
[262]	18	UHPC	94-136	Rec.-R	68-79	0-2.25	7.6	1.5, 3.3	165	0	260	0	S
[263]	16	UHPC	126-140	Rec.-R	37.5-81	0-1.5	5.1	4	100	0	124	0	S, F
[127]	14	UHPC	125-137	Rec.-R	65	2	2.2-7.8	0.9- 2.8	102-152	0	55-180	0	FS
[126]	10	UHPC	187-205	I-R&PS	65-67	0-2.5	2.1, 4.9	2.5	65	0,12.6	305	0, 0.6	S, F
[123]	8	UHPC	122-140	I-PS	75-125	1, 1.5	1.28	1.75-4.5	50	19.2	620	0	S
[264]	4	UHPC	142-159	I-R	81.3	0-2.5	2.2	4.4	50	0	225	0, 1	S, F
[265]	11	UHPC	163-185	I-R	75	0, 1, 2	6.2	3.3-3.5	60	0	310	0-2	S
[136]	7	RPC	149-171	I-PS	60-65	1.25-2.5	2.7	3.3	50	0-14.3	600	0	S
[10]	3	UHPC	100-200	Rec.-R	40	0, 2	4.1	2	200	0	300	0	S
[266]	9	UHPC	135	Rec.-R	80	0.4	3.9-4	1, 1.5, 2	120	0	150-270	0	S
[267]	7	UHPC	94-120	T-R	30-65	0.5-2	3.1	3.2	40	0	114	0-1.1	S, FS
[268]	4	RPC	104-107	I-R&PS	65	0.75	3.3, 3.6	2	70	0-6.6	350	0	S
[269]	8	UHPC	127-135	Rec.-R	65	0, 0.55	12-1.7	2.3	100	0	130	0, 1.3	S, F
[270]	7	UHPC	134-183	I-PS	60, 117	0-2.5	3.2, 2.5	3.8, 4.4	60	14.3,17.1	316	0	S
[271]	1	UHPC	202	I-PS	81	2.5	4.3	5.1	70	27	265	0	S
[159]	8	UHPC	167,174	Rec.-R	65	1.5	0.9-2.5	1.6-5.9	180	0	235, 383	0-0.8	S, F, FS
[272]	3	UHSC	199,215	Rec.-R	65	0, 2	3.6	2-6	200	0	300	0, 0.34	F, FS
[273]	5	UHPC	173	Rec.-R	25	1.5	3.6	0.79-4	80	0	350	0.47-1.7	FS
[274]	13	HPC	97-122	Rec.-R	80	0.4	1.4-6.1	1-3	100	0	167	0	FS
[275]	5	UHPC	135	Rec.-R	65	2	0.6-2.8	0.8-2.7	127, 152	0	56, 185	0	FS
[276]	1	UHPC	212	I-R	65	2.5	4.87	2.5	65	0	305	0	FS
[78]	7	UHPC	180-207	Rec.-R	60	0, 2.5	2.5-7.2	3.4-3.7	177-180	0	162-177	0	FS
[277]	31	RPC	123	Rec.-R	65	2	4.5-9.8	1-3.5	150	0	200, 219	0-0.58	S, F, FS
[278]	4	UHPC	167-181	I-R	62.5	0, 2	1.7, 2.6	1, 4.8	60	0	210	0-1.3	S, F
[279]	8	UHPC	121,143	I-R	54.6	0, 2	0.8-2.2	3.1	50	0	225	0	S, F, FS
[124]	12	UHPC	167-193	I-R&PS	65	1, 1.5, 2	1.9	2.5, 3.4	50	0-13.7	640	0	S
[280]	11	UHPC	144-152	I- R	65	1, 2, 3	2.5- 6.7	4, 6, 8	50	0	315, 397	0	S, F
[52]	4	UHPC	200	I-PS	65	2	1.6	2.2-13.6	152	12.3	808	0	S, F
[281]	6	HPC	137-147	I-R	65	0- 1.6	3.4	2.8	50	0	350	0, 1.3	S, F
[282]	4	UHPC	158-188	T-PS	65	2	0.4-0.5	2-3	120	1.4,1.7	500-1200	0, 0.37	F
[283]	6	UHPC	120-153	Rec.-R	65	0, 1, 2	1.1-2.2	2.5	76	0	86	0	S, F

Table 6.1 (cont'd)

Ref.	Test No	Concrete	f'_c (Mpa)	Section	$\frac{L_f}{d_f}$	V_f (%)	ρ_t (%)	a/d	b_w (mm)	$\sigma_p (MPa)$	d (mm)	ρ_v (%)	Failure Mode
[284]	8	UHPC	141	Rec.-R	65	2	1.1-5.2	1.6-3.5	150	0	174-188	0.4-1.1	F, FS
[285]	5	UHPC	145-172	Rec.-R	65	2	0- 2.5	2.3, 4.6	178	0	265	0	FS, F
[286]	3	HPC	106-114	Rec.-R	50	0-1	1	2	200	0	380	0, 0.19	S, FS
[287]	3	UHPC	137	I-R	60.5	1	3.5	2.3, 2.5	60	0	375	0, 0.84	S, F
[288]	8	RPC	111-125	I-R&PS	75	1.6	4.6	1.1-3	50	0-18.7	260	0.6, 1.3	S
[49]	10	UHPC	200-230	Rec.-R	65-100	0, 2	0.9-1.5	5	150	0	177,179	1.19	F
[289]	4	UHPC	146	Rec.-R	65	2	0.8-2.3	1.4	152	0	132	0	FS, F
[290]	7	RPC	97-121	Rec.-R	80	0, 1, 2	1.1, 2.4	3.3	110	0	130	0	S, F
[291]	18	RPC	78-151	Rec.-R	65	0- 2	3.4-5.9	2.5-4.5	100	0	112	0	S, FS
[61]	6	UHPC	190-197	Rec.-R	65	2	0-1.96	4.2-5.3	180	0	215-270	0	F
[292]	8	UHPC	130-177	Rec.-R	65	1, 2, 4	0, 1.7	3.1	100	0	130	0	FS, F
[293]	11	UHPC	136-155	I-R	54-62.5	1.5-2.5	1.5	1.25	50	0	223	0	S, FS
[294]	8	UHPC	133-167	Rec.-R	81.2	0, 1.5	0.9-4.3	3.1-3.9	150	0	180-220	0.67	F
[295]	8	UHPC	170	Rec.-R	86.7	2	0.67-3	5	150	0	212-224	0.25	F
[128]	4	UHPC	197	Rec.-R	65	2	0-1.71	3.9-4.7	200	0	222-270	0	F
[296]	7	UHPC	137-149	Rec.-R	50	0-1	0.72	2.9	150	0	210	1.31	F
[297]	6	UHPC	145	Rec.-R	65	2	0-5.1	1.5-3	152	0	76-152	0	F, FS
[113]	4	UHPC	143	Rec.-R	64	2.25	1.8-2.3	5.8-10.3	150,250	0	116,210	0.42,0.7	F
Avg.	-	-	145.8	-	60.5	1.5	3.6	2.9	108	1.6	249.2	0.2	-
Min.	-	-	78	-	0	0	0	0.8	40	0	54	0	-
Max	-	-	232	-	125	4	9.8	13.7	200	27	1200	2.1	-
Std.Dev.	-	-	29.8	-	24.3	0.8	2.3	1.4	47.4	4.7	152.7	0.4	-

*Rec.: Rectangular section; I: I-shaped section; T: T-shaped section; R: Reinforced beam; PS:Prestressed beam
F: Flexural failure; F-S: Flexural-shear failure; S: Shear failure

6.2.2 ML Algorithms

Three different ML algorithms, namely support vector machine (SVM), artificial neural networks (ANNs), and *k*-nearest neighbor (*k*-NN) were utilized to classify the failure mode of UHPC beams. A brief description of these algorithms is presented in this section, while the detailed information can be found in the published references [298–302]. It should be noted that different ML algorithms have been used in the domain of civil engineering. Yet, ML algorithms employed in this study were simply chosen to ensure best classification performance can be achieved since the applicability and effectiveness of these algorithms for various civil engineering applications have been previously demonstrated [225,260].

6.2.2.1 Support Vector Machine

SVM is a well-established ML algorithm utilized for classification tasks that employs the structural risk minimization principle, while introducing a kernel trick [298]. SVM problem originated from a supervised binary classification, in which most of the solutions are evaluated through obtaining a separating hyperplane among classes. The SVM algorithm can be illustrated by considering a data set $T = \{(x_i, y_i), i = 1, 2, \dots, N\}$, which refers to a training set (i.e. randomly assigned UHPC beams from the collected database, wherein each beam has a set of features). This data set consists of an N number of m-dimensional features vectors (data) x_i and their corresponding labels $y_i \in \{-1, 1\}$. SVM aims to find the separating boundary between two classes. This is done through maximizing the margin between the decision hyperplane and the data set, while minimizing the misclassification. The decision/separating hyperplane is defined as [298]

$$w^t x + b = 0, \tag{6-1}$$

where w represents the weight vector defining the direction of the separating boundary, whereas b denotes the bias. The decision function is defined as

$$f(x) = sgn(w^t x_i + b), \tag{6-2}$$

where $sgn(\alpha) = \begin{cases} 1, & \alpha \geq 0 \\ -1, & \alpha < 0 \end{cases}$. SVM algorithm aims to maximize the margin through minimizing $\|w\|$, which results in the following constrained optimization problem

$$\min_{w,\xi} \tau_1(w, \xi) = \min_{w,\xi} [\tfrac{1}{2} \left||w|\right|^2 + C \textstyle\sum_{i=1}^{N} \xi_i] \tag{6-3}$$

$$\text{subject to } y_i(w^t x_i + b) \geq 1 - \xi_i, \ \ \xi_i > 0, \ \ C > 0, \ \ i = 1, 2, \dots, N$$

in which $\tau_1(.), ||.||^2$, and ξ_i denote the objective function, L_2-norm, and slack variable, respectively. When the data is linearly inseparable, SVM offers an alternative solution for classification. To this end, SVM employs a kernel trick projecting the data into a higher dimensional feature space to make data divisible, as illustrated in Figure 6-1. The kernel function, in fact, defines the nonlinear mapping from the input space into a high dimensional feature space [298].

6.2.2.2 Support Vector Machine Regression

Support vector machine (SVM) is being mainly utilized for classification tasks. However, it can also be used for regression tasks (i.e., to approximate functions). The aim of SVM regression is to build a hyperplane, which is close to as many of the training data as possible [303–305]. Given SVM definition in previous sub-section, the hyperplane w is chosen with a small norm, while the distances from training points to the hyperplane has to be minimized. Such distances are computed using ε-insensitive loss function introduced by Cortes and Vapnik [298]

$$|y_i - (w.x_i + b)|_\varepsilon = \begin{cases} 0 & if \ |y_i - (w.x_i + b)| \leq \varepsilon \\ |y_i - (w.x_i + b)| - \varepsilon & otherwise \end{cases} \tag{6-4}$$

SVM regression is commonly solved through resorting to a standard dualization method using Lagrange multipliers. The aim is to minimize the quadratic programming problem associated with SVM regression defined as

$$\min_{w,b,\xi,\xi^*} \frac{1}{2}\|w\|^2 + C\sum_{i=1}^{N}(\xi_i + \xi_i{}^*) \qquad (6\text{-}5)$$

That is subjected to following constraints

$$y_i - (w.x_i + b) \le \varepsilon + \xi_i \quad with \quad \xi_i \ge 0 \qquad (6\text{-}6)$$

$$-y_i + (w.x_i + b) \le \varepsilon + \xi_i{}^* \quad with \quad \xi_i{}^* \ge 0$$

6.2.2.3 K-Nearest Neighbor

K-nearest neighbor (*K*-NN), a supervised learning ML algorithm, is a non-parametric classification approach belonging to the instance-based learning methods [302]. To express *k*-NN, assume the pair (x_i, $\varphi(x_i)$,) which denotes the feature vector x_i and its corresponding label $\varphi(x_i)$, where i=1, 2,…, n and $\varphi\{1, 2, \ldots, m\}$ (n and m are the number of training feature vectors and the number of classes, respectively). The distance between feature vectors x_i and x_j is determined as

$$d(i,j) = f(x_i, x_j), \qquad (6\text{-}6)$$

where $f(x_i, x_j) = (x_i - x_j)^T \sum(x_i - x_j)$. The distance vector $D(i) = \{d(i,j)|i = 1, \ldots, n_{test}, j = 1, \ldots, n_{train}\}$ is arranged in an increasing order $D_n(i)$ and the *k*-nearest vote vector is defined through the first K elements (number of neighbors) according to the following equation

$$V = \{\varphi(D_n(i)(1)), \ldots \varphi D_n(i)(K))\}. \qquad (6\text{-}7)$$

The classification is performed by determining the *k*-nearest vote vector V. Accordingly, the test feature x_i is classified to the class having the most votes in V [302].

6.2.2.4 Artificial Neural Network

Artificial neural network (ANN) consists of different layers; namely, input layer, hidden layer, and output layer. Each neuron in an ANN layer is connected to a neuron in the next layer [300]. The output of the neuron *i* in the hidden layer is defined as

$$s_i = \sigma(\sum_{j=1}^{N} w_{ij} x_j + T_i). \tag{6-8}$$

where $\sigma(.)$ denote the activation function, x_j is input feature, w_{ij} is weights, *N* is the number of neurons, and T_i is threshold term for hidden neurons. A two-layer (i.e., one-hidden layer with ten neurons and an output layer) feed-forward multilayer neural network adopted in the analysis is shown in Figure 6-1. Input features $x_1, x_2, \dots, x_{10}$ are parameters governing structural response of UHPC beams, whereas the output variables are three failure modes, i.e., shear (class 1), flexure-shear (class 2), and flexure (class 3). Among different activation functions, a sigmoid function was used herein. A sensitivity analysis was performed in this study, for which different ANN configurations were considered. The performance of ANN architectures was then evaluated in terms of the cross entropy error with respect to the number of epochs. Preliminary results showed that the ANN architecture shown in Figure 6-1 led to acceptable classification performance and therefore was chosen for the ANN analysis.

6.2.3 Failure Mode Prediction

To evaluate the performance of the ML framework for failure mode classification, data set collected from tests presented in section 6.2.1 were utilized as input to the computational ML framework. The experimental data was randomly divided into three sets: namely training set, validation set, and testing set. The training set was used to develop the learning/predictive model, validation set was used to determine the optimal hyper-parameters of ML algorithms, and the testing set was considered to explore the performance of the developed models. *K*-fold cross validation was used to prevent overfitting, which refers to the case when the model shows a good performance on training data, while it does not perform well in terms of predicting new blind data. To implement different ML algorithms (i.e., SVM, ANN, *k*-NN), the data set/patterns were classified into three classes i.e., shear failure mode (class 1), flexural-shear failure mode (class 2), and flexural failure mode (class 3). Matlab simulation environment was adopted to implement the computational framework and ML algorithms. The failure mode's classification accuracy was determined through dividing the number of patterns/beams with correctly predicted failure mode by the total number of patterns/beams. Several trial analyses were carried out with different size of data sets (for training, validation, and testing), based on which the failure classification accuracy was obtained. Results obtained from this analysis indicate that amongst different combinations, a combination in which 70% of data was used for training and validation and 30% for testing, led to the best classification accuracy with different ML algorithms. Therefore, results are presented based on this combination.

A dimensionality-reduction technique called principal component analysis (PCA) was used to project data set to its first two principal components (governing features), as depicted in Figure 6-3. These principal components are uncorrelated and retain maximum variance of the original data. As can be seen, the three classes for the failure classification of UHPC beams overlap even using the first two principal components, i.e., no decision boundary can be drawn to separate these three classes. This clearly indicates the necessity of the development of a computational framework that is capable of effectively classifying different failure modes with such experimental data.

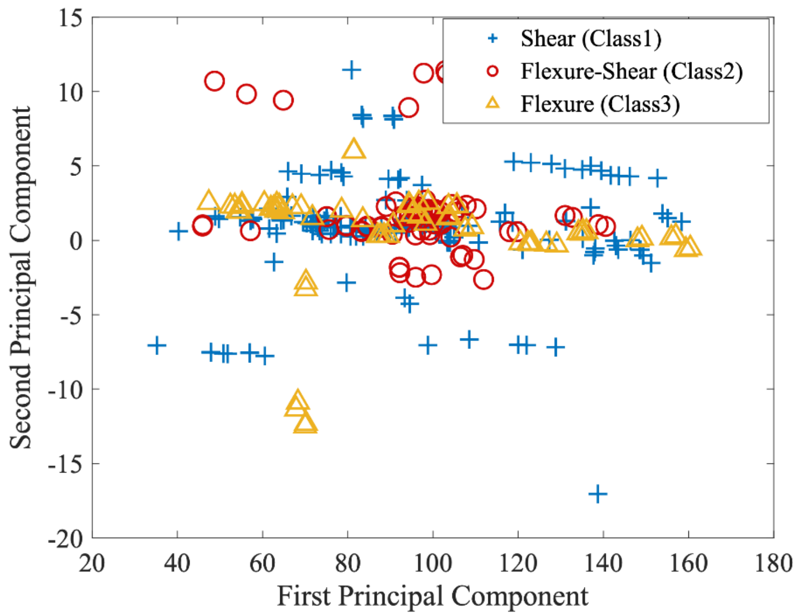

Figure 6-3. Data projection on to the first two principal components for failure classification of UHPC beams

As previously noted, SVM, *k*-NN and ANN algorithms were used for classification of failure mode of UHPC beams. Yet, to achieve the best classification performance, it is essential to select the optimal hyper-parameters for the ML algorithms. Preliminary results with SVM shown in Table 6-2 indicate that linear kernel led to the best classification performance. Thus, this kernel was chosen to assess the performance of SVM on test set. Further, to achieve the best classification performance with *k*-NN, the optimum number of neighbors (*k*) was obtained through computing the accuracy on validation data set. Table 6-3 presents the classification results with different *k* values. Results indicate that the best classification accuracy on validation data was achieved with $k = 20$. Thus, this value of *k* was selected to evaluate the performance of *k*-NN on test data. Finally, for the ANN algorithm, the architecture shown in Figure 6-1 was considered for the simulations. The cross-entropy with respect to the number of epochs (one backward and one forward pass for all the training dataset) that represents the performance of the ANN is presented in Figure 6-4 where the best validation performance is 0.06 at epoch 58.

Table 6-2. SVM kernel tuning

Kernel	Classification Accuracy (%)
Linear	81.5%
Polynomial	63%
Sigmoid	58%
Radial basis function	59%

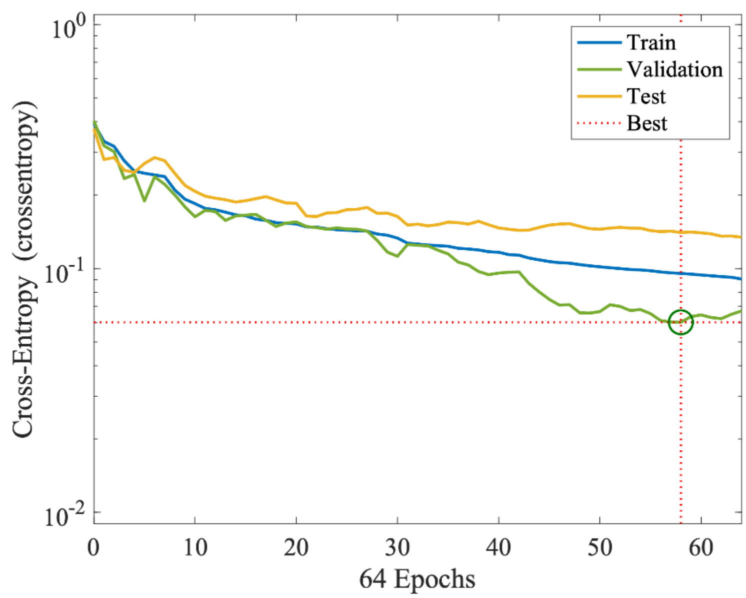

Figure 6-4. Performance evaluation of ANN in terms of cross-entropy against number of epochs

Table 6-3. *K*-NN hyper-parameter tuning

Number of Neighbors (*k*)	Classification Accuracy (%)
5	59%
10	63%
15	68%
20	72%
25	70%

To evaluate the performance of ML algorithms, a confusion matrix containing information on actual and predicted classifications was employed and plotted on test data set. Herein, the confusion matrix represents the actual/observed failure modes versus the predicted failure modes. The diagonal entries of the confusion matrix denote the failure modes that are correctly classified, while the off-diagonal entries represent the failure modes that are misclassified. As previously highlighted, classes 1, 2, and 3 corresponded to shear, flexural-shear, and flexural failure modes in UHPC beams, respectively. It is to be noted that the classification results presented in the confusion matrix can be inferred through the following metrics: (a) the column on the far right of the confusion matrix denotes the positive predictive value and false discovery rate, which are the percentile of correct and incorrect classifications for each predicted failure mode, respectively; (b) the row at the bottom of the confusion matrix represents the true positive rate and false negative rate that are the percentages of correct and incorrect predictions for each true class, respectively; (c) the cell in the far bottom right of the matrix indicates the total classification accuracy. Clearly, the high positive predictive value (precision) and high true positive rate (recall) imply efficiency in terms of detecting the failure mode of UHPC beams (as compared to that in real tests). It should be noted that precision is defined as the proportion of positive predictions that were correctly identified while recall is the ratio of correct positive predictions to the total positive examples.

The confusion matrix on test set for ML algorithms used in this study is presented in Figure 6-5, from which it can be observed that ANN outperforms SVM and *k*-NN. Results indicate that the overall accuracy based on SVM, *k*-NN, were 81.5%, 75%, while the performance of the ML framework significantly improved using ANN, with classification accuracy being 88.9%. According to the confusion matrices, the precision and recall for the shear failure mode were 87.3% and 100% based on SVM (see Figure 6-5 (a)), 73.3% and 100% based on *k*-NN (see Figure 6-5 (b)), and 89.5% and 98.6% using ANN (see Figure 6-5(c)). Similar results were observed for the flexural failure mode. However, the performance of ANN was superior compared to SVM and *k*-NN according to the results of precision and recall for the flexural-shear failure mode. For example, unlike SVM and *k*-NN that did not perform well on class 2 (e.g., 56.5% precision based on SVM and 55.6% precision with *k*-NN), the precision with ANN was 86.7% for this class. Another important observation was that the precision and recall for the shear failure mode (class 1) and flexural failure mode (class 3) were higher compared to that of flexural-shear failure mode (class 2) based on all *k*-NN and ANN algorithms.

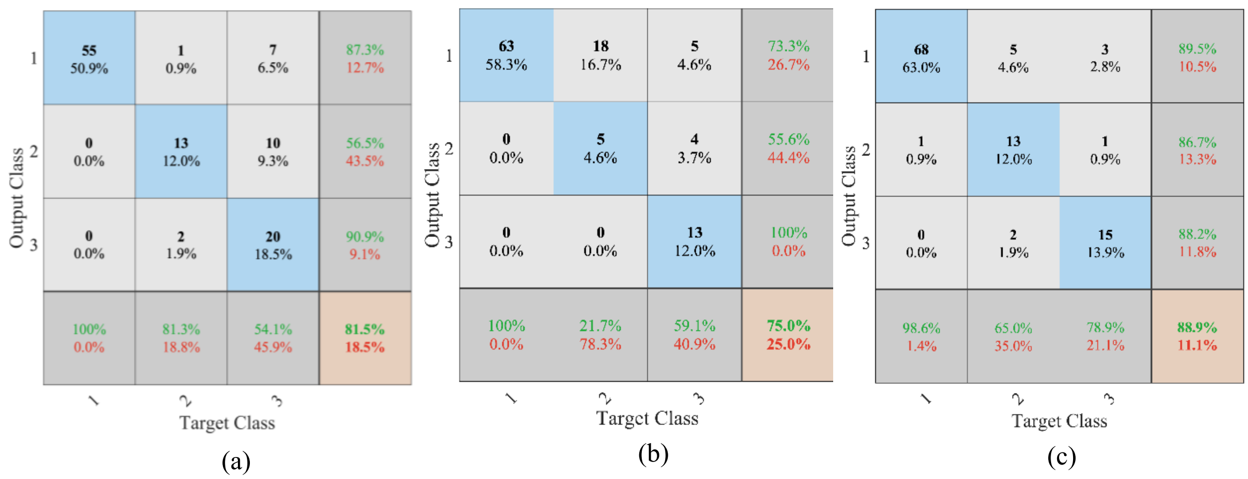

Figure 6-5. Confusion matrix using different ML algorithms (a) SVM, (b) k-NN, and (c) ANN; Classes 1, 2, and 3 represent shear, flexural-shear, and flexural failure modes

To further showcase the effectiveness of ANN algorithm in identifying the mode of failure, the receiver operating characteristic (ROC) curve was plotted and presented in Figure 6-6. The area under ROC curve (AUC) is a metric employed to evaluate the performance of the model. That is, an AUC value being 1 indicates the perfect performance (classification without any error). Accordingly, an AUC value closer to unity denotes better failure mode classification performance (higher accuracy). As can be seen, AUC values for classes 1 and 3 (i.e., shear and flexure modes) were 0.95 and 0.97, respectively, which are higher compared to that of class 2 (flexure-shear mode) being 0.91. This clearly confirms the results obtained based on the confusion matrices. Results infer that all ML algorithms perform satisfactory in terms of detecting the failure mode of UHPC beams. Specifically, results indicate that ML algorithms used in this study can successfully detect shear and flexural failure modes (classes 1 and 3). It is worth mentioning that the performance of each ML algorithm depends on the type of dataset (e.g. features used for classification, etc.). However, in this study, it is shown that performance of ANN is superior as compared to *k*-NN and SVM.

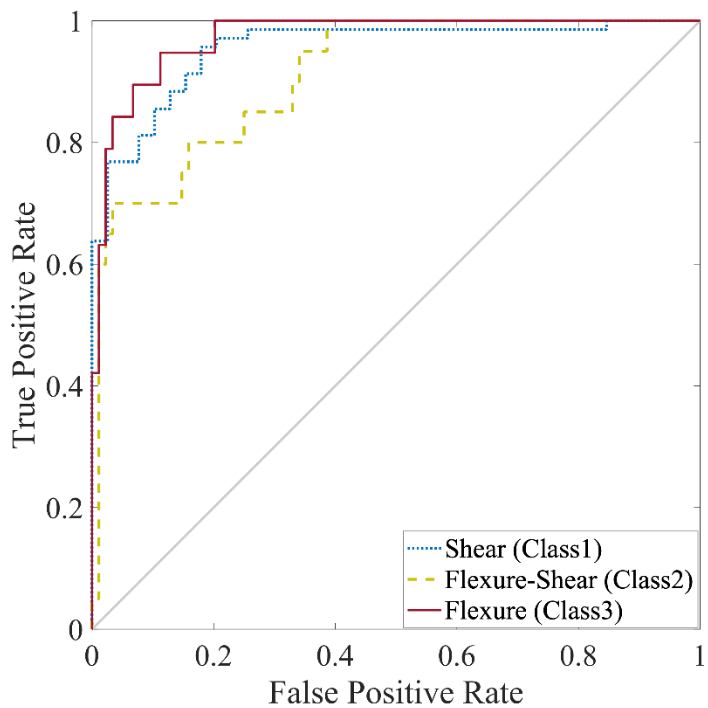

Figure 6-6. ROC curve based on ANN for failure mode classification of UHPC beams

6.2.4 Flexural Capacity Prediction

The ML framework shown in Figure 6-1 is used to predict flexural capacity of UHPC beams. To this end, SVM regression is employed to use governing features of compressive strength, width and effective depth of the beams, fiber volume fraction, fiber size and type, reinforcement ratio, and moment of inertia to predict flexural capacity. To obtain the best performance, the optimal kernel of SVM regression needs to be determined. In regard to this, comparison of flexural capacity of UHPC beams obtained from SVM regression model and experiments along with the corresponding R^2 on training and test data is plotted in Figure 6-7. In this figure the ideal fit line representing $\frac{M_{pred}}{M_{exp}} = 1$ is also shown. It can be clearly observed that among different kernels, polynomial kernel leads to achieve best performance with R^2 of 0.98 and 0.96 on training and test data, respectively (see Figure 6-7 (d)). Therefore, this kernel was selected as the optimal kernel for the analyses. In the next phase of analysis, the effect of different size of data subsets on the performance of the ML model was evaluated. Accordingly, 5 different cases listed below were considered:

- Case 1: 70% training set and 30% test set
- Case 2: 75% training set and 25% test set
- Case 3: 80% training set and 20% test set
- Case 4: 85% training set and 15% test set
- Case 5: 90% training set and 10% test set

Flexural capacity of UHPC beams predicted with SVM regression algorithm using polynomial kernel, based on different data subsets, and measured data from experiments are compared in Figure 6-8. Similarly, the corresponding R^2 on training and test data is shown in the plots. Results indicate that best performance is achieved based on case 5, for which 90% of data set was used for training and the remaining 10% was considered for test. According to the results, although R^2 on training data is similar for all cases, highest R^2 on test data is obtained using case 5, i.e., 0.96 (see Figure 6-8 (e)). Results clearly show that the proposed ML framework is capable of effectively predicting the flexural capacity of UHPC beams with different configurations.

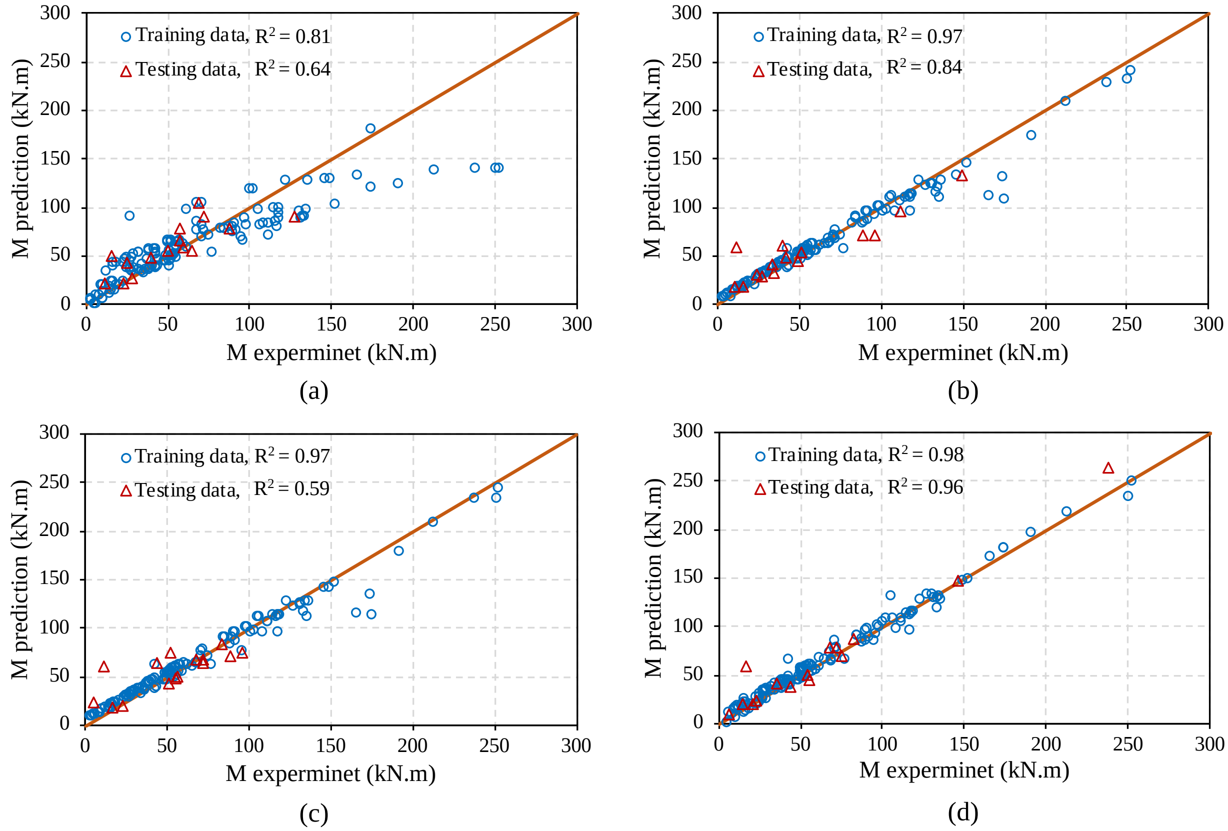

Figure 6-7. Comparison of flexural capacity of UHPC beams predicted by SVM regression and measured data from available experiments with different kernels: (a) linear, (b) Gaussian, (c) RBF, (d) Polynomial

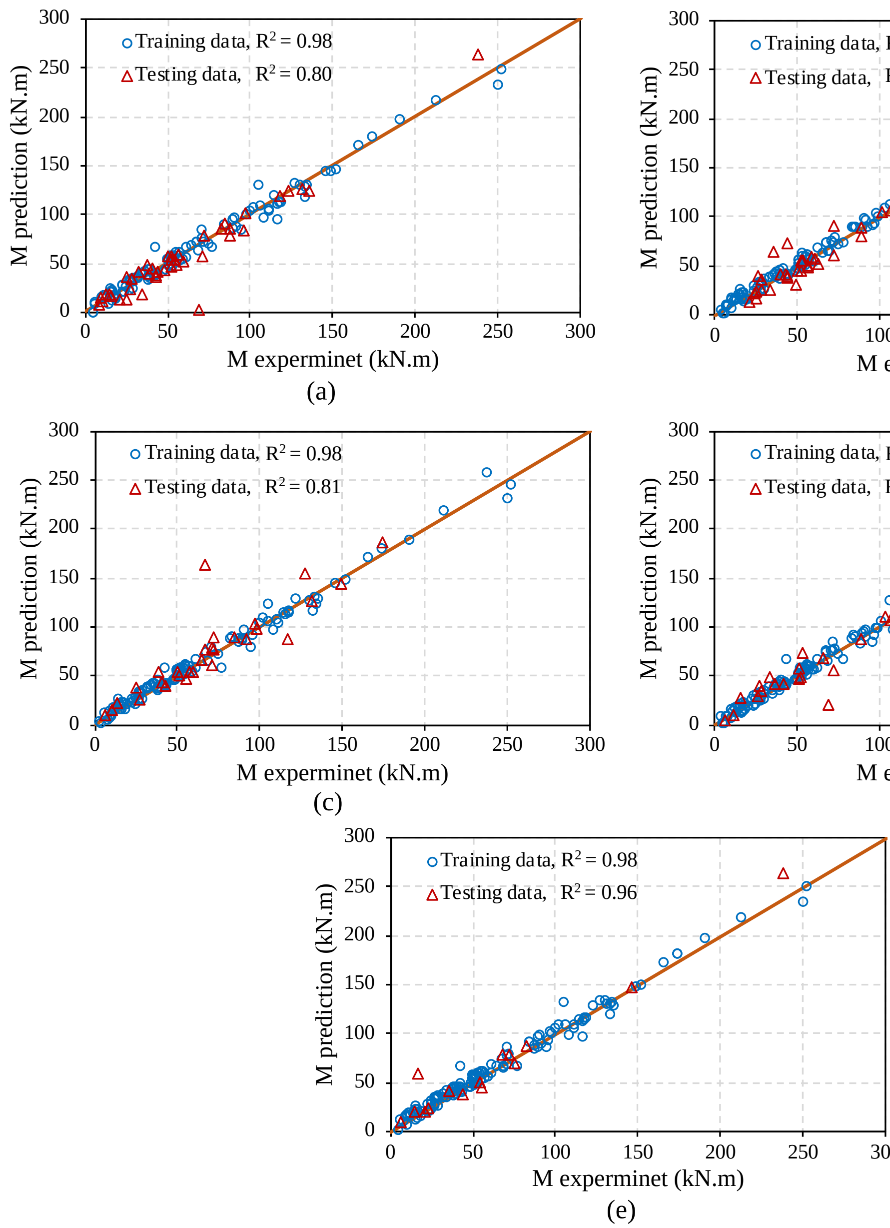

Figure 6-8. Comparison of flexural capacity of UHPC beams predicted by SVM regression and measured data from available experiments with different subset of dataset: (a) case 1, (b) case 2, (c) case 3, (d) case 4, (e) case 5

6.2.5 Shear Capacity Prediction

Following the identification of failure mode, an AI based approach was developed for the prediction of shear capacity of UHPC beams through GP analysis. For this purpose, the critical features governing shear capacity in beams are to be identified first. Feature selection techniques for pattern recognition were used to determine the governing variables; namely, compressive strength of concrete (f_c'), type of steel fiber (F), characteristic parameter of steel fiber ($\lambda = \frac{V_f L_f}{d_f}$) which is a function fiber volume fraction (V_f), length (L_f) and diameter of fiber (d_f), shear span (a), effective depth (d), width (b_w), tensile reinforcement ratio, or prestressing strand ratio (ρ_t), shear reinforcement ratio and yield stress (ρ_v, f_{ys}), level of prestress in section $\left(\sigma_P = \frac{P}{A_c}\right)$, where P and A_c are prestressing force and area of concrete cross section.

From the overall set of compiled beams, the beams that failed under flexure mode were omitted. Then, the above variables were input into GP algorithm. In GP, a set of formulae can be numerically derived to arrive at one-step and closed form mathematical relation(s) that can be used to represent a physical phenomenon (i.e. shear capacity of UHPC beams). The GP analysis starts by generating a population of random expressions, often referred to as “trees” (see Figure 6-9). These expressions contain both, mathematical operations (+, /, × etc.), power functions (^, exp), log functions (log, ln, etc.) etc., together with critical features arrived at in the initial stage and known to govern shear strength of UHPC. Each formula was then substituted to evaluate its prediction capability and fitness. Only the fittest solution remain active in the GP population (and hence the notion of GP resembling survival of the fittest) [306].

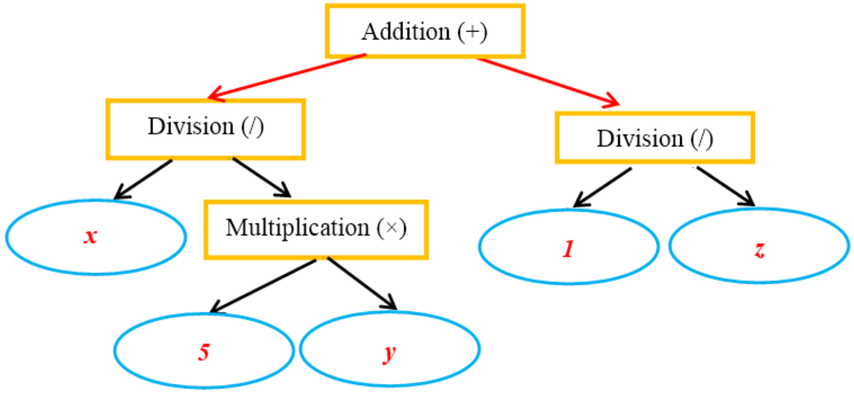

(a) Tree representation of an expression $\frac{x}{5y} + \frac{1}{z}$

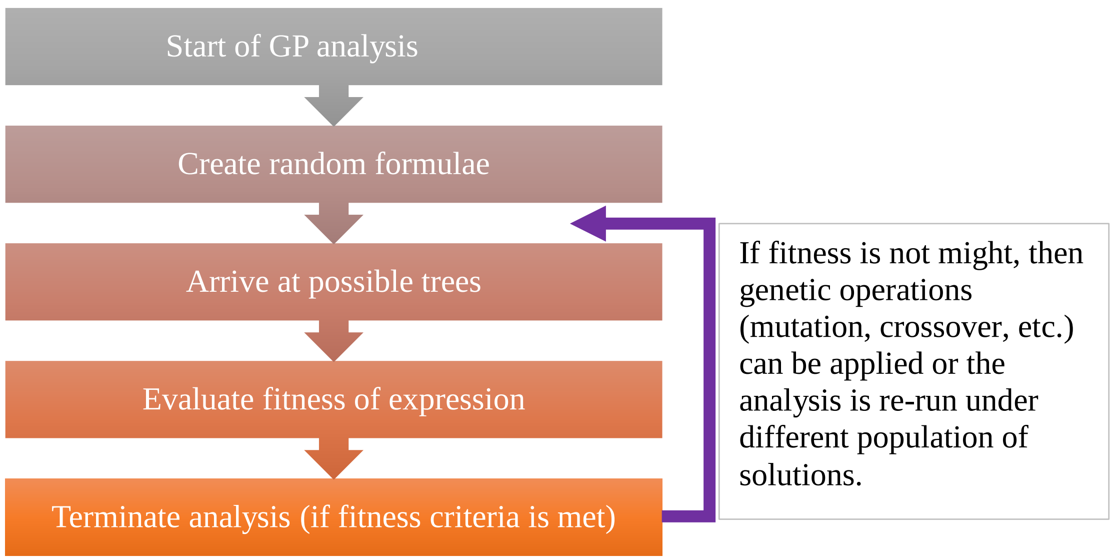

(b) Flowchart of GP procedure

Figure 6-9. Layout of GP analysis for evaluating shear capacity

The fittest solution is then selected and further manipulated by a number of genetically-inspired operations i.e., reproduction, crossover and mutation, depending on the level of GP analysis until fitness criteria are satisfied. Fitness criteria include reaching a certain level of accuracy and/or completing specified number of iterations. At the end of the GP analysis, the fittest formula was arrived at. This formula represents a governing relation that can directly link the governing factors to shear capacity of UHPC beam in one-step and via simple substitution. A flowchart representing the process of arriving at a suitable solution is shown in Figure 6-9.

The compiled dataset was divided into three sets of beams, namely nonprestressed beams without stirrups, nonprestressed beams with stirrups, and prestressed beams, as code equations follow a similar classification. There were 191, 52, and 45 test data available for the above mentioned three sets, respectively. It should be noted that the beams exhibited shear and flexural-shear failure were utilized to develop expressions for predicting shear capacity of UHPC beams. The developed expressions along with coefficient of determination (R^2) for each set is shown in Table 6-4.

Table 6-4. Derived expressions to be used to evaluate shear capacity of UHPC beams

Remarks	Derived expressions	R^2*(%)*
Nonprestressed UHPC beams without stirrups	$V = 37.82\,\rho_t + 2.12\,b_w + 1.05f_c' + 0.841\,\lambda + 1.57\,b_w\cos(F) + 553\cosh(\cos(F)\cos(0.6 + 0.107\,b_w)) - 739.64 - 9.49F - 41.27\frac{a}{d} - 175.97\cos(F) - 0.48\frac{a}{d}\,b_w$	83
Nonprestressed UHPC beams with stirrups	$V = 61.06\,\rho_v + 16.31\,\rho_t + 1.86\frac{a}{d}f_{ys} + 0.338\lambda\rho_t + \frac{1537.3}{\lambda - 93.75} - 0.096\,b_w - 0.299f_c' - 1.11\,\lambda + 2348.32 - 4.29f_{ys} - 10.32\,F - 942.81\frac{a}{d}$	93
Prestressed UHPC beams	$V = 504.63\frac{a}{d} + 51.24\,\rho_v + 19.17f_c' + 7.66\lambda + 5.96\,b_w + 3.85\sigma_P + 2.02F + 0.267\,{b_w}^2 + 0.088\,f_c'\frac{a}{d}\,b_w - 1123.9 - 71.73\,\rho_t - 0.124\,\lambda\,b_w - 0.26f_c'\,b_w - 5.46f_c'\frac{a}{d} - 9.61\frac{a}{d}\,b_w$	98

$\lambda = V_f L_f / d_f$

ρ_t, ρ_v, and V_f are in percentage; stresses are in MPa; *V* is in kN; dimensions are in mm and radians.

F=1 for hooked steel fibers, F=2 for combination of hooked and straight steel fibers; F=3 for straight steel fibers; F=4 for UHPC without fibers.

To establish the validity of the proposed expressions, shear capacity of the UHPC beams as obtained from proposed ML model was compared to the results from the reported experiments. Moreover, the accuracy of current recommendations for shear capacity of UHPC in codes and standards [25,26] were also evaluated through comparison with test data. For this purpose, the expressions for evaluating shear capacity of UHPC beams proposed in JSCE [26] and AFGC [25] was utilized. According to JSCE [26] and AFGC [25] recommendations, for shear design of UHPC beams, shear strength contribution of concrete, fibers, and stirrups are required to be calculated separately as shown in Table 6-5. In addition, expressions developed by Ahmad et al [198] for predicting shear capacity which is applicable to reinforced UHPC beams with or without stirrups was utilized for the comparative study. However, the expressions were developed based on very limited number of experiments and do not account for all the governing parameters [198].

Further, models proposed for predicting shear capacity of FRC beams by Imam et al [307], Sharma [308], Narayanan and Darwish [117], Ashour et al. [116], Kwak et al [114] were utilized to explore the applicability of fiber reinforced concrete (FRC) expressions for UHPC beams. These shear models are summarized in Table 6-5.

Graphical comparison of shear capacity of UHPC beams obtained from collected test data and predicted by the proposed ML-based model is depicted in Figure 6-10(a), while comparison between experimental data and above-noted models in literature is shown in Figure 6-10(b to i). It can be clearly observed in Figure 6-10 that the proposed model better estimated shear capacity of UHPC beams as compared to other expressions, since the calculated and measured shear capacity were more condense about the ideal fit line representing $\frac{V_{pred}}{V_{exp}} = 1$. Also, it can be seen that available expressions in literature for UHPC and FRC underestimate the shear capacity of the beams as compared to the proposed ML-based model. In order to highlight the graphical comparison results, the coefficient of determination (R^2) is also shown in Figure 6-10, confirming a strong correlation between predicted shear capacity and measured test data. This clearly demonstrates that the proposed ML-based predictive expressions can yield better estimation of shear capacity of UHPC beams.

Table 6-5. Summary of shear prediction equations from literature

Reference	Shear strength models	Type of Concrete
AFGC [25]	$V_u = V_c + V_f + V_s$ $V_C = \frac{0.21}{\gamma_E \gamma_b} k\sqrt{f_c'}\, bd,\ \gamma_E\gamma_b = 1.5\ (for\ reinforced\ beams)$ $k = 1 + \frac{3\sigma_{cm}}{f_{tj}}\ (in\ compression);\ k = 1 - \frac{0.7\sigma_{tm}}{f_{tj}}\ (in\ tension)$ $V_C = \frac{0.24}{\gamma_E \gamma_b}\sqrt{f_c'}\, bz,\ \gamma_E\gamma_b = 1.5\ (for\ prestressed\ beams)$ $V_f = \frac{0.9bd\sigma_p}{\gamma_{bf}\ tan\beta_u}$ $\sigma_p = \frac{1}{K}\frac{1}{w_{lim}}\int_0^{w_{lim}} \sigma(w)dw\ , w_{lim} = \max(w_{u,0.3\ mm})$ $V_s = 0.9\ d\ \frac{A_v}{S}\frac{f_{ys}}{\gamma_s}(sin\alpha + cos\alpha)$	UHPC
JSCE [26]	$V_u = V_c + V_f + V_s,\ \ V_c = \frac{0.18}{\gamma_b}\sqrt{f_c'} bd,\ \gamma_b = 1.3$ $V_f = \frac{f_{vd}}{\gamma_b\ tan\beta_u} b_w \frac{d}{1.15},\ \ V_s = \emptyset_b d\ \frac{A_v f_{ys}}{S}(sin\alpha + cos\alpha)$ $f_{vd} = \frac{1}{w_{lim}}\int_0^{w_{lim}} \phi\ \sigma(w)dw\ ,\ w_{lim} = \max(w_{u,0.3\ mm})\ , \phi = 0.8$	UHPC
Ahmad et al. [198]	$V_u = V_{c+f} + V_s;\ V_{c+f} = \left[0.35\sqrt{f_c'} + 132\rho\frac{d}{a} + 14F^{5.8}\left(\frac{d}{a}\right)^{1.1}\right] bd$ $F = \left(\frac{l_f}{d_f}\right) V_f \alpha,\ V_s = \frac{A_v\ f_{ys}\ d}{S}$	UHPC
Ashour et al. [116]	$for\ \ a/d > 2.5;\ \ V_c + V_f = \left[(2.11\sqrt[3]{f_c'} + 7F)\left(\rho\frac{d}{a}\right)^{0.333}\right] bd$ $for\ \ a/d < 2.5;$ $V_c + V_f = \left[(2.11\sqrt[3]{f_c'} + 7F)\left(\rho\frac{d}{a}\right)^{0.333}\frac{2.5}{a/d} + 0.41\tau\ F\ (2.5 - \frac{a}{d})\right] bd$ $F = \left(\frac{l_f}{d_f}\right) V_f \alpha,$ $\tau = 4.15\ MPa, \alpha = 0.5\ for\ smooth\ fiber\ and\ 1\ for\ hooked$	FRC
Narayanan and Darwish [117]	$V_c + V_f = \left[e\left(0.24 f_{spfc} + 80\rho\frac{d}{a}\right) + v_b\right] bd,$ $f_{spfc} = \frac{f_{cu}}{20 - \sqrt{F}} + 0.7 + \sqrt{F}$ $v_b = 0.41\tau\ F$	FRC
Imam et al. [307]	$V_c + V_f = \left[0.6\psi\sqrt[3]{\omega}\left(f_c'^{0.44} + 275\sqrt{\frac{\omega}{(a/d)^5}}\right)\right] bd,\ \ \omega = \rho(1 + 4F)$ $\psi = (1 + \sqrt{5.08/d_a})/(\sqrt{1 + d/(25d_a)})$	FRC
Sharma [308]	$V_c + V_f = \left[k f_t' (\frac{d}{a})^{0.25}\right] bd,$ $f_t' = Splittig\ tensile\ strength = 0.79\ \sqrt{f_c'}$	FRC
Kwak et al. [114]	$V_c + V_f = \left[2.1\ e\ \ f_{spfc}{}^{0.70}\left(\rho\frac{d}{a}\right)^{0.22} + 0.8\ v_b{}^{0.97}\right] bd,\ \ \ v_b = 0.41\tau\ F$ $e = 1\ for\ \frac{a}{d} > 3.5;\ e = 3.5\ \frac{d}{a}\ for\ \frac{a}{d}\ \leq 3.5$	FRC

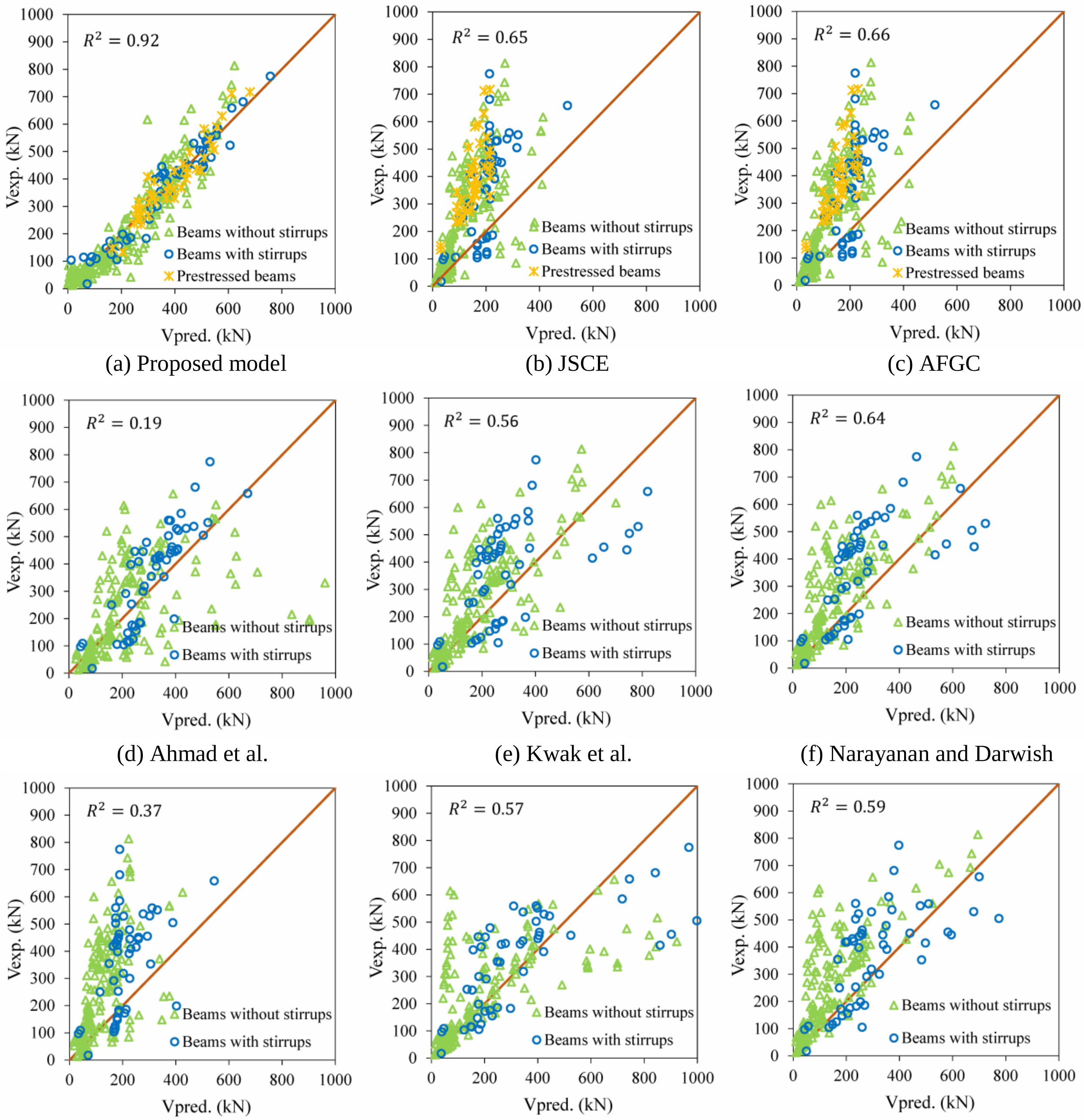

(a) Proposed model (b) JSCE (c) AFGC

(d) Ahmad et al. (e) Kwak et al. (f) Narayanan and Darwish

(g) Sharma (h) Imam et al. (i) Ashour et al.

Figure 6-10. Comparison of AI based predictive equations and available models for shear capacity of UHPC and FRC beams with test data

6.3 Limitations

The performance of any AI-based model strongly depends on the size, quality and distribution of parameters within the selected data set. This work utilized about 400 tests, this pool of experimental data for structural response of UHPC beams can be further enlarged given the interest in accelerated testing of UHPC as it is a relatively new material, with limited tests have been done so far. Also, the results from numerical studies from literature were not included in the data set, since numerical results are highly dependent upon the adopted material models, meshing practices, as well as other assumptions used in modeling. Although for this study all the available test data on UHPC beams were utilized for the data-driven ML framework, it is expected that by increasing the size of data set performance of the framework can be improved. Ongoing efforts are being carried out to overcome such limitations [309].

Readers of this work are to realize that the developed expressions are valid for the range of variables $(b_w, d, \rho_t, \rho_v, \frac{L_f}{d_f}, V_f, f_c')$ presented in the dataset as shown in Figure 6-2 and Table 6-1. As previously noted, Figure 6-2 presents the frequency of each specific value (or range) of variables appeared in the dataset. As can be seen, some values (or ranges) of features are not repeated too much in the dataset, i.e., the frequency of these values of variables in dataset is low. While the proposed framework remains valid, in order to guarantee reliable expressions that are applicable to the wide range of variables, additional test data is required. Further, having more test data on UHPC beams with various configurations and higher frequency of different ranges of variables can lead to the development of ML algorithms, which can be used to effectively derive separate equations for different configurations of UHPC beams (flanged sections: I-shaped or T-shaped, and rectangular sections).

6.4 Summary

A data-driven machine learning-based computational framework was proposed for predicting failure mode and then flexural and shear capacity in UHPC beams. For this purpose, results from a number of tests on UHPC beams with different geometric and loading configurations and material characteristic was collected and utilized as an input to the ML framework. Critical parameters governing response of UHPC beams were identified using pattern recognition techniques. ML algorithms such as SVM, ANN, and *k*-NN were used to classify three failure modes observed in the experiments, i.e., shear, flexural-shear, and flexural. Finally, GP and SVM regression were utilized to predict shear and flexural capacity of UHPC beams. Based on the results presented in this chapter, the following conclusions are drawn:

- Machine learning algorithms SVM, *k*-NN and ANN are quite effective in predicting different failure modes (shear, flexure-shear, and flexure) in UHPC beams. In this study, ANN prediction outperforms other ML algorithms with an overall accuracy of 89%.
- Both SVM and *k*-NN algorithms perform better in predicting shear and flexural failure modes as compared to flexural-shear mode.
- The proposed expressions using GP yield good predictions of shear capacity of UHPC beams with R^2 of 92%. Therefore, the developed expressions can be used for practical design purposes as they are derived based on data from different experimental programs.
- SVM regression algorithm can effectively predict flexural capacity of UHPC beams, with acceptable R^2 of 0.98 and 0.96 on training and test data, respectively.

CHAPTER 7

7 CONCLUSIONS

7.1 General

UHPFRC is a new class of cementitious material possessing high compressive and tensile strength, improved ductility, fracture toughness, energy absorption capacity, and enhanced post cracking tensile response [1–3]. These excellent properties result from highly homogenized microstructure achieved through optimizing the granular mixture along with a low water-to binder ratio, high fineness admixtures and effective presence of steel fibers [81]. As a result of these improved properties, UHPFRC has been finding increasing applications in infrastructural systems [5,6].

Despite recent research efforts to evaluate structural behavior of UHPFRC, currently there are limited guidelines and recommendations for structural design of UHPFRC in codes and standards. With the aim of developing design guidelines, seven large scale UHPFRC beams were fabricated and tested under different loading configurations to evaluate flexural and shear response of the beams. In addition, a sectional analysis and a finite element based numerical model was developed to trace comprehensive structural response of UHPFRC beams. The developed model was applied to conduct a set of parametric studies to evaluate effect of different parameters on structural response of UHPFRC beams. Finally, a machine learning-based data interpretation framework was utilized for predicting mode of failure (i.e. flexure, flexure-shear, and shear) and capacity of UHPFRC beams.

7.2 Key Findings

The following conclusions can be drawn based on information generated as part of this thesis:

1) The adopted improved mix design and procedure for preparing UHPFRC with coarse aggregates is successful to attain desired workability and strength characteristics. The mix can be prepared in a conventional ready-mix truck utilizing locally available materials, and at relatively lower cost. Also, combination of Styrofoam in the formworks and insulating blanket is effective to eliminate thermal gradients within concrete block leading to early age cracking. Further, it can facilitate effective use of heat of hydration of the cementitious binder in UHPFRC towards field thermal curing.
2) UHPFRC beams exhibit a distinct cracking pattern characterized by formation of multiple microcracks at initial stages, followed by propagation of a singular macrocrack at the critical section leading to failure. This improved cracking response in UHPFRC beams, as well as high ductility, is attributed to bridging effect facilitated by the presence of steel fibers in UHPFRC.
3) UHPFRC beams even without any stirrups possess high shear resistance arising from two mechanisms i.e. shear resistance of the uncracked portion of concrete and interface shear resistance. This high shear resistance of UHPFRC beams is due to high tensile and compressive strength of UHPFRC, combined with bridging effect at crack surfaces and high ultimate tensile strain, facilitated by presence of steel fibers.
4) Absence of shear reinforcement in UHPFRC beams does not lead to any reduction in either ductility or moment capacity of the beams even under dominant shear loading. In other words, UHPFRC beams without shear reinforcement, subjected to dominant shear loading, can attain ultimate moment capacity, without experiencing brittle failure before rebar yielding. However, presence of stirrups may result in less widening of the cracks and also change in the cracking pattern.

5) The proposed finite element based numerical model, utilizing concrete damage plasticity model with adjusted parameters, is capable of tracing the response of UHPC beams in the entire range of loading; from precracking stage till failure. The developed numerical model can account for various configurations in beams, including different loading patterns (flexure or shear), different types of UHPC with varying fiber volume fraction, and shear reinforcement configurations. The model is capable of quantifying contribution of stirrups, concrete, and mechanisms of beam and arch action to shear capacity of UHPC beams.

6) Tensile damage contour predictions along with principal direction, is an effective response parameter for tracing crack propagation zone and failure modes in UHPFRC beams. This damage parameter in tension gets activated after concrete attains its peak tensile strength. Therefore, damage contours replicate tensile cracking and the extent of damage increases with increase in strain (crack widening). Direction of the localized major crack leading to failure can be represented using direction of principal strain being perpendicular to crack direction.

7) A computational framework employing ML is proposed for predicting failure mode and flexural and shear capacity of UHPC beams. To this end, a comprehensive database on reported tests on UHPC beams with different geometric, fiber properties, loading, and material characteristics is collected. ML algorithms, including SVM, *k*-NN, and ANN are used for failure mode classification. In addition, GP and SVM regression are used for estimating shear and flexural capacity of UHPC beams. The results show that these algorithms are effective in predicting different failure modes (shear, flexure-shear, and flexure) in UHPC beams. In this study, ANN algorithm outperforms other ML algorithms

in predicting mode of failure. Further, GP and SVM regression algorithms perform satisfactory in predicting flexural and shear capacity of the beams with acceptable R^2.

7.3 Research Impact

The use of UHPC in structural applications is still limited and this is mainly due to lack of specifications and guidelines for the design of UHPC structural members. Being relatively a new material, the pool of experimental and numerical data on response of UHPC structural members is still limited. The research presented in this dissertation has contributed to the development of preliminary guidance on evaluating capacity of UHPC beams under different conditions. Possibility of designing UHPC beams with small cross sections and low tensile reinforcement ratio, and removing shear reinforcement, evaluated through experiments and numerical modeling in this study, can promote UHPC applications in civil infrastructures.

Also, the adopted improved mix design and procedure for preparing and curing UHPC with coarse aggregates can facilitate UHPC market acceptance as it can be prepared in a conventional ready-mix truck utilizing locally available materials. Further, developed ML-based computational framework utilizing test data from different experimental programs in literature can be effectively used for practical design purposes, leading to the development of codal provisions.

7.4 Future Research

This thesis provided comprehensive data from experiments as well as results from numerical modeling on the behavior of UHPC beams. However, there is much scope for further research in this area to close many knowledge gaps. The following are a few of the key recommendations for future research in this area:

- The feasibility of removing stirrups was explored through experiments on rectangular beams fabricated with UHPC with 1.5% volume fraction of straight steel fibers as well as numerical modeling. Further tests on UHPC beams with different cross sectional details, types and volume fraction of fibers, and loading configurations (shear span to depth ratio) will add value. Finding optimum percentage of steel fibers at which a UHPC beam without stirrups does not fail in shear before reaching ultimate flexural capacity, regardless of shear span to depth ratio remains to be explored.
- While the developed finite element model and analytical approach was successful in tracing structural response of UHPC beams, these approaches are complex, time consuming, and require high level of expertise for routine structural design. Similar to conventional concrete members, simplified design and analysis strategies are to be developed for structural members fabricated using UHPC.
- The performance of any AI-based model strongly depends on the size of the data set, as well as quality and distribution of parameters within the data set. Given the increasing interest in UHPC applications and research studies, the size of the data set on UHPC beams will be enlarged. Therefore, with increasing the size of data set generated from experiments on UHPC beams, predictions from AI-based framework can be improved for beams with wide range of features.
- UHPC offers unique strength and durability properties which make it an excellent material for building applications. However, fire is one of the critical parameters in building applications, and UHPC exhibits low fire resistance due to fire induced spalling resulting from high packing density and low porosity. Currently studies are underway at Michigan State University to characterize the fire performance of UHPC members and develop

solutions to minimize fire induced spalling. There is need for additional studies for developing design guidelines for UHPC members subjected to fire.

APPENDIX

Appendix A: Beam Design Calculations

A.1 Introductory Note

This appendix provides the design carried out for UHPFRC beams tested in this study. The flexural design process is based on ACI 544.4R [310] except for the tensile strength model. The revised tensile strength model proposed by Yoo [10] was utilized. Also, shear capacity of UHPFRC beams was calculated using recommendations in AFGC [25].

The UHPFRC used in this study includes 1.5% (by volume) straight steel fibers with length (l_f) of 13 mm and diameter (d_f) of 0.2 mm. Average compressive strength (f_c') and elastic modulus (E_c) of UHPFRC and steel yield strength (f_y) and elastic modulus (E_S) were considered to be 160 MPa, 41 MPa, 400 MPa, and 200,000 MPa, respectively. The cross sectional details of the beams and loading configurations are shown in Figure A-1. Further, shear force and bending moment diagrams for beams tested under flexural and dominant shear loading are shown schematically in Figure A-2.

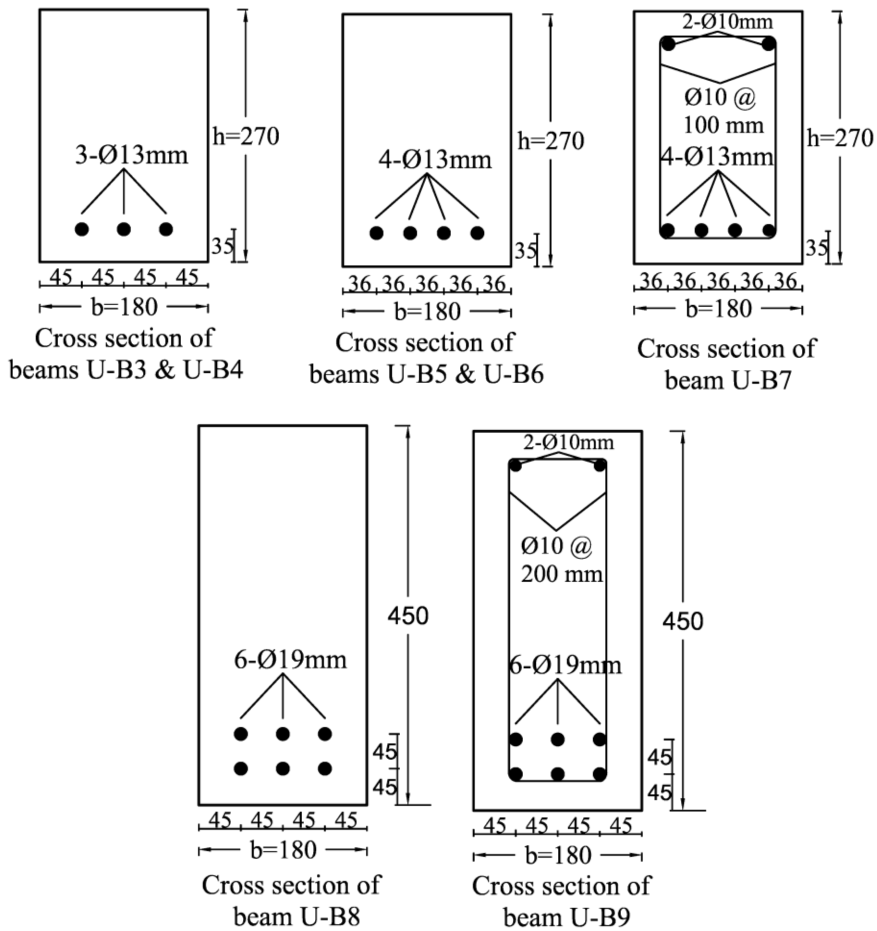

(a) Cross section

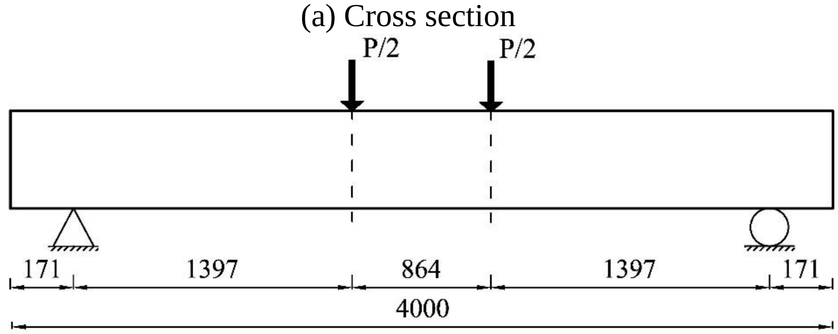

(a) Four-point flexural loading (U-B3 & U-B5)

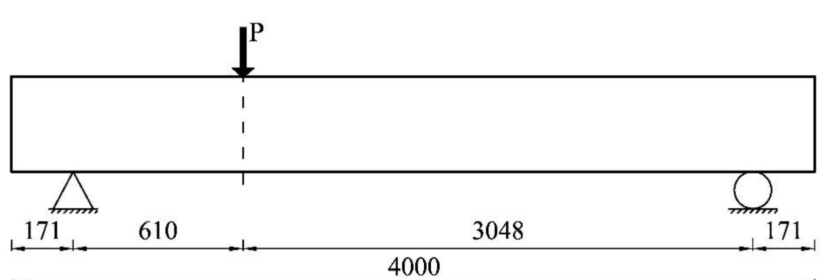

(b) Three-point shear loading (U-B4, U-B6-U-B9)

Figure A-1. Cross section and loading set up of UHPFRC beams

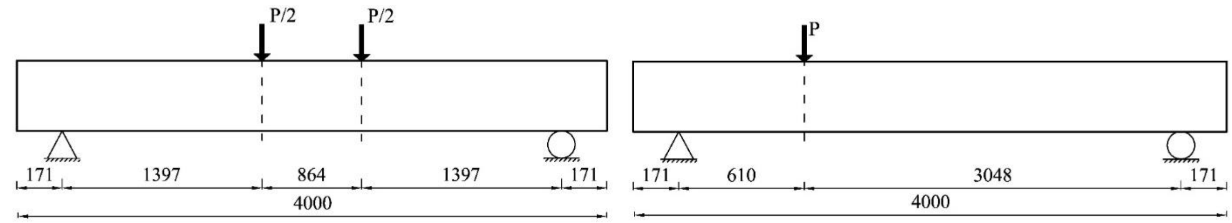

(a) Loading configuration

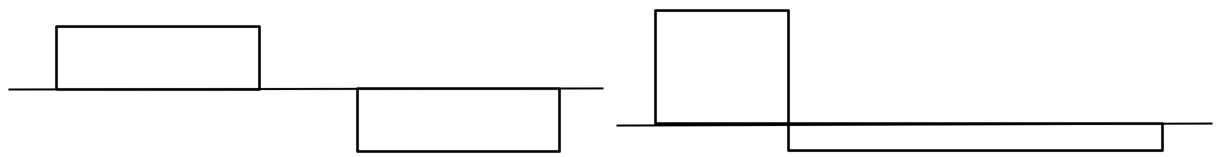

(b) Shear force diagram

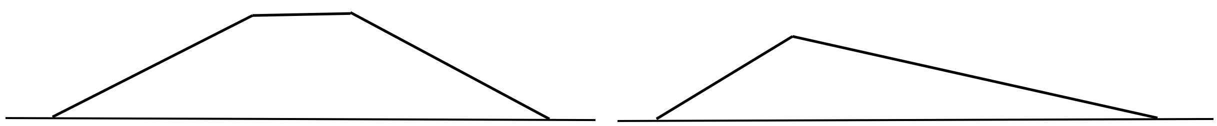

(c) Bending moment diagram

Figure A-2. Schematic of shear force and bending moment diagram for tested UHPFRC beams

A.2 Calculations of Moment Capacity

In order to calculate moment capacity of the beams, first tensile stress in fibrous concrete (σ_t) and tensile stress (σ_{sf}) and strain in fibers ($\varepsilon_{s,fibers}$) are to be calculated:

$$\sigma_t = 0.065\ \frac{L_f}{d_f}\rho_f F_{be} = 0.065 \times \frac{13}{0.2} \times 1.5 \times 1.2 = 7.61\ MPa$$

where F_{be} is bond efficiency of the fiber which varies from 1.0 to 1.2 depending upon fiber characteristics.

$$\sigma_{sf} = \frac{\tau_f \pi d_f\ l_f/2}{\frac{\pi}{4}\ {d_f}^2} = \frac{10.26 \times \pi \times 0.2 \times 13/2}{\frac{\pi}{4}(0.2)^2} = 1333.8\ MPa$$

τ_f, the average bond strength of fibers, for 1.5% volume fraction of fibers is considered to be 10.26 according to test results from Yoo et al. [4].

$$\varepsilon_{s,fibers} = \frac{\sigma_{sf}}{E_{sf}} = \frac{1333.8}{200000} = 0.00667$$

Using equilibrium and with assumption of rebar yielding, depth of compression block and then moment capacity is calculated:

$$C = 0.85\ f_c' ab$$

where b is the width of the beam, h is depth of the beam, d is effective depth of the beam, a is depth of equivalent rectangular stress block ($\beta_1 c$), c is depth of neutral axis, e is distance from extreme compression fiber to top of tensile stress block of fibrous concrete, A_s is the area of tensile reinforcement (see Figure A-3).

$$T = A_s\ f_y + \sigma_t\ b[h - e]$$

$$e = \frac{(\varepsilon_{s,fibers} + 0.0035)}{0.0035} c$$

$$M_n = A_s\ f_y \left(d - \frac{a}{2}\right) + \sigma_t\ b(h - e)\left(\frac{h}{2} + \frac{e}{2} - \frac{a}{2}\right)$$

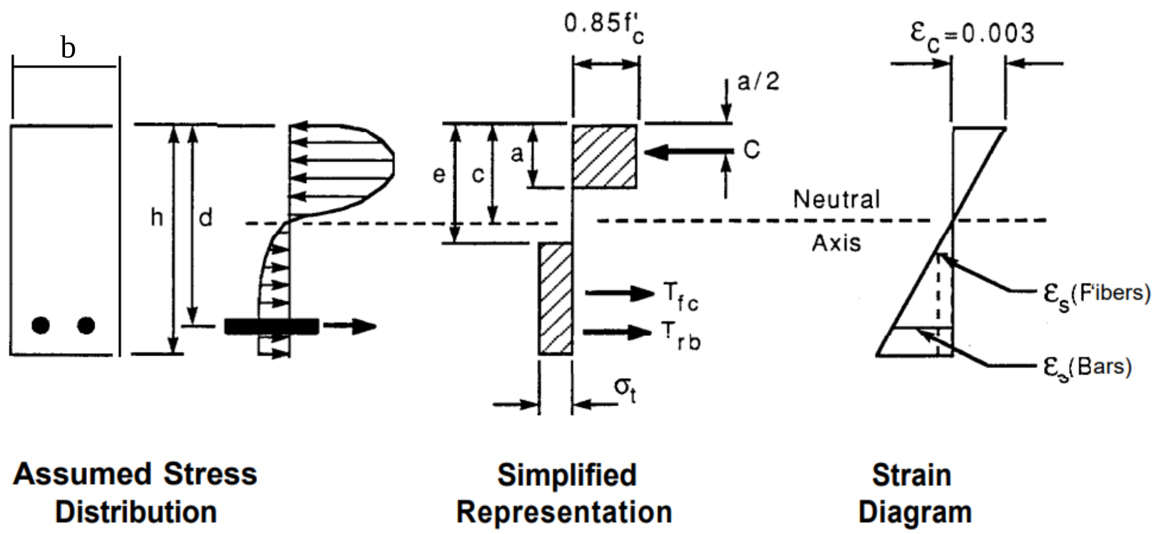

Figure A-3. Design assumptions for analysis of reinforced concrete beams containing steel fibers [310,311]

Beams U-B3 and U-B5:

$$C = 0.85\, f_c' ab = 0.85 \times 160 \times 0.65 \times\ c \times 180$$

$$T = A_s\, f_y + \sigma_t\, b(h - e)$$

$$T = A_s\, f_y + \sigma_t\, b\left(h - \frac{(\varepsilon_{s,fibers} + 0.0035)}{0.0035} c\right)$$

$$T = 3 \times \left(\frac{\pi}{4} \times 12.7^2\right) \times 400 + 7.61 \times 180 \times \left(270 - \frac{(0.00667 + 0.0035)}{0.0035} c\right)$$

$T = C$; therefore $c = 26.23\ mm$

Ultimate compressive strain of UHPFRC was assumed to be 0.0035 [10,310,312,313].

$$M_n = A_s\, f_y\left(d - \frac{a}{2}\right) + \sigma_t\, b(h - e)\left(\frac{h}{2} + \frac{e}{2} - \frac{a}{2}\right)$$

$$e = \frac{(0.00667 + 0.0035)}{0.0035} \times 26.23 = 76.22\ mm$$

$$M_n = 3 \times \left(\frac{\pi}{4} \times 12.7^2\right) \times 400 \times \left(235 - \frac{0.65 \times 26.23}{2}\right) + 7.61 \times 180$$
$$\times (270 - 76.22)\left(\frac{270}{2} + \frac{76.22}{2} - \frac{0.65 \times 26.23}{2}\right) = 78.1\ kN.m$$

$$\varepsilon_s = \left(\frac{d - c}{c}\right) \times 0.0035 = \left(\frac{235 - 26.23}{26.23}\right) \times 0.0035 = 0.028 > \varepsilon_y$$

Therefore, the assumption of rebar yielding is valid.

Beams U-B5, U-B6, and U-B7:

$$C = 0.85\, f_c' ab = 0.85 \times 160 \times 0.65 \times\ c \times 180$$

$$T = A_s\, f_y + \sigma_t\, b\left(h - \frac{(\varepsilon_{s,fibers} + 0.0035)}{0.0035} c\right)$$

$$T = 4 \times \left(\frac{\pi}{4} \times 12.7^2\right) \times 400 + 7.61 \times 180 \times \left(270 - \frac{(0.00667 + 0.0035)}{0.0035} c\right)$$

$T = C$; therefore $c = 28.78\ mm$

$$M_n = A_s f_y \left(d - \frac{a}{2}\right) + \sigma_t b(h-e)\left(\frac{h}{2} + \frac{e}{2} - \frac{a}{2}\right)$$

$$e = \frac{(0.00667 + 0.0035)}{0.0035} \times 28.78 = 83.63\, mm$$

$$M_n = 4 \times \left(\frac{\pi}{4} \times 12.7^2\right) \times 400 \times \left(235 - \frac{0.65 \times 28.78}{2}\right) + 7.61 \times 180$$
$$\times (270 - 83.63)\left(\frac{270}{2} + \frac{83.63}{2} - \frac{0.65 \times 28.78}{2}\right) = 88.5\, kN.m$$

$$\varepsilon_s = \left(\frac{d-c}{c}\right) \times 0.0035 = \left(\frac{235 - 28.78}{28.78}\right) \times 0.0035 = 0.025 > \varepsilon_y$$

Therefore, the assumption of rebar yielding is valid.

<u>Beams U-B8 and U-B9:</u>

$$C = 0.85\, f_c' ab = 0.85 \times 160 \times 0.65 \times c \times 180$$

$$T = A_s f_y + \sigma_t b\left(h - \frac{(\varepsilon_{s,fibers} + 0.0035)}{0.0035} c\right)$$

$$T = 6 \times \left(\frac{\pi}{4} \times 19.05^2\right) \times 400 + 7.61 \times 180 \times \left(450 - \frac{(0.00667 + 0.0035)}{0.0035} c\right)$$

$T = C$; therefore $c = 65.38\, mm$

$$M_n = A_s f_y \left(d - \frac{a}{2}\right) + \sigma_t b(h-e)\left(\frac{h}{2} + \frac{e}{2} - \frac{a}{2}\right)$$

$$e = \frac{(0.00667 + 0.0035)}{0.0035} \times 65.38 = 189.98\, mm$$

$$d = 450 - 45 - \frac{45}{2} = 382.5\, mm$$

$$M_n = 6 \times \left(\frac{\pi}{4} \times 19.05^2\right) \times 400 \times \left(382.5 - \frac{0.65 \times 65.38}{2}\right) + 7.61 \times 180$$
$$\times (450 - 189.98)\left(\frac{450}{2} + \frac{189.98}{2} - \frac{0.65 \times 65.38}{2}\right) = 353.5\, kN.m$$

$$\varepsilon_s = \left(\frac{d-c}{c}\right) \times 0.0035 = \left(\frac{382.5 - 65.38}{65.38}\right) \times 0.0035 = 0.017 > \varepsilon_y$$

Therefore, the assumption of rebar yielding is valid.

The longitudinal bars spacing, arrangment, and cover were designed as per ACI-318 requirements for conventional beams [161]. Minimum clear spacing between longitudinal bars is the greatest of 25 mm, diameter of bars, and $4/3\, d_{agg}$.

Two beams of U-B7 and U-B9 were provided with minimum shear reinforcement as per ACI-318 requirement.

$$A_{v,min} = 0.062\sqrt{f_c'}\,\frac{b_w S}{f_y} > 0.35\,\frac{b_w\, S}{f_y}$$

Also, $S \leq \frac{d}{2} \leq 600\, mm$

Using No. 3 stirrups, S for providing minimum shear reinforcement:

$$S = \frac{A_v f_y}{0.062\,\sqrt{f_c'}\, b_w} \leq \frac{A_v f_y}{0.35\, b_w}$$

$$S = \frac{2 \times \frac{\pi}{4} \times 9.525^2 \times 400}{0.062\ \times \sqrt{160}\ \times 180} = 403.8\, mm < \frac{A_v f_y}{0.35\, b_w}$$

$$S \leq \frac{d}{2};\ S \leq \frac{235}{2}\quad for\ beam\ U - B7$$

$$S \leq \frac{d}{2};\ S \leq \frac{382.5}{2}\quad for\ beam\ U - B9$$

Therefore, stirrups spacing of 100 mm and 200 mm was selected for beams U-B7 and U-B9, respectively.

A.3 Calculations of Shear Capacity

AFGC [25] recommends expressions as follows for calculating shear capacity of UHPFRC beams consisting of contribution of concrete (V_{UHPC}), fibers (V_f), and shear reinforcement (V_s). Since in the designed beams, stirrups did not contribute to shear capacity, only the contribution of concrete ($V_{UHPC} + V_f$) is calculated.

$$V_{UHPFRC} = V_{UHPC} + V_f$$

$$V_{UHPC} = \frac{0.21}{\gamma_E \gamma_b} k \sqrt{f_c'}\, bd,\ \gamma_E \gamma_b = 1.5\ (for\ reinforced\ beams)$$

$$k = 1 + \frac{3\sigma_{cm}}{f_{tj}}\ (in\ compression);\ k = 1 - \frac{0.7\sigma_{tm}}{f_{tj}}\ (in\ tension)$$

$$V_f = \frac{0.9 bd\sigma_p}{\gamma_{bf}\ tan\beta_u}$$

$$\sigma_p = \frac{1}{K}\frac{1}{w_{lim}}\int_0^{w_{lim}} \sigma(w)dw\,, w_{lim} = \max(w_u, 0.3\ mm)$$

where γ_E is the safety coefficient such that $\gamma_E \gamma_b = 1.5$, σ_m is the mean stress in the total section concrete under normal design force, f_{tj} is direct tensile strength, β_u is the inclination angle between a diagonal crack and longitudinal direction of the beam (a minimum value of 30º is recommended), K is the orientation coefficient for general effects, $\sigma(w)$ is experimental characteristic post-cracking stress for a crack width of w, w_u is ultimate crack width.

<u>Beams with b=180 mm and h=270mm:</u>

$$d = 270 - 35 = 235\ mm$$

$$V_{UHPC} = \frac{0.21}{1.5}\sqrt{160} \times 180 \times 235 = 74.9\ kN$$

$\int_0^{w_{lim}} \sigma(w)dw$ was obtained from tests conducted by Yoo et al. [4,51].

$$\sigma_p = \frac{1}{1.25 \ \times 6mm} \times 27\left(\frac{N}{mm}\right) = 3.6 \ \frac{N}{mm^2}$$

$$V_f = \frac{0.9 \ \times 180 \times 235 \times \ 3.6}{1.3 \times \ tan30} = 182.6 \ kN$$

$$V_{UHPC} = 74.9 + 182.6 = 257.5 \ kN$$

<u>Beams with b=180 mm and h=450mm:</u>

$$d = 450 - 45 - \frac{45}{2} = 382.5 \ mm$$

$$V_{UHPC} = \frac{0.21}{1.5}\sqrt{160} \times 180 \times 382.5 = 121.9 \ kN$$

$\int_0^{w_{lim}} \sigma(w)dw$ was obtained from tests conducted by Yoo et al. [4,51].

$$\sigma_p = \frac{1}{1.25 \ \times 6mm} \times 27\left(\frac{N}{mm}\right) = 3.6 \ \frac{N}{mm^2}$$

$$V_f = \frac{0.9 \ \times 180 \times 382.5 \times \ 3.6}{1.3 \times \ tan30} = 297.2 \ kN$$

$$V_{UHPC} = 121.9 + 297.2 = 419.1 \ kN$$

The summary of the designed beams is presented in Table A-1.

Table A-1. Summary of the designed UHPFRC beams

Beams	*b* (mm)	*h* (mm)	*L* (mm)	*Vf* (%)	Tensile Bars	*ρt* (%)	*ρv* (%)	*ρc* (%)	Type of loading	ACI 544 with modified tensile strength model	AFGC
										Moment capacity (kN.m)	Shear Capacity (kN)
U-B3	180	270	4000	1.5	3-D13	0.90	-	-	Flexural	78.1	257.5
U-B4	180	270	4000	1.5	3-D13	0.90	-	-	Shear	78.1	257.5
U-B5	180	270	4000	1.5	4-D13	1.20	-	-	Flexural	88.5	257.5
U-B6	180	270	4000	1.5	4-D13	1.20	-	-	Shear	88.5	257.5
U-B7	180	270	4000	1.5	4-D13	1.20	0.79	0.34	Shear	88.5	257.5
U-B8	180	450	4000	1.5	6-D19	2.48	-	-	Shear	353.5	419.1
U-B9	180	450	4000	1.5	6-D19	2.48	0.40	0.21	Shear	353.5	419.1

ρ_t, ρ_v, and ρ_c are tensile, shear, and compressive reinforcement ratio.
V_f is fibers volume fraction. *b, h,* and *L* are width, depth, and length of the beams.

REFERENCES

REFERENCES

[1] Kang S-T, Lee Y, Park Y-D, Kim J-K. Tensile fracture properties of an Ultra High Performance Fiber Reinforced Concrete (UHPFRC) with steel fiber. Compos Struct 2010;92:61–71.

[2] Xu M, Wille K. Fracture energy of UHP-FRC under direct tensile loading applied at low strain rates. Compos Part B Eng 2015;80:116–25.

[3] Empelmann M, Teutsch M, Steven G. Improvement of the post fracture behaviour of UHPC by fibres. Second Int. Symp. Ultra High Perform. Concr., 2008, p. 177.

[4] Yoo D-Y, Lee J-H, Yoon Y-S. Effect of fiber content on mechanical and fracture properties of ultra high performance fiber reinforced cementitious composites. Compos Struct 2013;106:742–53.

[5] Yang I-H, Joh C, Kim B-S. Flexural response predictions for ultra-high-performance fibre-reinforced concrete beams. Mag Concr Res 2011;64:113–127.

[6] Graybeal B, Tanesi J. Durability of an ultrahigh-performance concrete. J Mater Civ Eng 2007;19:848–54.

[7] Graybeal B, Brühwiler E, Kim B-S, Toutlemonde F, Voo YL, Zaghi A. International Perspective on UHPC in Bridge Engineering. J Bridge Eng 2020;25:04020094.

[8] Russell HG, Graybeal BA, Russell HG. Ultra-high performance concrete: a state-of-the-art report for the bridge community. United States. Federal Highway Administration; 2013.

[9] Graybeal B, Crane CK, Perry V, Corvez D, Ahlborn TM. Advancing ultra-high-performance concrete. Concr Int 2019;41:41–5.

[10] Yoo D. Performance enhancement of ultra-high-performance fiber-reinforced concrete and model development for practical utilization. 2014.

[11] Naaman AE. Fiber reinforcement for concrete. Concr Int 1985;7:21–5.

[12] Romualdi JP, Batson GB. Mechanics of crack arrest in concrete. 2008.

[13] Romualdi JP, Mandel JA. Tensile strength of concrete affected by uniformly distributed and closely spaced short lengths of wire reinforcement. vol. 61, 1964, p. 657–72.

[14] Kar DRL. Properties, applications: Slurry infiltrated fiber concrete (SIFCON). Concr Int 1984;6:44–7.

[15] Hackman LE, Farrell MB, Dunham OO. Slurry infiltrated mat concrete (SIMCON). Concr Int 1992;14:53–6.

[16] Li VC, Wu H-C. Conditions for pseudo strain-hardening in fiber reinforced brittle matrix composites 1992.

[17] Dinh HH. Shear Behavior of Steel Fiber Reinforced Concrete Beams without Stirrup Reinforcement. 2009.

[18] Yudenfreund M, Odler I, Brunauer S. Hardened portland cement pastes of low porosity I. Materials and experimental methods. Cem Concr Res 1972;2:313–30.

[19] Roy DM, Gouda G, Bobrowsky A. Very high strength cement pastes prepared by hot pressing and other high pressure techniques. Cem Concr Res 1972;2:349–66.

[20] Bache HH. Densified cement/ultra-fine particle-based materials. Aalborg Portland Aalborg, Denmark; 1981.

[21] Birchall J, Howard A, Kendall K. Flexural strength and porosity of cements. Nature 1981;289:388.

[22] Richard P, Cheyrezy M. Composition of reactive powder concretes. Cem Concr Res 1995;25:1501–11. https://doi.org/10.1016/0008-8846(95)00144-2.

[23] Acker P, Behloul M. Ductal® technology: A large spectrum of properties, a wide range of applications, 2004, p. 11–23.

[24] Chanvillard G, Rigaud S. Complete characterization of tensile properties of Ductal UHPFRC according to the French recommendations, 2003, p. 21–34.

[25] AFGC/SETRA. Ultra high performance fibre-reinforced concretes. Bagneux, France: French Civil Engineering Association; 2002.

[26] JSCE. Recommendations for design and construction of ultra–high strength fiber reinforced concrete structures. Japan Society of Civil Engineers; 2004.

[27] Naaman AE, Wille K. The path to ultra-high performance fiber reinforced concrete (UHP-FRC): five decades of progress. Proc Hipermat 2012:3–15.

[28] Abbas S, Nehdi M, Saleem M. Ultra-high performance concrete: Mechanical performance, durability, sustainability and implementation challenges. Int J Concr Struct Mater 2016;10:271–95.

[29] Schmidt M, Fehling E. Ultra-high-performance concrete: research, development and application in Europe. ACI Spec Publ 2005;228:51–78.

[30] Vernet CP. Ultra-durable concretes: structure at the micro-and nanoscale. MRS Bull 2004;29:324–7.

[31] Ma J, Schneider H. Properties of ultra-high-performance concrete. Leipz Annu Civ Eng Rep LACER 2002;7:25–32.

[32] Barnett SJ, Lataste J-F, Parry T, Millard SG, Soutsos MN. Assessment of fibre orientation in ultra high performance fibre reinforced concrete and its effect on flexural strength. Mater Struct 2010;43:1009–23.

[33] Yazıcı H. The effect of curing conditions on compressive strength of ultra high strength concrete with high volume mineral admixtures. Build Environ 2007;42:2083–9.

[34] Sbia LA. Contributions and mechanisms of action of graphite nanomaterials in ultra high performance concrete. Ph.D. Michigan State University, 2014.

[35] Xing F, Huang LD, Cao ZL, Deng LP. Study on preparation technique for low-cost green reactive powder concrete. vol. 302, Trans Tech Publ; 2006, p. 405–10.

[36] Chan Y-W, Chu S-H. Effect of silica fume on steel fiber bond characteristics in reactive powder concrete. Cem Concr Res 2004;34:1167–72.

[37] Matte V, Moranville M. Durability of reactive powder composites: influence of silica fume on the leaching properties of very low water/binder pastes. Cem Concr Compos 1999;21:1–9.

[38] de Larrard F, Sedran T. Optimization of ultra-high-performance concrete by the use of a packing model. Cem Concr Res 1994;24:997–1009.

[39] Gao R, Liu ZM, Zhang LQ, Stroeven P. Static properties of plain reactive powder concrete beams. vol. 302, Trans Tech Publ; 2006, p. 521–7.

[40] Wen-yu J, Ming-zhe A, Gui-ping Y, Jun-min W. Study on reactive powder concrete used in the sidewalk system of the Qinghai-Tibet railway bridge, 2004, p. 333–8.

[41] Sbia LA, Peyvandi A, Lu J, Abideen S, Weerasiri RR, Balachandra AM, et al. Production methods for reliable construction of ultra-high-performance concrete (UHPC) structures. Mater Struct 2017;50:7.

[42] Rougeau P, Borys B. Ultra high performance concrete with ultrafine particles other than silica fume. vol. 32, 2004, p. 213–25.

[43] Fehling E, Schmidt M, Geisenhanslueke C. International Symposium on Ultra High Performance Concrete 2004.

[44] Fehling E, Schmidt M, Stuerwald S. Second international symposium on ultra high performance concrete. Kassel Baustoffe Massivbau 10 2008.

[45] Wille K, Naaman AE, Parra-Montesinos GJ. Ultra-High Performance Concrete with Compressive Strength Exceeding 150 MPa (22 ksi): A Simpler Way. ACI Mater J 2011;108:46-54,A31-A34.

[46] Benjamin A. Graybeal. Flexural behavior of an ultrahigh-performance concrete I-girder. J Bridge Eng 2008;13:602–10.

[47] Graybeal BA. Material Property Characterization of Ultra-High Performance Concrete 2006.

[48] Yunsheng Z, Wei S, Sifeng L, Chujie J, Jianzhong L. Preparation of C200 green reactive powder concrete and its static–dynamic behaviors. Cem Concr Compos 2008;30:831–8.

[49] Yoo D-Y, Yoon Y-S. Structural performance of ultra-high-performance concrete beams with different steel fibers. Eng Struct 2015;102:409–23.

[50] Graybeal BA. Material property characterization of ultra-high performance concrete. United States. Federal Highway Administration. Office of Infrastructure …; 2006.

[51] Yoo D-Y, Kang S-T, Yoon Y-S. Effect of fiber length and placement method on flexural behavior, tension-softening curve, and fiber distribution characteristics of UHPFRC. Constr Build Mater 2014;64:67–81.

[52] Graybeal BA. Structural behavior of ultra-high performance concrete prestressed I-girders. United States. Federal Highway Administration. Office of Infrastructure …; 2006.

[53] Solhmirzaei R, Kodur V. Modeling the response of ultra high performance fiber reinforced concrete beams. Procedia Eng 2017;210:211–9.

[54] Sbia LA, Peyvandi A, Soroushian P, Balachandra AM. Optimization of ultra-high-performance concrete with nano- and micro-scale reinforcement. Cogent Eng 2014;1:990673.

[55] Ahmed Sbia L, Peyvandi A, Soroushian P, Lu J, Balachandra AM. Enhancement of ultrahigh performance concrete material properties with carbon nanofiber. Adv Civ Eng 2014;2014:e854729.

[56] Yoo D-Y, Shin H-O, Yang J-M, Yoon Y-S. Material and bond properties of ultra high performance fiber reinforced concrete with micro steel fibers. Compos Part B Eng 2014;58:122–33.

[57] Soroushian P, Lee C-D. Distribution and orientation of fibers in steel fiber reinforced concrete. Mater J 1990;87:433–439.

[58] Kim DJ, Park SH, Ryu GS, Koh KT. Comparative flexural behavior of hybrid ultra high performance fiber reinforced concrete with different macro fibers. Constr Build Mater 2011;25:4144–55.

[59] Aydın S, Baradan B. The effect of fiber properties on high performance alkali-activated slag/silica fume mortars. Compos Part B Eng 2013;45:63–9.

[60] Yoo D-Y, Zi G, Kang S-T, Yoon Y-S. Biaxial flexural behavior of ultra-high-performance fiber-reinforced concrete with different fiber lengths and placement methods. Cem Concr Compos 2015;63:51–66. https://doi.org/10.1016/j.cemconcomp.2015.07.011.

[61] Yang IH, Joh C, Kim B-S. Structural behavior of ultra high performance concrete beams subjected to bending. Eng Struct 2010;32:3478–87.

[62] Chen L, Graybeal BA. Modeling structural performance of second-generation ultrahigh-performance concrete pi-girders. J Bridge Eng 2011;17:634–43.

[63] Yoo D-Y, Banthia N, Yoon Y-S. Flexural behavior of ultra-high-performance fiber-reinforced concrete beams reinforced with GFRP and steel rebars. Eng Struct 2016;111:246–62.

[64] Collepardi S, Coppola L, Troli R, Collepardi M. Mechanical properties of modified reactive powder concrete. ACI Spec Publ 1997;173:1–22.

[65] Ma J, Orgass M, Dehn F, Schmidt D, Tue N. Comparative investigations on ultra-high performance concrete with and without coarse aggregates, 2004, p. 205–12.

[66] Yazıcı H, Yardımcı MY, Yiğiter H, Aydın S, Türkel S. Mechanical properties of reactive powder concrete containing high volumes of ground granulated blast furnace slag. Cem Concr Compos 2010;32:639–48.

[67] Yazıcı H, Yardımcı MY, Aydın S, Karabulut AŞ. Mechanical properties of reactive powder concrete containing mineral admixtures under different curing regimes. Constr Build Mater 2009;23:1223–31.

[68] Van Tuan N, Ye G, Van Breugel K, Fraaij AL, Dai Bui D. The study of using rice husk ash to produce ultra high performance concrete. Constr Build Mater 2011;25:2030–5.

[69] Ambily P, Umarani C, Ravisankar K, Prem PR, Bharatkumar B, Iyer NR. Studies on ultra high performance concrete incorporating copper slag as fine aggregate. Constr Build Mater 2015;77:233–40.

[70] Kang S-T, Kim J-K. Investigation on the flexural behavior of UHPCC considering the effect of fiber orientation distribution. Constr Build Mater 2012;28:57–65.

[71] El-Dieb A links open overlay panelAmr S. Mechanical, durability and microstructural characteristics of ultra-high-strength self-compacting concrete incorporating steel fibers. Mater Des 2009;30:4286–92.

[72] Graybeal BA. Compressive behavior of ultra-high-performance fiber-reinforced concrete. ACI Mater J 2007;104:146.

[73] Voit K, Kirnbauer J. Tensile characteristics and fracture energy of fiber reinforced and non-reinforced ultra high performance concrete (UHPC). Int J Fract 2014;188:147–57.

[74] Magureanu C, Sosa I, Negrutiu C, Heghes B. Mechanical properties and durability of ultra-high-performance concrete. ACI Mater J 2012;109:177.

[75] Graybeal BA, Davis M. Cylinder or cube: strength testing of 80 to 200 MPa (11.6 to 29 ksi) ultra-high-performance fiber-reinforced concrete. ACI Mater J 2008;106.

[76] Hassan A, Jones S, Mahmud G. Experimental test methods to determine the uniaxial tensile and compressive behaviour of ultra high performance fibre reinforced concrete (UHPFRC). Constr Build Mater 2012;37:874–82.

[77] Wu Z, Shi C, He W, Wu L. Effects of steel fiber content and shape on mechanical properties of ultra high performance concrete. Constr Build Mater 2016;103:8–14.

[78] Bunje K, Fehling E. About shear force and punching shear resistance of structural elements of Ultra High Performance Concrete, 2004, p. 401–11.

[79] Voit K, Kirnbauer J. Tensile characteristics and fracture energy of fiber reinforced and non-reinforced ultra high performance concrete (UHPC). Int J Fract 2014;188:147–57. https://doi.org/10.1007/s10704-014-9951-7.

[80] Park R, Paulay T. Reinforced concrete structures. New York: Jon Wiley and Sons, Inc.; 1975.

[81] Yoo D-Y, Lee J-H, Yoon Y-S. Effect of fiber content on mechanical and fracture properties of ultra high performance fiber reinforced cementitious composites. Compos Struct 2013;106:742–53. https://doi.org/10.1016/j.compstruct.2013.07.033.

[82] Yoo D-Y, Banthia N. Mechanical properties of ultra-high-performance fiber-reinforced concrete: A review. Cem Concr Compos 2016;73:267–80.

[83] Prabha SL, Dattatreya J, Neelamegam M, Seshagirirao M. Study on stress-strain properties of reactive powder concrete under uniaxial compression. Int J Eng Sci Technol 2010;2:6408–16.

[84] Wille K, Naaman AE. Pullout Behavior of High-Strength Steel Fibers Embedded in Ultra-High-Performance Concrete. ACI Mater J 2012;109.

[85] Wille K, Kim DJ, Naaman AE. Strain-hardening UHP-FRC with low fiber contents. Mater Struct 2011;44:583–598.

[86] Yoo D-Y, Kang S-T, Lee J-H, Yoon Y-S. Effect of shrinkage reducing admixture on tensile and flexural behaviors of UHPFRC considering fiber distribution characteristics. Cem Concr Res 2013;54:180–90.

[87] Ye Y, Hu S, Daio B, Yang S, Liu Z. Mechanical behavior of ultra-high performance concrete reinforced with hybrid different shapes of steel fiber. CICTP 2012 Multimodal Transp. Syst. Safe Cost-Eff. Effic., 2012, p. 3017–28.

[88] Wille K, El-Tawil S, Naaman A. Properties of strain hardening ultra high performance fiber reinforced concrete (UHP-FRC) under direct tensile loading. Cem Concr Compos 2014;48:53–66.

[89] Park SH, Kim DJ, Ryu GS, Koh KT. Tensile behavior of Ultra High Performance Hybrid Fiber Reinforced Concrete. Cem Concr Compos 2012;34:172–84. https://doi.org/10.1016/j.cemconcomp.2011.09.009.

[90] Wille K, Kim DJ, Naaman AE. Strain-hardening UHP-FRC with low fiber contents. Mater Struct 2011;44:583–98. https://doi.org/10.1617/s11527-010-9650-4.

[91] Zanni H, Cheyrezy M, Maret V, Philippot S, Nieto P. Investigation of hydration and pozzolanic reaction in reactive powder concrete (RPC) using 29Si NMR. Cem Concr Res 1996;26:93–100.

[92] Müller U, Meng B, Kühne H-C, Nemecek J, Fontana P, Fehling E. Micro texture and mechanical properties of heat treated and autoclaved Ultra High Performance Concrete (UHPC), 2008, p. 213–20.

[93] Cwirzen A. The effect of the heat-treatment regime on the properties of reactive powder concrete. Adv Cem Res 2007;19:25–33.

[94] Lee N, Chisholm D. Reactive Powder Concrete, Study Report SR 146 2005.

[95] Heinz D, Ludwig H-M. Heat treatment and the risk of DEF delayed ettringite formation in UHPC, 2004, p. 717–30.

[96] Teichmann T, Schmidt M. Influence of the packing density of fine particles on structure, strength and durability of UHPC, 2004, p. 313–23.

[97] Xing F, Huang LD, Cao ZL, Deng LP. Study on preparation technique for low-cost green reactive powder concrete. vol. 302, Trans Tech Publ; 2006, p. 405–10.

[98] Soutsos MN, Millard SG, Karaiskos K. Mix design, mechanical properties, and impact resistance of reactive powder concrete (RPC), 2005, p. 549–60.

[99] Bonneau O, Lachemi M, Dallaire E, Dugat J, Aitcin P-C. Mechanical properties and durability of two industrial reactive powder concretes. Mater J 1997;94:286–90.

[100] Akhnoukh AK, Xie H. Welded wire reinforcement versus random steel fibers in precast/prestressed ultra-high performance concrete I-girders. Constr Build Mater 2010;24:2200–7.

[101] GRANEWALD S, VAN LOENHOUT P. Application of Ultra High Performance Concrete: Outstanding projects from Hurks Beton. Betonw Fert-Tech 2008;74.

[102] Habel K, Charron J-P, Braike S, Hooton RD, Gauvreau P, Massicotte B. Ultra-high performance fibre reinforced concrete mix design in central Canada. Can J Civ Eng 2008;35:217–24.

[103] Yang S, Millard S, Soutsos M, Barnett S, Le TT. Influence of aggregate and curing regime on the mechanical properties of ultra-high performance fibre reinforced concrete (UHPFRC). Constr Build Mater 2009;23:2291–8.

[104] Park J-S, Kim YJ, Cho J-R, Jeon S-J. Early-age strength of ultra-high performance concrete in various curing conditions. Materials 2015;8:5537–53.

[105] Koh K-T, Park J-J, Ryu G-S, Kang S-T. Effect of the compressive strength of ultra-high strength steel fiber reinforced cementitious composites on curing method. J Korean Soc Civ Eng 2007;27:427–32.

[106] Empelmann M, Teutsch M, Steven G. Improvement of the post fracture behavior of UHPC by fibers. Ultra High Perform. Concr. UHPC Proc. Second Int. Symp. Ultra High Perform. Concr., Kassel, Germany: 2008, p. 177–84.

[107] Schumacher P. Rotation capacity of self-compacting SFRC. TU Delft, 2006.

[108] Yoo D-Y, Kim J, Zi G, Yoon Y-S. Effect of shrinkage-reducing admixture on biaxial flexural behavior of ultra-high-performance fiber-reinforced concrete. Constr Build Mater 2015;89:67–75.

[109] Uchida Y, Kurihara N. Determination of tension softening diagrams of various kinds of concrete by means of numerical analysis. Fram.-2, Germany: 1995.

[110] Kitsutaka Y. Fracture parameters by poly-linear tension softening analysis. J Eng Mech 1997;123:444–50.

[111] Wille K, Naaman A. Fracture energy of UHPFRC under direct tensile loading. Fram-7 Int Conf Jeju Korea 2010.

[112] Wille K, Naaman A. Fracture energy of UHPFRC under direct tensile loading. Fram.-7 Int. Conf., Jeju, Korea: 2010.

[113] Singh M, Sheikh A, Ali MM, Visintin P, Griffith M. Experimental and numerical study of the flexural behaviour of ultra-high performance fibre reinforced concrete beams. Constr Build Mater 2017;138:12–25.

[114] Kwak Y-K, Eberhard MO, Kim W-S, Kim J. Shear strength of steel fiber-reinforced concrete beams without stirrups. ACI Struct J 2002;99:530–8.

[115] Cho S-H, Kim Y-I. Effects of steel fibers on short beams loaded in shear. Struct J 2003;100:765–74.

[116] Ashour SA, Hasanain GS, Wafa FF. Shear behavior of high-strength fiber reinforced concrete beams. Struct J 1992;89:176–84.

[117] Narayanan R, Darwish I. Use of steel fibers as shear reinforcement. Struct J 1987;84:216–27.

[118] Elliott K, Peaston C, Paine KA. Experimental and theoretical investigation of the shear resistance of steel fibre reinforced prestressed concrete X-beams—Part II: Theoretical analysis and comparison with experiments. Mater Struct 2002;35:528.

[119] Casanova P, Rossi P. Can steel fibers replace transverse reinforcements in reinforced concrete beams? Mater J 1997;94:341–54.

[120] Mansur M, Ong K, Paramasivam P. Shear strength of fibrous concrete beams without stirrups. J Struct Eng 1986;112:2066–79.

[121] Meda A, Minelli F, Plizzari G, Riva P. Shear behaviour of steel fibre reinforced concrete beams. Mater Struct 2005;38:343–51.

[122] Cho J-S, Lundy J, Chao S-H. Shear strength of steel fiber reinforced prestressed concrete beams, 2009, p. 1–9.

[123] Voo YL, Poon WK, Foster SJ. Shear strength of steel fiber-reinforced ultrahigh-performance concrete beams without stirrups. J Struct Eng 2010;136:1393–400.

[124] Yang I-H, Joh C, Kim B-S. Shear behaviour of ultra-high-performance fibre-reinforced concrete beams without stirrups. Mag Concr Res 2012;64:979–93.

[125] Xia J, Mackie KR, Saleem MA, Mirmiran A. Shear failure analysis on ultra-high performance concrete beams reinforced with high strength steel. Eng Struct 2011;33:3597–609.

[126] Baby F, Marchand P, Toutlemonde F. Shear behavior of ultrahigh performance fiber-reinforced concrete beams. I: experimental investigation. J Struct Eng 2014;140:4013111.

[127] Pourbaba M, Joghataie A, Mirmiran A. Shear behavior of ultra-high performance concrete. Constr Build Mater 2018;183:554–64.

[128] Yoo D-Y, Banthia N, Yoon Y-S. Experimental and numerical study on flexural behavior of ultra-high-performance fiber-reinforced concrete beams with low reinforcement ratios. Can J Civ Eng 2016;44:18–28.

[129] Yao Y, Mobasher B, Wang J, Xu Q. Analytical approach for the design of flexural elements made of reinforced ultra-high performance concrete. Struct Concr 2020.

[130] Mahmud GH, Yang Z, Hassan AM. Experimental and numerical studies of size effects of Ultra High Performance Steel Fibre Reinforced Concrete (UHPFRC) beams. Constr Build Mater 2013;48:1027–34.

[131] Tysmans T, Wozniak M, Remy O, Vantomme J. Finite element modelling of the biaxial behaviour of high-performance fibre-reinforced cement composites (HPFRCC) using Concrete Damaged Plasticity. Finite Elem Anal Des 2015;100:47–53.

[132] Chen L, Graybeal BA. Modeling structural performance of ultrahigh performance concrete I-girders. J Bridge Eng 2011;17:754–64.

[133] Bahij S, Adekunle SK, Al-Osta M, Ahmad S, Al-Dulaijan SU, Rahman MK. Numerical investigation of the shear behavior of reinforced ultra-high-performance concrete beams. Struct Concr 2018;19:305–17.

[134] Baby F, Marchand P, Atrach M, Toutlemonde F. Analysis of flexure-shear behavior of UHPFRC beams based on stress field approach. Eng Struct 2013;56:194–206.

[135] Voo JYL, Foster DSJ, Gilbert R. Shear strength of fibre reinforced reactive powder concrete girders without stirrups. University of New South Wales, School of Civil and Environmental Engineering; 2003.

[136] Voo YL, Foster SJ, Gilbert RI. Shear Strength of Fiber Reinforced Reactive Powder Concrete Prestressed Girders without Stirrups. J Adv Concr Technol 2006;4:123–32. https://doi.org/10.3151/jact.4.123.

[137] Zhang J-P. Serie: Strength of Cracked Concrete, Part 1: Shear Strength of Conventional Reinforced Concrete Beams, Deep Beams, Corbels, and Prestressed Reinforced Concrete Beams Without Shear Reinforcement. 1994.

[138] Voo JYL, Foster SJ. Variable engagement model for the design of fibre reinforced concrete structures 2003.

[139] KCI. Design recommendations for ultra-high performance concrete K-UHPC. Seoul: Korea Concrete Institute; 2012.

[140] Orange G. A New Generation of UHP Concrete (DUCTAL), Damage Resistance and Micromechanical Analysis, RILEM Publications SARL; 1999, p. 101–11.

[141] Tadros MK, Sevenker A, Berry R. Ultra-High-Performance Concrete. Struct Mag n.d.:8–12.

[142] ACI Committee. Ultra-High-Performance Concrete: An Emerging Technology Report (ACI239R-18), American Concrete Institute; 2018.

[143] Resplendino J. First recommendations for Ultra-High-Performance Concretes and examples of application, 2004, p. 79–90.

[144] Hajar Z, Lecointre D, Simon A, Petitjean J. Design and construction of the world first ultra-high performance concrete road bridges, 2004, p. 39–48.

[145] Voo YL, Nematollahi B, Said ABM, Gopal BA, Yee TS. Application of ultra high performance fiber reinforced concrete—The Malaysia perspective. Int J Sustain Constr Eng Technol 2012;3:26–44.

[146] Voo YL, Foster SJ, Voo CC. Ultrahigh-performance concrete segmental bridge technology: Toward sustainable bridge construction. J Bridge Eng 2014;20:B5014001.

[147] Kim B-S, Joh C, Koh G-T, Park J, Kwon K, Park S-Y. KICT's Application of UHPC to the First UHPC Cable Stayed Roadway Bridge. vol. 1, Iowa State University Digital Press; 2016.

[148] Behioul M, Kim K, Comte G, Loisel M, CAUSSE G, Etienne D, et al. La Construction De La Passerelle De Seonyu-Un Arc En DUCTAL A Seoul. Travaux 2003.

[149] Graybeal BA. Structural behavior of a 2nd generation ultra-high performance concrete pi-girder. US Department of Transportation, Federal Highway Administration; 2009.

[150] NPCA White Paper. Ultra high performance concrete (UHPC), guide to manufacturing architectural precast UHPC elements. 2011.

[151] Delplace G, Hajar Z, Simon A, Chanut S, Weizmann L. Precast thin UHPFRC curved shells in a waste water treatment plant, 2013, p. 49–58.

[152] Azmee NM, Shafiq N. Ultra-high performance concrete: From fundamental to applications. Case Stud Constr Mater 2018;9:e00197.

[153] Yoo D-Y, Yoon Y-S. A review on structural behavior, design, and application of ultra-high-performance fiber-reinforced concrete. Int J Concr Struct Mater 2016;10:125–42.

[154] Fabbri R, Corvez D. Rationalisation of complex UHPFRC facade shapes, 2013, p. 27–36.

[155] Muttoni A, Brauen U, Jaquier J-L, Moullet D. A new roof for the olympic museum at Lausanne, Switzerland, 2013, p. 69–76.

[156] Menétrey P. UHPFRC cladding for the Qatar National Museum. vol. 360, 2013.

[157] Resplendino J, Toutlemonde F. The UHPFRC revolution in structural design and construction, 2013, p. 791–804.

[158] Mazzacane P, Ricciotti R, Teply F, Tollini E, Corvez D. MUCEM: The builder's perspective. Proc UHPFRC 2013:3–16.

[159] Kodur V, Solhmirzaei R, Agrawal A, Aziz EM, Soroushian P. Analysis of flexural and shear resistance of ultra high performance fiber reinforced concrete beams without stirrups. Eng Struct 2018;174:873–84.

[160] Solhmirzaei R, Kodur VK. Structural behavior of ultra high performance concrete beams without stirrups. Transp. Res. Board 97th Annu. Meet., 2018.

[161] ACI Committee 318. Building code requirements for structural concrete (ACI 318-19) and commentary, American Concrete Institute; 2019.

[162] Wang C, Yang C, Liu F, Wan C, Pu X. Preparation of ultra-high performance concrete with common technology and materials. Cem Concr Compos 2012;34:538–44.

[163] Chen Y, Matalkah F, Yu Y, Rankothge W, Balachandra A, Soroushian P. Experimental investigations of the dimensional stability and durability of ultra-high-performance concrete. Adv Mater Sci 2017;6:1–8.

[164] ASTM C143. Standard test method for slump of hydraulic-cement concrete. ASTM Stand 2015.

[165] Scheydt JC, Herold G, Müller HS, Kunt M, Fehling E, Schmidt M, et al. Development and application of UHPC convenience blends. Proc Second Int Symp Ultra High Perform Concr Kassel Ger March 05-07 2008 Bd 1 Ed E Fehling 2008.

[166] Ahlborn TM, Misson DL, Peuse EJ, Gilbertson CG. Durability and strength characterization of ultra-high performance concrete under variable curing regimes, 2008, p. 197–204.

[167] Wang D, Shi C, Wu Z, Xiao J, Huang Z, Fang Z. A review on ultra high performance concrete: Part II. Hydration, microstructure and properties. Constr Build Mater 2015;96:368–77. https://doi.org/10.1016/j.conbuildmat.2015.08.095.

[168] Sbia L, Peyvandi A, Harsini I, Lu J, Abideen SU, Weerasiri R, et al. Study on field thermal curing of ultra-high-performance concrete employing heat of hydration. ACI Mater J 2017;114.

[169] Kodur VKR, Bhatt PP, Soroushian P, Arablouei A. Temperature and stress development in ultra-high performance concrete during curing. Constr Build Mater 2016;122:63–71.

[170] Kim G-Y, Lee E-B, Nam J-S, Koo K-M. Analysis of hydration heat and autogenous shrinkage of high-strength mass concrete. Mag Concr Res 2011;63:377–89.

[171] ASTM C496. Standard test method for splitting tensile strength of cylindrical concrete specimens. ASTM Stand 1984.

[172] Kang S-T, Kim J-K. The relation between fiber orientation and tensile behavior in an Ultra High Performance Fiber Reinforced Cementitious Composites (UHPFRCC). Cem Concr Res 2011;41:1001–14. https://doi.org/10.1016/j.cemconres.2011.05.009.

[173] JCI. Method of Test for Load–Displacement Curve of Fiber Reinforced Concrete by Use of Notched Beam. Japan Concrete Institute; 2003.

[174] Gribniak V, Caldentey AP, Kaklauskas G, Rimkus A, Sokolov A. Effect of arrangement of tensile reinforcement on flexural stiffness and cracking. Eng Struct 2016;124:418–28.

[175] Pillai SU, Menon D. Reinforced concrete design. McGraw-Hill Education (India); 2003.

[176] Tim Stratford, Chris Burgoyne. Shear analysis of concrete with brittle reinforcement. J Compos Constr 2003;7:323–30.

[177] Cladera A, Mari A. Experimental study on high-strength concrete beams failing in shear. Eng Struct 2005;27:1519–27.

[178] Negrutiu C, Sosa IP, Constantinescu H, Heghes B. Crack analysis of reinforced high strength concrete elements in simulated aggressive environments. Procedia Technol 2016;22:4–12.

[179] Vandewalle L. Cracking behaviour of concrete beams reinforced with a combination of ordinary reinforcement and steel fibers. Mater Struct 2000;33:164–70.

[180] Theriault M, Benmokrane B. Effects of FRP reinforcement ratio and concrete strength on flexural behavior of concrete beams. J Compos Constr 1998;2.

[181] Ashour SA, Wafa FF. Flexural behavior of high-strength fiber reinforced concrete beams. Struct J 1993;90:279–87.

[182] Bernardo LFA, Lopes SMR. Neutral axis depth versus flexural ductility in high-strength concrete beams. J Struct Eng 2004;130:452–9.

[183] Lee T-K, Pan ADE. Estimating the relationship between tension reinforcement and ductility of reinforced concrete beam sections. Eng Struct 2003;25:1057–67.

[184] Pam HJ, Kwan AKH, Ho JCM. Post-peak behavior and flexural ductility of doubly reinforced normal- and high-strength concrete beams. Struct Eng Mech 2001;12:459–74.

[185] Islam MS. Shear capacity and flexural ductility of reinforced high-and normal-strength concrete beams. HKU Theses Online HKUTO 1996.

[186] Lecompte D, Smits A, Bossuyt S, Sol H, Vantomme J, Van Hemelrijck D, et al. Quality assessment of speckle patterns for digital image correlation. Opt Lasers Eng 2006;44:1132–45.

[187] Roux S, Réthoré J, Hild F. Digital image correlation and fracture: an advanced technique for estimating stress intensity factors of 2D and 3D cracks. J Phys Appl Phys 2009;42:214004.

[188] Pan B, Qian K, Xie H, Asundi A. Two-dimensional digital image correlation for in-plane displacement and strain measurement: a review. Meas Sci Technol 2009;20:062001.

[189] Yoneyama S, Kitagawa A, Iwata S, Tani K, Kikuta H. Bridge deflection measurement using digital image correlation. Exp Tech 2007;31:34–40.

[190] Solhmirzaei R, Kodur V, Banerji S. Shear Behavior of Ultra High Performance Concrete Beams without Stirrups. vol. 2, Iowa State University Digital Press; 2019.

[191] Timoshenko S. History of strength of materials: with a brief account of the history of theory of elasticity and theory of structures. Courier Corporation; 1983.

[192] ABAQUS. Version 6.14 documentation. Providence (RI): Dassault systems simulia crop; 2014.

[193] Kodur V, Agrawal A. Effect of temperature induced bond degradation on fire response of reinforced concrete beams. Eng Struct 2017;142:98–109.

[194] Lubliner J, Oliver J, Oller S, Onate E. A plastic-damage model for concrete. Int J Solids Struct 1989;25:299–326.

[195] Lee J, Fenves GL. Plastic-damage model for cyclic loading of concrete structures. J Eng Mech 1998;124:892–900.

[196] Speck K. Concrete under multiaxial loading conditions—a constitutive model for short-time loading of high performance concretes 2007.

[197] Luaay Hussein. Structural behavior of ultra high performance fiber reinforced concrete composite members. Ph.D. Ryerson University, 2015.

[198] Ahmad S, Bahij S, Al-Osta M, Adekunle S, Al-Dulaijan S. Shear Behavior of Ultra-High-Performance Concrete Beams Reinforced with High-Strength Steel Bars. ACI Struct J 2019;116:3–14.

[199] Van Gysel A, Taerwe L. Analytical formulation of the complete stress-strain curve for high strength concrete. Mater Struct 1996;29:529–33.

[200] Fehling E, Leutbecher T, Bunje K. Design relevant properties of hardened ultra high performance concrete. vol. 1, 2004, p. 327–38.

[201] Priestley MN, Seible F, Calvi GM, Calvi GM. Seismic design and retrofit of bridges. John Wiley & Sons; 1996.

[202] Cosenza E, Manfredi G, Realfonzo R. Analytical modelling of bond between FRP reinforcing bars and concrete. Non-Metallic (FRP) Reinforcement for Concrete StructuresÐProceedings of the Second International RILEM Symposium (FRPRCS-2)(ed. L. Taerwe). E & FN Spon, London, 1995. vol. 29, n.d., p. 164–71.

[203] Crisfield M. Accelerated solution techniques and concrete cracking. Comput Methods Appl Mech Eng 1982;33:585–607.

[204] Keuser M, Mehlhorn G. Finite element models for bond problems. J Struct Eng 1987;113:2160–73.

[205] Dinh HH, Parra-Montesinos GJ, Wight JK. Shear strength model for steel fiber reinforced concrete beams without stirrup reinforcement. J Struct Eng 2010;137:1039–51.

[206] Kodur VKR, Agrawal A. An approach for evaluating residual capacity of reinforced concrete beams exposed to fire. Eng Struct 2016;110:293–306.

[207] Singh B, Chintakindi S. An appraisal of dowel action in reinforced concrete beams. Proc Inst Civ Eng-Struct Build 2013;166:257–67.

[208] Parra-Montesinos GJ. Shear strength of beams with deformed steel fibers. Concr Int 2006;28:57–66.

[209] Park R, Paulay T. Reinforced concrete structures. John Wiley & Sons; 1975.

[210] Gunawan D, Okubo K, Nakamura T, Niwa J. Shear Capacity of RC Beams Based on Beam and Arch Actions. J Adv Concr Technol 2020;18:241–55.

[211] Fu L, Nakamura H, Furuhashi H, Yamamoto Y, Miura T. Mechanism of shear strength degradation of a reinforced concrete column subjected to cyclic loading. Struct Concr 2017;18:177–88.

[212] Nakamura H, Iwamoto T, Fu L, Yamamoto Y, Miura T, Gedik YH. Shear resistance mechanism evaluation of RC beams based on arch and beam actions. J Adv Concr Technol 2018;16:563–76.

[213] Tadros MK, Sevenker A, Berry R. Ultra-high-performance concrete: A game changer. Struct Mag-Build Blocks 2019:8–12.

[214] Voort TLV. Design and field testing of tapered H-shaped ultra high performance concrete piles. Iowa State University; 2008.

[215] Aïtcin P-C. Cements of yesterday and today: concrete of tomorrow. Cem Concr Res 2000;30:1349–59.

[216] PCI. Implementation of ultra-high-performance-concrete in long-span precast pretensioned elements for concrete buildings and bridges. Precast/Prestressed Concrete Institute; 2020.

[217] Fehling E, Schmidt M, Walraven J, Leutbecher T, Fröhlich S. Ultra-high performance concrete UHPC: Fundamentals, design, examples. John Wiley & Sons; 2015.

[218] Rebentrost M, Wight G, Fehling E. Experience and applications of ultra-high performance concrete in Asia. vol. 10, 2008, p. 19–30.

[219] Rebentrost M, Wight G. Experience and applications of ultra-high performance concrete, 2008.

[220] Lafarge North America Inc. Ductal n.d.

[221] Repette W. Concreto de Ultra-Alto Desempenho (UHPC) – Novas fronteiras e oportunidades na indústria de pré-fabricados, Estruturas Pré-Fabricadas de Concreto - Sustentabilidade, Produtividade, Inovação e Tecnologia; 2018.

[222] Schmidt M, Fehling E, Bornemann R, Bunje K, Teichmann T. Ultra-high performance concrete: Perspective for the precast concrete industry. Betonw Fert 2003;69:16–29.

[223] Tanaka Y, Maekawa K, Kameyama Y, Ohtake A, Musha H, Watanabe N. The innovation and application of UHPFRC bridges in Japan. Des Build UHPFRC 2011:149–88.

[224] Baby F. Contribution à l'identification et la prise en compte du BFUP à l'échelle de la structure [Contribution to identification of UHPFRC tensile constitutive behavior and accounting for structural design]. University of Paris-Est, 2012.

[225] Salehi H, Burgueno R. Emerging artificial intelligence methods in structural engineering. Eng Struct 2018;171:170–89.

[226] Salehi H, Biswas S, Burgueño R. Data interpretation framework integrating machine learning and pattern recognition for self-powered data-driven damage identification with harvested energy variations. Eng Appl Artif Intell 2019;86:136–53.

[227] Saeidpour A, Chorzepa MG, Christian J, Durham S. Parameterized fragility assessment of bridges subjected to hurricane events using metamodels and multiple environmental parameters. J Infrastruct Syst 2018;24:04018031.

[228] Gul M, Catbas FN. Statistical pattern recognition for Structural Health Monitoring using time series modeling: Theory and experimental verifications. Mech Syst Signal Process 2009;23:2192–204.

[229] Gui G, Pan H, Lin Z, Li Y, Yuan Z. Data-driven support vector machine with optimization techniques for structural health monitoring and damage detection. KSCE J Civ Eng 2017;21:523–34.

[230] Cheung A, Cabrera C, Sarabandi P, Nair K, Kiremidjian A, Wenzel H. The application of statistical pattern recognition methods for damage detection to field data. Smart Mater Struct 2008;17:065023.

[231] Salehi H, Das S, Chakrabartty S, Biswas S, Burgueño R. Structural damage identification using image-based pattern recognition on event-based binary data generated from self-powered sensor networks. Struct Control Health Monit 2018;25:e2135.

[232] Salehi H, Das S, Chakrabartty S, Biswas S, Burgueño R. Damage identification in aircraft structures with self-powered sensing technology: A machine learning approach. Struct Control Health Monit 2018;25:e2262.

[233] Salehi H, Chakrabartty S, Biswas S, Burgueño R. Localized damage identification in plate-like structures using self-powered sensor data: A pattern recognition strategy. Measurement 2019;135:23–38.

[234] Salehi H, Burgueño R. Pattern recognition framework using asynchronous discrete binary data for condition and damage assessment in plate-like structures. J Intell Mater Syst Struct 2019;30:1200–15.

[235] Salehi H, Das S, Biswas S, Burgueño R. Data mining methodology employing artificial intelligence and a probabilistic approach for energy-efficient structural health monitoring with noisy and delayed signals. Expert Syst Appl 2019;135:259–72.

[236] Jeong S, Hou R, Lynch JP, Sohn H, Law KH. A scalable cloud-based cyberinfrastructure platform for bridge monitoring. Struct Infrastruct Eng 2019;15:82–102.

[237] Salehi H, Das S, Chakrabartty S, Biswas S, Burgueño R. An algorithmic framework for reconstruction of time-delayed and incomplete binary signals from an energy-lean structural health monitoring system. Eng Struct 2019;180:603–20.

[238] Jeong S, Ferguson M, Hou R, Lynch JP, Sohn H, Law KH. Sensor data reconstruction using bidirectional recurrent neural network with application to bridge monitoring. Adv Eng Inform 2019;42:100991.

[239] Saeidpour A, Chorzepa MG, Christian J, Durham S. Probabilistic hurricane risk analysis of coastal bridges incorporating extreme wave statistics. Eng Struct 2019;182:379–90.

[240] Yan K, Shi C. Prediction of elastic modulus of normal and high strength concrete by support vector machine. Constr Build Mater 2010;24:1479–85.

[241] Dantas ATA, Leite MB, de Jesus Nagahama K. Prediction of compressive strength of concrete containing construction and demolition waste using artificial neural networks. Constr Build Mater 2013;38:717–22.

[242] Siddique R, Aggarwal P, Aggarwal Y. Prediction of compressive strength of self-compacting concrete containing bottom ash using artificial neural networks. Adv Eng Softw 2011;42:780–6.

[243] Naser M, Zhou H. Machine Learning to Derive Unified Material Models for Steel Under Fire Conditions. Intell. Data Anal. Decis.-Support Syst. Hazard Mitig., Springer; 2020, p. 213–25.

[244] Wang Z-L, Adachi Y. Property prediction and properties-to-microstructure inverse analysis of steels by a machine-learning approach. Mater Sci Eng A 2019;744:661–70.

[245] Guo S, Yu J, Liu X, Wang C, Jiang Q. A predicting model for properties of steel using the industrial big data based on machine learning. Comput Mater Sci 2019;160:95–104.

[246] Rafiei MH, Khushefati WH, Demirboga R, Adeli H. Neural Network, Machine Learning, and Evolutionary Approaches for Concrete Material Characterization. ACI Mater J 2016;113.

[247] Chou J-S, Tsai C-F, Pham A-D, Lu Y-H. Machine learning in concrete strength simulations: Multi-nation data analytics. Constr Build Mater 2014;73:771–80.

[248] Reddy TA, Devi KR, Gangashetty SV. Multilayer feedforward neural network models for pattern recognition tasks in earthquake engineering, Springer; 2011, p. 154–62.

[249] González MP, Zapico JL. Seismic damage identification in buildings using neural networks and modal data. Comput Struct 2008;86:416–26.

[250] Zhang Y, Burton HV, Sun H, Shokrabadi M. A machine learning framework for assessing post-earthquake structural safety. Struct Saf 2018;72:1–16.

[251] Xie Y, Ebad Sichani M, Padgett JE, DesRoches R. The promise of implementing machine learning in earthquake engineering: A state-of-the-art review. Earthq Spectra 2020:8755293020919419.

[252] Vu D-T, Hoang N-D. Punching shear capacity estimation of FRP-reinforced concrete slabs using a hybrid machine learning approach. Struct Infrastruct Eng 2016;12:1153–61.

[253] Lee S, Lee C. Prediction of shear strength of FRP-reinforced concrete flexural members without stirrups using artificial neural networks. Eng Struct 2014;61:99–112.

[254] Naser M. Machine Learning Assessment of Fiber-Reinforced Polymer-Strengthened and Reinforced Concrete Members. Struct J 2020;117:237–51.

[255] Gandomi AH, Alavi AH, Arjmandi P, Aghaeifar A, Seyednour R. Genetic programming and orthogonal least squares: a hybrid approach to modeling the compressive strength of CFRP-confined concrete cylinders. J Mech Mater Struct 2010;5:735–53.

[256] Naser M, Seitllari A. Concrete under fire: an assessment through intelligent pattern recognition. Eng Comput 2019:1–14.

[257] Castelli M, Vanneschi L, Silva S. Prediction of high performance concrete strength using genetic programming with geometric semantic genetic operators. Expert Syst Appl 2013;40:6856–62.

[258] Kara IF. Prediction of shear strength of FRP-reinforced concrete beams without stirrups based on genetic programming. Adv Eng Softw 2011;42:295–304.

[259] Solhmirzaei R, Salehi H, Kodur V, Naser M. Machine learning framework for predicting failure mode and shear capacity of ultra high performance concrete beams. Eng Struct 2020;224:111221.

[260] Reich Y. Machine learning techniques for civil engineering problems. Comput Civ Infrastruct Eng 1997;12:295–310.

[261] Lim W-Y, Hong S-G. Shear Tests for Ultra-High Performance Fiber Reinforced Concrete (UHPFRC) Beams with Shear Reinforcement. Int J Concr Struct Mater 2016;10:177–88. https://doi.org/10.1007/s40069-016-0145-8.

[262] Bermudez M, Hung C-C. Shear Behavior of Ultra-High Performance Hybrid Fiber Reinforced Concrete Beams. vol. 2, Iowa State University Digital Press; 2019.

[263] Yavaş A, Hasgul U, Turker K, Birol T. Effective fiber type investigation on the shear behavior of ultrahigh-performance fiber-reinforced concrete beams. Adv Struct Eng 2019;22:1591–605.

[264] Hasgul U, Yavas A, Birol T, Turker K. Steel Fiber Use as Shear Reinforcement on I-Shaped UHP-FRC Beams. Appl Sci 2019;9:5526.

[265] Mészöly T, Randl N. Shear behavior of fiber-reinforced ultra-high performance concrete beams. Eng Struct 2018;168:119–27.

[266] Aziz OQ, Yaseen SA. Optimum Position of Shear Reinforcement of High-Strength Reinforced Concrete Beams. Eng Technol J 2013;31:42–52.

[267] Qi J, Ding X, Wang Z, Hu Y. Shear strength of fiber-reinforced high-strength steel ultra-high-performance concrete beams based on refined calculation of compression zone depth considering concrete tension. Adv Struct Eng 2019;22:2006–18.

[268] Jin L-Z, Chen X, Fu F, Deng X-F, Qian K. Shear strength of fibre-reinforced reactive powder concrete I-shaped beam without stirrups. Mag Concr Res 2019:1–13.

[269] Kamal M, Safan M, Etman Z, Salama R. Behavior and strength of beams cast with ultra high strength concrete containing different types of fibers. HBRC J 2014;10:55–63.

[270] Hegger J, Bertram G. Shear carrying capacity of ultra-high performance concrete beams. Tailor Made Concr Struct 2008:341–7.

[271] Hegger J, Tuchlinski D, Kommer B. Bond anchorage behavior and shear capacity of ultra high performance concrete beams, 2004, p. 351–60.

[272] Bae BI, Choi HK, Choi CS. Flexural and Shear Capacity Evaluation of Reinforced Ultra-High Strength Concrete Members with Steel Rebars. vol. 577, Trans Tech Publ; 2014, p. 17–20.

[273] Yousef AM, Tahwia AM, Marami NA. Minimum shear reinforcement for ultra-high performance fiber reinforced concrete deep beams. Constr Build Mater 2018;184:177–85.

[274] Yaseen SA. An Experimental Study on the Shear Strength of High-performance Reinforced Concrete Deep Beams without Stirrups. Eng Technol J 2016;34:2123–39.

[275] Pourbaba M, Sadaghian H, Mirmiran A. A comparative study of flexural and shear behavior of ultra-high-performance fiber-reinforced concrete beams. Adv Struct Eng 2019:1727–38. https://doi.org/10.1177/1369433218823848.

[276] Rossi P, Daviau-Desnoyers D, Tailhan J-L. Probabilistic numerical model of cracking in ultra-high performance fibre reinforced concrete (UHPFRC) beams subjected to shear loading. Cem Concr Compos 2018;90:119–25.

[277] Cao X, Deng X-F, Jin L-Z, Fu F, Qian K. Shear capacity of reactive powder concrete beams using high-strength steel reinforcement. Proc Inst Civ Eng-Struct Build 2019:1–16.

[278] Magureanu C, Sosa I, Negrutiu C, Heghes B. Bending and shear behavior of ultra-high performance fiber reinforced concrete. High Perform Struct Mater V 2010;112:79.

[279] Yavas A, Goker CO. Impact of Reinforcement Ratio on Shear Behavior of I-Shaped UHPC Beams with and without Fiber Shear Reinforcement. Materials 2020;13:1525.

[280] Wu X, Han S-M. First diagonal cracking and ultimate shear of I-shaped reinforced girders of ultra high performance fiber reinforced concrete without stirrup. Int J Concr Struct Mater 2009;3:47–56.

[281] Pansuk W, Nguyen TN, Sato Y, Den Uijl J, Walraven J. Shear capacity of high performance fiber reinforced concrete I-beams. Constr Build Mater 2017;157:182–93.

[282] Yang I-H, Joh C, Kim B-S. Flexural strength of large-scale ultra high performance concrete prestressed T-beams. Can J Civ Eng 2011;38:1185+.

[283] Gomaa S, Alnaggar M. Transitioning from Shear to Flexural Failure of UHPC Beams by Varying Fiber Content. vol. 2, Iowa State University Digital Press; 2019.

[284] Chen S, Zhang R, Jia L-J, Wang J-Y. Flexural behaviour of rebar-reinforced ultra-high-performance concrete beams. Mag Concr Res 2018;70:997–1015.

[285] Wahba K, Marzouk H, Dawood N. Structural Behavior of UHPFRC Beams without Stirrups, 2012.

[286] Smarzewski P. Hybrid fibres as shear reinforcement in high-performance concrete beams with and without openings. Appl Sci 2018;8:2070.

[287] Zagon R, Matthys S, Kiss Z. Shear behaviour of SFR-UHPC I-shaped beams. Constr Build Mater 2016;124:258–68.

[288] Zheng H, Fang Z, Chen B. Experimental study on shear behavior of prestressed reactive powder concrete I-girders. Front Struct Civ Eng 2019;13:618–27.

[289] Pourbaba M, Sadaghian H, Mirmiran A. Flexural Response of UHPFRC Beams Reinforced with Steel Rebars. Adv Civ Eng Mater 2019;8:411–30.

[290] Mohammed M. Shear Behavior of Reactive Powder Concrete Beams with and without Coarse Aggregate. AUT J Civ Eng 2018;2:87–96.

[291] Ridha MM, Sarsam KF, Al-Shaarbaf IA. Experimental study and shear strength prediction for reactive powder concrete beams. Case Stud Constr Mater 2018;8:434–46.

[292] Kahanji C, Ali F, Nadjai A. Structural performance of ultra-high-performance fiber-reinforced concrete beams. Struct Concr 2017;18:249–58.

[293] Ţibea C, Bompa DV. Ultimate shear response of ultra-high-performance steel fibre-reinforced concrete elements. Arch Civ Mech Eng 2020;20:1–16.

[294] Hasgul U, Turker K, Birol T, Yavas A. Flexural behavior of ultra-high-performance fiber reinforced concrete beams with low and high reinforcement ratios. Struct Concr 2018;19:1577–90.

[295] Qiu M, Shao X, Zhu Y, Zhan J, Yan B, Wang Y. Experimental investigation on flexural cracking behavior of ultrahigh performance concrete beams. Struct Concr 2020.

[296] Khalil WI, Tayfur Y. Flexural strength of fibrous ultra high performance reinforced concrete beams. ARPN J Eng Appl Sci 2013;8:200–14.

[297] Shafieifar M, Farzad M, Azizinamini A. A comparison of existing analytical methods to predict the flexural capacity of Ultra High Performance Concrete (UHPC) beams. Constr Build Mater 2018;172:10–8.

[298] Cortes C, Vapnik V. Support-vector networks. Mach Learn 1995;20:273–97.

[299] Scholkopf B, Smola AJ. Learning with kernels: support vector machines, regularization, optimization, and beyond. MIT press; 2001.

[300] Hassoun MH. Fundamentals of artificial neural networks. MIT press; 1995.

[301] Zhang G, Patuwo BE, Hu MY. Forecasting with artificial neural networks:: The state of the art. Int J Forecast 1998;14:35–62.

[302] Keller JM, Gray MR, Givens JA. A fuzzy k-nearest neighbor algorithm. IEEE Trans Syst Man Cybern 1985:580–5.

[303] Martin M. On-line support vector machine regression, Springer; 2002, p. 282–94.

[304] Yang H, Chan L, King I. Support vector machine regression for volatile stock market prediction, Springer; 2002, p. 391–6.

[305] Luu K, Ricanek K, Bui TD, Suen CY. Age estimation using active appearance models and support vector machine regression, IEEE; 2009, p. 1–5.

[306] Koza JR, Koza JR. Genetic programming: on the programming of computers by means of natural selection. vol. 1. MIT press; 1992.

[307] Imam M, Vandewalle L, Mortelmans F. Shear–moment analysis of reinforced high strength concrete beams containing steel fibres. Can J Civ Eng 1995;22:462–70.

[308] Sharma A. Shear strength of steel fiber reinforced concrete beams. vol. 83, 1986, p. 624–8.

[309] Naser M. AI-based cognitive framework for evaluating response of concrete structures in extreme conditions. Eng Appl Artif Intell 2019;81:437–49.

[310] ACI Committee 544. Design considerations for steel fiber reinforced concrete (ACI 544.4R), American Concrete Institute; n.d.

[311] Henager CH, Doherty TJ. Analysis of reinforced fibrous concrete beams. J Struct Div 1976;102.

[312] Swamy R, Sa'ad A. Deformation and ultimate strength in flexure of reinforced concrete beams made with steel fiber concrete. vol. 78, 1981, p. 395–405.

[313] Hassoun M, Sahebjam K. Plastic hinge in two-span reinforced concrete beams containing steel fibers. Proc Can Soc Civ Eng 1985:119–39.